UNIVERSITY OF CALIFORNIA, MERCED

On the Interactions between Charges, Phonons and Photons in Electric Field Tunable Quantum Dot Molecules

A dissertation submitted in partial satisfaction of the
requirements for the degree of
Doctor of Philosophy

in

Physics

by

Mark L. Kerfoot

Committee in charge:

Professor Kevin Mitchell, Chair
Professor David Kelley
Professor Michael Scheibner

2015

The dissertation of Mark L. Kerfoot, titled On the Interactions between Charges, Phonons and Photons in Electric Field Tunable Quantum Dot Molecules, is approved, and it is acceptable in quality and form for publication on microfilm and electronically:

Chair _____ Date _____

Professor Kevin Mitchell

_____ Date _____

Professor David Kelley

_____ Date _____

Professor Michael Scheibner

University of California, Merced

2015

Contents

Abstract

On the Interactions between Charges, Phonons and Photons in Electric Field Tunable Quantum Dot Molecules

by

Mark L. Kerfoot

Doctor of Philosophy in Physics

University of California, Merced

Professor Kevin Mitchell, Chair

This dissertation focuses on the optical properties of single InAs/GaAs quantum dot molecules. A quantum dot molecule consists of a pair of quantum dots coupled by a nanometer scale tunneling barrier. Compared to single quantum dots, quantum dot molecules provide greatly enhanced versatility – with the ease of an electric field control, one gains broad flexibility to tune electronic energy levels and manipulate particle tunneling within a QDM. As a consequence, individual QDMs are being intensely studied as controllable interfaces of charge, spin and photonic quantum states at the single particle level. On the other hand, phonons – the quantized vibrations of the underlying crystal lattice – have mostly been left outside the realm of coherent control. In the domain of solid-state quantum technologies, the ubiquitous phonons are mainly considered for the limitations they impose. Omnipresent electron-phonon interactions and the predominantly dissipative nature of phonons are typically a major source of decoherence of the atom-like quantum states hosted by low-dimensional solid-state structures, such as QDMs.

Here, we report experimental and theoretical results on the interactions between charges, photons and phonons in electric field tunable quantum dot molecules. Using an effective mass perturbation model, we compute the low energy biexciton states of a quantum dot molecule and apply them to provide a theoretical description of the dipole-dipole interaction between two excitons occupying separate dots in a quantum dot molecule. The expected properties of these so called dipolar states are presented, and we highlight their potential application as a switch for manipulating the transition energy and tunneling properties of the ground state neutral exciton. We then present results from a comprehensive investigation of the quantum confined Stark effect in quantum dot molecules, in which we studied the electric-field dependent energy shifts of exciton states as a function of the tunneling barrier width. Our experimental and computational results reveal that molecular wavefunction formation in quantum dot

molecules strongly affects the quantum confined Stark effect, even as the dots are tuned far from resonance for particle tunneling.

This dissertation culminates with our report of a novel mechanism by which phonons are made non-dissipative and coherent via electric field control and the optically driven formation of a molecular polaron in a quantum dot molecule. The coherent interaction of a single optical phonon with individual electronic states is revealed via a Fano-type quantum interference that produces a phonon-induced transparency in the optical absorption of individual quantum dot molecules. Experimentally, we find that the transparency is widely tunable by electronic and optical means, and provides a mechanism for amplifying weak coupling channels. This work is significant in that it demonstrates a specific mechanism by which typically incoherent and dissipative phonons are made to behave in a coherent and non-dissipative manner. As such, we demonstrate that phonons may enter the realm of mutual control of quantum states on the single particle level, which so far has been dominated by photons, electrons and spins.

List of Figures

List of Tables

List of Abbreviations

0D	zero-dimensional
AC	anti-crossing
CGS	crystal ground state
CW	continuous wave
e-h	electron-hole
MO	microscope objective
NA	numerical aperture
NRL	Naval Research Laboratory
PL	photoluminescence
PLE	photoluminescence excitation
QCSE	quantum confined Stark effect
QD	quantum dot
QDM	quantum dot molecule
ROI	region of interest
SK	Stranski-Krastanov

Acknowledgments

I would like to thank my family and friends for supporting me during graduate school (and before). I could not have done it without your help! Thank you to my advisor Prof. Michael Scheibner, my committee members Prof. Kevin Mitchell and Prof. David Kelley, my collaborators at Ohio University Prof. Eric Stinaff and Prof. Sasha Govorov. Thank you to the folks that supported me at the University of California, Merced, including my graduate student friends and classmates, my colleagues in the Quantum Matter Group, faculty and staff in the School of Natural Sciences, faculty and staff at the Center for Research and Teaching Excellence and the Graduate Division staff.

Mark L. Kerfoot

mkerfoot2@ucmerced.edu

EDUCATION

University of California, Merced — May 2015
Ph.D. Physics
Overall GPA: 3.93

California State University, Sacramento — May 2008
B.S. Physics, Minor in Mathematics
Senior Award for Physics, 2007
Sigma Pi Sigma Honors Society Inductee, 2006

American River College, Sacramento — June 2002 - May 2004 *(enrolled)*
Physical Sciences Student

University of California, Davis — June 1999
B.A. International Relations, Minor in Economics
Graduated with Honors

NOTABLE SKILLS

Multi-lingual: Fluent in English (native language) and high proficiency in Spanish.
Programming Languages: Mathematica, MATLAB, LabVIEW, LaTeX, C, R.

RESEARCH EXPERIENCE

Semiconductor Optics — September 2009 – present
University of California, Merced

- Collaborated with research advisor to set-up and develop the Quantum Matter Group Laboratory at UC Merced for optical spectroscopy of man-made nanostructures.
- Investigated few-particle interactions between electronic states, photons and phonons in single InAs/GaAs quantum dot molecules (QDMs).
- Key member of the research team that discovered the molecular polaron, a novel quasi-particle in QDM systems. Demonstrated a highly tunable optical transparency in QDM systems via Fano resonance of the molecular polaron.

Physics Education — August 2010 – April 2012
University of California, Merced

- Developed, implemented and assessed a supplemental curriculum to provide early exposure to advanced concepts in an introductory modern physics course.
- Study results revealed improved understanding of quantum mechanics for a majority of students and a strong, positive correlation between final grade and participation in the supplemental curriculum.

Biophysics — August 2008 – August 2009
University of California, Merced

- Conducted x-ray diffraction studies and atomic force microscope imaging of lipid mixtures in solution, investigating the role of cholesterol and lipid constituents in cell membrane structure.

Computational Physics — June 2007 – May 2008
California State University, Sacramento

- Developed an algorithm in Mathematica to optimize the performance of a three prism laser tracking system (undergraduate senior research project).

Electronics and Instrumentation Summers 2005 – 2006
California State University, Sacramento

- Designed and assembled two temperature regulated ovens and a photo-ionization chamber for use with a gas chromatography analyzer.

TEACHING EXPERIENCE

Adjunct Instructor Spring 2015 – present
Fresno City College

- Instructor of record for PHYS 2B, a non-calculus level introductory physics course covering electromagnetism, optics and modern physics.
- Performed all course teaching functions, including design and instruction of lectures, laboratory instruction, design of homework and exams, grading, gradebook management and office hours.

Teaching Assistant Fall 2008 – Fall 2014
University of California, Merced

- Taught discussion sections and laboratory sections, graded homework and exams, wrote quiz and exam problems, proctored exams, managed student gradebook and held office hours.
- Physics Courses: Introductory mechanics, electromagnetism and optics for physical science, chemistry and engineering majors; Introductory calculus-level mechanics, thermodynamics, fluids, waves, electromagnetism and optics for premedical and bioscience majors; Modern physics (lower division). Waves and vibrations; Special relativity (upper division).
- Math Courses: Multivariable calculus; Linear algebra and differential equations; Probability and statistics.

Special Services Tutor Fall 2007
California State University, Sacramento

- Physics tutor for students with learning disabilities.

Learning Assistant Spring 2006
California State University, Sacramento

- Assisted the professor for 2.5 hours per week with instruction of an enquiry-based physics course for future elementary school teachers.
- Independently planned and managed a subset of course lesson plans, assisted in leading class discussions, offered guidance during group activities.

Group Physics Tutor Fall 2003 – Spring 2004
American River College, Merced

- Recruited 10−15 students per semester to participate in a voluntary 2-hour weekly tutoring section for community college physics courses.
- Developed problem sets and group activities for students, offered guidance during group activities, coordinated weekly with course professor on content and performance.
- Completed concurrently a course on strategies for effective group learning.

Volunteer Tutor Fall 2004 – Spring 2008
California State University, Sacramento

- Volunteered several hours each week to assist students in the physics tutoring center.

PUBLICATIONS

M. Kerfoot, A. Govorov, C. Czarnocki, D. Lu, Y. Gad, A. Bracker, D. Gammon, M. Scheibner, *Optophononics with Coupled Quantum Dots*, Nat. Commun. 5:3299 (2014).

S. Ramanathan, G. Petersen, K. Wijesundara, R. Thota, E. A. Stinaff, **M. Kerfoot**, M. Scheibner, A. Bracker, D. Gammon, *Quantum-confined Stark effects in coupled InAs/GaAs quantum dots*, APL 102, 213101 (2013).

M. Kerfoot, *Thinking like an Expert: Scaffolding Mathematical Concepts in Physics Courses*, in Creating Academic Community for First-Generation College Students: A Graduate Student Instructor Guidebook, Center for Research on Teaching Excellence, UC Merced. eScholarship, University of California (2012).

PRESENTATIONS

"Artificial Matter for Novel Technologies, Frontiers in Science and Engineering Talk, Castle Air Museum, Atwater, CA, March 2014.

"Custom Physics with Artificial Atoms, Science Caf Talk, Coffee Bandits, Merced, CA, March 2014.

"Phonon-induced Transparency in Quantum Dot Molecules", Poster, EP2DS-20/MSS-16, Wroclaw University of Technology, Wroclaw, Poland, July 2013.

"Exploring Quantum Mechanics with Artificial Atoms and Molecules", CSUS Physics and Astronomy Colloquium Series, May 2013.

"Phonon-induced Transparency in Quantum Dot Molecules", Contributed Talk, APS March Meeting, Baltimore Convention Center, March 2013.

"Exploring Quantum Mechanics with Artificial Atoms and Molecules", ARC Physics for Lunch, October 2012.

"Resonant Fluorescence from Quantum Dot Excitonic Transitions", Contributed Talk, APS March Meeting, Dallas Convention Center, March 2011.

"Long-range Interactions for Networking Quantum Structures (LInQS)", Qualifying Examination for Advancement to Candidacy for Ph.D. in Physics, University of California, Merced, December 2010.

"Analysis and Optimization of a 3-Element Doublet Prism System for Laser Beam Steering", CSUS Physics and Astronomy Colloquium Series, Senior Project Talk, May 2008.

"Special Relativity and the Geometry of Space-time", ARC Physics for Lunch, December 2005.

Chapter 1

Introduction

This dissertation focuses on investigations of coupled pairs of solid state semiconductor quantum dots (QDs), commonly known as quantum dot molecules (QDMs). Quantum dots are often referred to as artificial atoms due to their atom-like spectra, which exhibit ultra-sharp, discrete transition lines. This is a consequence of their nanometer-scale size, which leads to quantum confinement in all three dimensions. The first solid state semiconductor QDs were developed by researchers in the early 1990's [1, 2, 3]. By the mid-1990's, the innovation of single QD optical spectroscopy allowed researchers to perform detailed studies of individual QDs [4, 5, 6]. Since then, numerous studies of QDs under the influence of external fields (electric, magnetic and optical) have revealed that QDs have atom-like fine structures and can be made to exhibit all the features of a resonantly driven two-level system [6, 7, 8, 9, 10, 11, 12, 13, 14]. As a consequence of their atom-like properties and the maturity of semiconductor processing techniques, much applied research has focused on developing electronic and spin states in QDs as potential qubits and single photon emitters for use in quantum information technologies [15, 16, 17, 18, 19, 20, 21, 22].

Quantum dot molecules consist of two individual QDs separated by a nanometer scale tunneling barrier. Compared to single QDs, QDMs offer improved versatility and manifest novel physical properties. Using a built-in electric field control, QDM electronic energy levels may be Stark shifted over a range of tens of meV [23, 24]. By tuning the electronic energy levels in separate QDs to resonance, one observes a hallmark feature of QDMs: the tunneling of charge carriers (electrons and holes) between separate dots and the formation of delocalized carrier wavefunctions that spread across the entire QDM [25, 26, 27]. Like QDs, QDMs are considered an attractive candidate for implementing quantum information technologies and are being intensely studied as controllable interfaces of charge, spin and photonic states at the single particle level [28, 29, 30, 31, 32].

This dissertation presents results from investigations of the optical properties of individual QDMs under the influence of different internal and external perturbation

mechanisms. Chapter 5 presents a theoretical calculation of the low-energy biexciton states in a QDM, computed from a perturbation theory model. The quantitative expressions for the biexciton states and their transitions are of general interest given the current proposals for using the biexciton-to-crystal ground state emission cascade in QDMs as a potential source of entangled photons [33, 34, 35]. We make use of the biexciton states to provide a theoretical description and analysis of a class of dipolar biexciton transitions. Such transitions have the potential for realizing sensitive charge detection in QDMs. They involve a dipole coupling interaction mechanism that could potentially be used as a switch for shifting the ground state exciton transition energy or manipulating particle tunneling in a QDM.

Chapter 6 presents results from a study of the quantum confined Stark shift of exciton states in QDMs. The experimental dependence of the permanent dipole moment and the polarizability of direct and indirect exciton states as a function of tunneling barrier width have been measured. We observe differences in the Stark shifts of QDMs compared to single QDs, which are attributed to the formation of molecular wavefunctions in QDMs. This chapter is the product of a collaboration with researchers from Ohio University, where the experiments were conducted. My contributions to the project included detailed clarifications of the theoretical model of the Stark shift and the role of resonant versus non-resonant tunneling, culminating in significant edits and additions to the paper manuscript. The results presented in this Chapter were previously published in the journal Applied Physics Letters [36].

In Chapter 7, we demonstrate a novel phonon-induced transparency in QDMs. This phonon-induced transparency is realized via the formation of a molecular polaron, the result of a Fano-type quantum interference. To validate the Fano effect, we provide a theoretical model that is in good qualitative agreement with the experimental data. Experimentally, we find that the transparency is widely tunable by electronic and optical means, and provides a mechanism for amplifying weak coupling channels. This work is significant in that it demonstrates a mechanism by which typically incoherent and dissipative phonons are made to behave in a coherent and non-dissipative manner. As such, we demonstrate that phonons may enter the realm of mutual control of quantum states on the single particle level, which so far has been dominated by photons, electrons and spins. This work represents a collaborative effort. The experimental measurements and data analysis were performed at the University of California, Merced by members of the Quantum Matter Group, while the theoretical model was provided by A. O. Govorov of Ohio University. The results presented in this Chapter were previously published in the journal Nature Communications [37].

The contents of this dissertation are organized as follows. Chapter 2 details the fabrication methodology of the quantum dot molecules that we have investigated. In Chapter 3, we provide a theoretical description of semiconductor QDs and QDMs, laser driven two-level systems, Fano interference, phonons and polarons. The theory section is given in significant detail in order to make the dissertation theoretically clear

and self-contained. In Chapter 4, we describe the experimental methods employed in these investigations. The procedures and methodologies are presented in sufficient detail in hope that they may be useful to current/future persons working in the Quantum Matter Group at the University of California, Merced. Chapters 5 through 7 present the theoretical and experimental results of our investigations and Chapter 8 is the conclusion. The dissertation also contains the following appendices: (i) Appendix A presents model calculations of the single particle wavefunctions in a QD, (ii) Appendix B describes the laboratory procedure for generating a PL Bias Map in the Quantum Matter Group at the University of California, Merced, (iii) Appendix C presents the complete biexciton Hamiltonian matrix described in Chapter 5 and (iv) Appendix D derives the power dependence formulas used in Chapter 7 to describe the non-linearity of the phonon-induced Fano effect.

Chapter 2

Sample Fabrication Methodology

2.1 Self-Assembled InAs/GaAs QDMs

The InAs/GaAs quantum dot molecules used for the optical studies in this dissertation were provided by the United States Naval Research Laboratory (NRL). The QDMs were engineered to exhibit hole tunneling using the Stranski-Krastanov (SK) self-assembled growth mode and were embedded in a Schottky diode structure to provide electric field control [2, 23, 38].

QDs are formed in the SK growth mode by using atomic layer deposition methods to control the growth of solid state crystals on a substrate [1]. As shown in Figure 2.1, hot gases of semiconductor material are introduced into an evacuated chamber, where they condense onto the substrate and crystallize one monolayer at a time. The height of the crystal growth is controlled via the temperature, concentration and deposition

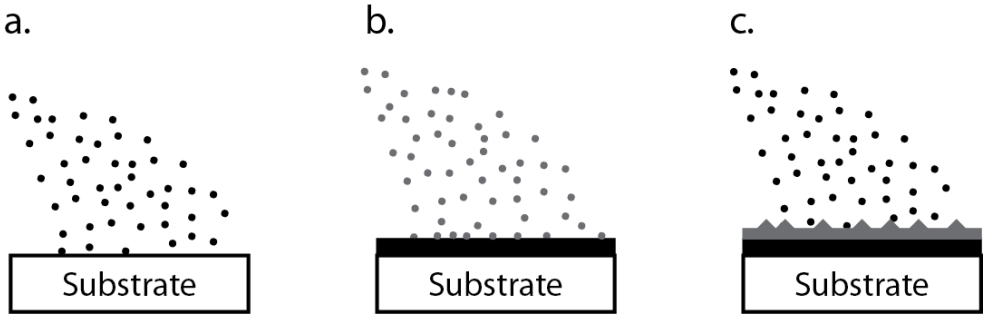

Figure 2.1: SK growth mode of self-assembled QDs. (a) A gas beam of semiconductor material is deposited on a substrate, forming a semiconductor crystal one monolayer at a time. (b) A second semiconductor material with a different lattice constant is deposited, which self-organizes into nano-sized islands atop a wetting layer. (C) The nascent QDs are then covered with the initial semiconductor material.

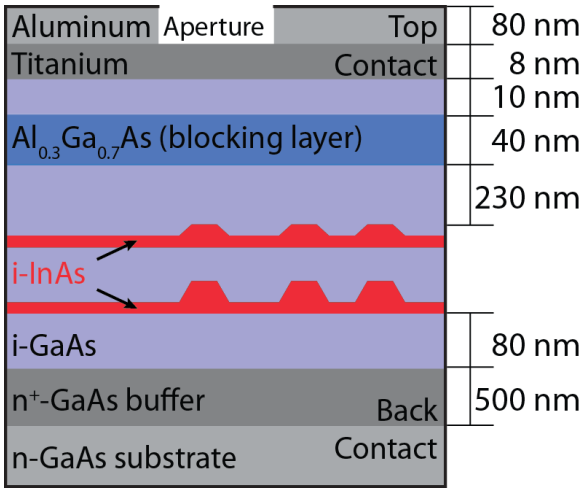

Figure 2.2: Layer structure of the InAs/GaAs QDM samples studied in this dissertation.

time [39]. To create QDs, layers of lattice-mismatched materials – semiconductors with a common crystal structure, but different lattice constants – are deposited on top of one another. A layer of the first material is initially deposited on the substrate. The second material is then deposited and forms a thin layer, strained by the first material, called the *wetting layer*. After the wetting layer reaches a characteristic height, the second material self-organizes into nano-sized islands to relieve the strain of the lattice mismatch.[1] These islands are then covered with the first material to form embedded, solid state QDs. QDMs may be formed by growing a second layer of QDs, which preferentially align atop the initial QDs due to residual strain, thereby creating vertically stacked QD pairs [3].

The layer structure of our InAs/GaAs QDM samples is shown in Figure 2.2. The samples are grown on a (001) n-type GaAs substrate. The layer structure consists of a 500 nm buffer of n^+-GaAs (heavily doped with Te at $\sim 5 \times 10^{17}\text{cm}^{-3}$), 80 nm of i-GaAs (i.e., undoped or intrinsic GaAs), the i-InAs QDMs, 230 nm of i-GaAs, a 40 nm blocking layer of $Al_{0.3}Ga_{0.7}As$, a 10 nm capping layer of i-GaAs, an 8 nm top contact of titanium and an 80 nm aluminum shadow mask. The n^+-GaAs buffer and titanium contacts form an $n-i$ Schottky diode that provides a tunable electric field along the growth direction when a bias voltage is applied. The blocking layer provides a large band gap material to reduce carrier tunneling between the QDs and the metal layers. The aluminum shadow mask is equipped with apertures on the order of 1 μm diameter to isolate single QDMs for optical study. The finished sample

[1]The lattice mismatch of InAs and GaAs is 7% and the InAs wetting layer has a thickness of 1.75 monolayers, or about ∼0.6 nm [2].

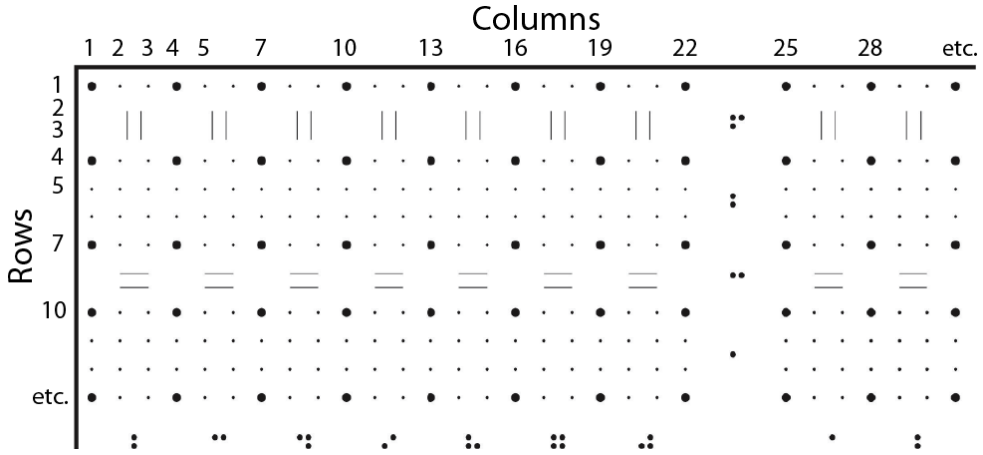

Figure 2.3: An aperture map, showing patterned features that have been etched into a QDM sample to locate apertures for optical investigation. The smallest dots indicate the location of the viewing apertures that may contain anywhere from zero to many QDMs. A naming scheme for the sample apertures in terms of numbered rows and columns is illustrated.

is attached to a pin chip with electrical leads so that it can be easily mounted inside the microscopy chamber of a cryostat and connected to an external power supply.

The InAs QDs in our samples have heights ranging from 2.5 to 4.0 nm and base widths of about $20 - 25$ nm. The quantum confinement energy of the QDs is thus dominated by their height. To control QD height, the indium-flush technique is used, whereby the exposed QDs are partially covered with GaAs and then annealed at high temperature [40]. This effectively melts the top of the InAs islands to the height of the GaAs covering layer, producing disk-shaped QDs with nanometer precision height. The coupled QD pairs are separated by a GaAs tunneling barrier, which in our samples range from $2 - 6$ nm thick. To engineer the QDMs for hole tunneling with the $n - i$ Schottky diode, the top QD is grown with a smaller height, and thus greater confinement energy, than the bottom QD [38]. This allows the hole energy levels of the top and bottom QDs to be tuned to resonance when the Schottky diode is operated in reverse bias (see also Figure 3.6 in Section 3.2). In addition, when both dots are nominally set to the same height during fabrication, it is found that the top dots exhibit a higher band gap than the bottom dots. This is attributed to a larger lateral growth of the dots in the upper layer, which causes a different evolution of the dots during the indium flush. Such QDMs, therefore, also predominantly exhibit hole tunneling [38, 41].

The viewing apertures in the aluminum shadow mask are either randomly located (made from Styrofoam balls embedded in the aluminum layer and then blown away) or lithographically etched in a pattern. Figure 2.3 shows a diagram of the aperture

pattern for a lithographically etched sample. In general, the samples are rotated during MBE growth to assure uniform layer deposition. However, the rotation is paused during QD growth in order to establish a density gradient of QDs across the sample. Thus, apertures may be found that contain anywhere from a single to many QDMs.

Chapter 3

Theoretical Background

3.1 Basics of Semiconductor Physics

The Schrödinger Equation

In quantum mechanics, all information about a quantum system is specified by its state vector $|\Psi(t)\rangle$. The time evolution of the state vector is determined by the Hamiltonian operator $\hat{H}$, which contains all physical information about the system, as given by the Schrödinger equation:

$$i\hbar\frac{d}{dt}|\Psi(t)\rangle = \hat{H}|\Psi(t)\rangle, \tag{3.1}$$

where $\hbar$ is the reduced Plank's constant. By expanding equation (3.1) in the basis of position eigenstates, one arrives at the Schrödinger wave equation for the time evolution of the spatial wavefunction $\Psi(\mathbf{r}, t)$:

$$i\hbar\frac{d\Psi(\mathbf{r}, t)}{dt} = \hat{H}\Psi(\mathbf{r}, t). \tag{3.2}$$

For a single particle of mass m subject to a potential $U(\mathbf{r}, t)$, the Hamiltonian is given by:

$$\hat{H} = -\frac{\hbar^2}{2m}\nabla^2 + U(\mathbf{r}, t), \tag{3.3}$$

where the Laplacian operator in Cartesian coordinates is $\nabla^2 = \frac{\partial^2}{\partial x^2} + \frac{\partial^2}{\partial y^2} + \frac{\partial^2}{\partial z^2}$. Inserting (3.3) into equation (3.2), yields the time-dependent Schrödinger equation for a single particle:

$$i\hbar\frac{d\Psi(\mathbf{r}, t)}{dt} = \left(-\frac{\hbar^2}{2m}\nabla^2 + U(\mathbf{r}, t)\right)\Psi(\mathbf{r}, t). \tag{3.4}$$

If the potential $U = U(\mathbf{r})$ is time-independent, we may write the wavefunction as a product of time and position dependent functions:

$$\Psi(\mathbf{r}, t) = \psi(\mathbf{r})\phi(t). \tag{3.5}$$

Applying the method of separation of variables to equation (3.4) yields the following separate equations for the time and position functions:

$$\left(-\frac{\hbar^2}{2m}\nabla^2 + U(\mathbf{r})\right)\psi(\mathbf{r}) = \varepsilon\psi(\mathbf{r}), \tag{3.6a}$$

$$\frac{d\phi(t)}{dt} = -\frac{i}{\hbar}\,\varepsilon\phi(t), \tag{3.6b}$$

where ε is the energy of the system in state $\psi(\mathbf{r})$. The solution of equation (3.6b) is readily found to be $\phi(t) = e^{-i\varepsilon t/\hbar}$, which yields the phase of the particle in state $\psi(\mathbf{r})$. Equation (3.6a) is called the time-independent Schrödinger equation. Solving (3.6a) with appropriate boundary conditions yields the stationary states (i.e., energy eigenstates) of the system and its respective energy levels. Equation (3.6a) represents the fundamental equation to solve in order to calculate the allowed energy levels of a quantum particle subject to a time-independent potential $U(\mathbf{r})$.

Band Structure

The fundamental physics of crystalline solids originates from their geometry – they consist of atoms bound together in a periodic lattice. In principle, the Schrödinger equation for a crystal is a many-body problem involving all the atoms of the crystal. Despite today's computational power, however, such a problem is still intractable to solve. Instead, it is usually sufficient to simply calculate the energy levels of the most highly excited (and weakly bound) valence electrons in order to understand the basic electronic properties of crystalline materials. In this approximation, the nuclei and core electrons are considered to comprise a lattice of stationary ions. Then, the interactions of a single valence electron with the lattice ions and other valence electrons can be represented by a single effective potential $U(\mathbf{r})$. This approximation is known as the *independent particle approximation*. Importantly, regardless of its detailed form, $U(\mathbf{r})$ inherits the periodicity of the crystal lattice. That is, $U(\mathbf{r} + \mathbf{R}) = U(\mathbf{r})$, where $\mathbf{R}$ is any vector with the periodicity of the crystal lattice. Thus, to determine the energy levels of the most weakly bound valence electrons in a crystalline solid, we must solve the time-independent Schrödinger equation of (3.6a) with appropriate

boundary conditions for an independent electron subject to the periodic potential $U(\mathbf{r})$:

$$\left(-\frac{\hbar^2}{2m_e}\nabla^2 + U(\mathbf{r})\right)\psi(\mathbf{r}) = \varepsilon\,\psi(\mathbf{r}), \tag{3.7}$$

where m_e is the electron mass, $\psi(\mathbf{r})$ is the electron wavefunction and ε is the electron energy. Solving this problem leads to Bloch's theorem, which states that the solutions of (3.7) for any such $U(\mathbf{r})$ take the form:

$$\psi_{n\mathbf{k}}(\mathbf{r}) = e^{i\mathbf{k}\cdot\mathbf{r}}\,u_{n\mathbf{k}}(\mathbf{r}), \tag{3.8a}$$

$$\varepsilon_{n\mathbf{k}} = \varepsilon_n(\mathbf{k}), \tag{3.8b}$$

where $\mathbf{k}$ is the Bloch wave vector, $\varepsilon_{n\mathbf{k}}$ is the electron energy in state $\psi_{n\mathbf{k}}$ and the Bloch function $u_{n\mathbf{k}}(\mathbf{r}) = u_{n\mathbf{k}}(\mathbf{r}+\mathbf{R})$ has the periodicity of the crystal lattice. This solution has the form of a plane wave modulated by the periodic Bloch function and is known as a Bloch wavefunction. The subscript n is known as the band index, which represents the fact that many independent eigenstates exist for each wave vector $\mathbf{k}$. In each single energy band n, the electron energy $\varepsilon_{n\mathbf{k}}$ as a function of the Bloch wave vector defines the *dispersion relation*.

The effect of the electron interactions with the ion cores is to generate a series of energy bands with continuous energy levels and energy gaps for which there are no allowed particle states. The distinction between metals, insulators and semiconductors is then determined by the crystal's band structure and how it is populated with Bloch electrons at absolute zero temperature. Since electrons are fermions of spin 1/2, the Pauli exclusion principle allows no more than one electron per quantum state. Thus, each energy eigenstate of equation (3.8a) may be populated by at most two electrons with opposite spin projections. The electron eigenstate is then specified by its spatial wavefunction according to (3.8a) and its spin projection. The occupation of electron states in a crystal at absolute zero then proceeds according to the Pauli principle by first populating the least energetic states in equation (3.8b) and continuing in sequence to higher energies until all the electrons are accommodated.

A crystal behaves like a metal if one or more bands are partly filled, since then there are a continuum of nearby energy states for an electron to move into under the influence of an electric field, permitting electrical conductivity. If the bands are either completely filled or empty, and the filled bands do not overlap in energy with the empty bands, then the crystal cannot conduct electricity at absolute zero and is called either an insulator or semiconductor. The distinction between insulators and semiconductors depends purely on the magnitude of the energy gap separating the highest filled energy band and the lowest unoccupied band. To these most important

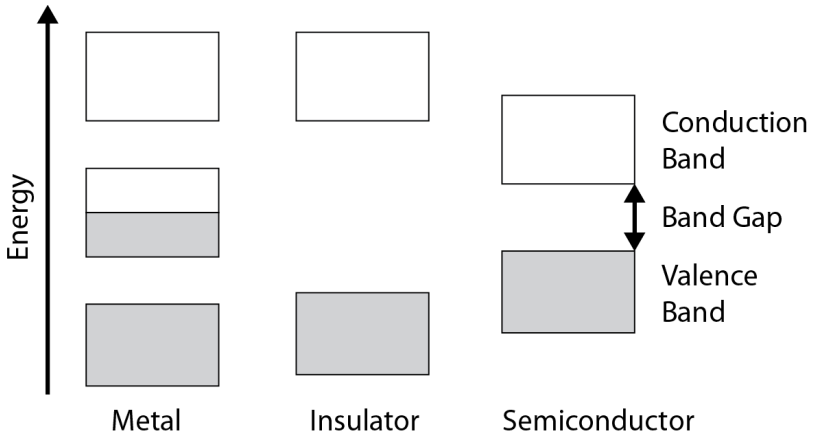

Figure 3.1: Energy band structure and electron occupancy (in gray) of different types of crystalline material at absolute zero temperature. For the semiconductor crystal, the valence band, conduction band and fundamental band gap are indicated.

energy bands, we give the names *valence band* to the highest filled energy band and *conduction band* to the lowest unoccupied energy band. The energy gap separating the valence and conductions bands is called the *fundamental band gap*, or simply the *band gap*. In semiconductors, the band gap is small enough so that thermal energy is sufficient to excite electrons from the valence band into the conduction band and permit electrical conductivity at reasonably low temperatures. Materials with a band gap greater than 3 eV are usually not considered semiconductors. As an example of band gap values at room temperature (300 K), the semiconductors silicon and indium arsenide have gaps of 1.12 eV and 0.35 eV, respectively, while the insulator diamond has a gap of 5.5 eV [42]. Figure 3.1 shows the electron occupancy of energy bands at absolute zero for the different types of crystalline materials [43].

The Effective Mass Approximation for Electrons and Holes

A basic process of interest in semiconductor physics is the excitation of a valence band electron into the conduction band. The electron energy in the conduction band is determined by the dispersion relation in equation (3.8b). Near the energy minimum, this equation is approximately parabolic. For many semiconductors, including those of interest in this dissertation, i.e., InAs and GaAs, this minimum occurs at $\mathbf{k} = 0$ and the conduction band dispersion relation for small $\mathbf{k}$ can be written as:

$$\varepsilon_c(k) = \frac{\hbar^2 k^2}{2m_{eff,e}}. \tag{3.9}$$

Equation (3.9) is known as the *effective mass approximation* for the electron energy in the conduction band [44]. It has the same form as the dispersion relation for a free electron with momentum $\mathbf{p} = \hbar\mathbf{k}$, except that the free electron mass m_e is replaced by the so called *effective mass* $m_{eff,e}$. The effective mass describes the parabolic dependence of $\varepsilon_c(k)$ near its energy minimum and may differ significantly from the free electron mass. For example, in InAs $m_{eff,e} = 0.023m_e$ and in GaAs it is $0.063m_e$ [45, 46]. In general, the effective mass may be anisotropic, in which case different values are associated with different directions in the crystal.

The effective mass approximation provides a powerful simplification for understanding semiconductor physics. It states that conduction band electrons behave like free particles with effective mass $m_{eff,e}$ and quasi-momentum (i.e., crystal momentum) $\mathbf{p} = \hbar\mathbf{k}$ for a given Bloch wave vector. It is widely valid since conduction band electrons typically populate states near the conduction band minimum – also known as the *conduction band edge* – and we will make use of it throughout this dissertation.

The effective mass approximation is equally valid for describing states in the valence band. The excitation of a valence band electron into the conduction band leaves behind a missing electron in the valence band. If the missing electron originated from an energy state near the valence band maximum, also called the *valence band edge*, then the dispersion relation is approximately parabolic and we can again make the effective mass approximation. However, a missing electron in a sea of negative charges behaves like a positively charged particle. We therefore speak of a missing valence band electron as a positive *hole* in the valence band, i.e., a positively charged particle of elementary charge $e = 1.6 \times 10^{-19}$ C. If the valence band maxima occurs at $\mathbf{k} = 0$, as it does for InAs and GaAs, then we may write the dispersion relation for the valence band in the effective mass approximation as:

$$\varepsilon_v(k) = -\frac{\hbar^2 k^2}{2m_{eff,h}}, \tag{3.10}$$

where $m_{eff,h}$ is the hole effective mass. The negative sign in equation (3.10) indicates a negative curvature in the dispersion relation for *electrons* near the valence band maxima. For holes we drop the negative sign, which means that the hole energy is a minimum at the top of the valence band (at $\mathbf{k} = 0$) and *increases* as you move *downwards* through the valence band.

Angular Momentum and The Band Structure of Bulk InAs

The Bloch solutions to the Schrödinger equation (3.7) may be considered as arising from a linear combination of atomic orbitals that interact to form bands. These bands retain the symmetry of the atomic orbitals from which they are derived [44]. For cubic semiconductors such as InAs and GaAs, the conduction band is s-orbital like, while the valence band is p-orbital like. Consequently, the orbital angular momentum

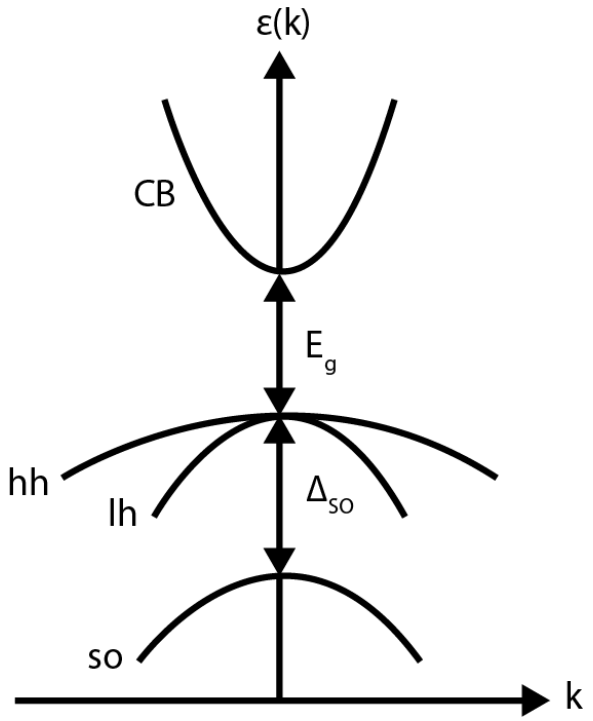

Figure 3.2: The band structure of bulk InAs. The valence band is degenerate at the band edge for light and heavy holes, while the degeneracy of the split-off band is broken due to the spin-orbit interaction.

quantum number is $l = 0$ for the conduction band states and $l = 1$ for the valence band. As in atomic physics, the spin-orbit interaction couples the intrinsic carrier spin with the orbital angular momentum to produce a new quantum number of total angular momentum $\mathbf{J} = \mathbf{L} + \mathbf{S}$, with values ranging from $|l - s| \leq j \leq |l + s|$.

Spin-orbit coupling does not effect the conduction band ($j = s = 1/2$), which remains two-fold degenerate. However, the valence band is divided into two states with total angular momentum $j = 3/2$ and $j = 1/2$. The spin-orbit interaction splits the energy of these states at the $\mathbf{k} = 0$ band edge, decreasing the energy of the twice degenerate 'split-off' states with $j = 1/2$ by an amount Δ_{SO}. This split-off energy is significant in InAs, with $\Delta_{SO} = 410$ meV exceeding the band gap energy $E_g = 354$ meV at 300 K [45]. Since we are generally interested in electrons and holes near the band edges, the split-off band can usually be neglected.

The valence band states with $j = 3/2$ have projections of total angular momentum of $j_z = 3/2, 1/2, -1/2$ and $-3/2$. At the $\mathbf{k} = 0$ valence band edge, these states are four-fold degenerate. For zinc-blende type materials such as InAs and GaAs, these states are separated for $\mathbf{k} \neq 0$ into the 'heavy holes' with $j_z = \pm 3/2$ and the 'light

holes' with $j_z = \pm 1/2$ by their different effective masses ($m_{hh} >> m_{lh}$). Figure 3.2 shows a diagram of the dispersion relations for the conduction and valence bands for bulk InAs in the effective mass approximation [44].

Excitons

When an electron is excited from the valence band to the conduction band, as may occur by thermal or optical stimulation, we create an electron in the conduction band and a hole in the valence band. The electron and hole, being oppositely charged particles, may form a bound state called an *exciton* or *electron-hole pair* and denoted by the symbol X^0. An exciton consisting of an electron-hole pair at their respective band edges has a slightly lower energy than the band gap on account of the Coulomb binding energy. In a bulk crystal, an exciton is free to move around and may be described in the effective mass approximation by the wavefunctions of the hydrogen atom. The spatial extent of the exciton is described by its Bohr radius, which for bulk InAs is 35 nm [43]. Typically, excitons do not exist in thermodynamic equilibrium, but are excited via external stimulation and exist for a certain average lifetime before they are *annihilated* or *recombine* (i.e., the electron falls back into the valence band with a commensurate exchange of energy) [44].

3.2 Zero-dimensional Systems

Quantum Dots

Quantum confinement causes drastic changes to the energy level structure of semiconductors. For zero-dimensional (0D) structures such as QDs, all three spatial directions are on the order of or smaller than the bulk exciton Bohr radius, which determines the confinement length scale. The major consequences of spatial confinement in 0D structures are the appearance of a discrete energy level spectrum and a blue shift of the band gap energy.

To determine the energy levels of a particle (e.g., an electron or hole) trapped inside a QD, one can solve the single particle time-independent Schrödinger equation of (3.6a) with appropriate boundary conditions. Things are greatly simplified by making the effective mass approximation, in which case the lattice periodic potential may be ignored and only the confinement potential need be considered. The solutions to (3.6a) for a given QD confinement potential yield the single particle wavefunctions (i.e., orbitals) and energies for conduction band electrons and valence band holes inside the QD.

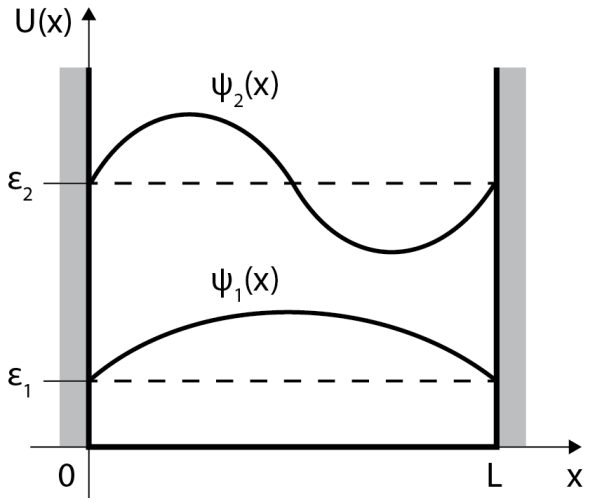

Figure 3.3: The one-dimensional infinite square well (i.e., the particle in a box). The potential $U(x)$ is zero for $0 < x < L$ and infinite elsewhere, trapping particles inside the well. The first two energy levels ε_1, ε_2 and their wavefunctions ψ_1, ψ_2 are shown superimposed inside the well.

The simplest example of a 0D confinement potential is the infinite square well potential with quantum confined side length L (see Figure 3.3):

$$U(\mathbf{r}) = \begin{cases} 0, & \text{if x, y, z are all between 0 and L,} \\ \infty, & \text{otherwise.} \end{cases} \tag{3.11}$$

The well-known stationary state solutions to this problem are:

$$\psi_{n_x,n_y,n_z}(\mathbf{r}) = \sqrt{\frac{8}{L^3}} \sin(\frac{n_x \pi x}{L}) \sin(\frac{n_y \pi y}{L}) \sin(\frac{n_z \pi z}{L}), \tag{3.12a}$$

$$\varepsilon_{n_x,n_y,n_z} = \frac{\pi^2 \hbar^2}{2 m_{eff} L^2} (n_x^2 + n_y^2 + n_z^2). \tag{3.12b}$$

In the above equation, m_{eff} is the particle effective mass and $n_i \in \mathbb{N}$ $(i = x, y, z)$ is the quantum number associated with confinement in each of the three spatial directions. This simple solution neatly illustrates the main consequences of 0D reduced dimensionality: the condition $n_i \in \mathbb{N}$ yields a discrete energy spectrum and the quantum confinement energy $\varepsilon_{n_x,n_y,n_z}$ increases with decreasing size length L, thereby producing a blue shift of the band gap energy.[1]

[1]In Appendix A, we solve the single particle energies for the somewhat more realistic confinement

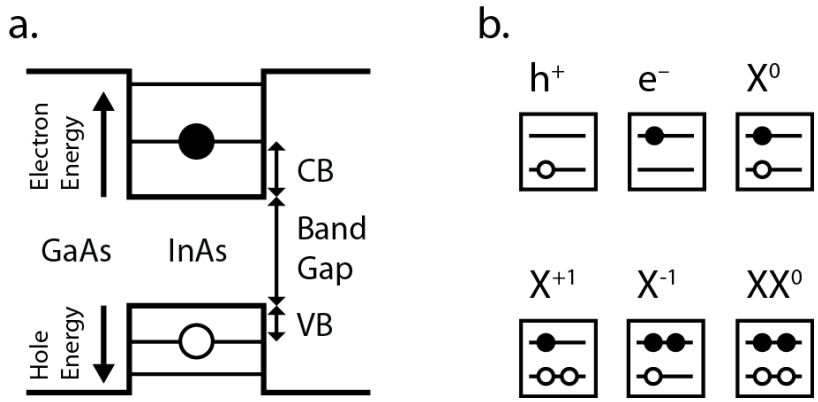

Figure 3.4: (a) Band diagram of an InAs/GaAs QD. The energy offsets of the conduction and valence bands of the two semiconductors provide confinement potentials for electrons and holes that lead to discrete energy levels and a blueshift of the band energy. An electron (solid circle) and hole (hollow circle) are shown populating their ground state energy levels to form an exciton. The exciton energy (excluding interaction effects) is a sum of the strained InAs band gap energy and the quantum confinement energies of electrons in the conduction band (CB) and holes in the valence band (VB). (b) Excitonic state diagrams of the bare hole h^+, bare electron e^-, exciton X^0, positive trion X^{+1}, negative trion X^{-1} and biexciton XX^0 in their ground states.

In real QDs, the confinement potential is a more complicated function with a lesser degree of symmetry. In fact, all real QD are unique due to slight variations in size, material composition, etc. that occur during the growth process and lead to differences in the confinement potential. As a result, energy levels in real QDs vary from one dot to another and the degeneracy observed in equation (3.12b) is typically broken. Nevertheless, the basic features of equation (3.12b), namely the discreet energy level spectrum and size dependence of the quantization energy, hold true for real QDs.

The energies of the single particle states determined by solving the Schrödinger equation, such as given in equation (3.12b), describe the quantum confinement energy of a single hole or electron in a QD due to the 0D confinement potential. To calculate the energy of an exciton in a QD, one must sum together the contribution of multiple energy terms with different magnitudes. The largest of these are the strained band

potential of a 2D harmonic oscillator in the lateral direction and a finite potential well, equal to the band offset of the QD host and embedding matrix materials, in the vertical direction. The advantage of this potential is that it also yields simple analytical solutions that may be used for calculations, while better approximating the true confinement potential of a QD than the infinite square well of equation (3.11).

gap energy of the QD host material and the single particle quantum confinement energies of the electron and hole [39]. Figure 3.4a shows a schematic band diagram of an InAs/GaAs QD, illustrating the main energy components of the exciton state. The bulk InAs band gap energy is 354 meV at 300 K, though this value increases significantly for QDs due to heterostructure interface strain and cryogenic operating temperatures [45, 47]. The quantum confinement energies in InAs/GaAs QDs are calculated to be on the order of hundreds of meV for electrons and tens of meV for holes (see also Appendix A).[2] Smaller contributions to the exciton state energy arise from interactions between the electron and hole. The Coulomb interaction yields an exciton binding energy on the order of a few to few tens of meV, while the electron-hole exchange interaction produces fine structure energies up to several hundred μeV [25]. In our samples, with nominal dot heights of 4 nm, the ground state exciton energies typically range from 1275 to 1320 meV. A more detailed account of exciton energy calculations is given in Appendix A, while a perturbation treatment of the particle interaction energies is provided in Section 3.3 on QDMs.

Finally, a complete description of the single particle states of a QD must include the electron and hole spin states. InAs/GaAs QDs inherit the bulk electron and hole spin structure discussed in Section 3.1, with one important change: the strain of self-assembled QDs breaks the degeneracy of the light and heavy hole bands by at least several tens of meV. Consequently, the more energetic light holes can typically be ignored [48]. This leaves the exciton ground state to be constructed from the pseudo-spin 1/2 heavy hole with angular momentum $j = 3/2,\ j_z = \pm 3/2$ and the electron with angular momentum $s = 1/2,\ s_z = \pm 1/2$. Combining these spins yields four exciton states characterized by their angular momentum projections: $j_z + s_z = \pm 1,\ \pm 2$. The ± 2 states are termed *dark excitons* because conservation of angular momentum prevents them from coupling with spin 1 photons, rendering them optically inactive. On the other hand, the ± 1 *bright exciton* states readily couple to photons.

In addition to the exciton states consisting of a single electron and hole, various other QD states with different numbers of charge carriers are commonly observed. Figure 3.4b presents the state diagrams and nomenclature for common excitonic ground states with different numbers of particles. The state diagrams display the conduction and valence band energy levels and the number of electrons and holes in each (they represent a simplified version of the band diagram in Fig. 3.4a). According to the Pauli exclusion principle, only two electrons or holes may populate a single energy level at a time.

[2] The difference in confinement energies between electrons and heavy holes is due to their different effective masses and band offset confinement potentials.

Quantum Dot Molecules

A quantum dot molecule consists of two QDs separated by a narrow tunneling barrier on the order of several nanometers thick. The additional spatial freedom of a QDM leads to richer physics and greater experimental control compared to single QDs. Depending on the spatial distribution of the charge carriers, different types of excitonic states are possible that exhibit different physical properties. In some of these states, the particles are localized in the top or bottom QDs, while in other cases they may be delocalized across the entire QDM, similar to what occurs with molecular bonding in natural molecules. Another important distinction between QDMs and single QDs is their behavior under the influence of an external electric field: unlike with single QDs, QDM energy levels may be easily tuned across a wide range of energy values *in situ* simply by applying an external electric field.

Direct and Indirect Exciton States in a QDM

It is often the case that the charge carriers in a QDM are localized to either the top or bottom QD. This situation suggests that we may describe the particles in a QDM to first approximation by using the localized single particle states described in Section 3.2. In this description, the resulting basis of QDM excitonic states is termed the *localized particle basis*. It provides an intuitively simple spatial description of the QDM states, often with good accuracy, and serves as a starting point for perturbative calculations of the QDM energies and charge distributions under the influence of tunnel coupling and many-body interactions.

In the localized particle description, two spatially distinct types of exciton states are possible. When the electron and hole both reside in the same dot, we call this a *direct* or *intradot* exciton and denote the state by the symbol X^0 (same as for an exciton in a single QD). On the other hand, an exciton with the charge carriers in opposite dots is called an *indirect* or *interdot* exciton and is denoted by the symbol iX^0. Figure 3.5 shows a schematic band representation of the direct and indirect exciton states, along with the state diagrams of other common QDM excitonic states. Similar terminology and nomenclature is applied to the other QDM states to describe their spatial charge configurations in the localized particle description.

The direct and indirect exciton states are most clearly distinguished by their different behavior in an applied electric field, which can be understood in terms of their different dipole moments. In our samples, the built in Schottky diode generates a tunable electric field directed along the QDM growth axis. The indirect exciton, with its large dipole moment oriented along the field axis, experiences a predominantly linear energy shift as a function of electric field according to the equation:

$$\Delta\varepsilon = -\mathbf{p} \cdot \mathbf{F}, \tag{3.13}$$

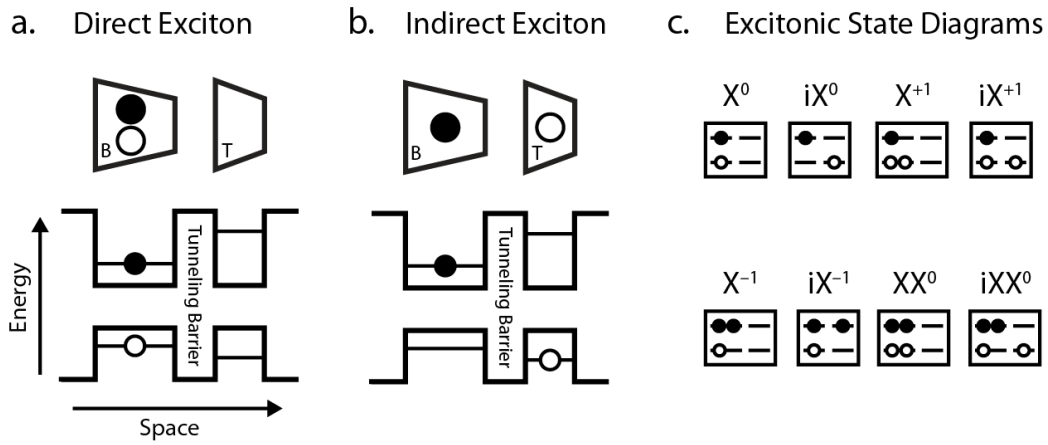

Figure 3.5: Diagram of (a) direct and (b) indirect exciton states in a QDM. The bottom (B) and top (T) dots of the QDM are represented pictorially above their respective positions in the band diagram, with the top QD chosen to be the smallest. The solid circles represent electrons and the hollow circles holes. The spatial axis is directed along the QDM vertical growth direction. (c) State diagrams and nomenclature for common excitonic ground states in a QDM. In the state diagrams, the bottom and top dot energy levels are separated to the left and right, respectively.

where $\mathbf{F}$ is the applied electric field and $\mathbf{p} = e\mathbf{a}$ is the exciton dipole moment, with $\mathbf{a}$ the effective displacement between the electron and hole.[3] The direct exciton, on the other hand, has little energy dependence on the electric field since the electron and hole occupy the same QD and their effective separation is tiny. The difference in dipole moments of the direct and indirect excitons may be observed in Fig. 3.5, where the electric field is directed in the QDM growth direction along the axis labeled 'space'. In Chapter 6, we provide a detailed analysis of the behavior of direct and indirect excitons under the influence of an externally applied electric field.

The application of an electric field not only provides a wide tuning range of the indirect exciton energy, but it also enables relative tuning of the top and bottom dot energy levels in a QDM. This is illustrated in Figure 3.6, which depicts how an applied electric field bends the QDM band structure. In the flat band configuration of Fig. 3.6a, the hole energy level of the bottom dot is above that of the top dot and the indirect exciton energy (dashed arrow) is greater than the direct exciton energy (solid arrow). With the Schottky diode operated in reverse bias, as shown in Fig. 3.6b, the electric field bends the band structure in such a way that the top and bottom dot hole levels are brought into resonance (i.e., equal energies) and the

[3] We use the symbol $\mathbf{a}$ to denote the displacement of the electric dipole in order to avoid confusion with the tunneling barrier width, which we denote by d.

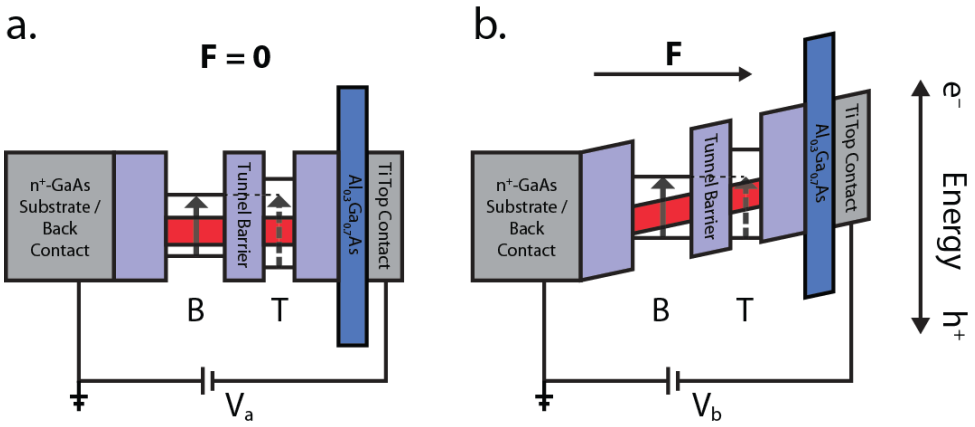

Figure 3.6: Electric field tuning of a QDM. The bottom (B) and top (T) dots of the QDM are indicated, with horizontal lines showing the ground state energy levels of conduction band electrons (above) and valence band holes (below). The vertical extent of the sample materials (color coded to Fig. 2.2 in the fabrication section) indicates the fundamental energy band gaps. Electron energies increase vertically upwards, while hole energies increase downwards. In the horizontal direction, an applied bias V generates an electric field $\mathbf{F}$ directed along the QDM growth axis. (a) Flat band bias tuning, showing non-resonant electron and hole energy levels, with the indirect exciton (dashed arrow) more energetic than the direct exciton (solid arrow). (b) At reverse bias ($V_b < V_a$), the ground state hole energy levels in both QDs are tuned to resonance and the direct and indirect exciton energies become comparable.

direct and indirect exciton energies become comparable. Thus, QDMs present a clear advantage over single QDs in their capacity for *in situ* tunability. A more detailed treatment of the tunability and electric field dependence of the direct and indirect exciton states is given in Section 3.3, where we introduce a quantitative model of the QDM states.

Tunneling and Molecular States in a QDM

The propensity for charge carriers to tunnel means that the localized particle representation of a QDM is not always accurate. Localization is a good description when the energy levels in the top and bottom dots are mis-matched, making particle tunneling unlikely (e.g., as shown in Fig. 3.6a). However, as the energy levels in separate dots come into resonance (e.g., the hole levels in Fig. 3.6b), the energy matching condition makes particle tunneling increasingly likely. In fact, at an exact energy resonance, the stationary state wavefunctions become delocalized across the entire QDM. Such delocalized states are represented in the localized particle basis as

superpositions of the top and bottom dot states. These superpositions can be additive (symmetric) or subtractive (anti-symmetric) depending on the relative quantum phase, which affects the extent to which the wavefunctions penetrate the tunneling barrier and leads to level repulsion of the quantum state energies. This division into symmetric and anti-symmetric superposition states is analogous to the formation of bonding and anti-bonding states in real molecules. Hence, the origin of the name *quantum dot molecule*. In the following Section 3.3, we provide a quantitative account of molecular state formation in QDMs.

3.3 Effective Mass Perturbation Model of a QDM

To describe the low-energy, multi-particle excitonic states of a QDM, we use an effective mass perturbation theory model developed by Ponomarev, et. al. [49]. In Chapter 5, we use this model to calculate the biexciton states in a QDM.

Theoretical Description

The localized particle basis states for a QDM populated with a fixed number of charge carriers are constructed from the single particle wavefunctions and spin states of electrons and holes described in Section 3.2 for single QDs (see also Appendix A). To determine the energy levels of the system, we calculate the matrix representation of the QDM Hamiltonian in the localized particle basis and then diagonalize the matrix to yield the stationary states and their energies. The excitonic state transition energies are calculated as the energetic difference between quantum states with optically allowed transitions. If the photoluminescence intensities are desired, they may be calculated using Fermi's golden rule.

In the localized particle basis, single particle orbitals for electrons and holes describe charge carriers localized to the top or bottom QD. We truncate the basis to include only the lowest energy orthonormal s-state orbital wavefunctions $\psi_M^{\alpha i}(\mathbf{r}_\alpha)$, where α, i indicate the respective particle type (e or h) and numeric label and $M = B, T$ indicates whether the particle is in the top or bottom dot.[4] These orbital wavefunctions, calculated in the efffective mass approximation, are called 'envelope wavefunctions'. They may be written in bra-ket notation as $|M^{\alpha i}\rangle$.

The z-component of spin is taken along the QDM growth axis where the quantum confinement is greatest. For electron spin, we use the following notation: $|\downarrow\rangle \equiv |s_z^e = -\frac{1}{2}\rangle$ and $|\uparrow\rangle \equiv |s_z^e = +\frac{1}{2}\rangle$. The heavy-hole spin states ($j = \frac{3}{2}, j_z = \pm\frac{3}{2}$) are treated as a pseudo-spin 1/2 system and notated as follows: $|\Uparrow\rangle \equiv |-\frac{1}{2}\rangle \equiv |j_z^h = +\frac{3}{2}\rangle$ and $|\Downarrow\rangle \equiv |+\frac{1}{2}\rangle \equiv |j_z^h = -\frac{3}{2}\rangle$. The reverse sign of the pseudo-spin 1/2 for the heavy holes

[4] Recall that the p-orbital like nature of the hole states is already accounted for with the hole pseudo-spin.

is to avoid phase multipliers; for practical purposes, this implies that the eigenvalues of the Pauli operators for hole spins have opposite signs compared to electron spins [49]. For two identical particles, the following spin bases of singlet and triplet states will be used for electrons:

$$\begin{gathered}|\mathcal{S}^e\rangle = 2^{-\frac{1}{2}}(|\uparrow\rangle|\downarrow\rangle - |\downarrow\rangle|\uparrow\rangle), \quad |\mathcal{T}_0^e\rangle = 2^{-\frac{1}{2}}(|\uparrow\rangle|\downarrow\rangle + |\downarrow\rangle|\uparrow\rangle), \\ |\mathcal{T}_+^e\rangle = |\uparrow\uparrow\rangle, \quad |\mathcal{T}_-^e\rangle = |\downarrow\downarrow\rangle,\end{gathered} \tag{3.14}$$

and for holes:

$$\begin{gathered}|\mathcal{S}^h\rangle = 2^{-\frac{1}{2}}(|\Uparrow\rangle|\Downarrow\rangle - |\Downarrow\rangle|\Uparrow\rangle), \quad |\mathcal{T}_0^h\rangle = 2^{-\frac{1}{2}}(|\Uparrow\rangle|\Downarrow\rangle + |\Downarrow\rangle|\Uparrow\rangle), \\ |\mathcal{T}_+^h\rangle = |\Uparrow\Uparrow\rangle, \quad |\mathcal{T}_-^h\rangle = |\Downarrow\Downarrow\rangle.\end{gathered} \tag{3.15}$$

As we are dealing with fermions, the many-particle basis configurations for QDM states containing identical particles are constructed from anti-symmetrized products of single-particle states.

In the envelope wavefunction approximation, the Hamiltonian of the QDM system consists of three parts:

$$\begin{aligned}\hat{H} &= \hat{H}_{single\ particles} + \hat{H}_{Coulomb} + \hat{H}_{exch}^{eh} \\ &= \sum_{\alpha,i} \hat{h}_{\alpha,i} + \frac{1}{4\pi\epsilon} \sum_{\alpha,i;\beta,j} \frac{e_\alpha e_\beta}{|\mathbf{r}_{\alpha,i} - \mathbf{r}_{\beta,j}|} + \hat{H}_{exch}^{eh},\end{aligned} \tag{3.16}$$

where $\alpha, \beta = e$ or h, i, j indicate the particle number, $e_{\alpha(\beta)}$ is the elementary charge (positive for holes, negative for electrons) and ϵ is the static dielectric constant (i.e., electric permittivity) of the QDM material. When energy is measured in meV and the average dielectric constant of InAs and GaAs $\epsilon/\epsilon_0 \cong 13.5$ is used, we calculate $e^2/4\pi\epsilon \cong 106.5$ meV$\cdot$nm [45, 46]. The first term represents single particle Hamiltonians, the second term describes the Coulomb interactions and the third term describes the electron-hole (e-h) exchange interaction. The Coulomb and e-h exchange interactions are treated as perturbations to the single particle Hamiltonian.[5]

An applied electric field F along the QDM growth axis changes the energies of charge carriers in the top dot with respect to the bottom dot of the QDM by an amount:

$$f(F) = e\bar{d}F(i - j), \tag{3.17}$$

where e is the elementary charge, $\bar{d} = d + (h_B + h_T)/2$ is the distance between the centers of the two dots and i, j are the numbers of electrons and holes in the top dot,

[5]Particle tunneling can also be considered a perturbation to the localized particle energy states.

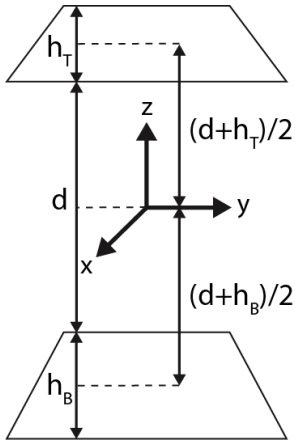

Figure 3.7: Dimensions and coordinate system of a QDM. The lengths h_T and h_B denote the QD heights, while d denotes the tunneling barrier width. The coordinate system is used to parameterize the matrix element integral calculations described in Section 3.2. The top and bottom single particle QD orbitals may be parameterized as follows: $\psi_T(\mathbf{r}_T) = \psi_T\left(\mathbf{r} - \left(\frac{d+h_T}{2}\right)\hat{\mathbf{z}}\right)$ and $\psi_B(\mathbf{r}_B) = \psi_B\left(\mathbf{r} + \left(\frac{d+h_B}{2}\right)\hat{\mathbf{z}}\right)$.

respectively. The lengths h_B, h_T and d correspond to the heights of the bottom and top dots and the width of the GaAs tunneling barrier separating the dots. These dimensions are illustrated in Figure 3.7.

The single particle Hamiltonians have the following matrix elements: $\langle B^{\alpha,i}|\hat{h}_{\alpha,i}|B^{\alpha,i}\rangle = \varepsilon_B^\alpha$, $\langle T^{\alpha,i}|\hat{h}_{\alpha,i}|T^{\alpha,i}\rangle = \varepsilon_T^\alpha + f$, $\langle B^{\alpha,i}|\hat{h}_{\alpha,i}|T^{\alpha,i}\rangle = -t_\alpha$, where ε_B^α and ε_T^α are the respective energies of particle α in the top and bottom dots and t_α is the interdot particle tunneling rate.[6]

The Coulomb part of the Hamiltonian generates integrals of the following form:

$$\begin{aligned} V_{i,j;k,l}^{\alpha;\beta} &= \langle i^\alpha|\langle k^\beta|\hat{H}_{Coulomb}|j^\alpha\rangle|l^\beta\rangle \\ &= \frac{e_\alpha e_\beta}{4\pi\epsilon}\int d^3\mathbf{r}_\alpha d^3\mathbf{r}_\beta \frac{\psi_i^{\alpha*}(\mathbf{r}_\alpha)\psi_j^\alpha(\mathbf{r}_\alpha)\psi_k^{\beta*}(\mathbf{r}_\beta)\psi_l^\beta(\mathbf{r}_\beta)}{|\mathbf{r}_\alpha - \mathbf{r}_\beta|}. \end{aligned} \tag{3.18}$$

In equation (3.18), the Coulomb interaction is between charged particles α and β and the indices $i, j\,(k, l) = T, B$ indicate the location of particle $\alpha\,(\beta)$ in the respective bra and ket states. The integral is positive for repulsive interactions (i.e., $e_\alpha = e_\beta$) and negative for attractive interactions (i.e., $e_\alpha = -e_\beta$). The diagonal Coulomb matrix elements describe charge interaction energies of many particle states, while off-

[6]The individual particle energies ε_B^α and ε_T^α include the quantum confinement energies and a contribution from the strained InAs band gap.

diagonal Coulomb elements of the form $V^{\alpha;\beta}_{i,j;j,j}, i \neq j$ describe charge induced tunneling that modifies the single particle tunneling rates $t_{e(h)}$.

The e-h exchange interaction, since electrons and holes are considered distinguishable particles, is given by the short-range effective Hamiltonian for symmetric exchange:[7]

$$\hat{H}^{eh}_{exch} = A \sum_{i,j} \delta(\mathbf{r}_{ei} - \mathbf{r}_{hj}) \hat{\sigma}^z_{ei} \hat{\sigma}^z_{hj}, \tag{3.19}$$

where A is a coupling constant, δ is the Dirac delta function and $\hat{\sigma}^z_{ei(hj)}$ are Pauli matrices for the $z-$component of spin of the $i^{\text{th}}(j^{\text{th}})$ electron (hole). The constant A may be measured from experimental data and is typically on the order of tens to a few hundred meV. The spatial part of the e-h exchange interaction generates integrals of the following form:

$$J^{e;h}_{i,j;k,l} = \langle i^e | \langle k^h | \hat{H}^{eh}_{exch} | j^e \rangle | l^h \rangle = A \int d^3\mathbf{r} \; \psi^{e*}_i(\mathbf{r}) \psi^e_j(\mathbf{r}) \psi^{h*}_k(\mathbf{r}) \psi^h_l(\mathbf{r}). \tag{3.20}$$

The e-h exchange matrix elements of the form $J^{e;h}_{i,i;i,i}$ describe the energy splitting between bright and dark exciton states, on the order of hundreds of μeV, while the remaining e-h exchange matrix elements yield negligible energy contributions and can generally be ignored.

To estimate the values of the Coulomb and e-h exchange matrix elements of equations (3.18) and (3.20), we may compute the integrals using the single particle wavefunctions given in Appendix A. The coordinate parameterizations for the top and bottom QDs are given in Figure 3.7. The results reveal a hierarchy in the magnitudes of the energy parameters $\varepsilon^{\alpha}_{B(T)}$, t_α, $V^{\alpha;\beta}_{i,j;k,l}$ and $J^{e;h}_{i,j;k,l}$, which allow us to identify their relative importance for the model. As mentioned in Section 3.2, the greatest contribution to the overall energy of the quantum state is from the quantum confinement and band gap energies contained in $\varepsilon^{\alpha}_{B(T)}$, with values ranging in the hundreds of meV for InAs/GaAs QDs. The next largest energy contribution is from diagonal Coulomb integrals of the form $V^{\alpha;\beta}_{i,i;i,i}$ (i.e., two charge carriers confined to the same QD), which range from about $20-30$ meV independent of the QDM barrier separation. Coulomb integrals with charge carriers in separate spatial locations range from about $9-16$

[7]Here, we use an e-h exchange Hamiltonian that is rotationally invariant (i.e., symmetric) in the Pauli operators. This symmetric exchange operator splits the bright and dark exciton state energies, but does not mix these states. An asymmetric exchange operator can be used to more accurately model the rotational anisotropy of the crystal (see, for example, reference [48]). The asymmetric term always mixes the dark states and, for crystal symmetries less than D2d, also mixes the bright states. However, the energy splittings of the mixed bright exciton states are on the order of a few μeV and can be safely ignored in this analysis. By ignoring the asymmetric term, the spin states remain eigenstates of the angular momentum projection operator.

meV for forms like $V^{\alpha;\beta}_{i,i;j,j}, i \neq j$ or $0.003 - 7$ meV for forms like $V^{\alpha;\beta}_{i,j;j,j}, i \neq j$, with the energy increasing for smaller barrier separations (the values given here are calculated for tunneling barriers ranging from $2-8$ nm). The remaining Coulomb integrals of the form $V^{\alpha;\beta}_{i,j;i,j}, i \neq j$ have the smallest magnitude for any given pair of charge carriers, ranging from less than 10^{-6} meV for hole-hole interactions at 8 nm barrier width up to 2 meV for electron-electron interactions at 2 nm barrier width.[8] The single particle tunneling rates $t_{e(h)}$ range from about $0.05 - 1$ meV for holes and roughly ten times greater for electrons due to their smaller effective mass, with a strong dependence on the tunneling barrier thickness. Finally, the smallest energy contributions are from the e-h exchange matrix elements $J^{e;h}_{i,j;k,l}$. The largest of these, the diagonal matrix element $J^{e;h}_{i,i;i,i}$, is responsible for the bright-dark exciton splitting and has a magnitude of a few hundred μeV. The other e-h exchange matrix elements are negligibly small.

Calculation of the Exciton Ground States

We now apply the model of the previous section to calculate the neutral exciton ground states in a QDM, providing a quantitative description of the exciton states discussed in Section 3.2. The complete basis of the exciton states consists of all possible spatial and spin configurations of one electron and one hole in a QDM. In the localized particle basis, the electrons states alone are $\{|B^e\rangle|\uparrow\rangle,\ |B^e\rangle|\downarrow\rangle,\ |T^e\rangle|\uparrow\rangle,\ |T^e\rangle|\downarrow\rangle\}$ and the hole states are $\{|B^h\rangle|\Uparrow\rangle,\ |B^h\rangle|\Downarrow\rangle,\ |T^h\rangle|\Uparrow\rangle,\ |T^h\rangle|\Downarrow\rangle\}$. From these, we form all possible combinations of one hole and one electron to yield a basis of $4 \times 4 = 16$ states. In the absence of a magnetic field and with the symmetric e-h exchange Hamiltonian (see Section 3.2, footnote 7), there is a degeneracy between each pair of states that transform into themselves under the operation of flipping both the electron and hole spins. Since we are not considering magnetic fields in this dissertation, we can avoid this degeneracy and reduce the number of states by half if we simply require the electron to always have spin-up. We note that this change introduces the following difference between the model and the physical system: each individual transition line generated from the model will correspond to two orthogonally polarized transition lines in the physical system. With this consideration, and ordering the basis to separate the bright and dark excitons, the localized particle basis for the exciton

[8] In this case, the electron-electron interactions across separate QDs yield larger energy values than the hole-hole or electron-hole interactions because the electron wavefunctions penetrate the tunneling barrier to a much greater extent than the hole wavefunctions (see also Chapter 6 and Appendix A).

states is the following:

$$\begin{aligned}\{|1\rangle = |B^e\rangle|\uparrow\rangle|B^h\rangle|\Downarrow\rangle,\ |2\rangle = |B^e\rangle|\uparrow\rangle|T^h\rangle|\Downarrow\rangle,\ |3\rangle = |T^e\rangle|\uparrow\rangle|B^h\rangle|\Downarrow\rangle,\\ |4\rangle = |T^e\rangle|\uparrow\rangle|T^h\rangle|\Downarrow\rangle,\ |5\rangle = |B^e\rangle|\uparrow\rangle|B^h\rangle|\Uparrow\rangle,\ |6\rangle = |B^e\rangle|\uparrow\rangle|T^h\rangle|\Uparrow\rangle,\\ |7\rangle = |T^e\rangle|\uparrow\rangle|B^h\rangle|\Uparrow\rangle,\ |8\rangle = |T^e\rangle|\uparrow\rangle|T^h\rangle|\Uparrow\rangle\}.\end{aligned} \tag{3.21}$$

The exciton Hamiltonian from equation 3.16 is:

$$\hat{H}_{X^0} = \hat{h}_e(\mathbf{r}_e) + \hat{h}_h(\mathbf{r}_h) - \frac{e^2}{4\pi\epsilon}\frac{1}{|\mathbf{r}_e - \mathbf{r}_h|} + A\delta(\mathbf{r}_e - \mathbf{r}_h)\hat{\sigma}_e^z\hat{\sigma}_h^z. \tag{3.22}$$

We must determine the matrix representation of $\hat{H}_{X^0}$ in the localized particle basis. First, we work out the spin portion of the exchange operator acting on the spin states alone:[9]

$$\hat{\sigma}_e^z\hat{\sigma}_h^z|\uparrow\rangle|\Downarrow\rangle = +|\uparrow\rangle|\Downarrow\rangle, \tag{3.23a}$$

$$\hat{\sigma}_e^z\hat{\sigma}_h^z|\uparrow\rangle|\Uparrow\rangle = -|\uparrow\rangle|\Uparrow\rangle. \tag{3.23b}$$

Equation (3.23) reveals that the spin exchange term produces matrix elements along the main diagonal equal to $+J^{e,h}_{ii,kk},\ i,k = B,T$ for base states 1 through 4 (i.e., the bright excitons) and $-J^{e,h}_{ii,kk},\ i,k = B,T$ for base states 5 through 8 (i.e., the dark excitons), while all off-diagonal elements are equal to zero. As noted, these terms are responsible for the bright-dark spin exchange splitting of the exciton states. This splitting is greatest when both charge carriers are in a single QD, which allows for significant wavefunction overlap between the electron and hole. It is negligible when the carriers are in separate QDs.

Of the remaining terms in the Hamiltonian, the single particle term yields matrix elements for the single particle energies along the main diagonal and spin-conserving off-diagonal tunneling terms $t_{e(h)}$. The Coulomb Hamiltonian also generates both diagonal and off-diagonal terms. After calculating all of the matrix elements, we arrive at the following matrix representation of the exciton Hamiltonian in the localized particle basis:

$$H_{X^0} = \left[\begin{array}{c|c} H_B & 0_{4\times4} \\ \hline 0_{4\times4} & H_D \end{array}\right]_{8\times8}, \tag{3.24a}$$

[9]Recall that the signs of the eigenvalues for hole spins are reversed compared to the electron spins.

$$H_B = \begin{bmatrix} H_{11} & V^{eh}_{BBTB} - t_h & V^{eh}_{TBBB} - t_e & V^{eh}_{TBTB} \\ V^{eh}_{BBTB} - t_h & H_{22} & V^{eh}_{TBBT} & V^{eh}_{TBTT} - t_e \\ V^{eh}_{TBBB} - t_e & V^{eh}_{TBBT} & H_{33} & V^{eh}_{TTTB} - t_h \\ V^{eh}_{TBTB} & V^{eh}_{TBTT} - t_e & V^{eh}_{TTTB} - t_h & H_{44} \end{bmatrix}, \tag{3.24b}$$

$$H_D = \begin{bmatrix} H_{55} & V^{eh}_{BBTB} + t_h & V^{eh}_{TBBB} + t_e & V^{eh}_{TBTB} \\ V^{eh}_{BBTB} + t_h & H_{66} & V^{eh}_{TBBT} & V^{eh}_{TBTT} + t_e \\ V^{eh}_{TBBB} + t_e & V^{eh}_{TBBT} & H_{77} & V^{eh}_{TTTB} + t_h \\ V^{eh}_{TBTB} & V^{eh}_{TBTT} + t_e & V^{eh}_{TTTB} + t_h & H_{88} \end{bmatrix}, \tag{3.24c}$$

$$\begin{aligned} H_{11} &= \varepsilon^e_B + \varepsilon^h_B + V^{eh}_{BBBB} + J^{eh}_{BBBB}, \\ H_{22} &= \varepsilon^e_B + \varepsilon^h_T + V^{eh}_{BBTT} + J^{eh}_{BBTT} + f_-(F), \\ H_{33} &= \varepsilon^e_T + \varepsilon^h_B + V^{eh}_{TTBB} + J^{eh}_{TTBB} + f_+(F), \\ H_{44} &= \varepsilon^e_T + \varepsilon^h_T + V^{eh}_{TTTT} + J^{eh}_{TTTT}, \\ H_{55} &= \varepsilon^e_B + \varepsilon^h_B + V^{eh}_{BBBB} - J^{eh}_{BBBB}, \\ H_{66} &= \varepsilon^e_B + \varepsilon^h_T + V^{eh}_{BBTT} - J^{eh}_{BBTT} + f_-(F), \\ H_{77} &= \varepsilon^e_T + \varepsilon^h_B + V^{eh}_{TTBB} - J^{eh}_{TTBB} + f_+(F), \\ H_{88} &= \varepsilon^e_T + \varepsilon^h_T + V^{eh}_{TTTT} - J^{eh}_{TTTT}, \end{aligned} \tag{3.24d}$$

where $0_{4\times4}$ is the 4×4 zero matrix, and $f_-(F) = -e\bar{d}F$ and $f_+(F) = +e\bar{d}F$ determine the energy dependence of the indirect states as a function of the applied electric field F.

Equation (3.24) reveals that H_{X^0} consists of two uncoupled 4×4 sub-matrices for the bright ($H_B,\ J_z = \pm1$) and dark ($H_D,\ J_z = \pm2$) excitons. These sub-matrices are identical, except for the e-h exchange matrix elements along the main diagonal that produce the bright-dark energy splitting. Recall that the dark excitons are not optically active. Nevertheless, they are the final states in the radiative recombination of certain biexciton states and are thus important in understanding the optical emission spectra of QDMs.

We can simplify the bright exciton Hamiltonian in equation (3.24b) by observing that the matrix elements responsible for particle exchange between different dots (i.e., V^{eh}_{TBBT} and V^{eh}_{TBTB}) are negligibly small compared to the rest of the terms and can be set to zero. Additionally, we observe that the remaining off-diagonal Coulomb terms

contribute to the tunneling energy, so we may define the following Coulomb adjusted tunneling rates: $-t_h^{(B)} = V_{BBTB}^{eh} - t_h$, $-t_h^{(T)} = V_{TTTB}^{eh} - t_h$, $-t_e^{(B)} = V_{TBBB}^{eh} - t_e$ and $-t_e^{(T)} = V_{TBTT}^{eh} - t_e$. Then, we may write the bright exciton Hamiltonian sub-matrix in the following simplified form:

$$H_B = \begin{bmatrix} E_1 & -t_h^{(B)} & -t_e^{(B)} & 0 \\ -t_h^{(B)} & E_2(F) & 0 & -t_e^{(T)} \\ -t_e^{(B)} & 0 & E_3(F) & -t_h^{(T)} \\ 0 & -t_e^{(T)} & -t_h^{(T)} & E_4 \end{bmatrix}, \tag{3.25a}$$

$$\begin{aligned} E_1 &\equiv H_{11} = \varepsilon_B^e + \varepsilon_B^h + V_{BBBB}^{eh} + J_{BBBB}^{eh}, \\ E_2(F) &\equiv H_{22} = \varepsilon_B^e + \varepsilon_T^h + V_{BBTT}^{eh} + J_{BBTT}^{eh} + f_-(F), \\ E_3(F) &\equiv H_{33} = \varepsilon_T^e + \varepsilon_B^h + V_{TTBB}^{eh} + J_{TTBB}^{eh} + f_+(F), \\ E_4 &\equiv H_{44} = \varepsilon_T^e + \varepsilon_T^h + V_{TTTT}^{eh} + J_{TTTT}^{eh}. \end{aligned} \tag{3.25b}$$

For convenience, below we restate the bright exciton localized particle basis states that accompany equation (3.25):

$$\begin{aligned} \{|1\rangle = |B^e\rangle|\uparrow\rangle|B^h\rangle|\Downarrow\rangle,\ |2\rangle = |B^e\rangle|\uparrow\rangle|T^h\rangle|\Downarrow\rangle, \\ |3\rangle = |T^e\rangle|\uparrow\rangle|B^h\rangle|\Downarrow\rangle,\ |4\rangle = |T^e\rangle|\uparrow\rangle|T^h\rangle|\Downarrow\rangle\}. \end{aligned} \tag{3.26}$$

In the limit of vanishing tunnel coupling, the localized particle base states of equation (3.26) are the stationary states, with energies $E_i,\ i = 1, 2, 3, 4$ given by equation (3.25b). The indirect state energies $E_2(F)$ and $E_3(F)$ are functions of the electric field F, while the direct state energies E_1 and E_4 are constant. With finite tunneling, we must diagonalize the Hamiltonian in equation (3.25a) to yield the correct stationary states and eigenenergies, which we call the *molecular basis* since the single particle wavefunctions are delocalized across both QDs near a tunneling resonance, similar to what occurs in the molecular bonding of real atoms.

To solve for the stationary state solutions of the exciton states, we need to diagonalize the Hamiltonian in (3.25a). This requires solving a fourth degree polynomial equation. While an analytical solution exists, the length of this expression is so long as to render it meaningless to inspection. Instead, it is better to seek the following two strategies: (i) diagonalize the Hamiltonian numerically or (ii) make further approximations to simplify the Hamiltonian so that meaningful analytical solutions are possible.

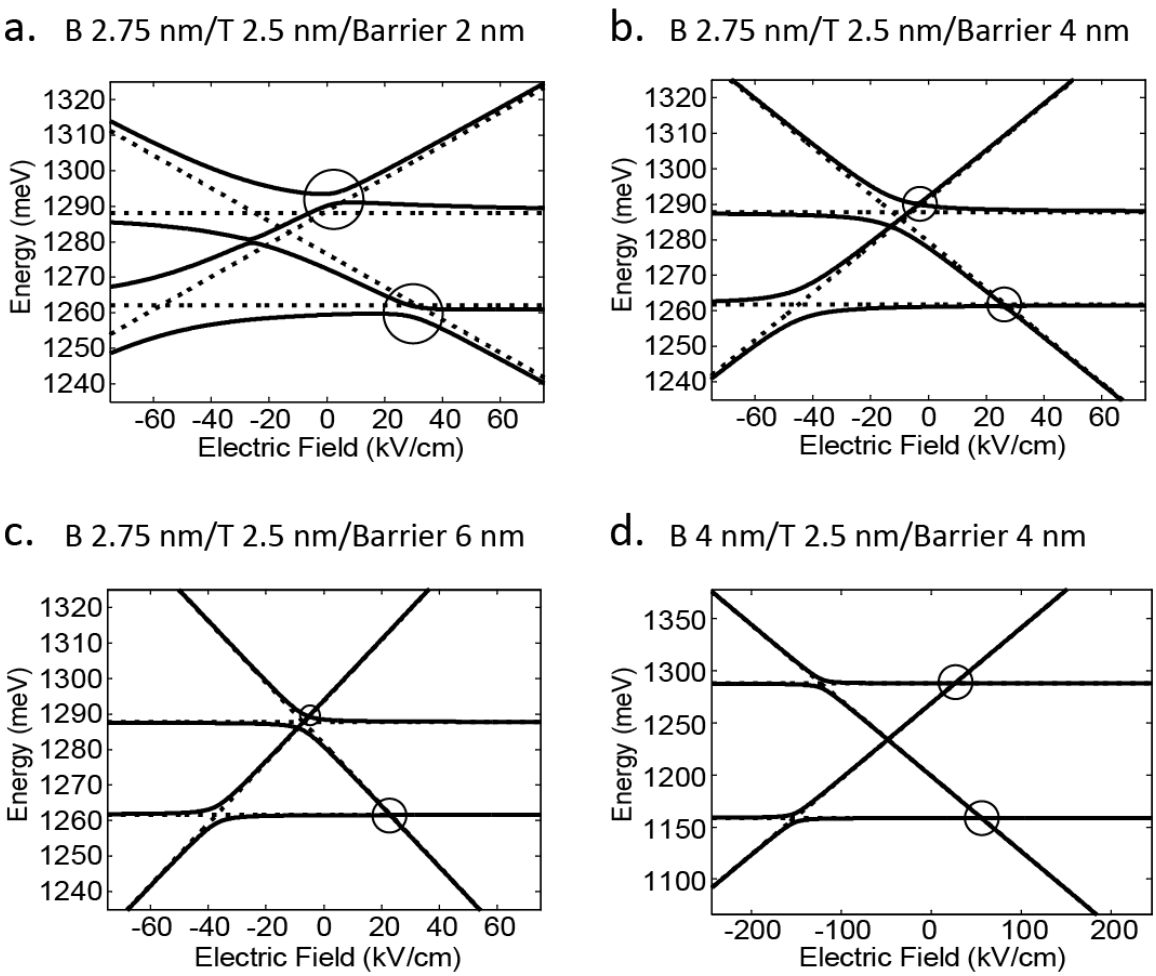

Figure 3.8: Plots of numerical solutions for the bright exciton stationary state energies as a function of applied electric field for QDMs with different dimensions of bottom QD height (B), top QD height (T) and tunneling barrier width. Continuous lines represent the energy eigenstates, while dashed lines show the localized particle energies. Large electron tunneling ACs are easily observed at negative field values, while the much smaller hole tunneling ACs (circled for clarity) are hard to observe at this energy scale. We point out that figures (b) and (d) have the same tunneling barrier, but different scale ranges for the energy axis, revealing that QDMs with greater dot asymmetry have more isolated tunneling resonances.

Numerical Solution of the Exciton Stationary State Energies

It is possible to get excellent approximations of the stationary state energies of the exciton states by numerically diagonalizing the matrix in equation (3.25a). Figure 3.8 shows various plots made in this way for QDMs with asymmetric dot heights and various tunneling barrier widths. The stationary state energies (solid lines) are plotted as a function of the applied electric field, with the localized particle energies (dashed lines) shown for comparison. In Fig. 3.8, we have assumed that the top QD is smaller and therefore more energetic, which is how our experimental samples have been engineered. Reversing the order of the dot heights simply results in a reversal of order for the electron and hole tunneling resonances with respect to the electric field axis. To calculate parameter values for the electron and hole quantum confinement energies, the Coulomb matrix elements and the e-h exchange matrix elements, we have used the single particle wavefunctions calculated in Appendix A. Parameter values for the tunneling rates are approximated from experimental data and the band gap energy of InAs strained by GaAs was determined according to the method of Barker, et. al. (see Appendix A for the numerical value) [47].

Figure 3.8 reveals prominent features of the stationary state energy spectrum of a QDM. We identify the steeply sloped energy levels of the indirect exciton states and the flat slopes of the direct excitons with negligible electric field dependence (this is most apparent in Fig. 3.8d). Moreover, as the tunneling barrier increases, and with it the dipole moment of the indirect exciton, we observe a steady increase in the indirect energy slopes. Quantitatively, the electric field dependence of the indirect lines is given by the equation:

$$f_{\pm}(F) = \pm(\bar{d}/10)F, \tag{3.27}$$

where $\bar{d}$ is the effective separation between the electron and hole in nanometers, F is the electric field measured in kV/cm and $f_{\pm}(F)$ is the energy shift in meV. In practice, $\bar{d}$ is easily calculated by measuring the indirect exciton slope and using equation 3.27.

The tell-tale sign of molecular state formation in Fig. 3.8 is observed in the level repulsion or anti-crossings (ACs) of the direct and indirect exciton levels as they approach an energy resonance. The electron ACs, occurring at negative electric field values in Fig. 3.8, are roughly ten times greater than the hole AC's because of the electron's smaller effective mass, which increases the tunneling rate. It is also apparent from comparing Figures 3.8a-c that both the tunneling energy and the extent of the tunneling resonance (as measured by the electric field range of the AC) increase with decreasing tunneling barrier width, as a smaller barrier increases the tunneling rate. Finally, the size dependence of the quantum confinement energy is evident when we compare the direct exciton energies of the top and bottom dots. The more confined top QD, which has a consistent value of about 1287 meV in Figures 3.8a-d, always exceeds the exciton energy of the larger bottom dot.

We note that the exciton energy levels, such as those seen in Fig. 3.8, are directly comparable to experimentally measurable transition energies. This is a special case true for the exciton states because each state recombines radiatively to the same common crystal ground state (CGS) (i.e., the state of an unoccupied QDM). In general, the QDM transition energies are calculated as the difference between the initial and final state energy levels.

In practice, samples are engineered for either electron or hole tunneling since the Schottky diode structure only yields stable excitonic state when operated in reverse bias. Moreover, only the transitions from the least energetic direct and indirect exciton states (i.e., the metastable ground states) are typically observed in non-resonant laser excitation experiments because excited exciton states undergo ultrafast non-radiative relaxation to these metastable ground states. Thus, for hole tunneling samples like the ones used in this dissertation, the experimental window for observing exciton emission corresponds to the lower right (i.e., hole tunneling) region in Figures 3.8a-d.

Approximate Analytical Solutions of the Exciton States

It is often possible to simplify the Hamiltonian matrix of equation (3.25a) so that approximate analytical solutions may be found that provide an insightful, quantitative description of the exciton states in a QDM. A glance at Fig. 3.8 reveals that the exciton eigenenergies are predominantly linear functions of the electric field, corresponding to localized direct or indirect exciton states, except for in the regions where the energy levels approach a tunneling resonance. This is particularly true for asymmetrically engineered QDMs with moderately thick tunneling barriers (e.g., $d \geq 4$ nm), which yield electron and hole tunneling resonances that are widely separated from one another (e.g., see Fig. 3.8d). In this case, we may obtain a very good approximation to the molecular eigenenergies by considering the electron and hole tunneling resonances to be decoupled from one another. This allows us to separate equation (3.25a) into four uncoupled 2×2 matrices, one for each different tunneling resonance. Each of these matrices then represents a two-state system expanded in the localized particle basis, consisting of one direct and one indirect exciton state, which can be solved analytically.

We use this analytical method to solve the 2×2 system for hole tunneling while the electron is localized in the lower energy bottom QD. To solve this problem, we use the time-dependent Schrödinger equation of (3.1), which yields analytical expressions for the stationary state eigenvectors and eigenenergies and determines the free evolution of an isolated exciton state. In this case, the decoupled 2×2 Hamiltonian matrix

taken from equation (3.25a) is:

$$H = \begin{bmatrix} E_1 & -t_h^{(B)} \\ -t_h^{(B)} & E_2(F) \end{bmatrix}. \tag{3.28}$$

The localized particle basis for this two state system consists of the direct exciton state $|1\rangle = |B^e\rangle|\uparrow\rangle|B^h\rangle|\Downarrow\rangle$ with energy $E_1 = \varepsilon_B^e + \varepsilon_B^h + V_{BBBB}^{eh} + J_{BBBB}^{eh}$ and the indirect exciton state $|2\rangle = |B^e\rangle|\uparrow\rangle|T^h\rangle|\Downarrow\rangle$ with energy $E_2(F) = \varepsilon_B^e + \varepsilon_T^h + V_{BBTT}^{eh} + J_{BBTT}^{eh} + f_-(F)$, as given by equation (3.25b). The general quantum state is then given by:

$$|\Psi(t)\rangle = C_1(t)|1\rangle + C_2(t)|2\rangle, \tag{3.29}$$

where $C_1(t) = \langle 1|\Psi(t)\rangle$ and $C_2(t) = \langle 2|\Psi(t)\rangle$ are the quantum amplitudes of the exciton state $|\Psi(t)\rangle$ in the localized particle basis. Our objective is to solve for the stationary state eigenvectors and eigenenergies, and then determine the time dependence of the quantum amplitudes.

Since we are free to choose a new energy reference point without affecting the underlying physics, we may simplify our notation by setting $E_1 = 0$ and referencing all energies to this level. Then, we may write the re-calibrated energies $E_1^\star$, $E_2^\star(F)$ in equation (3.28) as:

$$E_1^\star = E_1 - E_1 = 0, \tag{3.30a}$$

$$\begin{aligned} E_2^\star(F) &= E_2(F) - E_1 \\ &= \left[(\varepsilon_T^h - \varepsilon_B^h) + (V_{BBTT}^{eh} - V_{BBBB}^{eh}) + (J_{BBTT}^{eh} - J_{BBBB}^{eh})\right] + f_-(F) \\ &= g(B,T) + f_-(F) \\ &\equiv E(F), \end{aligned} \tag{3.30b}$$

where $g(B,T) \equiv (\varepsilon_T^h - \varepsilon_B^h) + (V_{BBTT}^{eh} - V_{BBBB}^{eh}) + (J_{BBTT}^{eh} - J_{BBBB}^{eh})$ represents the energy difference between localized particle states in the bottom (B) and top (T) QDs arising purely from height asymmetry, while $f_-(F)$ contains the electric field dependence according to equation (3.27). Note that $E(F)$ represents the localized particle energy of the indirect exciton state $|2\rangle$.

Substituting in the re-calibrated energies of equation (3.30) and setting $t_h^{(B)} \equiv t_0$ for simplicity, we may write the Hamiltonian of (3.28) as:

$$H = \begin{bmatrix} 0 & -t_0 \\ -t_0 & E(F) \end{bmatrix}. \tag{3.31}$$

Inserting equation (3.31) into the Schrödinger equation (3.1) and expanding in the localized particle basis yields the following matrix equation for the quantum amplitudes $C_1(t)$ and $C_2(t)$:

$$i\hbar \frac{d}{dt}\mathbf{C}(t) = H\mathbf{C}(t), \qquad \mathbf{C}(t) = \begin{bmatrix} C_1(t) \\ C_2(t) \end{bmatrix}. \tag{3.32}$$

This equation may be solved by the ansatz:

$$\mathbf{C}(t) = \boldsymbol{\psi}\, e^{\lambda t}, \qquad \boldsymbol{\psi} = \begin{bmatrix} k_1 \\ k_2 \end{bmatrix} e^{\lambda t}, \tag{3.33}$$

where k_1, k_2, λ are constants. Inserting equation (3.33) into equation (3.32) and canceling the common factor $e^{\lambda t}$ yields:

$$i\hbar\lambda\boldsymbol{\psi} = H\boldsymbol{\psi}. \tag{3.34}$$

Setting $\varepsilon \equiv i\hbar\lambda$, we arrive at the equation for the stationary state eigenenergies and eigenvectors:

$$\begin{gathered} H\boldsymbol{\psi} = \varepsilon\boldsymbol{\psi}, \\ \begin{bmatrix} 0 & t_0 \\ t_0 & E(F) \end{bmatrix} \begin{bmatrix} k_1 \\ k_2 \end{bmatrix} = \varepsilon \begin{bmatrix} k_1 \\ k_2 \end{bmatrix}. \end{gathered} \tag{3.35}$$

Solving equation (3.35) yields the following eigenenergies and corresponding orthonormal eigenvectors as a function of the electric field F and tunneling ampitude t_0:

$$\varepsilon_{\pm}(F, t_0) = \frac{1}{2}\Big(E(F) \pm \kappa(F, t_0)\Big), \tag{3.36a}$$

$$\boldsymbol{\psi}_{\pm}(F, t_0) = \begin{bmatrix} \dfrac{-E \pm \kappa}{\sqrt{(2t_0)^2 + (-E \pm \kappa)^2}} \\[2ex] \dfrac{-2t_0}{\sqrt{(2t_0)^2 + (-E \pm \kappa)^2}} \end{bmatrix}, \tag{3.36b}$$

where for simplicity we have defined $\kappa(F, t_0)$ as:

$$\kappa(F, t_0) \equiv \sqrt{(E(F))^2 + (2t_0)^2}. \tag{3.37}$$

In Dirac notation, we may express the exciton stationary states $|\psi_\pm(F,t_0)\rangle$ of equation (3.36b) in the localized particle basis as follows:

$$|\psi_\pm(F,t_0)\rangle = \left(\frac{-E\pm\kappa}{\sqrt{(2t_0)^2+(-E\pm\kappa)^2}}\right)|1\rangle + \left(\frac{-2t_0}{\sqrt{(2t_0)^2+(-E\pm\kappa)^2}}\right)|2\rangle. \quad (3.38)$$

Notice in equation (3.38) that since $\kappa(F,t_0)=\sqrt{(E(F))^2+(2t_0)^2} > E(F)$ for all F whenever $t_0>0$, the superposition of localized particle states is out of phase by 180^o for $|\psi_+\rangle$, while it is in phase for $|\psi_-\rangle$. As a result, we call $|\psi_+\rangle$ an anti-symmetric superposition of the localized particle states, while $|\psi_-\rangle$ is a symmetric superposition.

We will return to solve for the general time-evolution of $|\Psi(t)\rangle$ in the next section, but first we analyze the stationary state solutions of equation (3.36). Figure 3.9 plots the localized particle energies $E_1^\star=0$, $E_2^\star=E(F)$ (black) alongside the eigenenergies $\varepsilon_\pm(F,t_0)$ (colored) of equation (3.36a) as a function of the electric field F at a fixed value of t_0. Here, we have used the same parameter values as in Fig. 3.8d (the two figures may be compared in the region of the low energy hole tunneling resonance). In particular, the energy difference $g(B=4\,\text{nm}, T=2.5\,\text{nm}) \cong 41$ meV determines the electric field value F_{AC} at which the hole tunneling AC occurs (in this case, $F_{AC}\cong 56.5$ kV/cm).

Inspection of Fig. 3.9 reveals that the eigenenergies ε_+, ε_- are separated by an anti-crossing energy difference equal to $2t_0$ at the hole tunneling resonance (here $2t_0\cong 0.6$ meV), while away from the resonance they asymptotically approach the energy values of the localized particle states. This behavior is confirmed by taking limits of the analytical eigenenergies in equation (3.36a). First, note that at the hole tunneling resonance F_{AC}, the localized particle energies of the direct and indirect excitons cross and $E(F_{AC})=0$, $\kappa(F_{AC},t_0)=2|t_0|$. Taking the difference of eigenenergies in this limit yields:

$$\begin{aligned}\varepsilon_+-\varepsilon_- &= \frac{1}{2}\Big(E(F_{AC})+\kappa(F_{AC},t_0)\Big)-\frac{1}{2}\Big(E(F_{AC})-\kappa(F_{AC},t_0)\Big)\\ &= \kappa(F_{AC},t_0)\\ &= 2|t_0|.\end{aligned} \quad (3.39)$$

Away from the hole tunneling resonance we observe that $[E(F)]^2 >> (2t_0)^2$, which implies that $\kappa(F,t_0)\cong|E(F)|$. Thus, in the limit that $F << F_{AC}$, we have $\varepsilon_+\cong E(F)$ and $\varepsilon_-\cong 0$, while for $F >> F_{AC}$, we have $\varepsilon_+\cong 0$ and $\varepsilon_-\cong E(F)$. This confirms our earlier statements in Section 3.2 that the localized particle states are excellent approximations to the stationary states away from any tunneling resonances.

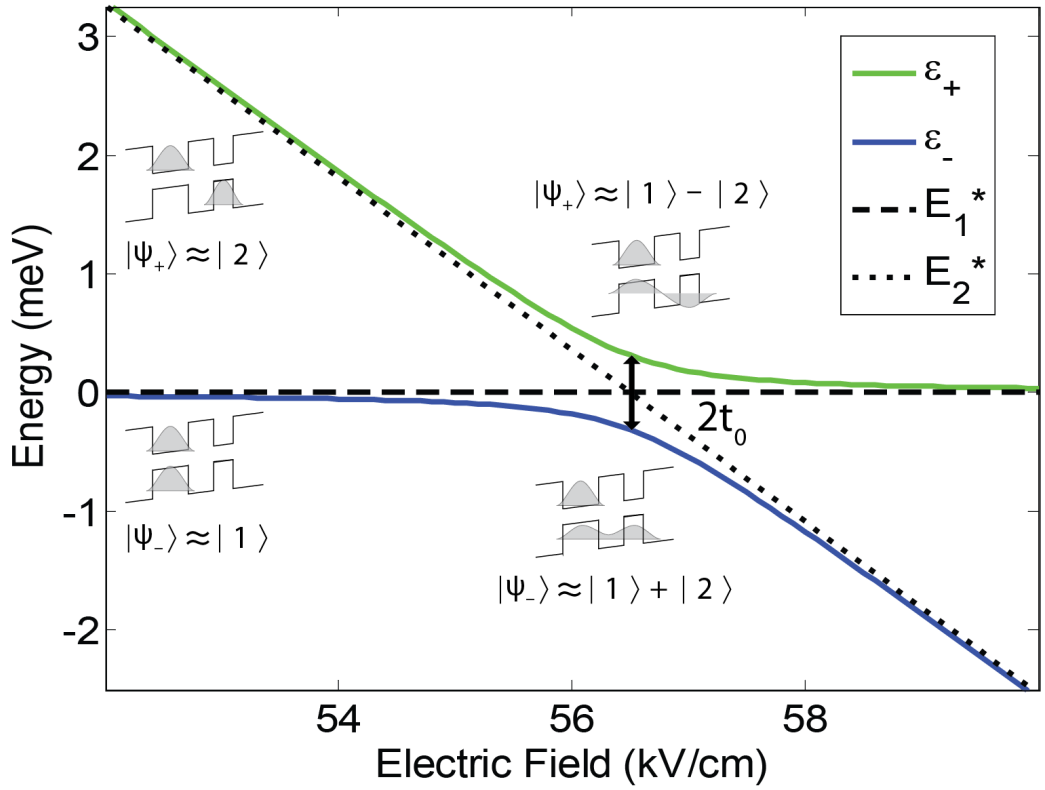

Figure 3.9: Plot of the eigenenergies ε_-, ε_+ and the localized particle energies $E_1^\star$, $E_2^\star$ versus electric field F for a fixed, positive hole tunneling amplitude t_0. At the tunneling resonance $F_{AC} \cong 56.5$ kV/cm, the eigenenergies level-repel with an anti-crossing energy of $2t_0 \cong 0.6$ meV. The inset QDM band diagrams show the carrier wavefunction distributions for the eigenstates at different values of the electric field. At the hole tunneling resonance, the eigenstates $|\psi_-\rangle$, $|\psi_+\rangle$ are symmetric and anti-symmetric superpositions of the localized particle states $|1\rangle$, $|2\rangle$. Away from the resonance, the eigenstates limit smoothly to the localized particle states.

To understand the formation of molecular states, it is insightful to inspect the stationary state eigenvectors. At a tunneling resonance, equation (3.38) becomes:

$$|\psi_{\pm}(F_{AC}, t_0)\rangle = \pm\frac{1}{\sqrt{2}}\,|1\rangle - \frac{t_0}{\sqrt{2{t_0}^2}}\,|2\rangle. \tag{3.40}$$

This reveals that the stationary states are equally weighted symmetric and anti-symmetric superpositions of the localized particle states. Moreover, the sign of the tunneling amplitude t_0 determines the symmetry of the eigenstates. Expanding equation (3.40) in the position representation reveals that the hole wavefunctions are delocalized across both QDs in the QDM:

$$\begin{aligned}\psi_{\pm}(\mathbf{r_e}, \mathbf{r_h}, t_0) &= \langle \mathbf{r_e}, \mathbf{r_h} | \psi_{\pm}(F_{AC}, t_0)\rangle \\ &= \pm\frac{1}{\sqrt{2}}\,\psi_B^e(\mathbf{r_e})\,\psi_B^h(\mathbf{r_h}) - \frac{t_0}{\sqrt{2{t_0}^2}}\,\psi_B^e(\mathbf{r_e})\,\psi_T^h(\mathbf{r_h}) \\ &= \frac{1}{\sqrt{2}}\,\psi_B^e(\mathbf{r_e})\left(\pm\psi_B^h(\mathbf{r_h}) - \frac{t_0}{|t_0|}\,\psi_T^h(\mathbf{r_h})\right),\end{aligned} \tag{3.41}$$

where $\psi_B^e(\mathbf{r_e})$, $\psi_B^h(\mathbf{r_h})$, $\psi_T^h(\mathbf{r_h})$ are localized particle wavefunctions of the electron and hole. These symmetric and anti-symmetric wavefunctions are superimposed on the inset band diagrams in Fig. 3.9, revealing the molecular-like sharing of the hole between the top and bottom QDs. In real molecules, symmetric superposition states are less energetic and yield stable molecular ground states known as *bonding* states, while the more energetic anti-symmetric states are termed *anti-bonding* states. This is also the case for the QDM depicted in Fig. 3.9, where the hole tunneling amplitude t_0 is taken to be positive. In real QDMs, the sign of t_0 determines the symmetry of the exciton ground state according to equation (3.40). For holes, the sign of t_0 is a function of the barrier thickness, so the actual molecular ground state of an exciton in a QDM may be either a bonding or an anti-bonding state [50].

Finally, we examine the eigenstates of equation (3.38) in the limit that we are far from the tunneling resonance. Recalling in this case that $\kappa(F, t_0) \cong |E(F)|$, we observe in the limit of $F << F_{AC}$ that $|\psi_+\rangle \cong |2\rangle$ and $|\psi_-\rangle \cong |1\rangle$, while in the opposite limit of $F >> F_{AC}$ we have $|\psi_+\rangle \cong |1\rangle$ and $|\psi_-\rangle \cong |2\rangle$. This confirms our assertion that the stationary states limit to the localized particle base states away from a tunneling resonance.

Free Evolution of an Exciton State in a QDM

We now complete our analysis of the two state exciton system near a hole tunneling resonance by computing the general time evolution of the quantum amplitudes

$C_1(t) = \langle 1|\Psi(t)\rangle$ and $C_2(t) = \langle 2|\Psi(t)\rangle$. The solution provides further insight into the molecular resonances and the dynamics of carrier tunneling in QDMs, while reinforcing the conclusion that tunneling effects may be greatly enhanced by tuning the QDM to an energy level resonance of the top and bottom dots.

We assume that the QDM system is closed (i.e., the level populations are conserved) and is free to evolve without the effects of damping or external driving. In this case, the quantum dynamics are governed by equation (3.32), which we re-state below:

$$\begin{bmatrix} i\hbar\,\dfrac{dC_1(t)}{dt} \\ i\hbar\,\dfrac{dC_2(t)}{dt} \end{bmatrix} = \begin{bmatrix} -t_0\,C_2(t) \\ -t_0\,C_1(t) + E(F)\,C_2(t) \end{bmatrix}. \tag{3.42}$$

The general solution to this equation is obtained by forming a superposition of the two independent solutions from the ansatz in equation (3.33), which yields the following solution vector:

$$\mathbf{C}(t) = \alpha\,\boldsymbol{\psi}_+ e^{\lambda_+ t} + \beta\,\boldsymbol{\psi}_- e^{\lambda_- t}, \tag{3.43}$$

where α, β are constants to be determined by the initial conditions, subject to the normalization condition $|C_1(0)|^2 + |C_2(0)|^2 = 1$. From the previous section, we recall that $\lambda_\pm = \varepsilon_\pm / i\hbar$ and the solutions for $\varepsilon_\pm, \psi_\pm$ are given in equation (3.36). Combining these results, we can write the solution for the components of $\mathbf{C}(t)$ as follows:

$$C_1(t) = \alpha \left(\frac{\kappa - E}{\sqrt{(2t_0)^2 + (\kappa - E)^2}} \right) e^{-i\varepsilon_+ t/\hbar} + \beta \left(\frac{-2t_0}{\sqrt{(2t_0)^2 + (\kappa - E)^2}} \right) e^{-i\varepsilon_- t/\hbar}, \tag{3.44a}$$

$$C_2(t) = \alpha \left(\frac{-(\kappa + E)}{\sqrt{(2t_0)^2 + (\kappa + E)^2}} \right) e^{-i\varepsilon_+ t/\hbar} + \beta \left(\frac{-2t_0}{\sqrt{(2t_0)^2 + (\kappa + E)^2}} \right) e^{-i\varepsilon_- t/\hbar}, \tag{3.44b}$$

where we recall from equation (3.36a) that $\varepsilon_\pm(F, t_0) = (1/2)\,[E(F) \pm \kappa(F, t_0)]$ and $\kappa(F, t_0) = \sqrt{(E(F))^2 + (2t_0)^2}$. Thus, the quantum amplitudes $C_1(t)$, $C_2(t)$ are functions of the electric field F and the hole tunneling amplitude t_0, though for simplicity this is not explicitly shown in equation (3.44).

An inspection of equation (3.44) reveals that the choices of the constants $\alpha = 0$, $\beta = 1$ and $\alpha = 1$, $\beta = 0$ correspond to the time-evolution of the stationary states

$|\psi_+\rangle$ and $|\psi_-\rangle$, respectively. A more interesting situation occurs if the system is initially prepared in a localized particle state. For example, suppose that the system is initially prepared in the direct exciton localized particle state $|1\rangle$, i.e., both the electron and hole are localized in the bottom QD. In this case, $C_1(0) = 1$, $C_2(0) = 0$ and the constants α, β are found to be:

$$\alpha = \frac{\sqrt{(2t_0)^2 + (-E+\kappa)^2}}{2\kappa}, \tag{3.45a}$$

$$\beta = -\frac{(E+\kappa)\sqrt{(2t_0)^2 + (-E+\kappa)^2}}{4\kappa t_0}. \tag{3.45b}$$

Inserting (3.45) into the general solution (3.44) yields the time evolution equations for the quantum amplitudes of an exciton initially prepared in the direct state $|1\rangle$:

$$\begin{aligned} C_1(t) &= \left(\frac{\kappa - E}{2\kappa}\right) e^{-i\varepsilon_+ t/\hbar} + \left(\frac{\kappa + E}{2\kappa}\right) e^{-i\varepsilon_- t/\hbar} \\ &= e^{-iEt/2\hbar}\left[\cos\left(\frac{\kappa}{2\hbar}t\right) + i\left(\frac{E}{\kappa}\right)\sin\left(\frac{\kappa}{2\hbar}t\right)\right], \end{aligned} \tag{3.46a}$$

$$\begin{aligned} C_2(t) &= -\left[\left(\frac{\kappa + E}{2\kappa}\right)\sqrt{\frac{(2t_0)^2 + (\kappa - E)^2}{(2t_0)^2 + (\kappa + E)^2}}\right]\left(e^{-i\varepsilon_+ t/\hbar} + e^{-i\varepsilon_- t/\hbar}\right) \\ &= ie^{-iEt/2\hbar}\left[\left(\frac{\kappa + E}{\kappa}\right)\sqrt{\frac{(2t_0)^2 + (\kappa - E)^2}{(2t_0)^2 + (\kappa + E)^2}}\right]\sin\left(\frac{\kappa}{2\hbar}t\right). \end{aligned} \tag{3.46b}$$

The corresponding probabilities of measuring the exciton to be localized in states $|1\rangle$ and $|2\rangle$ at any time $t \geq 0$ are:

$$|C_1(t)|^2 = \cos^2\left(\frac{\kappa}{2\hbar}t\right) + \left(\frac{E}{\kappa}\right)^2 \sin^2\left(\frac{\kappa}{2\hbar}t\right), \tag{3.47a}$$

$$|C_2(t)|^2 = \left(\frac{\kappa + E}{\kappa}\right)^2 \left[\frac{(2t_0)^2 + (\kappa - E)^2}{(2t_0)^2 + (\kappa + E)^2}\right] \sin^2\left(\frac{\kappa}{2\hbar}t\right). \tag{3.47b}$$

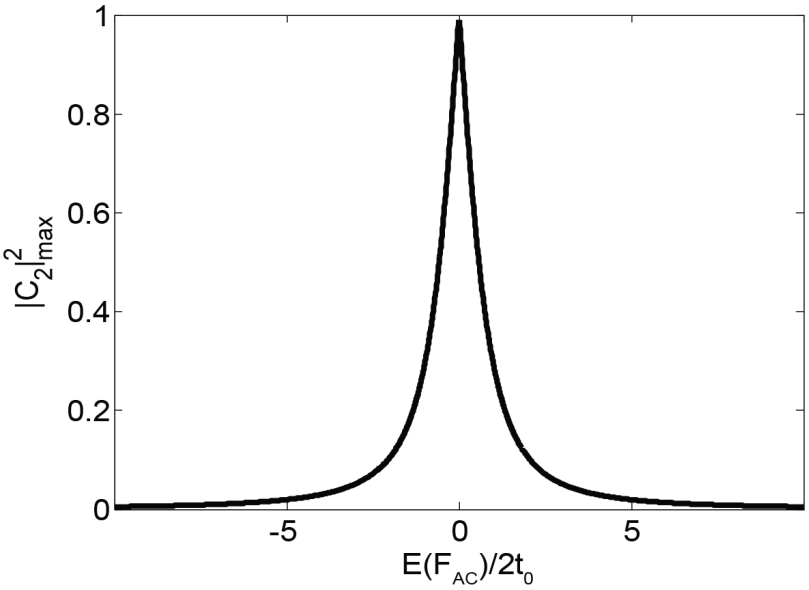

Figure 3.10: Plot of the maximum probability of an exciton initially prepared in state $|1\rangle$ to be later measured in state $|2\rangle$ as a function of the ratio of the energy difference between localized particle states to the tunneling energy. As the two level system gets further away from the resonance condition $E(F_{AC}) = 0$, it becomes increasingly less probable that the hole will tunnel from the bottom to the top QD of the QDM.

Inspection of equation (3.47) reveals that the probabilities oscillate with a period T and frequency ω given by:[10]

$$T = \frac{2\pi\hbar}{\kappa} = \frac{2\pi\hbar}{\sqrt{(E(F))^2 + (2t_0)^2}}, \tag{3.48a}$$

$$\omega = \frac{\kappa}{\hbar} = \frac{\sqrt{(E(F))^2 + (2t_0)^2}}{\hbar}. \tag{3.48b}$$

In particular, we observe that the oscillation frequency between states $|1\rangle$ and $|2\rangle$ increases in proportion to the energy difference $E(F)$ between the direct and indirect exciton states at a fixed tunneling amplitude t_0. Moreover, equation (3.47) reveals that the maximum probability of measuring the exciton to be in state $|2\rangle$ after initially

[10]Recall that the frequency of $\sin^2(x)$ is twice that of $\sin(x)$.

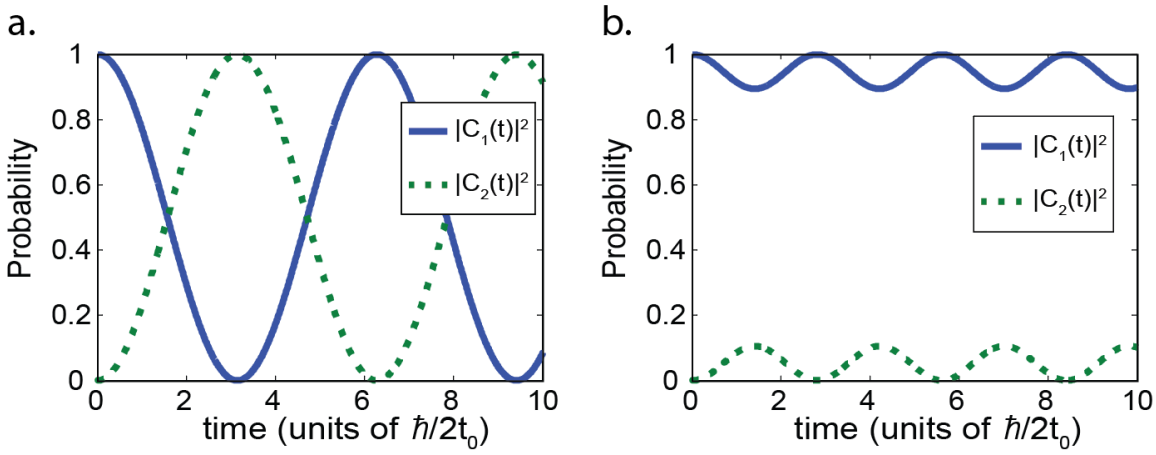

Figure 3.11: Plots of $|C_1(t)|^2, |C_2(t)|^2$ versus time for an exciton initially prepared in the direct state $|1\rangle$ at $t = 0$. (a) At a tunneling resonance with $E(F_{AC}) = 0$. (b) Away from the tunneling resonance with $E(F) = 2$ meV. In both plots, the tunneling energy is $2t_0 = 1$ meV and $|C_1(t)|^2 + |C_2(t)|^2 = 1$ at all times.

starting out in state $|1\rangle$ is:

$$|C_2(t)|^2_{max} = \left(\frac{\kappa + E}{\kappa}\right)^2 \left[\frac{(2t_0)^2 + (\kappa - E)^2}{(2t_0)^2 + (\kappa + E)^2}\right]$$
$$= \left[\frac{\sqrt{1 + \left(\frac{2t_0}{E}\right)^2} + 1}{\sqrt{1 + \left(\frac{2t_0}{E}\right)^2}}\right] \left[\frac{\left(\frac{2t_0}{E}\right)^2 + \left(\sqrt{1 + \left(\frac{2t_0}{E}\right)^2} - 1\right)^2}{\left(\frac{2t_0}{E}\right)^2 + \left(\sqrt{1 + \left(\frac{2t_0}{E}\right)^2} + 1\right)^2}\right]. \quad (3.49)$$

Notice that $|C_2(t)|^2_{max}$ is a function of the ratio of the energy difference between the direct and indirect states to the hole anti-crossing energy, i.e., $E(F)/2t_0$. Equation (3.49) is plotted in Figure 3.10. We observe that the maximum probability of making a transition to the indirect state $|2\rangle$ reaches unity at an exact energy resonance of the localized particle states (i.e., $E(F_{AC}) = 0$). Away from the tunneling resonance, the maximum transition probability decreases to zero at a rate controlled by the tunneling amplitude t_0. This provides another quantitative measure of the extent of the tunneling resonance as a function of the electric field.

These trends are nicely illustrated in Figure 3.11, which plots the probability amplitudes $|C_1(t)|^2$, $|C_2(t)|^2$ for two different values of the ratio $E(F)/2t_0$. In the

case of an exact energy resonance, Fig. 3.11a shows a perfectly symmetric oscillation of the probabilities for observing the exciton to be in the direct or indirect state. We may interpret this to mean that the hole dynamically tunnels between the top and bottom dots with an angular rate given by equation (3.48b). In Fig. 3.11b, we plot the slightly off-resonance case where $E/2t_0 = 2$. In this case, we already observe an increased oscillation frequency combined with a reduced probability for the hole to tunnel from the bottom to the top dot at any time $t \geq 0$. Once again, this confirms the impact that energy level tuning between top and bottom dots has on tunneling effects, and underscores the utility of electric field tuning to achieve such control.

3.4 Laser Driven Two-level System

All of the experimental results in this dissertation have been obtained by illuminating QDM samples with quasi-monochromatic lasers. Consequently, it is imperative to understand the effect of laser illumination on a QDM system in order to understand the results of this dissertation.

During off-resonant laser excitation, the metastable QDM stationary states described in Section 3.3 are populated via ultra-fast relaxation from higher energy excited states near the laser excitation energy. These populations are maintained for a characteristic lifetime, until the metastable states relax to the QDM crystal ground state on account of environmental perturbations. Thus, the QDM emission spectra from non-resonant laser excitation is well-described by the theory of Section 3.3.

The situation of a metastable ground state driven by a quasi-resonantly tuned laser is quite different. In this case, coherence between the laser and the quantum system can lead to a periodic population transfer between the states, a phenomenon known as *Rabi oscillations* [51]. Moreover, coherence with the driving laser may result in interference effects that produce a pronounced enhancement or reduction in the absorption of laser light. In Chapter 7, we demonstrate such an interference effect for QDMs when an indirect exciton state is tunnel coupled to a direct polaron state with a continuum of energy levels, resulting in a Fano interference.

To understand the various dynamics of a laser driven QDM system, we present a theoretical description of a resonantly driven two-level quantum system in the semi-classical approach. The ground state exciton results from the excitation of an electron between discrete valence and conduction band energy levels. Moreover, the polarization and line width of the driving laser may be chosen such that only one of the bright exciton states is radiatively coupled. Under these conditions, a bright exciton state in a QD may be described as a two-level system [52]. In this case, the crystal ground state represents the lower level and the metastable bright exciton state the upper level.

In the following, we first describe the dynamics of an isolated two-level quantum system (i.e., free of environmental perturbations) driven by a quasi-monochromatic laser. Afterwards, we present the more realistic situation of a driven system in the presence of environmental damping, which leads to a loss of coherence and state relaxation with characteristic time constants. Moreover, we show that the power dependence of the optical spectrum can lead to the non-linear effects of saturation and power broadening.

Undamped Driving

Here, we describe the interaction of an isolated two-level quantum system interacting with a quasi-monochromatic laser in the semi-classical description. The idealized isolated system interacts only with the laser field and is otherwise undamped by the environment. The resulting solution reveals that the laser field drives a periodic oscillation in the population of the two-level system known as a Rabi oscillations.

We consider a two-level quantum system for a particle with charge q consisting of two orthogonal stationary states denoted by $|a\rangle$, $|b\rangle$ and with corresponding discrete energy levels ε_a, ε_b. Our goal is to determine the time-evolution of the general quantum state $|\Psi(t)\rangle$ under the influence of quasi-resonant laser illumination. The general solution, expanded in the basis of unperturbed eigenstates, may be written as:

$$\begin{aligned} |\Psi(t)\rangle &= \big[\langle a\,|\Psi(t)\rangle\big]|a\rangle + \big[\langle b\,|\Psi(t)\rangle\big]|b\rangle \\ &= \Big[\gamma_a(t)e^{-i\varepsilon_a t/\hbar}\Big]|a\rangle + \Big[\gamma_b(t)e^{-i\varepsilon_b t/\hbar}\Big]|b\rangle. \end{aligned} \tag{3.50}$$

In the above equation, we have separated the expansion coefficients $\langle n\,|\Psi(t)\rangle$ for $n = a, b$ into a product of terms representing the laser-induced time evolution $\gamma_n(t)$ and the free evolution $\exp(-i\varepsilon_n t/\hbar)$ of the quantum system. The general solution is then determined by using the Schrödinger equation (3.1) to calculate the coefficients $\gamma_n(t)$ with a total Hamiltonian given by:

$$\hat{H}(t) = \hat{H}_0 + \hat{H}_I(t). \tag{3.51}$$

In the above equation, $\hat{H}_0$ is the time-independent Hamiltonian of the undriven quantum system and $\hat{H}_I$ is a time-dependent Hamiltonian representing the light-matter interaction. The probability of measuring the particle to be in the state $|a\rangle$ or $|b\rangle$ at any time $t \geq 0$ is then given by $|\gamma_a(t)|^2$ and $|\gamma_b(t)|^2$, respectively. We point out that one may use perturbation theory to solve this problem if the laser driving is weak. However, for the case of a two-level system driven by a quasi-resonant laser, a non-perturbative analytical solution may be obtained by invoking the so called *rotating*

wave approximation.[11] We take this latter approach, which is valid for arbitrary laser intensities.

To begin, we set the lower energy level ε_a equal to zero and define the transition energy between states $|a\rangle$ and $|b\rangle$ as:

$$\hbar\omega_0 = \varepsilon_b - \varepsilon_a = \varepsilon_b > 0. \tag{3.52}$$

Then, the eigenbasis representation of the Hamiltonian of the two-level system alone is given by:

$$H_0 = \begin{bmatrix} 0 & 0 \\ 0 & \hbar\omega_0 \end{bmatrix}. \tag{3.53}$$

The laser field is described in the classical approximation as an electromagnetic field, which we take to have the following plane wave form:[12]

$$\mathbf{E}(\mathbf{r}, t) = E_0\, \hat{\mathbf{e}} \cos(\omega t - \mathbf{k}\cdot\mathbf{r}), \tag{3.54a}$$

$$\mathbf{B}(\mathbf{r}, t) = \frac{\mathbf{k}\times\hat{\mathbf{e}}}{\omega} E_0 \cos(\omega t - \mathbf{k}\cdot\mathbf{r}), \tag{3.54b}$$

$$\mathbf{E}_0 \cdot \mathbf{k} = 0, \tag{3.54c}$$

$$|\mathbf{k}| = \frac{2\pi}{\lambda}, \tag{3.54d}$$

where $\mathbf{E}(\mathbf{r}, t)$ and $\mathbf{B}(\mathbf{r}, t)$ are the time-dependent electric and magnetic fields, E_0 is the magnitude of the electric field, ω is the laser frequency, $\hat{\mathbf{e}}$ is a unit vector parallel to the direction of the electric field that describes the polarization of the light wave, $\mathbf{k}$ is the wave vector that points in the direction of wave propagation and λ is the material dependent wavelength of the laser light.

To describe the light-matter interaction, we assume that the laser wavelength is long compared to the dimensions of the quantum system. This is known as the long-wavelength approximation.[13] In this case, the electric field may be considered to be

[11] This approximation is more fittingly described as the *quasi-resonant* approximation, since it assumes a laser energy that is quasi-resonant with the transition energy.

[12] For clarity, in this section we describe the electric field part of the light wave by the conventional symbol $\mathbf{E}$.

[13] This is an excellent approximation for InAs QDMs, since the QDM dimensions are $\lesssim 25$ nm, while the infrared laser wavelengths are $\gtrsim 850$ nm.

spatially constant over the extent of the quantum system. Using this approximation, the light-matter interaction may be described by the electric dipole operator:

$$\boldsymbol{\mu}_{op} = q(\mathbf{r}_{op} - \mathbf{r}_0), \tag{3.55}$$

where $\mathbf{r}_{op}$ is the position operator, $\mathbf{r}_0$ is the center of mass position of the quantum system and q is the charge of the particle.[14] The time-dependent interaction Hamiltonian between the laser and the quantum system may then be given by the so called *electric dipole Hamiltonian*, which has the form of the interaction energy of a classical electric dipole in an electric field:

$$\hat{H}_I(t) = -\boldsymbol{\mu}_{op} \cdot \mathbf{E}(\mathbf{r}_0, t). \tag{3.56}$$

We shall represent the electric dipole Hamiltonian of equation (3.56) in the two-state eigenbasis. Based on symmetry arguments, the diagonal matrix elements of the electric dipole Hamiltonian typically vanish, and we will assume this to be the case in what follows [51].[15] For the off-diagonal matrix element $H_{I,\,ba}(t)$, we write:

$$\begin{aligned} H_{I,\,ba}(t) &= \langle b| - \boldsymbol{\mu}_{op} \cdot \mathbf{E}(\mathbf{r}_0, t)|a\rangle \\ &= -E_0 \cos\left(\omega t - \mathbf{k} \cdot \mathbf{r}_0\right) \langle b|\boldsymbol{\mu}_{op} \cdot \hat{\mathbf{e}}|a\rangle \\ &= \hbar\Omega_1 \cos\left(\omega t + \phi\right), \end{aligned} \tag{3.57}$$

where we have defined the so called *Rabi frequency* Ω_1 as:

$$\Omega_1(E_0) \equiv -\frac{E_0}{\hbar} \langle b|\boldsymbol{\mu}_{op} \cdot \hat{\mathbf{e}}|a\rangle, \tag{3.58}$$

and the constant phase of the time-dependence as:

$$\phi \equiv -\mathbf{k} \cdot \mathbf{r}_0. \tag{3.59}$$

In equation (3.58), we choose the arbitrary phases of the quantum states $|a\rangle$ and $|b\rangle$ in such a way that Ω_1 is a positive real number. Moreover, $H_{I,\,ba}(t) = H_{I,\,ab}(t)$ since $\hat{H}_I$ is a hermitian operator. We also point out that the Rabi frequency is linearly proportional to the electric field strength E_0. The total Hamiltonian of the quantum system in the eigenbasis representation is then given by combining equations (3.53) and (3.57) to yield:

$$H(t) = H_0 + H_I(t) = \begin{bmatrix} 0 & \hbar\Omega_1 \cos\left(\omega t + \phi\right) \\ \hbar\Omega_1 \cos\left(\omega t + \phi\right) & \hbar\omega_0 \end{bmatrix}. \tag{3.60}$$

[14] In the case of an exciton in a QD, q is equal to the elementary charge e.

[15] For example, since the dipole Hamiltonian operator has odd parity, it does not couple states with the same parity.

To solve for the time-evolution of the two-state system, we use the Schrödinger equation (3.1) and substitute in the general state vector of equation (3.50) and the above total Hamiltonian. Since $\varepsilon_a = 0$ and $\varepsilon_b = \hbar\omega_0$, the general state vector in the eigenbasis representation may be written as:

$$|\Psi(t)\rangle = \begin{bmatrix} \gamma_a(t) \\ \gamma_b(t)\, e^{-i\omega_0 t} \end{bmatrix}. \tag{3.61}$$

Applying the Schrödinger equation to this vector with the total Hamiltonian in (3.60) then yields the following system of differential equations, given in vector form:

$$\begin{bmatrix} i\hbar \dfrac{d}{dt}\, \gamma_a(t) \\ i\hbar \dfrac{d}{dt}\, \gamma_b(t)\, e^{-i\omega_0 t} \end{bmatrix} = \begin{bmatrix} \hbar\Omega_1 \cos(\omega t + \phi)\, e^{-i\omega_0 t}\, \gamma_b(t) \\ \\ \hbar\Omega_1 \cos(\omega t + \phi)\, \gamma_a(t) + \hbar\omega_0\, e^{-i\omega_0 t}\, \gamma_b(t) \end{bmatrix}. \tag{3.62}$$

After some mathematical simplification, the above equation may be re-written as:

$$\begin{bmatrix} i\dfrac{d}{dt}\, \gamma_a(t) \\ i\dfrac{d}{dt}\, \gamma_b(t) \end{bmatrix} = \begin{bmatrix} \dfrac{\Omega_1 e^{i\phi}}{2}\, e^{i(\omega-\omega_0)t}\, \gamma_b(t) + \dfrac{\Omega_1 e^{-i\phi}}{2}\, e^{-i(\omega+\omega_0)t}\, \gamma_b(t) \\ \dfrac{\Omega_1 e^{-i\phi}}{2}\, e^{-i(\omega-\omega_0)t}\, \gamma_a(t) + \dfrac{\Omega_1 e^{i\phi}}{2}\, e^{i(\omega+\omega_0)t}\, \gamma_a(t) \end{bmatrix}. \tag{3.63}$$

Next, we make the rotating wave approximation and drop the terms with imaginary exponential powers of $\omega + \omega_0$. These terms are negligible in the regime of quasi-resonant excitation, where $\omega + \omega_0 >> |\omega - \omega_0|$ and the right hand side of the inequality is close to zero (i.e., the laser energy is quasi-resonant with the transition energy) [51]. Thus, for quasi-resonant excitation, equation (3.63) may be replaced to excellent approximation by:

$$\begin{bmatrix} i\dfrac{d}{dt}\, \gamma_a(t) \\ i\dfrac{d}{dt}\, \gamma_b(t) \end{bmatrix} = \begin{bmatrix} \dfrac{\Omega_1 e^{i\phi}}{2}\, e^{i(\omega-\omega_0)t}\, \gamma_b(t) \\ \dfrac{\Omega_1 e^{-i\phi}}{2}\, e^{-i(\omega-\omega_0)t}\, \gamma_a(t) \end{bmatrix}. \tag{3.64}$$

To further simplify this system of equations, we define the laser detuning from resonance:

$$\delta = \omega - \omega_0, \tag{3.65}$$

and make the following change of variables:

$$\tilde{\gamma}_a(t) = \gamma_a(t)\, e^{-i\delta t/2}, \tag{3.66a}$$

$$\tilde{\gamma}_b(t) = \gamma_b(t)\, e^{i\delta t/2}. \tag{3.66b}$$

We point out that since $|\tilde{\gamma}_a(t)|^2 = |\gamma_a(t)|^2$ and $|\tilde{\gamma}_b(t)|^2 = |\gamma_b(t)|^2$, the transition probabilities are directly obtainable from the new variables. The system of equations in (3.64) may then be written as:

$$\begin{bmatrix} i\dfrac{d}{dt}\,\tilde{\gamma}_a(t) \\ i\dfrac{d}{dt}\,\tilde{\gamma}_b(t) \end{bmatrix} = \begin{bmatrix} \dfrac{\delta}{2}\,\tilde{\gamma}_a(t) + \dfrac{\Omega_1 e^{i\phi}}{2}\,\tilde{\gamma}_b(t) \\ \dfrac{\Omega_1 e^{-i\phi}}{2}\,\tilde{\gamma}_a(t) - \dfrac{\delta}{2}\,\tilde{\gamma}_b(t) \end{bmatrix}. \tag{3.67}$$

Equation (3.67) is a 1st order homogeneous system of differential equations with constant coefficients, very similar to the system of equations for a QDM under the time-independent tunneling interaction treated in Section 3.3, and may be solved by the same eigenvalue method. The resulting general solution is:

$$\begin{aligned} \begin{bmatrix} \tilde{\gamma}_a(t) \\ \tilde{\gamma}_b(t) \end{bmatrix} = &\left(\frac{\alpha\, e^{-i\Omega t/2}}{\sqrt{\Omega_1^2\, e^{-i\phi} + (\delta+\Omega)^2\, e^{i\phi}}} \right) \begin{bmatrix} (\delta+\Omega)\, e^{i\phi/2} \\ \Omega_1 e^{-i\phi/2} \end{bmatrix} \\ &+ \left(\frac{\beta\, e^{i\Omega t/2}}{\sqrt{\Omega_1^2\, e^{-i\phi} + (\delta-\Omega)^2\, e^{i\phi}}} \right) \begin{bmatrix} (\delta-\Omega)\, e^{i\phi/2} \\ \Omega_1 e^{-i\phi/2} \end{bmatrix}. \end{aligned} \tag{3.68}$$

In the above equation, α, β are constants to be determined by the initial conditions and are subject to the normalization condition $|\tilde{\gamma}_a(0)|^2 + |\tilde{\gamma}_b(0)|^2 = 1$. We have also introduced the *generalized Rabi frequency* $\Omega(E_0)$, defined as:

$$\Omega(E_0) \equiv \sqrt{\delta^2 + \Omega_1(E_0)^2}. \tag{3.69}$$

We are interested in the case in which the particle starts out in the lower state $|a\rangle$ at time $t = 0$, which corresponds to the initial condition $\tilde{\gamma}_a(0) = 1,\ \tilde{\gamma}_b(0) = 0$. Inserting this initial condition into equation (3.68), we find the constants α, β to be:

$$\alpha = \frac{\sqrt{\Omega_1^2\, e^{-i\phi} + (\delta+\Omega)^2\, e^{i\phi}}}{2\,\Omega\, e^{i\phi/2}}, \tag{3.70a}$$

$$\beta = -\frac{\sqrt{\Omega_1^2\, e^{-i\phi} + (\delta-\Omega)^2\, e^{i\phi}}}{2\,\Omega\, e^{i\phi/2}}. \tag{3.70b}$$

Then, inserting (3.70) into the general solution (3.68), we find the following particular solutions for $\tilde{\gamma}_a(t)$, $\tilde{\gamma}_b(t)$:

$$\tilde{\gamma}_a(t) = \cos\left(\frac{\Omega t}{2}\right) - i\frac{\delta}{\Omega}\sin\left(\frac{\Omega t}{2}\right), \tag{3.71a}$$

$$\tilde{\gamma}_b(t) = -i\frac{\Omega_1 e^{-i\phi}}{\Omega}\sin\left(\frac{\Omega t}{2}\right). \tag{3.71b}$$

The probability of measuring a particle initially prepared in the lower state at time $t = 0$ to be in the states $|a\rangle$ or $|b\rangle$ under quasi-resonant laser driving with detuning δ is then given by:

$$|\tilde{\gamma}_a(t)|^2 = \cos^2\left(\frac{\Omega t}{2}\right) + \frac{\delta^2}{\delta^2 + \Omega_1^2}\sin^2\left(\frac{\Omega t}{2}\right), \tag{3.72a}$$

$$|\tilde{\gamma}_b(t)|^2 = \frac{\Omega_1^2}{\delta^2 + \Omega_1^2}\sin^2\left(\frac{\Omega t}{2}\right), \tag{3.72b}$$

where we recall that $\Omega = \sqrt{\delta^2 + \Omega_1^2}$. The maximum probability for the particle to transition to the upper state $|b\rangle$ is:

$$|\tilde{\gamma}_b(t)|^2_{max} = \frac{\Omega_1^2}{\delta^2 + \Omega_1^2}. \tag{3.73}$$

Figure 3.12 plots $|\tilde{\gamma}_b(t)|^2_{max}$ versus the detuning parameter δ in units of the Rabi frequency Ω_1. When the laser is at an exact resonance ($\delta = 0$), the maximum probability of making a transition to the upper state is unity. For non-zero detuning, the maximum transition probability has a Lorentzian line shape with full width at half max equal to $2\Omega_1$. Thus, the width of the resonance increases in linear proportion to the electric field amplitude E_0 of the driving laser.

In Figure 3.13, we plot the transition probability to the higher energy state $|b\rangle$ as a function of time for two different values of the laser detuning δ. On resonance, the probability of a transition to the upper state reaches unity after a time $t = \pi/\Omega_1$ and then continues to Rabi oscillate between zero and one with a period equal to $T = 2\pi/\Omega_1$. Off resonance, the Rabi oscillations persist, but with an increased frequency and reduced maximum transition probability given by equation (3.73). In general, the Rabi oscillation period as a function of the laser detuning and electric field amplitude is:

$$T = \frac{\pi}{\Omega} = \frac{\pi}{\sqrt{\delta^2 + \Omega_1(E_0)^2}}. \tag{3.74}$$

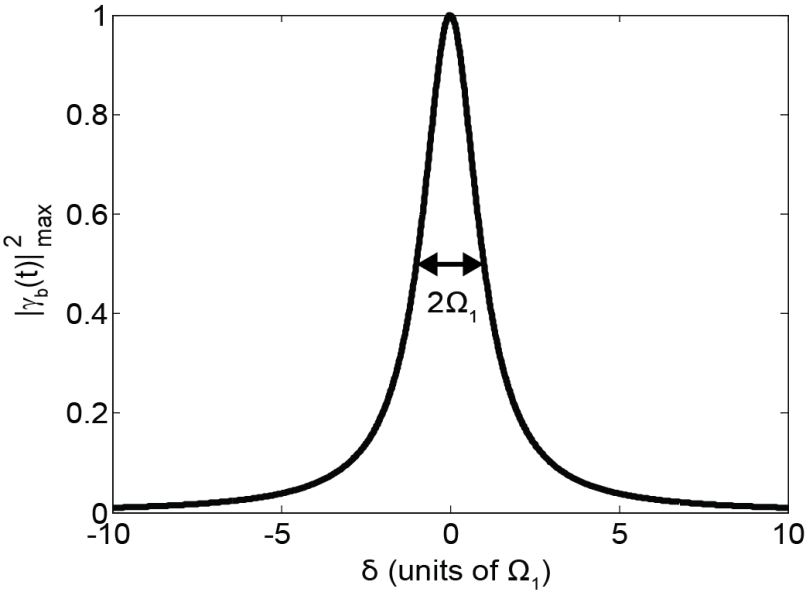

Figure 3.12: Plot of the maximum probability for a particle initially prepared in the lower energy state $|a\rangle$ to transition to the higher energy state $|b\rangle$ as a function of the laser detuning δ in units of the Rabi frequency Ω_1. Transitions are unlikely far from resonance. However, the probability of off-resonant transitions increases in proportion to the electric field magnitude of the laser since the full width at half max of the resonance is equal to $2\Omega_1 \propto E_0$.

Thus, the frequency of Rabi oscillations may also be increased by increasing the power of the laser.

We point out that Rabi oscillations are a general phenomena that may be observed in various two-state systems under quasi-resonant laser excitation. On resonance, it is possible to deterministically transfer the population from the lower to upper energy state if the duration of the laser interaction is fixed at π/Ω_1 (this is known as a π-*pulse excitation*). In this case, we may think of the quantum two-level system as absorbing a photon of energy $\hbar\omega_0$ from the laser field. In real systems, of course, the amplitude $|\gamma_b(t)|$ of the upper energy state decreases with time due to environmental damping. Thus, to observe Rabi oscillations experimentally, the generalized Rabi frequency must exceed the radiative decay rates of the quantum states involved.

Finally, we wish to highlight the linear dependence of the Rabi frequency on the electric field magnitude of the laser. We have seen that this leads to an increase in the Rabi frequency and a broadening of the resonance line width at increased laser powers. In the next section, we find that a similar dependence leads to power broadening and saturation when we consider a laser driven two-level system with damping.

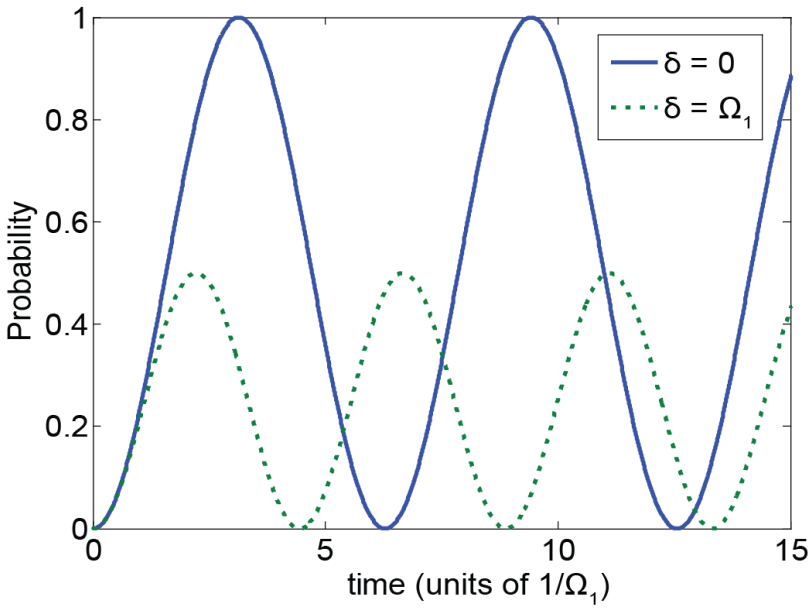

Figure 3.13: Rabi oscillations of the transition probability $|\tilde{\gamma}_b(t)|^2$ versus time at a fixed Rabi frequency Ω_1 for two different laser detunings: (i) $\delta = 0$ (on resonance) and $\delta = \Omega_1$.

Damped Driving

We now consider a more realistic laser driven two-level system by including the effects of damping. The inclusion of relaxation terms means that the laser driven excitation to the upper energy level is offset by spontaneous emission back to the lower energy level on a characteristic time scale. Analytical results reveal that the indefinite Rabi oscillations of the previous section may become exponentially damped out or disappear entirely. Moreover, relaxation causes the system to reach a steady state average population in the upper and lower levels after a characteristic decay time. Analysis of the steady state population reveals a non-linear dependence of the absorption spectrum on the laser intensity, producing the well-known effects of saturation and power broadening. Two-level saturation plays an important role in the non-linearity of the phonon-induced Fano effect described in Chapter 7.

To include the effects of environmental damping on a laser driven two-level system, we employ the density matrix formalism. This allows us to analyze the properties of the damped two-level system without requiring a detailed analysis of the environmental perturbations responsible for the damping [51]. Once again, we have in mind a two-level system of an electron in a QD, with the lower state the crystal ground state and the upper state the bright exciton state. In this case, the lower level is indefinitely stable (i.e., it does not relax) and the total population of the two state

system remains constant (i.e., the system is closed). Moreover, the two-level system can be represented by a state vector $|\Psi(t)\rangle$, which in the context of the density matrix treatment is called a *pure state*. Under these conditions, we define the density operator $\hat{\sigma}$ to be equal to the following projection operator:

$$\hat{\sigma} = |\Psi(t)\rangle\langle\Psi(t)|. \tag{3.75}$$

The representation of $\hat{\sigma}$ in the stationary state basis is known as the density matrix. The probabilities of measuring the system to be in the states $|a\rangle$, $|b\rangle$, respectively, are given by the diagonal elements $\sigma_{aa}(t) = \langle a|\hat{\sigma}|a\rangle$, $\sigma_{bb}(t) = \langle b|\hat{\sigma}|b\rangle$ of the density matrix. These diagonal elements are commonly referred to as the *populations* of the states $|a\rangle$, $|b\rangle$. For a closed system, the conservation of probability (and hence population) leads to the following condition:

$$Tr\hat{\sigma} = \sigma_{aa} + \sigma_{bb} = 1. \tag{3.76}$$

Since the density matrix is hermitian, the off-diagonal elements $\sigma_{ab}(t) = \langle a|\hat{\sigma}|b\rangle$, $\sigma_{ba}(t) = \langle b|\hat{\sigma}|a\rangle$ are complex conjugates of one another:

$$\sigma_{ab}(t) = \sigma^*_{ba}(t). \tag{3.77}$$

The off-diagonal elements are called *coherences* since they depend on the relative phases of the stationary states. They often play an important role in coherent manipulations of the state vector.

In the absence of damping, the time evolution of $\hat{\sigma}$ may be deduced from the Schrödinger equation (3.1) to be:

$$\frac{d\hat{\sigma}}{dt} = \frac{1}{i\hbar}\big[\hat{H},\, \hat{\sigma}\big]. \tag{3.78}$$

The above equation involves the commutator of the system Hamiltonian and the density operator. By representing equation (3.78) in the basis of stationary states $|a\rangle$, $|b\rangle$, we arrive at a system of coupled differential equations that describes the rates of change of the individual components of the density matrix under the influence of the system Hamiltonian.

The *average* effects of weak environmental interactions on the two-level system may be included in the density matrix formulation by adding a relaxation operator to equation (3.78) [51]. It is easiest to describe the various relaxation terms by stating their effect on the rates of change of the individual elements of the density matrix. For the diagonal terms, the population rates of change due to relaxation are given by:

$$\left\{\frac{d}{dt}\sigma_{ii}\right\}_{rel} = -\sum_{j\neq i}\Gamma_{i\to j}\sigma_{ii} + \sum_{j\neq i}\Gamma_{j\to i}\sigma_{jj}, \qquad i,j = a,b. \tag{3.79}$$

In the above equation, the transition rates $\Gamma_{i\to j}$, $\Gamma_{j\to i}$ indicate how transitions to and from state $|j\rangle$ change the population σ_{ii} of state $|i\rangle$. The relaxation terms of the off-diagonal coherences are described by a different set of relaxation rates, denoted $\gamma_{i,j}$, according to:

$$\left\{\frac{d}{dt}\sigma_{ij}\right\}_{rel} = -\gamma_{i,j}\sigma_{ij}. \tag{3.80}$$

The general expressions given in equations (3.79) and (3.80) are valid for a wide variety of two-level systems. Here, we specifically consider a closed two-level system and we assume that spontaneous emission is the dominant source of relaxation from the upper to lower energy level. In this case, the diagonal relaxation terms are given by:

$$\left\{\frac{d}{dt}\sigma_{bb}\right\}_{rel} = -\Gamma_{sp}\,\sigma_{bb}, \tag{3.81a}$$

$$\left\{\frac{d}{dt}\sigma_{aa}\right\}_{rel} = \Gamma_{sp}\,\sigma_{bb}, \tag{3.81b}$$

while the relaxation of the coherences is described by:

$$\left\{\frac{d}{dt}\sigma_{ba}\right\}_{rel} = -\gamma\sigma_{ba}. \tag{3.82}$$

Notice that in (3.81), the spontaneous emission rate Γ_{sp} serves to transfer the population from the upper to the lower level. The decay rate γ in equation (3.82) is called the *decoherence* or *dephasing* rate since it disrupts the phase relationship between the lower and upper states that appears in the off-diagonal elements of the density matrix.

It is customary to define characteristic time constants of the two-level system based on equations (3.81) and (3.82). We define the *radiative lifetime* T_1 from the spontaneous emission rate Γ_{sp}, which specifies the average duration that a particle remains in the upper level before it relaxes to the ground state via spontaneous emission:

$$T_1 = \frac{1}{\Gamma_{sp}}. \tag{3.83}$$

The dephasing rate γ is related to the spontaneous emission rate Γ_{sp}. In particular, if the coherences decay purely as a result of spontaneous emission, then the following relation holds [53]:

$$\gamma = \frac{\Gamma_{sp}}{2}. \tag{3.84}$$

In general, γ may include contributions from processes other than spontaneous emission that destroy phase coherence. These processes may include scattering interactions with phonons (i.e., vibrations of the crystal lattice), interactions with other electronic states or coupling to electric and magnetic field fluctuations in the local environment [53]. For this general case, the decoherence rate may be written as:

$$\gamma = \frac{\Gamma_{sp}}{2} + \gamma_{pd}, \tag{3.85}$$

where the so called *pure* dephasing rate γ_{pd} describes the loss of coherence due to all dephasing processes other than spontaneous emission.

We may define two additional time constants for the two-level system based on equation (3.85) that are related to the radiative lifetime T_1 as follows:

$$\gamma \equiv \frac{1}{T_2} = \frac{1}{2T_1} + \frac{1}{T_2^*}. \tag{3.86}$$

In the above equation, T_2 is alternately called the *phase-relaxation*, *decoherence* or *dephasing* time. The time constant T_2^* is called the *pure dephasing* time and is related to the pure dephasing rate according to:

$$T_2^* = \frac{1}{\gamma_{pd}}. \tag{3.87}$$

In the following, we assume all the above decay rates, and their associated time constants, to be positive real numbers.

We now return to study the time evolution of the density matrix. Before including the relaxation terms, we consider the equations arising purely from the Hamiltonian terms in equation (3.78). The system Hamiltonian in this case is identical to that of the undamped laser driven two-level system in the previous section. For simplicity, however, we assume that the phase of the electric field is equal to zero. In this case, the system Hamiltonian becomes:

$$H(t) = \begin{bmatrix} 0 & \hbar\Omega_1 \cos(\omega t) \\ \hbar\Omega_1 \cos(\omega t) & \hbar\omega_0 \end{bmatrix}, \tag{3.88}$$

where we recall that $\Omega_1 = -E_0 \langle b|\boldsymbol{\mu}_{op} \cdot \hat{\mathbf{e}}|a\rangle/\hbar$ is the Rabi frequency.

Representing the time evolution equation (3.78) for the density operator in the stationary state basis and inserting the above Hamiltonian yields the following set of equations for the elements of the density matrix:

$$\frac{d}{dt}\sigma_{aa} = -i\Omega_1 \cos\omega t \left(\sigma_{ba} - \sigma_{ab}\right), \tag{3.89a}$$

$$\frac{d}{dt}\sigma_{bb} = i\Omega_1 \cos\omega t \left(\sigma_{ba} - \sigma_{ab}\right), \tag{3.89b}$$

$$\frac{d}{dt}\sigma_{ab} = i\omega_0\sigma_{ab} - i\Omega_1 \cos\omega t \left(\sigma_{bb} - \sigma_{aa}\right), \tag{3.89c}$$

$$\frac{d}{dt}\sigma_{ba} = -i\omega_0\sigma_{ba} + i\Omega_1 \cos\omega t \left(\sigma_{bb} - \sigma_{aa}\right). \tag{3.89d}$$

In the above equations, we observe that $\dfrac{d}{dt}(\sigma_{aa} + \sigma_{bb}) = 0$, while equations (3.89c) and (3.89c) are complex conjugates of one another. The former condition implies the conservation of population, while the latter results from the hermiticity of the density matrix.

We may simplify equations (3.89) by making the quasi-resonant approximation, in which case only one of the complex exponential components of $\cos\omega t$ makes an appreciable contribution to the time evolution. To determine which components are negligible, we observe that as Ω_1 tends to zero, σ_{ab} varies as $\exp(i\omega_0 t)$ according to equation (3.89c). Inserting this result into equation (3.89a), for example, we may distinguish the slow from the fast oscillating terms. We drop the fast oscillating terms, which yield huge denominators upon integration and are therefore negligible compared to the slow oscillating terms. With this simplification, the above equations then become:

$$\frac{d}{dt}\sigma_{aa} = -\frac{i\Omega_1}{2}\left(e^{i\omega t}\sigma_{ba} - e^{-i\omega t}\sigma_{ab}\right), \tag{3.90a}$$

$$\frac{d}{dt}\sigma_{bb} = \frac{i\Omega_1}{2}\left(e^{i\omega t}\sigma_{ba} - e^{-i\omega t}\sigma_{ab}\right), \tag{3.90b}$$

$$\frac{d}{dt}\sigma_{ab} = i\omega_0\sigma_{ab} - \frac{i\Omega_1}{2}e^{i\omega t}\left(\sigma_{bb} - \sigma_{aa}\right), \tag{3.90c}$$

$$\frac{d}{dt}\sigma_{ba} = -i\omega_0\sigma_{ba} + \frac{i\Omega_1}{2}e^{-i\omega t}\left(\sigma_{bb} - \sigma_{aa}\right). \tag{3.90d}$$

We now add the relaxation terms from equations (3.81) and (3.82) to (3.90), which yields the following set of equations, generally known as the *optical Bloch equations*:

$$\frac{d}{dt}\sigma_{aa} = -\frac{i\Omega_1}{2}\left(e^{i\omega t}\sigma_{ba} - e^{-i\omega t}\sigma_{ab}\right) + \Gamma_{sp}\sigma_{bb}, \tag{3.91a}$$

$$\frac{d}{dt}\sigma_{bb} = \frac{i\Omega_1}{2}\left(e^{i\omega t}\sigma_{ba} - e^{-i\omega t}\sigma_{ab}\right) - \Gamma_{sp}\sigma_{bb}, \tag{3.91b}$$

$$\frac{d}{dt}\sigma_{ab} = i\omega_0\sigma_{ab} - \frac{i\Omega_1}{2}e^{i\omega t}\left(\sigma_{bb} - \sigma_{aa}\right) - \gamma\sigma_{ab}, \tag{3.91c}$$

$$\frac{d}{dt}\sigma_{ba} = -i\omega_0\sigma_{ba} + \frac{i\Omega_1}{2}e^{-i\omega t}\left(\sigma_{bb} - \sigma_{aa}\right) - \gamma\sigma_{ba}. \tag{3.91d}$$

To facilitate solving these equations, we make the following change of variables to eliminate the complex exponential terms:

$$\tilde{\sigma}_{ab} = e^{-i\omega t}\sigma_{ab}, \tag{3.92a}$$

$$\tilde{\sigma}_{ba} = e^{i\omega t}\sigma_{ba}, \tag{3.92b}$$

$$\tilde{\sigma}_{aa} = \sigma_{aa}, \tag{3.92c}$$

$$\tilde{\sigma}_{bb} = \sigma_{bb}. \tag{3.92d}$$

Then, equations (3.91) may be re-written in the following simplified form:

$$\frac{d}{dt}\tilde{\sigma}_{aa} = -\frac{i\Omega_1}{2}\left(\tilde{\sigma}_{ba} - \tilde{\sigma}_{ab}\right) + \Gamma_{sp}\tilde{\sigma}_{bb}, \tag{3.93a}$$

$$\frac{d}{dt}\tilde{\sigma}_{bb} = \frac{i\Omega_1}{2}\left(\tilde{\sigma}_{ba} - \tilde{\sigma}_{ab}\right) - \Gamma_{sp}\tilde{\sigma}_{bb}, \tag{3.93b}$$

$$\frac{d}{dt}\tilde{\sigma}_{ab} = i(\omega_0 - \omega)\tilde{\sigma}_{ab} - \frac{i\Omega_1}{2}\left(\tilde{\sigma}_{bb} - \tilde{\sigma}_{aa}\right) - \gamma\tilde{\sigma}_{ab}, \tag{3.93c}$$

$$\frac{d}{dt}\tilde{\sigma}_{ba} = -i(\omega_0 - \omega)\tilde{\sigma}_{ba} + \frac{i\Omega_1}{2}\left(\tilde{\sigma}_{bb} - \tilde{\sigma}_{aa}\right) - \gamma\tilde{\sigma}_{ba}. \tag{3.93d}$$

Solving the above set of equations with appropriate initial conditions determines the time evolution of the density matrix for all future times. It is important to point out, however, that these equations are based on average environmental perturbations and, as such, the solutions to (3.93) represent the statistical average behavior of an ensemble of such systems. While a general solution in analytical form exists for the optical Bloch equations of (3.93), it is quite lengthy and we do not attempt to present it here. Instead, we shall analyze the equations for special conditions of interest.

First, consider the case in which the upper level is initially populated and there is no laser driving. Intuitively, we expect that the upper level should decay to the lower level via spontaneous emission after a time on the order of the radiative lifetime T_1. Turning to equations (3.93), we set $\Omega_1 = 0$ since the laser is turned off, which decouples the population equations from the coherences to yield:

$$\frac{d}{dt}\sigma_{aa} = \Gamma_{sp}\sigma_{bb}, \tag{3.94a}$$

$$\frac{d}{dt}\sigma_{bb} = -\Gamma_{sp}\sigma_{bb}. \tag{3.94b}$$

These equations are easily solved for the initial condition $\tilde{\sigma}_{bb} = 1$, $\tilde{\sigma}_{aa} = 0$, which describes a system starting out in the upper level at time $t = 0$. The solution is:

$$\sigma_{aa}(t) = e^{-\Gamma_{sp}\,t} = e^{-t/T_1}, \tag{3.95a}$$

$$\sigma_{bb}(t) = 1 - e^{-\Gamma_{sp}\,t} = 1 - e^{-t/T_1}. \tag{3.95b}$$

The above equations reveal that the probability of remaining in the upper level decreases to $1/e \cong 0.37$ after a duration of time T_1. Thus, our expectation that spontaneous emission will lead to relaxation from the excited state on the order of the radiative lifetime is confirmed.

Next, we consider the case of Rabi oscillations. We assume that the relaxation terms Γ_{sp} and γ are equal to zero and the laser is resonantly tuned. Under these conditions, we anticipate a resonant Rabi oscillation identical to that seen in Figure 3.13 from the section on undamped laser driving. For simplicity, we define the population difference η as:

$$\eta = \sigma_{bb} - \sigma_{aa}. \tag{3.96}$$

With this definition and the conditions given above, the optical Bloch equations of (3.93) become:

$$\frac{d}{dt}\eta = i\Omega_1\left(\tilde{\sigma}_{ba} - \tilde{\sigma}_{ab}\right), \tag{3.97a}$$

$$\frac{d}{dt}\tilde{\sigma}_{ab} = -\frac{i\Omega_1}{2}\eta, \tag{3.97b}$$

$$\frac{d}{dt}\tilde{\sigma}_{ba} = \frac{i\Omega_1}{2}\eta. \tag{3.97c}$$

Assuming the system starts in the lower level at time $t = 0$, the initial condition is the following: $\eta = -1$, $\tilde{\sigma}_{ab} = \tilde{\sigma}_{ba} = 0$. The system in (3.97) may then be solved by the eigenvalue method to yield the following solution:

$$\eta(t) = -\cos(\Omega_1 t), \tag{3.98a}$$

$$\tilde{\sigma}_{ab} = \frac{i}{2}\sin(\Omega_1 t), \tag{3.98b}$$

$$\tilde{\sigma}_{ba} = -\frac{i}{2}\sin(\Omega_1 t). \tag{3.98c}$$

We then solve for the transition probability to the upper level by using the conservation of population condition (3.76) along with equation (3.98a) to yield:

$$\sigma_{bb}(t) = \sin^2\left(\frac{\Omega_1 t}{2}\right). \tag{3.99}$$

This result is identical to the undamped transition probability given in equation (3.72b) under the condition of resonant driving, confirming that the optical Bloch equations yield undamped Rabi oscillations in the absence of relaxation terms.

We now consider the effect of damping on the Rabi oscillations. For resonant driving with relaxation terms, the optical Bloch equations are:

$$\frac{d}{dt}\tilde{\sigma}_{aa} = -\frac{i\Omega_1}{2}\left(\tilde{\sigma}_{ba} - \tilde{\sigma}_{ab}\right) + \Gamma_{sp}\tilde{\sigma}_{bb}, \tag{3.100a}$$

$$\frac{d}{dt}\tilde{\sigma}_{bb} = \frac{i\Omega_1}{2}\left(\tilde{\sigma}_{ba} - \tilde{\sigma}_{ab}\right) - \Gamma_{sp}\tilde{\sigma}_{bb}, \tag{3.100b}$$

$$\frac{d}{dt}\tilde{\sigma}_{ab} = -\frac{i\Omega_1}{2}\left(\tilde{\sigma}_{bb} - \tilde{\sigma}_{aa}\right) - \gamma\tilde{\sigma}_{ab}, \tag{3.100c}$$

$$\frac{d}{dt}\tilde{\sigma}_{ba} = \frac{i\Omega_1}{2}\left(\tilde{\sigma}_{bb} - \tilde{\sigma}_{aa}\right) - \gamma\tilde{\sigma}_{ba}. \tag{3.100d}$$

These equations may be solved to yield the following formula for the transition probability to the upper level:

$$\sigma_{bb}(t) = \frac{\Omega_1 e^{-t(\gamma+\Gamma_{sp}+\alpha)/2}}{4\alpha(\gamma\,\Gamma_{sp} + \Omega_1^2)}\times \left[\gamma\Big(1 - e^{\alpha t}\Big) + \Gamma_{sp}\Big(1 - e^{\alpha t}\Big) - \alpha\Big(1 + e^{\alpha t} - 2e^{t(\gamma+\Gamma_{sp}+\alpha)/2}\Big)\right], \tag{3.101}$$

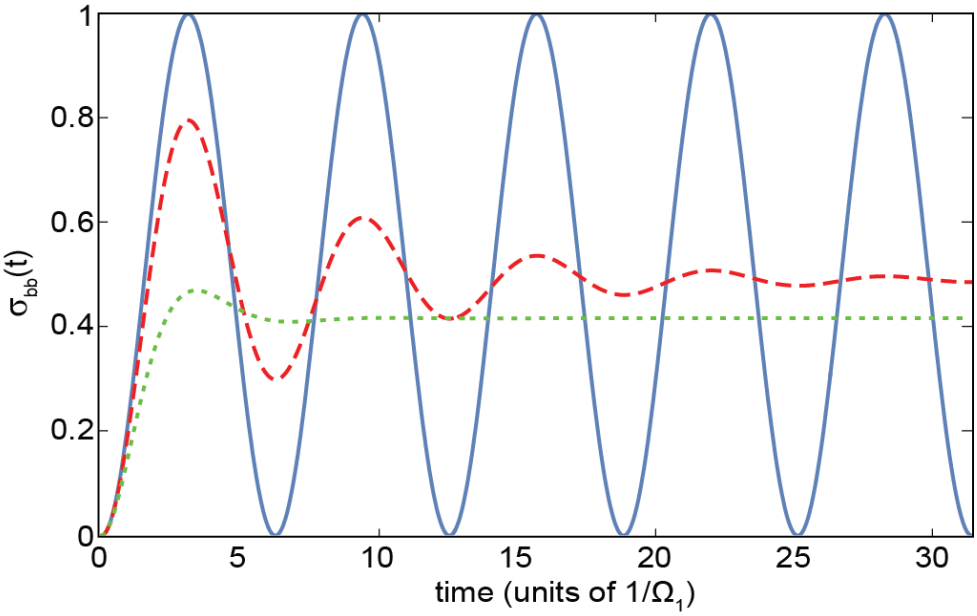

Figure 3.14: Plots of the transition probability $\sigma_{bb}(t)$ from equation (3.101) for different values of the relaxation parameters at a fixed Rabi frequency Ω_1. The relaxation terms for the various plots are: (i) Solid blue line: $\Gamma_{sp} = \gamma = 0$, (ii) Dashed red line: $\Gamma_{sp} = 0.2\,\Omega_1$, $\gamma = \Gamma_{sp}/2$, (iii) Green dotted line $\Gamma_{sp} = 0.2\,\Omega_1$, $\gamma = 5\,\Gamma_{sp}$.

where for simplicity we have defined α as:

$$\alpha = \sqrt{(\gamma - \Gamma_{sp})^2 - 4\Omega_1^2}. \tag{3.102}$$

It is evident from equation (3.101) that the relaxation rates γ and Γ_{sp} lead to exponential damping of the transition probability.

In Figure 3.14, we plot equation (3.101) for various values of the relaxation parameters Γ_{sp} and γ at a fixed Rabi frequency Ω_1. The solid blue curve shows the undamped case of perpetual Rabi oscillations with complete population transfer, similar to Fig. 3.13 from the previous section. The dashed red and dotted green lines show the effects of finite damping on the transition probability. Rabi oscillations may still be present (e.g., the dashed red curve), but they are exponentially damped and the transition probability never reaches unity. Moreover, the populations in the lower and upper levels approach a steady state value as the laser driving and relaxation terms come to equilibrium. The dashed red curve shows the case in which the dephasing is due solely to spontaneous emission (i.e., $\gamma = \Gamma_{sp}/2$). In the plot, we observe several Rabi oscillations before the steady state population levels off at a value slightly less than 1/2. The dotted green curve has the same spontaneous emission rate as the dashed

red curve, but includes an additional damping contribution from pure dephasing γ_{pd}. In this case, rapid decoherence from the additional dephasing completely obscures any Rabi oscillations and causes the system to quickly reach its steady state population. In general, the appearance of Rabi oscillations requires that the Rabi frequency Ω_1 be at least several times greater than the dephasing rate γ, which requires a large laser intensity and minimal environmental perturbations.

Finally, we analyze the steady state population of the laser driven two-level system with damping. To determine the steady state solution, we set the time derivatives in equations (3.100) to zero and then solve for the populations and the coherences. Doing this, we find for the steady state populations:

$$\sigma_{bb} = \frac{1}{2}\left[\frac{\Omega_1^2\left(\gamma/\Gamma_{sp}\right)}{\delta^2+\gamma^2+\Omega_1^2\left(\gamma/\Gamma_{sp}\right)}\right], \tag{3.103a}$$

$$\sigma_{aa} = 1-\sigma_{bb}, \tag{3.103b}$$

where we recall that $\delta = \omega - \omega_0$ is the laser detuning.

The absorption of the two-level system is proportional to the steady state population in the upper level given by equation (3.103a). Inspection of this equation reveals that the absorption has a Lorentzian-like line shape, where the amplitude and width depend on the parameters Ω_1, Γ_{sp} and γ. Moreover, we observe that the excited state population σ_{bb} is a function of the laser intensity through its dependence on Ω_1^2. At low intensity levels, the excited state population (and hence the absorption) depends linearly on the laser intensity. At higher intensities, however, equation (3.103a) reveals that the excited state population approaches a limiting value equal to 1/2. In this case, the system is said to reach *saturation*, meaning that additional absorption is not possible by simply increasing the laser power. Inspection of equation (3.103a) reveals that saturation first occurs for resonant excitation, and then continues to spread to both sides of the resonance as the laser intensity is further increased.

These trends are nicely illustrated in Figure 3.15, which plots equation (3.103a) for various values of the Rabi frequency at a fixed total relaxation rate. The solid blue curve shows the linear absorption regime, characterized by a Lorentzian line shape and a small excited state population. The dashed green and dotted red curves show the onset of saturation with increasing laser intensity. Fig. 3.15 also reveals that the absorption line width increases with the laser intensity, an effect known as *power broadening*. Thus, a realistic laser driven two-level system in the steady state transitions from a linear regime of Lorentzian absorption at low power to a high power regime characterized by saturation and power broadening of the absorption line.

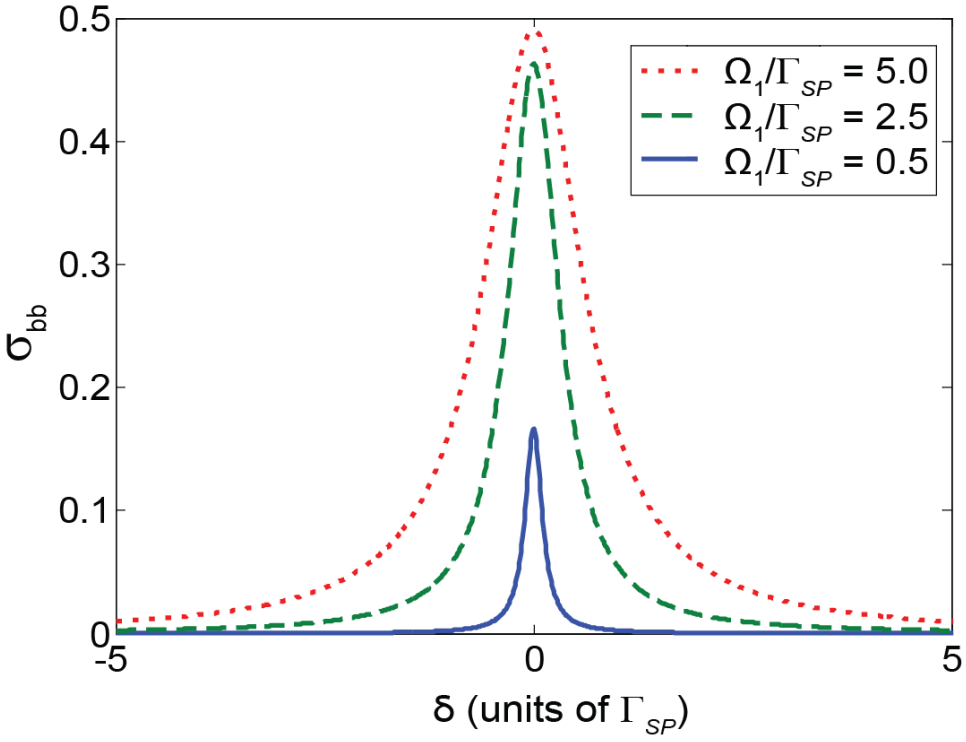

Figure 3.15: Plots of the excited state population σ_{bb} versus the laser detuning δ under steady state conditions according to equation (3.103a). The curves are for different values of the Rabi frequency Ω_1 in proportion to the fixed spontaneous emission rate Γ_{sp}. The dephasing rate is $\gamma = \Gamma_{sp}/2$ (i.e., due purely to spontaneous emission).

3.5 Fano Interference

The Fano effect, also known as Fano interference or Fano resonance, is a quantum mechanical interference effect that arises in various systems that involve a discrete excited state interacting with a continuum of energy states. Its defining feature is a characteristic asymmetry that appears in the transition line shape of the system as a function of the transition energy [54].[16] In Chapter 7 of this dissertation, we present a novel Fano interference effect in the absorption line shape of QDMs that results from a coherent interaction between individual electronic states, single phonons (i.e., quanta of lattice vibrations) and single photons (i.e., quanta of light). In this section, we provide a quantitative analysis of the Fano resonance following the method of Ugo Fano, the first person to describe the effect [56]. The main result of this analysis is the derivation of a formula for the transition probabilities that introduces the q_{Fano} factor,

[16] Similar interference effects arise in the context of classical physics, an example being a system of two coupled oscillators with external driving [55].

a quantity which governs the characteristic asymmetry of the Fano resonance. We also find an intuitively simple interpretation of the Fano effect in terms of a quantum mechanical interference between separate pathways in the excitation process.

To begin, we describe the fundamental conditions necessary to realize a Fano interference. Three sorts of states are involved: a discrete ground state $|\phi_0\rangle$, a discrete excited state $|\phi_1\rangle$ and an ensemble of extended states $|\psi_{\varepsilon'}\rangle$ forming a continuum of energy levels. We may think of this as a two-level system with an additional continuum of energy states overlapping the discrete excited state. Transitions from the ground state to the discrete excited state (i.e., $|\phi_0\rangle \rightarrow |\phi_1\rangle$) and to the continuum states (i.e., $|\phi_0\rangle \rightarrow |\psi_{\varepsilon'}\rangle$) are possible via an external excitation. In addition, there must also exist an intrinsic interaction within the system that couples the discrete excited state to the continuum of states (i.e., $|\phi_1\rangle \leftrightarrow |\psi_{\varepsilon'}\rangle$). Examples of such intrinsic interactions may include Auger auto-ionization or tunneling between the discrete and continuum states [57]. The intrinsic interaction couples the otherwise separate discrete and continuous component systems, leading to a new set of stationary states formed as a superposition of the states of the component systems. To determine the excitation profile of the Fano resonance, we must then calculate the transition probabilities for excitation from the discrete ground state to the hybridized stationary states. In the case of optical excitation, this yields the absorption profile of the system.

We now proceed to solve the Fano problem analytically. We consider a quantum system composed of a two-state system and a continuum of states. In the absence of coupling between these two component systems, the two-level system has stationary eigenstates $|\phi_0\rangle$ and $|\phi_1\rangle$ with energies $\varepsilon_0 = 0$ (i.e., the ground state reference energy) and $\varepsilon_1 > 0$, while the continuum stationary states $|\psi_{\varepsilon'}\rangle$ have a continuous range of eigenenergies specified by the real number ε' and overlapping with ε_1. The stationary states of the non-interacting systems are considered to be non-degenerate and orthogonal due to prior specification of a complete set of commuting observables. Accordingly, we may write the system Hamiltonian as a sum of two terms:

$$\hat{H} = \hat{H}_0 + \hat{V}_{\varepsilon'}. \tag{3.104}$$

In the above equation, $\hat{H}_0$ consists of two block diagonal sub-matrices that specify the energies of the uncoupled discrete and continuum component systems, while the operator $\hat{V}_{\varepsilon'}$ describes the internal interaction that couples the discrete and continuum component systems. We consider $\hat{V}_{\varepsilon'}$ as a perturbation to $\hat{H}_0$ and point out that it is time-independent, but may be a function of the energy ε' (as the notation suggests).

While the system Hamiltonian is uncountably infinite because of the continuum states, its individual matrix elements are entirely specified in the eigenbasis of the component systems by the following equations:

$$\langle \psi_{\varepsilon''} | \hat{H} | \psi_{\varepsilon'} \rangle = \varepsilon' \, \delta(\varepsilon'' - \varepsilon'), \tag{3.105a}$$

$$\langle \phi_1 | \hat{H} | \phi_1 \rangle = \varepsilon_1, \tag{3.105b}$$

$$\langle \psi_{\varepsilon'} | \hat{H} | \phi_1 \rangle = V_{\varepsilon'}, \tag{3.105c}$$

$$\langle \psi_{\varepsilon'} | \hat{H} | \phi_0 \rangle = 0, \tag{3.105d}$$

$$\langle \phi_1 | \hat{H} | \phi_0 \rangle = 0, \tag{3.105e}$$

$$\langle \phi_0 | \hat{H} | \phi_0 \rangle = 0. \tag{3.105f}$$

The above set of equations reveals that, in the absence of the external excitation mechanism, the ground state is decoupled from both the excited and continuum states. Consequently, it can be ignored as we seek to diagonalize the elements of the remaining sub-matrix. This diagonalization process will determine a new set of stationary states $|\Psi_\varepsilon\rangle$ for each energy ε within the range of ε'. These eigenstates of $\hat{H}$ may be written as a weighted superposition of the discrete excited state with the continuum states as follows:

$$|\Psi_\varepsilon\rangle = \alpha |\phi_1\rangle + \int d\varepsilon' \beta_{\varepsilon'} |\psi_{\varepsilon'}\rangle, \tag{3.106}$$

where the expansion coefficients $\alpha(\varepsilon) = \langle \phi_1 | \Psi_\varepsilon \rangle$ and $\beta_{\varepsilon'}(\varepsilon) = \langle \psi_{\varepsilon'} | \Psi_\varepsilon \rangle$ are functions of the energy ε, though we only indicate this explicitly when necessary.

Our first objective is to solve for the expansion coefficients α and $\beta_{\varepsilon'}$ of the hybridized stationary states. Once these coefficients are known, we can then calculate the transition probabilities from the ground state $|\phi_0\rangle$ to the hybridized states $|\Psi_\varepsilon\rangle$ of (3.106), thereby determining the absorption profile of the system in the case of optical excitation.

By forming the products $\langle \phi_1 | \hat{H} | \Psi_\varepsilon \rangle$ and $\langle \psi_{\varepsilon'} | \hat{H} | \Psi_\varepsilon \rangle$ and using equations (3.105) and (3.106), we arrive at the following equations for the expansion coefficients:

$$\alpha \, \varepsilon_1 + \int d\varepsilon' \, {V_{\varepsilon'}}^* \beta_{\varepsilon'} = \alpha \, \varepsilon, \tag{3.107a}$$

$$\alpha \, V_{\varepsilon'} + \beta_{\varepsilon'} \, \varepsilon' = \varepsilon \, \beta_{\varepsilon'}. \tag{3.107b}$$

These equations may be solved exactly, but require a careful analysis to handle certain singularities that arise on account of the continuous energy spectrum.

We shall first rearrange equation (3.107b) to express $\beta_{\varepsilon'}$ in terms of α in order that we may insert the result into (3.107a). Partially completing this procedure yields from (3.107b):

$$\frac{\beta_{\varepsilon'}(\varepsilon - \varepsilon')}{\alpha\, V_{\varepsilon'}} = 1. \tag{3.108}$$

We need to be careful in dividing both sides by the quantity $(\varepsilon - \varepsilon')$, which is singular for $\varepsilon = \varepsilon'$. To maintain equality upon division, we must add to one side of (3.108) a multiple of the Dirac delta function $\delta\,(\varepsilon - \varepsilon')$ [58]. Doing this yields the following equation for $\beta_{\varepsilon'}$:

$$\beta_{\varepsilon'} = \left[\frac{1}{(\varepsilon - \varepsilon')} + z(\varepsilon)\delta\,(\varepsilon - \varepsilon')\right] \alpha\, V_{\varepsilon'}, \tag{3.109}$$

where the function $z(\varepsilon)$ is the multiple of the delta function. To solve for $z(\varepsilon)$, we may substitute (3.109) into (3.107a), where we should take the principal value of the integral involving the singular term $1/(\varepsilon - \varepsilon')$ [56]. Making this substitution and canceling the common factor α yields the following equation:

$$\varepsilon_1 + f(\varepsilon) + z(\varepsilon)|V_\varepsilon|^2 = \varepsilon, \tag{3.110}$$

where $|V_\varepsilon|^2$ has units of energy and $f(\varepsilon)$ is the principal value integral:

$$f(\varepsilon) = P \int d\varepsilon' \frac{|V_{\varepsilon'}|^2}{\varepsilon - \varepsilon'}. \tag{3.111}$$

We then have for $z(\varepsilon)$:

$$z(\varepsilon) = \frac{\varepsilon - [\varepsilon_1 + f(\varepsilon)]}{|V_\varepsilon|^2}. \tag{3.112}$$

In the above equation, the numerator represents the energy difference between the hybridized state energy ε and the energy of the discrete state resonance ε_1, shifted by an amount $f(\varepsilon)$. The energy shift $f(\varepsilon)$ is typically small and is identically zero if V_ε is independent of ε, as indicated by equation (3.111). As the hybridized state energy passes through the discrete excited state resonance, $z(\varepsilon)$ abruptly changes sign. We will see that this behavior of equation (3.112) plays an important role in governing the characteristic asymmetry of the Fano resonance.

To fully specify our solution of the hybridized stationary states Ψ_ε in equation (3.106), we must now solve for the expansion coefficient α. This may be achieved by carrying out the ortho-normalization procedure for Ψ_ε. Using an arbitrary pair of eigenstates with the energies ε and $\tilde{\varepsilon}$, we may write:

$$\langle \Psi_{\tilde{\varepsilon}} | \Psi_\varepsilon \rangle = \alpha^*(\tilde{\varepsilon})\alpha(\varepsilon) + \int d\varepsilon' \beta^*_{\varepsilon'}(\tilde{\varepsilon})\beta_{\varepsilon'}(\varepsilon) = \delta\,(\tilde{\varepsilon} - \varepsilon), \tag{3.113}$$

where upon inserting (3.109) into the above equation yields:

$$\alpha^*(\tilde{\varepsilon})\,\alpha(\varepsilon)\Bigg\{1+\int d\varepsilon'\,V_{\varepsilon'}^*\,V_{\varepsilon'}\left[\frac{1}{\tilde{\varepsilon}-\varepsilon'}+z(\tilde{\varepsilon})\,\delta\left(\tilde{\varepsilon}-\varepsilon'\right)\right]\times \left[\frac{1}{\varepsilon-\varepsilon'}+z(\varepsilon)\,\delta\left(\varepsilon-\varepsilon'\right)\right]\Bigg\}=\delta\left(\tilde{\varepsilon}-\varepsilon\right). \tag{3.114}$$

Special care must be taken to correctly evaluate the integral at the point of double singularity where $\tilde{\varepsilon}=\varepsilon$. Following reference [56], the factor $1/(\tilde{\varepsilon}-\varepsilon')(\varepsilon-\varepsilon')$ may be resolved into partial fractions according to:

$$\frac{1}{(\tilde{\varepsilon}-\varepsilon')(\varepsilon-\varepsilon')}=\frac{1}{\tilde{\varepsilon}-\varepsilon}\left(\frac{1}{\varepsilon-\varepsilon'}-\frac{1}{\tilde{\varepsilon}-\varepsilon'}\right)+\pi^2\delta\left(\tilde{\varepsilon}-\varepsilon'\right)\delta\left(\varepsilon-\varepsilon'\right). \tag{3.115}$$

Then, substituting (3.115) into (3.114) and making use of the relation $\delta\left(\varepsilon-\varepsilon'\right)g(\varepsilon')=\delta\left(\varepsilon-\varepsilon'\right)g(\varepsilon)$ for an arbitrary function g, (3.114) reduces to:

$$|\alpha(\varepsilon)|^2\,|V_\varepsilon|^2\left[\pi^2+z^2(\varepsilon)\right]\delta\left(\tilde{\varepsilon}-\varepsilon\right)+\alpha^*(\tilde{\varepsilon})\,\alpha(\varepsilon)\times \left\{1+\frac{1}{\tilde{\varepsilon}-\varepsilon}\Big(f(\varepsilon)-f(\tilde{\varepsilon})+z(\varepsilon)|V_\varepsilon|^2-z(\tilde{\varepsilon})|V_{\tilde{\varepsilon}}|^2\Big)\right\}=\delta\left(\tilde{\varepsilon}-\varepsilon\right). \tag{3.116}$$

The expression in curly brackets is identically zero on account of equation (3.110), which implies that equation (3.116) is satisfied for:

$$|\alpha(\varepsilon)|^2=\frac{1}{|V_\varepsilon|^2\left[\pi^2+z^2(\varepsilon)\right]}=\frac{|V_\varepsilon|^2}{(\varepsilon-[\varepsilon_1+f(\varepsilon)])+\pi^2|V_\varepsilon|^4}. \tag{3.117}$$

The above equation, in conjunction with (3.109), yields the solution for the expansion coefficients of the hybridized stationary states $|\Psi_\varepsilon\rangle$.

We pause briefly to comment on the importance of equation (3.117), which gives the contribution of the discrete excited state to the hybridized stationary states $|\Psi_\varepsilon\rangle$. It is a Lorentzian function of the energy, centered at the discrete resonance value $\varepsilon_1+f(\varepsilon)$, with a full-width at half-maximum equal to $2\pi|V_\varepsilon|^2$. Conversely, we may consider the discrete excited state to be broadened by an amount $2\pi|V_\varepsilon|^2$ from its coupling to the continuum that renders it unstable. According to the time-energy uncertainty principle, if the system were prepared in the discrete state $|\phi_1\rangle$, it would undergo irreversible relaxation to a stationary state $|\Psi_\varepsilon\rangle$ after a mean time on the order of $\hbar/\pi|V_\varepsilon|^2$. This time scale, which is governed by the strength of the intrinsic coupling interaction $|V_\varepsilon|^2$, has practical significance for the experimental observation

of the Fano effect since it competes with other irreversible decay processes, most notably spontaneous emission. In particular, we may conclude that the observation of Fano interference is not precluded by spontaneous emission or other dephasing mechanisms, granted that these mechanisms operate on a time scale that is long compared to $\hbar/\pi|V_\varepsilon|^2$.

We now complete our solution of the expansion coefficients α and $\beta_{\varepsilon'}$ for the hybridized stationary states $|\Psi_\varepsilon\rangle$. Based on equation (3.112), we define the quantity Δ according to:

$$\tan\Delta = -\frac{\pi}{z(\varepsilon)} = -\frac{\pi\,|V_\varepsilon|^2}{\varepsilon - [\varepsilon_1 + f(\varepsilon)]}. \tag{3.118}$$

The above expression allows us to write α, to within a phase factor, in the simplified form:

$$\alpha = \frac{\sin\Delta}{\pi V_\varepsilon} = \frac{1}{\pi V_\varepsilon}\left[\frac{-\pi|V_\varepsilon|^2}{\sqrt{(\varepsilon - [\varepsilon_1 + f(\varepsilon)])^2 + \pi^2|V_\varepsilon|^4}}\right]. \tag{3.119}$$

Substituting this result into (3.109) yields for $\beta_{\varepsilon'}$, to within the *same phase factor* as α:

$$\beta_{\varepsilon'} = \frac{V_{\varepsilon'}}{V_\varepsilon}\left[\frac{\sin\Delta}{\pi(\varepsilon - \varepsilon')} - \cos\Delta\,\delta\,(\varepsilon - \varepsilon')\right], \tag{3.120}$$

where:

$$\cos\Delta = \frac{\varepsilon - [\varepsilon_1 + f(\varepsilon)]}{\sqrt{(\varepsilon - [\varepsilon_1 + f(\varepsilon)])^2 + \pi^2|V_\varepsilon|^4}}. \tag{3.121}$$

Finally, inserting equations (3.119) and (3.120) into (3.106) yields the following solution for $|\Psi_\varepsilon\rangle$ in the basis of the unperturbed component states, to within an arbitrary global phase constant:

$$\begin{aligned}
|\Psi_\varepsilon\rangle &= \left(\frac{\sin\Delta}{\pi\,V_\varepsilon}\right)|\phi_1\rangle + \int d\varepsilon'\left(\frac{V_{\varepsilon'}}{V_\varepsilon}\left[\frac{\sin\Delta}{\pi(\varepsilon - \varepsilon')} - \cos\Delta\,\delta\,(\varepsilon - \varepsilon')\right]\right)|\psi_{\varepsilon'}\rangle \\
&= \frac{\sin\Delta}{\pi\,V_\varepsilon}\left[|\phi_1\rangle + P\int d\varepsilon'\frac{V_{\varepsilon'}}{\varepsilon - \varepsilon'}|\psi_{\varepsilon'}\rangle\right] - \cos\Delta\,|\psi_\varepsilon\rangle \\
&= \frac{\sin\Delta}{\pi\,V_\varepsilon}|\Phi_1\rangle - \cos\Delta\,|\psi_\varepsilon\rangle.
\end{aligned} \tag{3.122}$$

In the above equation, we have defined:

$$|\Phi_1\rangle = |\phi_1\rangle + P\int d\varepsilon'\frac{V_{\varepsilon'}}{\varepsilon - \varepsilon'}|\psi_{\varepsilon'}\rangle, \tag{3.123}$$

as the discrete excited state $|\phi_1\rangle$, modified by an admixture of states from the unperturbed continuum $|\psi_{\varepsilon'}\rangle$. In the case that $V_{\varepsilon'}$ and $|\psi_{\varepsilon'}\rangle$ are independent of ε', then $|\Phi_1\rangle$ reduces to $|\phi_1\rangle$.

We are now in a position to determine the transition probability function (and hence the absorption profile for optical excitation) from the discrete ground state $|\phi_0\rangle$ to the hybridized final states $|\Psi_\varepsilon\rangle$. The external excitation mechanism may be represented as a transition operator that we denote by $\hat{T}$. The transition probability is then equal to the modulus squared of the transition amplitude $\langle\Psi_\varepsilon|\hat{T}|\phi_0\rangle$, which according to (3.122) is:

$$\langle\Psi_\varepsilon|\hat{T}|\phi_0\rangle = \frac{\sin\Delta}{\pi\, V_\varepsilon^*}\langle\Phi_1|\hat{T}|\phi_0\rangle - \cos\Delta\,\langle\psi_\varepsilon|\hat{T}|\phi_0\rangle. \tag{3.124}$$

Inspection of (3.124) reveals that the transition amplitude $\langle\Psi_\varepsilon|\hat{T}|\phi_0\rangle$ is affected by an *interference* between the two amplitudes $\langle\Phi_1|\hat{T}|\phi_0\rangle$ and $\langle\psi_\varepsilon|\hat{T}|\phi_0\rangle$ that depends on the quantity Δ. In particular, equations (3.120) and (3.121) reveal that $\sin\Delta$ is an even function of $\varepsilon - [\varepsilon_1 - f(\varepsilon)]$, whereas $\cos\Delta$ is an odd function of this quantity. Consequently, these amplitudes interfere *with opposite phase* on either side of the discrete resonance $\varepsilon_1 - f(\varepsilon)$, leading to the characteristic asymmetry of the Fano resonance.

If we consider the rules for combining quantum amplitudes as set forth by Feynman, we may interpret equation (3.124) as an interference of amplitudes between two indistinguishable pathways both leading to the final excited state $|\Psi_\varepsilon\rangle$ [59]. From this point of view, the system may end up in $|\Psi_\varepsilon\rangle$ by transitioning through the modified discrete state $|\Phi_1\rangle$ or through the unperturbed continuum states $|\psi_\varepsilon\rangle$. As there is no way to distinguish these pathways, their separate amplitudes must be summed together to calculate the total transition amplitude. We illustrate this interpretation of the Fano effect in Figure 3.16.

In discussing the transition probability to the hybridized states $|\Psi_\varepsilon\rangle$, it is customary to compare it with the transition probability to the unperturbed continuum states in terms of the ratio $|\langle\Psi_\varepsilon|\hat{T}|\phi_0\rangle|^2/|\langle\psi_\varepsilon|\hat{T}|\phi_0\rangle|^2$, which we denote by $I(\varepsilon)$. This is reasonable since the transitions to the unperturbed continuum provide a slowly varying background upon which the rapidly varying function $|\langle\Psi_\varepsilon|\hat{T}|\phi_0\rangle|^2$ is superimposed.[17] To calculate this probability ratio, we first divide equation (3.124) by $\langle\psi_\varepsilon|\hat{T}|\phi_0\rangle$ to

[17]More precisely, $|\langle\Psi_\varepsilon|\hat{T}|\phi_0\rangle|^2$ is a rapidly varying function of the energy ε in the vicinity of the resonance $\varepsilon \approx \varepsilon_1 + f(\varepsilon)$, while $|\langle\psi_\varepsilon|\hat{T}|\phi_0\rangle|^2$ is a slowly varying function of the energy.

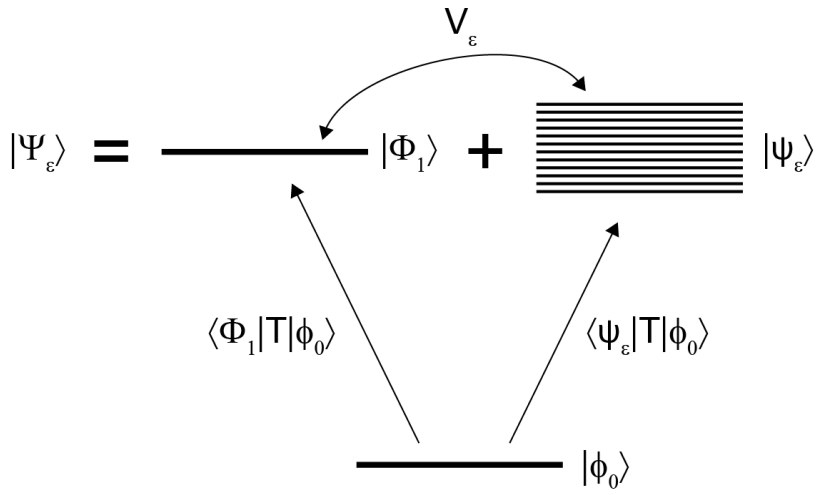

Figure 3.16: Diagram showing the transition amplitudes $\langle\Phi_1|\hat{T}|\phi_0\rangle$ and $\langle\psi_\varepsilon|\hat{T}|\phi_0\rangle$, which correspond to separate indistinguishable pathways that must be added together in order to calculate the total transition amplitude to the hybridized state $|\Psi_\varepsilon\rangle$. The amplitude V_ε represents the intrinsic interaction coupling the discrete excited state to the unperturbed continuum.

give:

$$\begin{aligned}\frac{\langle\Psi_\varepsilon|\hat{T}|\phi_0\rangle}{\langle\psi_\varepsilon|\hat{T}|\phi_0\rangle} &= \frac{1}{\pi\, V_\varepsilon^*}\frac{\langle\Phi_1|\hat{T}|\phi_0\rangle}{\langle\psi_\varepsilon|\hat{T}|\phi_0\rangle}\sin\Delta\ -\cos\Delta, \\ &= q\sin\Delta\ -\cos\Delta,\end{aligned} \tag{3.125}$$

where the quantity:

$$q = \frac{1}{\pi\, V_\varepsilon^*}\frac{\langle\Phi_1|\hat{T}|\phi_0\rangle}{\langle\psi_\varepsilon|\hat{T}|\phi_0\rangle}. \tag{3.126}$$

is known as the *Fano factor*. Next, we square (3.125), which after some algebra reduces to:

$$\frac{|\langle\Psi_\varepsilon|\hat{T}|\phi_0\rangle|^2}{|\langle\psi_\varepsilon|\hat{T}|\phi_0\rangle|^2} = \frac{(q-\cot\Delta)^2}{\csc^2\Delta}. \tag{3.127}$$

At this point, we define the reduced energy variable ξ as:

$$\xi = -\cot\Delta = \frac{\varepsilon - [\varepsilon_1 + f(\varepsilon)]}{\pi\,|V_\varepsilon|^2} = \frac{\varepsilon - [\varepsilon_1 + f(\varepsilon)]}{\Gamma/2}, \tag{3.128}$$

where:

$$\Gamma = 2\pi \left|V_\varepsilon\right|^2, \tag{3.129}$$

represents the broadening of the discrete state $|\phi_1\rangle$ due to coupling with the continuum.

Finally, inserting (3.128) into (3.127) yields for the ratio of transition probabilities:

$$I(\xi) \equiv \frac{|\langle\Psi_\varepsilon|\hat{T}|\phi_0\rangle|^2}{|\langle\psi_\varepsilon|\hat{T}|\phi_0\rangle|^2} = \frac{(q+\xi)^2}{1+\xi^2}. \tag{3.130}$$

Equation (3.130) is the most important result of this section, with the Fano factor q governing the asymmetry of the transition probability. If the transition operator $\hat{T}$ represents optical excitation, then $I(\xi)$ determines the absorption line shape of the system for a given value of q.

There are exactly one minimum and one maximum of the Fano resonance that may be determined from equation (3.130):

$$I_{min} = I(-q) = 0, \tag{3.131a}$$

$$I_{max} = I(1/q) = 1 + q^2. \tag{3.131b}$$

At the minimum, the amplitudes in equation (3.124) undergo perfectly destructive interference such that the transition probability vanishes. At the maximum, these amplitudes reach their greatest constructive interference for a given value of q. In reality, these extrema represent idealized limits that may not be fully reached in experimental systems. For example, the inclusion of additional interactions, such as couplings to other energy states or environmental perturbations, may cause deviations from this simplified model.

To get a sense of the Fano resonance, Figure 3.17 plots normalized values of $I(\varepsilon)$ for different values of the Fano factor q and the broadening parameter Γ, which we consider to be constants over the region of interest. Fig. 3.17a illustrates the various symmetries of the Fano resonance as a function of q. For large q, the transition to the continuum states is weak and the line shape displays the standard Lorentzian profile for a transition to an uncoupled discrete state (dashed red line in Fig. 3.17a). When q is on the order of unity, transitions to the discrete and unperturbed continuum states become comparable in strength. In this case, the two amplitudes interfere to produce a highly asymmetric line shape that dips and rises sharply on opposite sides of the discrete resonance (solid blue line in Fig. 3.17a). For very small values of q, the transition probability displays a pronounced dip or anti-resonance at $\xi = 0$ (dash-dotted green line in Fig. 3.17a). In the case of optical driving, this latter condition implies that there is no absorption at the resonance and the material becomes transparent.

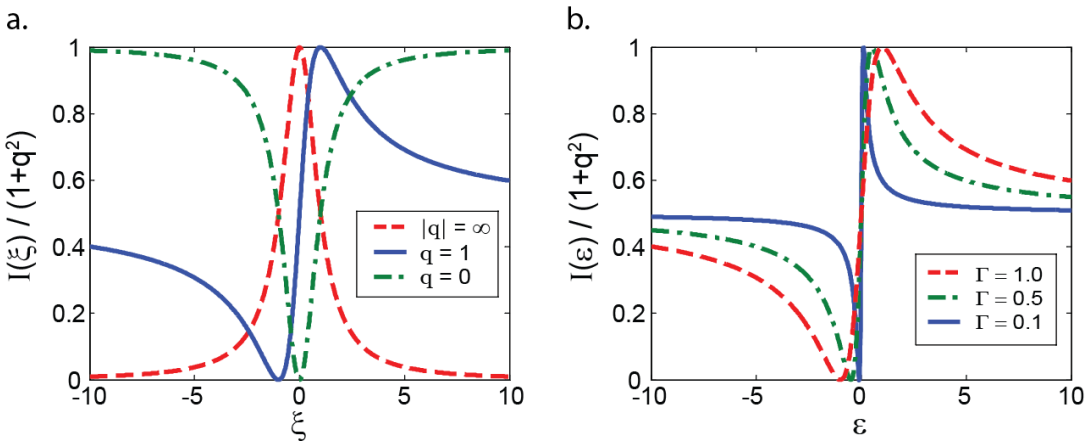

Figure 3.17: Normalized plots showing different line shapes of the Fano resonance. (a) The dependence of the Fano line shape $I(\xi)$ on the asymmetry parameter q. (b) Plot of the function $I(\varepsilon) = (q+2\varepsilon/\Gamma)^2/[1+(2\varepsilon/\Gamma)^2]$ for different values of Γ and fixed $q = 1$. In both graphs, equation (3.130) has been normalized to unity by dividing by $I_{max} = (1 + q^2)$. The plots have been made for $q > 0$; for $q < 0$, the symmetry is reflected about the line $\xi = 0$.

The effect of the broadening parameter $\Gamma = 2\pi|V_\varepsilon|^2$ on the Fano profile is shown in Fig 3.17b. For a fixed value of q, we observe that the energy width of the resonance grows broader as Γ increases in value, as we should expect. In general, the value of q may be either negative or positive. A change in the sign of q results in a reflection of $I(\xi)$ about the line $\xi = 0$.

3.6 Phonons and Polarons

So far, we have considered the electronic states of crystalline matter with the simplifying assumption that the underlying ionic lattice remains static. In this section, we relax that assumption so that the ionic cores are allowed to vibrate about their equilibrium positions in the crystal lattice. This leads to vibrational waves in the crystal, which may be quantized in the form of phonons. Moreover, phonons may couple with electronic states in matter to produce new hybridized quasi-particles called *polarons*. In QDM systems, acoustic and optical phonons often play an important role in the relaxation of excited electronic states, generating heat as a by product. Phonons also are a major source of decoherence of the atom-like quantum states in QDs and QDMs [60, 61]. In Chapter 7 of this dissertation, we demonstrate the less common case in which individual phonons are made to interact coherently with electronic states in a QDM, leading to a Fano interference and phonon-induced transparency. In this

section, we present an elementary theory of the vibrational states formed in solid state crystalline systems. We begin with a classical description of the normal modes of oscillation of a crystal lattice and then precede to a quantum description of lattice vibrations in terms of phonons and the hybridized polarons.

Normal Modes of a One-Dimensional Diatomic Crystal

A basic understanding of the important vibrational processes in diatomic crystalline matter, such as InAs or GaAs, may be obtained from a classical description of the normal modes of a simple one-dimensional diatomic crystal. Such a system is composed of a regular one-dimensional lattice with a basis consisting of two types of atomic species. The solution for the normal modes of the lattice vibrations reveal two distinct classes of waves that depend on the relative motion of the ion cores of the different atoms. Lower energy acoustic waves occur for in phase motion of the distinct ions cores, while higher energy optical waves occur when this motion is out of phase. Both longitudinal and transverse displacements are possible for the two classes of wave motion.

To begin our analysis, we consider a one-dimensional crystal in which adjacent lattice sites are separated by a lattice constant of length a. Then, the vector $\mathbf{R} = na$ describes the distinct lattice sites of the finite crystal for $n = 1, 2, \ldots, N$. At each lattice site, there is a basis consisting of two distinct species of ion core, which we distinguish by the labels A and B. The distinct ion cores have separate masses indicated by m_A and m_B. For simplicity, we assume an equidistant spacing between adjacent ion cores, which yields a linear array of alternating ion types that are separated by a distance of $a/2$ when the crystal is in equilibrium. We may then describe the displacement of the distinct ions from their equilibrium positions at the n^{th} lattice site by the coordinates $u_{A,n}$ and $u_{B,n}$, respectively. We note that the equilibrium positions of the two ionic species at the n^{th} lattice site are na for the A species and $na + a/2$ for the B species.

As the ions are displaced from their equilibrium positions, they exert forces on one another. If the displacements are small, we may assume that the force between ions is linearly proportional to the difference in their displacements from equilibrium. This assumption is known as the *harmonic approximation*, since it implies that the potential energy of the crystal is a quadratic function of the relative displacement of adjacent ions [42]. For brevity, we also assume that each ion interacts only with its two nearest neighbors. In this case, the harmonic approximation is equivalent to assuming that each ion is connected to its neighbors by a spring obeying Hooke's law. Figure 3.18 shows such a model of the one-dimensional diatomic crystal lattice. For simplicity, we have assumed that the ion displacements are directed along the crystal lattice axis, a situation that describes *longitudinal* vibrations. In general, the ions

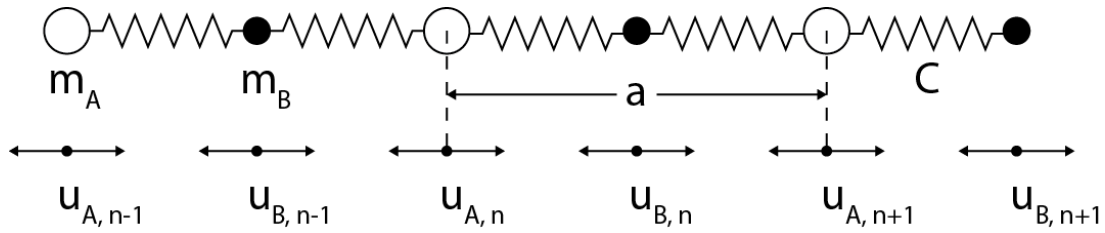

Figure 3.18: Diagram of a one-dimensional diatomic crystal structure with a basis of two distinct ions of masses m_A, m_B. The longitudinal displacements of the ions from their equilibrium positions are denoted by $u_{A,n-1}$, $u_{A,n}$, $u_{A,n+1}$, ... and $u_{B,n-1}$, $u_{B,n}$, $u_{B,n+1}$, ..., respectively. The ions are shown in their undisplaced positions and it is seen that the crystal structure repeats with a lattice constant of length a. The interaction between neighboring ions is equivalent to a Hooke's law interaction with a spring constant C.

may vibrate in any of the three spatial dimensions, thereby permitting two additional *transverse* modes of vibration.

Using Figure 3.18 as a guide, we may write the net force exerted on the two ionic species at the n^{th} lattice site as:

$$F_{A,\,n} = C(u_{B,\,n} + u_{B,\,n-1} - 2u_{A,\,n}), \tag{3.132a}$$

$$F_{B,\,n} = C(u_{A,\,n+1} + u_{A,\,n} - 2u_{B,\,n}), \tag{3.132b}$$

where $F_{A,\,n}$, $F_{B,\,n}$ are the net forces on ionic species A, B, respectively, due to nearest neighbor interactions and C is a constant governing the strength of the interaction (i.e., the spring constant).[18] The equations of motion for the two ionic species at the n^{th} lattice site are then given by:

$$m_A \frac{d^2}{dt^2} u_{A,\,n} = C(u_{B,\,n} + u_{B,\,n-1} - 2u_{A,\,n}), \tag{3.133a}$$

$$m_B \frac{d^2}{dt^2} u_{B,\,n} = C(u_{A,\,n+1} + u_{A,\,n} - 2u_{B,\,n}). \tag{3.133b}$$

We seek solutions to (3.133) in the form of traveling waves, in which all the ions oscillate with the same temporal frequency ω:

[18] If the equilibrium positions of the ions of the diatomic basis were not equidistantly spaced, then there would be separate force constants for the two nearest neighbor interactions. However, this would not fundamentally change the mathematical form of the resulting wave motion.

$$u_{A,\,n} = A_0 e^{i(kna-\omega t)}, \tag{3.134a}$$

$$u_{B,\,n} = B_0 e^{i(kna-\omega t)}. \tag{3.134b}$$

In the above equation, A_0, B_0 are complex constants that determine the amplitude and phase of the ions of species A and B, respectively, and k is a wave vector related to the spatial wavelength of the motion according to:

$$|k| = \frac{2\pi}{\lambda}. \tag{3.135}$$

The physical motion of the ions is then given by either the real or imaginary parts of equation (3.134).

The allowed values of k are restricted by the boundary conditions for a finite crystal. Since we are not typically concerned with edge effects for vibrations in bulk crystals, it is convenient to employ the Born-von Karman boundary conditions [42].[19] This is equivalent to requiring that the first and last ions of the one-dimensional lattice interact as if they were connected by a spring with spring constant C. This condition is enforced by the following requirements:

$$u_{B,\,0} = u_{B,\,N}, \tag{3.136a}$$

$$u_{A,\,N+1} = u_{A,\,1}. \tag{3.136b}$$

Here, we recall that $n = 1$ is the first site and $n = N$ is the last site of the crystal lattice. Inserting (3.136) into (3.134), we find that the following condition must hold:

$$e^{ikNa} = 1. \tag{3.137}$$

Equation (3.137), in turn, requires k to have the following form:

$$k = \frac{2\pi}{a}\frac{n}{N}, \qquad n \text{ an integer}. \tag{3.138}$$

Notice that if k is changed by an amount $2\pi/a$, the displacements given by equation (3.134) are unaffected. Thus, there are only N values of k consistent with (3.138) that yield distinct solutions. By convention, we take these to be the values of k within the range $-\pi/a \ \leq k \leq +\pi/a$, which is called the *first Brillouin zone* of the crystal lattice.

[19] Even for QDMs, such as those investigated in this dissertation, the optical phonons may be considered bulk-like to excellent approximation [5].

At this point, we substitute the wave solutions (3.134) into the equations of motion (3.133), which after some algebra yields the following coupled system of linear equations:

$$(2C - \omega^2 m_A)A_0 - C(1 + e^{-ika})B_0 = 0, \tag{3.139a}$$

$$-C(1 + e^{ika})A_0 + (2C - \omega^2 m_B)B_0 = 0. \tag{3.139b}$$

A solution to (3.139) exists as long as the determinant of the coefficients vanishes:

$$\begin{vmatrix} (2C - \omega^2 m_A) & C(1 + e^{-ika}) \\ -C(1 + e^{ika}) & (2C - \omega^2 m_B) \end{vmatrix} = 0, \tag{3.140}$$

or equivalently:

$$(m_A m_B)\omega^4 - 2C(m_A + m_B)\omega^2 + 2C^2[1 - \cos(ka)] = 0. \tag{3.141}$$

Equation (3.141) may be solved for ω^2 as a function of the wave vector k, yielding:

$$\omega^2 = \frac{C}{m_A m_B}\left[(m_A + m_B) \pm \sqrt{m_A^2 + m_B^2 + 2m_A m_B \cos(ka)}\right]. \tag{3.142}$$

The result in (3.142) describes the dispersion relation of the wave motion. We observe that for each of the N values of k, there are two solutions for ω with distinct positive frequencies. These two solutions are referred to as the *acoustic* and *optical branches* of the dispersion relation. For the longitudinal motion considered here, this yields a total of $2N$ normal modes of oscillation. Including the two transverse directions of motion, which each have acoustic and optical branches, there are a total of 6 branches in the dispersion relation: one longitudinal acoustic (LA), one longitudinal optical (LO), two transverse acoustic (TA) and two transverse optical (TO). Each of these branches has N normal modes of oscillation, yielding of total of $6N$ normal modes for the one-dimensional diatomic crystal lattice. In general, for a crystalline structure with a basis consisting of p atoms, there are $3p$ branches in the dispersion relation: 3 acoustic branches and $3p - 3$ optical branches [43]. The normal modes represent a complete solution to the vibrational motion of the crystal. Any general motion of the ions may be described by a superposition of the normal mode solutions, accompanied by appropriate initial conditions for the velocities and displacements of the ions.

In Figure 3.19, we plot the acoustic and optical branches of the dispersion relation for the case where $m_A > m_B$. The acoustic branch results from the negative sign

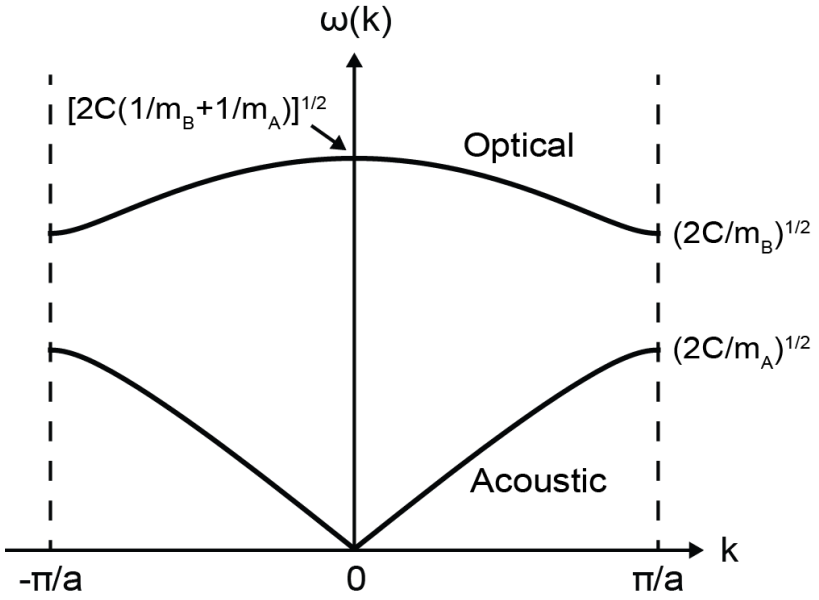

Figure 3.19: Plot of the dispersion relation of a one-dimensional diatomic crystal, showing the (longitudinal) acoustic and optical branches for the case where $m_A > m_B$.

in equation (3.142), while the optical branch results from the positive sign. It is insightful to calculate the limiting values of $\omega(k)$ for the two branches when $k << 1$ and $ka = \pm\pi$, at the edge of the first Brillouin zone. Using Taylor's theorem, we find that the acoustic branch is approximately linear in k for $ka << 1$ (i.e., the long wavelength limit):

$$\omega_{ac}(k) \cong \sqrt{\frac{C}{2(m_A + m_B)}} \cdot ka, \qquad ka << 1. \tag{3.143}$$

Sound waves also display a linear dispersion relation, hence the name *acoustic* given to this branch. The optical branch, on the other hand, achieves its maximum frequency at $k = 0$ and is stationary to first order for $ka << 1$:

$$\omega_{op}(k) \cong \sqrt{2C\left(\frac{1}{m_A} + \frac{1}{m_B}\right)}, \qquad ka << 1. \tag{3.144}$$

The constancy of equation (3.144) for small k reveals why the optical branch is sometimes called *dispersionless*. At the edge of the first Brillouin zone, where k reaches its maximum amplitude of π/a, the two roots of equation (3.142) are:

$$\omega_{op} = \sqrt{\frac{2C}{m_B}}, \tag{3.145a}$$

$$\omega_{ac} = \sqrt{\frac{2C}{m_A}}. \tag{3.145b}$$

We observe that there is a frequency gap at the boundary of the first Brillouin zone, dividing the acoustic and optical branches, for which no wave solutions exist for any value of k (see Fig. 3.19). Equation (3.145) reveals that this gap disappears if the ions are identical (i.e., $m_A = m_B$); this simply represents the case of a monatomic lattice, in which the optical branch ceases to exist altogether.

Finally, we point out important differences in the oscillatory motion of the acoustic and optical branches. For the optical branch at $k = 0$, substitution of (3.144) into (3.139) yields the following ratio of displacement amplitudes for the distinct ions species:

$$\left(\frac{A_0}{B_0}\right)_{op} = -\frac{m_B}{m_A}, \qquad k = 0. \tag{3.146}$$

Thus, the distinct ions of a given lattice site oscillate 180^o out of phase in the optical mode, with displacements weighted by their respective masses. For the acoustic mode, on the other hand, we find from (3.139) that the distinct ions oscillate in phase and with the same displacement in the limit that k approaches zero:

$$\left(\frac{A_0}{B_0}\right)_{ac} = 1, \qquad k = 0. \tag{3.147}$$

Figure 3.20 depicts the motion of the acoustic and optical branches for $k \approx 0$. In both cases, the long wavelength regime implies that the motion at nearby lattice sites is nearly identical. For the acoustic branch, all the ions move together with the same displacement, so that the connecting springs are hardly stretched. As a result, the frequency of vibration vanishes with k, as does the energy carried by the wave. For the optical branch, however, the distinct ions at each lattice site oscillate out of phase, so that the connecting springs are periodically stretched at a maximal rate. Consequently, both the oscillation frequency and the energy carried by the wave are maximum at $k = 0$. If the distinct ions of the basis are oppositely charged, then this motion may be excited by the electric field of a light wave. The resulting oscillations are accompanied by a time-varying dipole moment. Consequently, the name *optical* is given to this branch. Such excitation typically occurs at $k = 0$ due to the negligible linear momentum transferred to the lattice by the incident light wave.

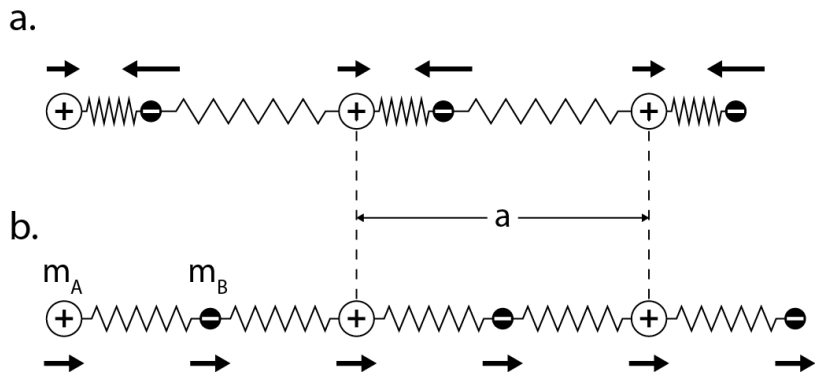

Figure 3.20: Longitudinal (a) optical and (b) acoustic waves in a one-dimensional diatomic crystal of lattice constant a for $k \approx 0$. Here, $m_A > m_B$ and the distinct ions A, B carry opposite charges. Arrows indicate the direction and magnitude of the ion displacements. In the optical mode, distinct ions at a lattice site move 180° out of phase, while their center of mass remains stationary. In the acoustic mode, all the ions move in phase with the same displacement.

Phonons - Quantized Lattice Vibrations

The classical lattice vibrations of the previous section may be quantized to yield discrete energy states associated with each normal mode of vibration. These quanta of lattice vibrations are quasi-particles called *phonons*. They are ubiquitous in all matter systems, where they are responsible for the storage and exchange of heat energy. In solid state systems, they often play a dissipative role in the damping and relaxation of electronic states. Phonons may also be optically excited.

Here, we demonstrate phonons by quantizing the elastic waves of a monatomic one-dimensional lattice. We consider N identical particles of mass m forming a one-dimensional linear array with a lattice constant of length a. As in the previous section, particles interact with their two nearest neighbors via a Hooke's law force with spring constant C. As before, the boundary conditions are fixed by the Born-von Karman condition. The Hamiltonian of such a system is:

$$\hat{H} = \sum_{n=1}^{N} \left[\frac{\hat{p}_n^2}{2m} + \frac{C}{2}(\hat{q}_{n+1} - \hat{q}_n)^2 \right], \tag{3.148}$$

where $\hat{q}_n$ and $\hat{p}_n$ are the displacement and momentum operators for the n^{th} particle of the lattice [43]. The operators $\hat{q}_n$, $\hat{p}_n$ obey the canonical commutation relation:

$$[\hat{q}_n, \hat{p}_{n'}] = i\hbar\,\delta_{n,n'}, \tag{3.149}$$

where $\delta_{n,n'}$ is the Kronecker delta, which equals 1 for $n = n'$ and 0 otherwise.

The Hamiltonian of (3.148) represents the classical expression for the total kinetic and potential energy of the lattice particles. It closely resembles the Hamiltonian of a simple harmonic oscillator and we may solve for its eigenstates and eigenvalues using the familiar method of creation and annihilation operators [43]. To begin, we introduce the canonically conjugate phonon coordinates $\hat{Q}_k$, $\hat{P}_k$, which are related to the coordinates $\hat{q}_n$, $\hat{p}_n$ by the following Fourier transformations:

$$\hat{q}_n = N^{-1/2} \sum_k \hat{Q}_k e^{ikna}, \tag{3.150a}$$

$$\hat{Q}_k = N^{-1/2} \sum_n \hat{q}_n e^{-ikna}, \tag{3.150b}$$

and

$$\hat{p}_n = N^{-1/2} \sum_k \hat{P}_k e^{-ikna}, \tag{3.151a}$$

$$\hat{P}_k = N^{-1/2} \sum_n \hat{p}_n e^{ikna}. \tag{3.151b}$$

The canonical commutation relations hold for $\hat{Q}$, $\hat{P}$:

$$\left[\hat{Q}_k,\, \hat{P}_{k'}\right] = i\hbar\, \delta_{k,k'}. \tag{3.152}$$

As in the previous section, the boundary conditions restrict the wave vector k in (3.150) to the following values:

$$k = \frac{2\pi n}{aN}, \qquad n = \pm 1, \pm 2, \cdots, \pm N/2. \tag{3.153}$$

By substituting (3.150a) and (3.151a) into (3.148) and using (3.152), we find that the Hamiltonian may be expressed in terms of the phonon coordinates as:

$$\hat{H} = \sum_k \left[\frac{1}{2m} \hat{P}_k \hat{P}_{-k} + \frac{1}{2} m\omega_k^2 \hat{Q}_k \hat{Q}_{-k} \right], \tag{3.154}$$

where the frequency ω_k is defined as:

$$\omega_k = \left[\left(\frac{2C}{m} \right) (1 - \cos ka) \right]^{1/2}. \tag{3.155}$$

We now define the phonon creation and annihilation operators in terms of the phonon coordinates as follows:

$$\hat{b}_k^\dagger = (2\hbar)^{-1/2}\left[(m\omega_k)^{1/2}\hat{Q}_{-k} - i(m\omega_k)^{-1/2}\hat{P}_k\right], \tag{3.156a}$$

$$\hat{b}_k = (2\hbar)^{-1/2}\left[(m\omega_k)^{1/2}\hat{Q}_k + i(m\omega_k)^{-1/2}\hat{P}_{-k}\right]. \tag{3.156b}$$

The inverse relations are:

$$\hat{Q}_k = \left(\frac{\hbar}{2m\omega_k}\right)^{1/2}(\hat{b}_k + \hat{b}_{-k}^\dagger), \tag{3.157a}$$

$$\hat{P}_k = i\left(\frac{\hbar m\omega_k}{2}\right)^{1/2}(\hat{b}_k^\dagger - \hat{b}_{-k}). \tag{3.157b}$$

The phonon creation and annihilation operators obey the following commutation relations:

$$\left[\hat{b}_k,\, \hat{b}_{k'}^\dagger\right] = \delta_{k,k'}. \tag{3.158}$$

Upon inserting (3.157) into (3.154), we find that the Hamiltonian may be written as the sum of simple harmonic oscillators for each wave vector or mode:

$$\hat{H} = \sum_k \hbar\omega_k\left(\hat{b}_k^\dagger\hat{b}_k + \frac{1}{2}\right). \tag{3.159}$$

The Hamiltonian of (3.159) assumes the well known solutions of a quantum simple harmonic oscillator for each mode k [43]. Let $|j_k\rangle$ be an eigenstate of $\hat{H}$ with $j \in \mathbb{N}$ for each k. The creation and annihilation operators then have the following properties:

$$\hat{b}_k^\dagger|j_k\rangle = (j+1)^{1/2}\,|(j+1)_k\rangle, \tag{3.160a}$$

$$\hat{b}_k|j_k\rangle = j^{1/2}\,|(j-1)_k\rangle, \tag{3.160b}$$

from which it follows that:

$$\hat{b}_k^\dagger\,\hat{b}_k|j_k\rangle = j|j_k\rangle, \tag{3.161}$$

so that $|j_k\rangle$ is an eigenstate of $\hat{b}_k^\dagger\,\hat{b}_k$ with eigenvalue j. We interpret this to mean that when the phonon mode k is in the eigenstate $|j_k\rangle$, there are j phonons in that

mode, each with the same discrete energy. The number operator $\hat{b}_k^\dagger \hat{b}_k$ counts the phonons in a given mode. Consequently, the energy eigenvalues for each mode k of the Hamiltonian are:

$$\hat{H}_k|j_k\rangle = \hbar\omega_k \left(\hat{b}_k^\dagger \hat{b}_k + \frac{1}{2}\right)|j_k\rangle = \left(j + \frac{1}{2}\right)\hbar\omega_k|j_k\rangle, \tag{3.162}$$

and the eigenvalues of the entire Hamiltonian for all modes k are:

$$U = \sum_k \left(j + \frac{1}{2}\right)\hbar\omega_k. \tag{3.163}$$

We observe that the energy stored in each vibrational mode with classical frequency ω_k is obtained by multiplying the discrete phonon energy $\hbar\omega_k$ by the number of phonons in that mode, plus an additional energy amount $\hbar\omega_k/2$. This extra energy exists in the absence of any phonons and is called the *zero point energy*. The phonon creation and annihilation operators are seen to increase or decrease the number of phonons in a given mode by one. That is, they create and annihilate phonons within the lattice.

Although we have quantized phonons for the case of a monatomic crystal lattice, equivalent results hold for crystals with multiple branches and polarizations for each value of the wave vector k. In particular, we find many materials in which optical branch phonons are generated during laser excitation. Similarly, the relaxation of an excited electronic state may involve the emission of phonons. In this case, it is common to observe phonon satellite emission, i.e., the emission of less energetic *photons* of light, which are accompanied by phonon emission.

Polarons - Hybridized Electronic and Phononic States

In a semiconductor crystal whose ions exhibit at least partial ionic binding, the presence of an additional charged particle will polarize the crystal lattice. Excited electronic states in the crystal, such as conduction band electrons or valence band holes, have precisely this effect. Figure 3.21 depicts the response of a crystal lattice to a conduction band electron. In this case, the crystal shown is diatomic and the lattice is populated by alternating ionic species with positive and negative net charge. In the presence of the electron, the ions are displaced from their equilibrium lattice sites, with the positive ions attracted and the negative ions repulsed in proportion to the Coulomb interaction strength. The polarized lattice is said to form a *phonon cloud* that surrounds the charge carrier. In semiconductors, the crystal binding is weakly ionic and yields a phonon cloud whose radius is larger than the lattice constant, ensuring that an effective mass description of the carrier remains valid [53]. As the charge carrier moves through the lattice, it drags the phonon cloud along with it. The

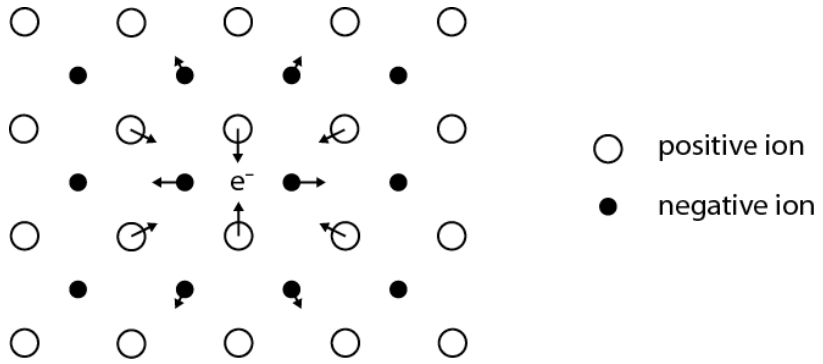

Figure 3.21: Diagram of the lattice distortion in a partially ionic semiconductor crystal in the presence of a negative charge carrier, illustrating the polaron concept. For a positive charge carrier, the direction of the ionic displacements are reversed.

combined entity of charge carrier plus phonon cloud constitutes a new quasi-particle called a *polaron*. The phonon cloud reduces the charge carrier's mobility and screens its electric field, resulting in the polaron having a slightly increased effective mass and reduced electrostatic energy compared to the bare charge carrier (i.e., electron or hole).

To describe the polaron state quantitatively, we may write an effective mass Hamiltonian including three terms:

$$\hat{H} = \hat{H}_e + \hat{H}_{ph} + \hat{H}_{e-ph}, \tag{3.164}$$

where $\hat{H}_e$ and $\hat{H}_{ph}$ represent diagonal operators for the uncoupled electronic and phononic energy eigenstates, respectively, while $\hat{H}_{e-ph}$ represents the interaction between electronic and phononic states. For brevity, we have ignored carrier-carrier interactions in (3.164) so that we may focus solely on the carrier-phonon interaction.[20] The electronic states may represent either a conduction band electron or a valence band hole, though we shall speak of an electron without loss of generality.

The phonon Hamiltonian $\hat{H}_{ph}$ is given by equation (3.159) from the previous section, expressed in terms of the phonon creation and annihilation operators. However, in order to reserve $\mathbf{k}$ for the Bloch wave vector of the electronic states, we label the

[20]Equation (3.164) is exact for single particle electronic states. The complete Hamiltonian for multiple particle electronic states would contain additional terms for the carrier-carrier interactions, but these terms do not involve phonons.

phonon wave vector by $\mathbf{q}$:[21]

$$\hat{H}_{ph} = \sum_{\mathbf{q}} \hbar\omega_{\mathbf{q}} \left(\hat{b}^{\dagger}_{\mathbf{q}} \hat{b}_{\mathbf{q}} + \frac{1}{2} \right), \tag{3.165}$$

where $\mathbf{q}$ is in the first Brillouin zone. For brevity of notation, we have ignored the multiple branches and polarizations of the phonons.

We may also describe the electronic states in the language of creation and annihilation operators. Ignoring spin and carrier-carrier interactions for brevity, we may write the Hamiltonian describing conduction band electrons in stationary states labeled by wave vector $\mathbf{k}$ as:

$$\hat{H}_e = \sum_{\mathbf{k}} \varepsilon_{\mathbf{k}} \hat{c}^{\dagger}_{\mathbf{k}} \hat{c}_{\mathbf{k}}, \tag{3.166}$$

where $\hat{c}^{\dagger}_{\mathbf{k}}$, $\hat{c}_{\mathbf{k}}$ are the creation and annihilation operators for an electron of Bloch wave vector $\mathbf{k}$ and energy $\varepsilon_{\mathbf{k}}$.[22] The electron creation and annihilation operators are analogous to the phonon creation and annihilation operators. However, unlike phonons, which are bosons, electrons are fermions and the population of each unique electronic state is limited to 0 or 1. We define the electronic eigenstates of wave vector $\mathbf{k}$ and population 0 or 1 by the kets $|0\rangle$ and $|\mathbf{k}\rangle$, respectively. Then, the electronic creation and annihilation operators have the following properties:

$$\hat{c}^{\dagger}_{\mathbf{k}} |0\rangle = |\mathbf{k}\rangle, \tag{3.167a}$$

$$\hat{c}_{\mathbf{k}} |\mathbf{k}\rangle = |0\rangle. \tag{3.167b}$$

As with the phonons, the electron number operator $\hat{c}^{\dagger}_{\mathbf{k}} \hat{c}_{\mathbf{k}}$ counts the population of the electronic state indexed by $\mathbf{k}$.

In the absence of the electron-phonon coupling term $\hat{H}_{e-ph}$, the energy eigenstates of the system are direct product states of the non-interacting electronic and phononic eigenstates. We may write the phononic eigenstate with j phonons per mode $\mathbf{q}$ as the product state $\prod_{\mathbf{q}} |j_{\mathbf{q}}\rangle$. Similarly, the electronic eigenstates may be written as $\prod_{\mathbf{k}} |i_{\mathbf{k}}\rangle$, where $i = 0, 1$ specifies the electron occupancy of state $\mathbf{k}$. Then, the eigenstates of the non-interacting Hamiltonian $\hat{H}_e + \hat{H}_{ph}$ may be written as $\prod_{\mathbf{k}} |i_{\mathbf{k}}\rangle \otimes \prod_{\mathbf{q}} |j_{\mathbf{q}}\rangle$. In

[21] Do not confuse the phonon wave vector $\mathbf{q}$ in this section with the generalized position operator $\hat{q}$ from the previous section.

[22] Here, we have written the Hamiltonian for conduction band electrons in a bulk crystal whose quantum states (ignoring spin) are specified their Bloch wave vectors $\mathbf{k}$. In lower dimensional or multi-band systems, the Hamiltonian (3.166) remains the same, but the quantum states are described by some other appropriate set of quantum numbers.

the case where we have just one electronic state and only a single phonon mode is populated, we may use the simplified notation $|i\mathbf{k}, j\mathbf{q}\rangle$, where $i = 0, 1$ and $j \in \mathbb{N}$ specify the electron and phonon occupancies, respectively.

The electron-phonon interaction Hamiltonian $\hat{H}_{e-ph}$ may also be written in terms of the electron and phonon creation and annihilation operators. The part that is linear in the phonon operators is written as:

$$\hat{H}_{e-ph} = \sum_{\mathbf{k},\mathbf{q}} \gamma\hbar\omega_{\mathbf{q}}\, \hat{c}^{\dagger}_{\mathbf{k}+\mathbf{q}}\hat{c}_{\mathbf{k}} \left(\hat{b}_{\mathbf{q}} + \hat{b}^{\dagger}_{-\mathbf{q}}\right) = \sum_{\mathbf{k},\mathbf{q}} \gamma\hbar\omega_{\mathbf{q}} \left(\hat{c}^{\dagger}_{\mathbf{k}+\mathbf{q}}\hat{c}_{\mathbf{k}}\hat{b}_{\mathbf{q}} + \hat{c}^{\dagger}_{\mathbf{k}-\mathbf{q}}\hat{c}_{\mathbf{k}}\hat{b}^{\dagger}_{\mathbf{q}}\right), \quad (3.168)$$

where γ is a dimensionless matrix element that determines the strength of the electron-phonon interaction and $\omega_{\mathbf{q}}$ is the phonon angular frequency of oscillation [62]. From the form of equation (3.168), we observe that in the linear regime $\hat{H}_{e-ph}$ couples any two states $\prod_{\mathbf{k}}|i_{\mathbf{k}}\rangle \otimes \prod_{\mathbf{q}}|j_{\mathbf{q}}\rangle$ that differ by one phonon of a single mode $\mathbf{q}$. In particular, transitions between such states occur when an electron emits or absorbs a phonon, accompanied by a simultaneous change in the electronic wave vector to conserve the total crystal momentum. For example, an electron initially with wave vector $\mathbf{k}$ may transition to a state with wave vector $\mathbf{k}+\mathbf{q}$ either by absorbing a phonon of mode $\mathbf{q}$ or emitting a phonon of mode $-\mathbf{q}$. Thus, $\mathbf{q}$ represents the crystal momentum transfer during the transition.[23] We note that quadratic and higher order terms in the creation and annihilation operators are usually small and can typically be neglected. They are only important for phonons which are not coupled to electrons by the linear interaction [62].

The electron-phonon interaction Hamiltonian given in equation (3.168) is general since the matrix element γ is not specified for any particular interaction mechanism. In a crystal, there are a number of interaction mechanisms that may couple electronic states with phonons. Here, we briefly describe the most important such mechanisms in semiconductors. The Fröhlich interaction couples charge carriers to the electric field that accompanies optical phonons, preferentially with longitudinal polarization. Deformation potential coupling arises from phonon-induced lattice strain, including hydrostatic deformation and shear strain, and it couples charge carriers to both acoustic and optical phonons. Finally, in non-centrosymmetric crystals, an electric field appears as a consequence of strain, which couples charge carriers to preferentially acoustic phonons [53]. In the following, we elaborate on the Fröhlich interaction, which is the dominant mechanism that couples charge carriers to long wavelength LO phonons in InAs and GaAs. As we describe later in Chapter 7, polarons formed in this

[23] In general, the crystal momentum will be conserved only up to an arbitrary reciprocal lattice vector $\mathbf{K}$. Thus, an electron initially in state $\mathbf{k}$ may absorb a phonon of wave vector $\mathbf{q}$ and be scattered into any state $\mathbf{k}+\mathbf{q}+\mathbf{K}$. However, normal scattering ($\mathbf{K} = 0$) usually dominates over Umklapp scattering ($\mathbf{K} \neq 0$), so we have neglected the latter process in writing equation (3.168) [43].

way play a fundamental role in the process of Fano interference and phonon-induced transparency in QDMs.

We now consider the coupling of a single conduction band electron of wave vector $\mathbf{k}$ to long wavelength LO phonons via the Fröhlich interaction in a bulk semiconductor crystal. In this case, the electron-phonon coupling term $\gamma_F(\mathbf{q})$ is given by [63]:

$$\gamma_F(\mathbf{q}) = -\frac{i}{\mathbf{q}} \left(\frac{\hbar}{2m_{eff}\omega_{LO}} \right)^{1/4} \left(\frac{4\pi\alpha}{V} \right)^{1/2}, \tag{3.169}$$

where the dimensionless Fröhlich coupling constant α is defined as:

$$\alpha = \frac{e^2}{2\hbar\omega_{LO}} \left(\frac{2m_{eff}\omega_{LO}}{\hbar} \right)^{1/2} \left(\frac{1}{\epsilon_\infty} - \frac{1}{\epsilon} \right)^{1/2}. \tag{3.170}$$

In the above equations, e is the elementary charge, m_{eff} is the carrier effective mass, V is the crystal volume of interest, ω_{LO} is the LO phonon angular frequency, ϵ_∞ is the electronic (i.e., high frequency) dielectric constant and ϵ is the static dielectric constant. In the derivation of the Fröhlich coupling term, it is assumed that the spatial extension of the polaron is large compared to the lattice constant so that the crystal may be treated as a continuum. Then, the dielectric constants of the crystal determine the electron-phonon interaction strength for a given material, which is summarized by the Fröhlich coupling constant α. In addition, it is assumed that the long wavelength LO phonons have a constant oscillation frequency of ω_{LO} for all $\mathbf{q}$, i.e., the LO phonons are dispersionless [64].

We may use perturbation theory to determine the eigenenergies and eigenstates of the total Hamiltonian in (3.164) if α is sufficiently small (i.e. $\alpha < 1$), which is typically the case for semiconductors (e.g., $\alpha = 0.052$ for InAs and 0.058 for GaAs) [65]. At zero temperature, the initial unperturbed state consists of a vacuum of phonons and a single electron of wave vector $\mathbf{k}$, which in ket notation we may write as $|\mathbf{k}, 0\rangle$.[24] This state is coupled via phonon emission to the states with a single phonon of mode $\mathbf{q}$ and an electron with momentum $\mathbf{k}-\mathbf{q}$, namely $|\mathbf{k}-\mathbf{q}, 1\mathbf{q}\rangle$. The zero order energies of the unperturbed states $|\mathbf{k}, 0\rangle$ and $|\mathbf{k}-\mathbf{q}, 1\mathbf{q}\rangle$ are:

$$\varepsilon_0(\mathbf{k}) = \frac{\hbar^2 k^2}{2m_{eff}}, \tag{3.171a}$$

$$\varepsilon_0(\mathbf{k}, \mathbf{q}) = \frac{\hbar^2(\mathbf{k}-\mathbf{q})^2}{2m_{eff}} + \hbar\omega_{LO}, \tag{3.171b}$$

[24] In fact, this is the initial unperturbed state of the system for any finite temperature in which $k_B T << \hbar\omega_{LO}$.

where we have ignored the zero point energy of the oscillators, $\sum_{\mathbf{q}} \hbar\omega_{LO}/2$. The matrix elements of the perturbing Hamiltonian $\hat{H}_{e-ph}$ are:

$$\langle \mathbf{k}-\mathbf{q}, 1\mathbf{q}|\hat{H}_{e-ph}|\mathbf{k}, 0\rangle = \gamma_F(\mathbf{q})\hbar\omega_{LO}, \tag{3.172a}$$

$$\langle \mathbf{k}, 0|\hat{H}_{e-ph}|\mathbf{k}, 0\rangle = \langle \mathbf{k}-\mathbf{q}, 1\mathbf{q}|\hat{H}_{e-ph}|\mathbf{k}-\mathbf{q}, 1\mathbf{q}\rangle = 0. \tag{3.172b}$$

Using the results of (3.172) along with standard perturbation theory, we find that to 2nd order the perturbed energy of the initial state is:

$$\varepsilon(\mathbf{k}) = \varepsilon_0(\mathbf{k}) - \sum_{\mathbf{q}} \frac{(\hbar\omega_{LO})^2|\gamma_F(\mathbf{q})|^2}{\varepsilon_0(\mathbf{k},\mathbf{q}) - \varepsilon_0(\mathbf{k})}, \tag{3.173a}$$

$$= \frac{\hbar^2 k^2}{2m_{eff}} - 2m_{eff}\omega_{LO}^2 \sum_{\mathbf{q}} \frac{|\gamma_F(\mathbf{q})|^2}{(\mathbf{k}-\mathbf{q})^2 + 2m_{eff}\omega_{LO}/\hbar - \mathbf{k}^2}. \tag{3.173b}$$

The corresponding perturbed eigenstate $|\psi_{pol}\rangle$, to 1st order correction, is given by:

$$|\psi_{pol}\rangle = |\mathbf{k}, 0\rangle + \sum_{\mathbf{q}} a_{\mathbf{q}} |\mathbf{k}-\mathbf{q}, \mathbf{q}\rangle, \tag{3.174}$$

where:

$$a_{\mathbf{q}} = -\sum_{\mathbf{q}} \frac{\hbar\omega_{LO}\gamma_F(\mathbf{q})}{\varepsilon_0(\mathbf{k},\mathbf{q}) - \varepsilon_0(\mathbf{k})} = -\frac{2m_{eff}\omega_{LO}}{\hbar} \sum_{\mathbf{q}} \frac{\gamma_F(\mathbf{q})}{(\mathbf{k}-\mathbf{q})^2 + 2m_{eff}\omega_{LO}/\hbar - \mathbf{k}^2}. \tag{3.175}$$

We may integrate equation (3.173), in which case we find the following expression for the energy of the polaron state $|\psi_{pol}\rangle$ [62]:

$$\varepsilon(\mathbf{k}) = \frac{\hbar^2 k^2}{2m_{eff}} - \frac{\alpha q_0 \hbar\omega_{LO}}{k} \arcsin\left(\frac{k}{q_0}\right), \tag{3.176}$$

where:

$$q_0 = \sqrt{\frac{2m_{eff}\omega_{LO}}{\hbar}}. \tag{3.177}$$

For an electron near the band edge with $k << q_0$, equation (3.176) simplifies to:

$$\varepsilon(\mathbf{k}) \cong \frac{\hbar^2 k^2}{2m^*_{eff}} - \alpha\hbar\omega_{LO}, \tag{3.178}$$

where the enhanced effective mass of the polaron is:

$$m^*_{eff} = \frac{m_{eff}}{1 - \alpha/6} \cong m_{eff}(1 + \alpha/6). \tag{3.179}$$

The term $\alpha\hbar\omega_{LO}$ in equation (3.178) represents the polaron binding energy.

We observe from equation (3.174) that, as a result of the electron-phonon interaction, the unperturbed electronic state becomes superimposed with the manifold of one phonon states. The resulting polaron state $|\psi_{pol}\rangle$ is a hybridization of the electronic and phononic states. Moreover, the electron-phonon interaction provides the mechanism to optically excite a polaron state consisting of one electron and one phonon, i.e., $|\mathbf{k} - \mathbf{q}, 1\mathbf{q}\rangle$, directly from the crystal ground state by absorption of a single photon of commensurate energy.

The polaron formation discussed in this section also extends to excitonic states in QDMs. For an exciton, both the electron and hole are coupled to the LO phonons by the Fröhlich interaction. The resulting quasi-particle is an excitonic polaron, a hybridized state of an exciton and LO phonons. In QDMs, confinement can lead to an enhancement of the Fröhlich coupling constant α, thereby increasing the electron-phonon interaction strength [66]. Moreover, realistic phonon states represent a continuum of energy levels, meaning that the excitonic polaron states form continuous energy bands in QDMs.

Chapter 4

Experimental Methods

Laser spectroscopy is a powerful tool for studying atoms, molecules and bulk matter. Much of this utility is derived from the advantages of modern lasers, which are capable of providing highly coherent, quasi-monochromatic light over a broad range of wavelengths and intensity levels. The essence of laser spectroscopy is to gain knowledge about, or exert control over, the stationary and dynamic processes of matter by illuminating a sample with laser light and observing the re-emitted, reflected or transmitted light. In this chapter, we first give a brief overview of PL and PLE spectroscopy, which form the core experimental tools for the optical studies presented in this dissertation. Then, we provide a detailed description of the experimental methods employed in the execution of this dissertation, including the experimental setup, laser spectroscopy techniques and data analysis methodologies.

4.1 Brief Overview of Laser Spectroscopy Techniques

Photoluminescence Spectroscopy

A common form of laser spectroscopy is that which employs a continuous wave (CW) laser to illuminate the sample. CW laser spectroscopy is ideal for studying steady state conditions, characterizing stationary properties and even provides some information on dynamical processes.

A powerful type of spectroscopy that may be performed with a CW laser is photoluminescence (PL) spectroscopy. PL spectroscopy has the advantage of being a non-destructive measurement technique capable of generating relatively large emission intensities, while achieving high rejection of the elastically scattered laser light. In this technique, the laser is made to illuminate a sample of interest. During illumination, some of the incident laser photons are absorbed, which induce within the

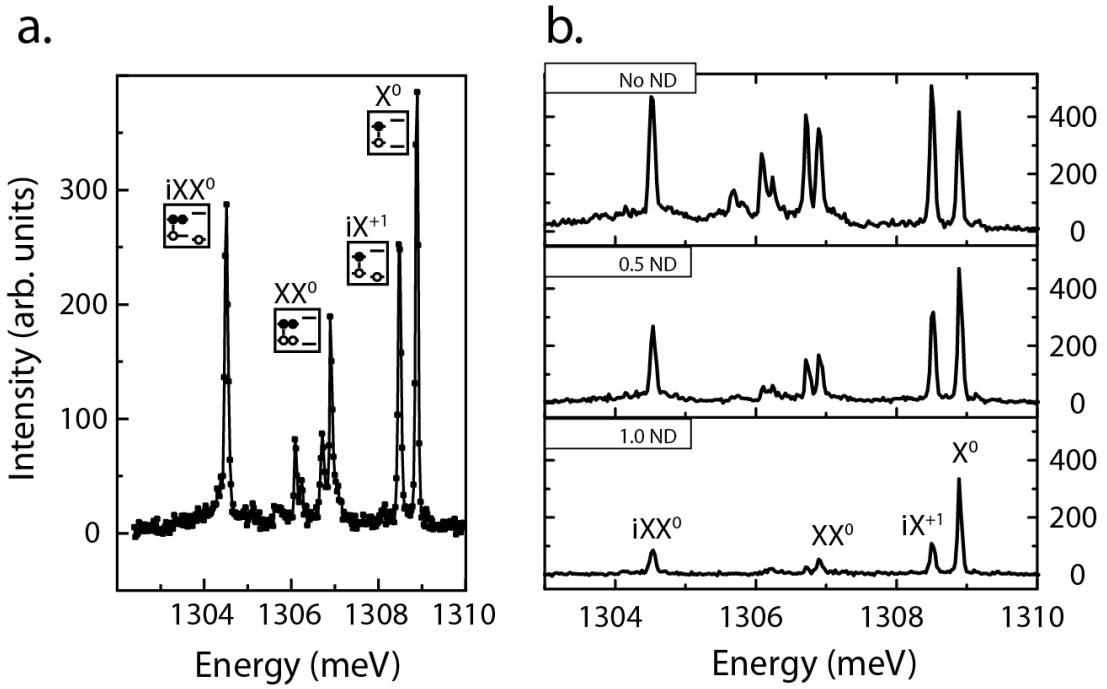

Figure 4.1: (a) PL collected from a QDM. (b) PL from the same QDM excited at different laser powers by working with neutral density filters (ND), with the power increasing from bottom to top.

sample transitions to excited states. After some time, the sample relaxes back to lower energy states and the re-emitted light (i.e., PL) is collected for analysis. The energy and relative intensity of the emitted light yields a PL spectrum that is characteristic of the sample. From this spectrum, information about the sample may be obtained, such as the energy level structure, excited state lifetimes and relative intensities, fine structures, etc.

Figure 4.1 displays example PL spectra collected from a QDM. The intensity is plotted in arbitrary units as a function of the photon energy. Various discrete energy resonances are observed, but their identification is not easily made from a single PL spectrum. In order to characterize the transitions unambiguously, it is useful to observe how the PL spectra evolves under the influence of changing experimental parameters (e.g., applied electric fields, laser power, polarization, etc.). For example, an electric field dispersed PL map (i.e., bias map), which we discuss in detail in Section 4.3, makes use of an externally electric field to aid in the characterization process.

A standard setup to perform PL spectroscopy typically consists of a laser, the sample under investigation (often mounted in a cryostat), and a spectrometer with a

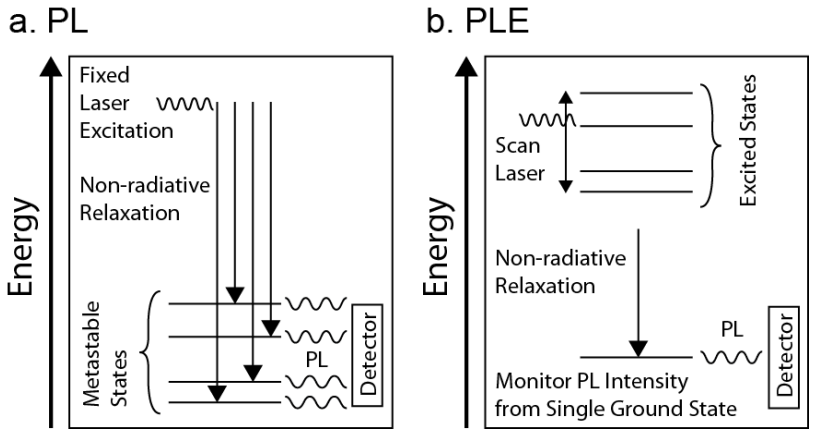

Figure 4.2: Diagrams depicting the processes of (a) non-resonant PL spectroscopy and (b) PLE spectroscopy, as discussed in the main text.

detector to disperse and collect the PL. The resolution of spectral features is limited by the dispersing power of the spectrometer and the sensitivity of the detection device. It is common to tune the laser to a higher energy than the transitions to be investigated, a procedure known as non-resonant PL. In this procedure, excited states at the laser energy are initially populated and then quickly undergo non-radiative relaxation to lower energy metastable states (see Figure 4.2a). These metastable states then emit PL, which is collected for study. Non-resonant PL provides the ability to filter out the higher energy incident laser light from the PL signal of interest, which is a great advantage since the laser intensity dwarfs that of the PL signal (this is particularly true for tiny samples such as QDs).

It is also possible to perform resonant PL spectroscopy, in which the PL signal and incident laser have equal energies. However, separating the desired signal from the flood of scattered laser light requires more sophisticated procedures. This may be achieved, for example, by using high extinction crossed polarizers to filter the laser light or by embedding the sample in a waveguide that prevents scattered laser light from reaching the detector [29, 67]. Another method, which we describe in Section 4.3, is to resonantly excite a transition and then monitor the less energetic re-emitted light of the phonon satellite.

If high spatial resolution is desired, it is possible to use various types of pinholes or apertures to isolate small regions of the sample for laser excitation, such as the $\sim 1\,\mu$m diameter apertures used to isolate the individual QDMs studied in this work (see Chapter 2). Specialized microscopes may also be used to increase the spatial resolution. The minimum diffraction limited resolution is about $0.61\lambda/\mathrm{NA}$, where λ is the wavelength of light used and NA is the numerical aperture. For good microscope objectives, the NA can reach values up to one or greater. Confocal microscopes can

improve upon diffraction limited resolution by a factor of $1/\sqrt{2}$. Meanwhile, near field scanning optical microscopes using fiber tips with dimensions much less than λ can achieve resolution down to 100 nm or less. However, the cost of beating the diffraction limit by these methods is low optical through-put of the pinholes or fiber tips. [53]

PL spectroscopy may be adjusted in various ways so that different information may be gained from the sample. Tuning the laser power allows one to access different optical regimes. At low power, one observes the linear optical regime, in which the PL intensity is a linear function of the power. After a certain threshold of higher power, one reaches the nonlinear optical regime, in which the laser illumination affects reversible modifications to the optical response of the sample, producing new phenomena not observed at lower powers. Some examples of non-linear phenomena include power broadening and intensity saturation, both of which are discussed in theory Section 3.4. In Fig. 4.1b, we show the evolving PL spectrum of a QDM as a function of the laser power. Additionally, the wavelength and polarization state of the incident laser may also be tuned, enabling one to probe particular transition energies and polarization related anisotropies of a sample. Also, the sample environment under investigation may be manipulated in a controlled manner to study different physical properties. For example, external electric or magnetic fields may be applied to investigate Stark shifts and Zeeman splittings and the temperature may be adjusted to investigate various phonon processes. [53]

Photoluminescence Excitation Spectroscopy

Photoluminescence Excitation Spectroscopy (PLE) makes use of non-resonant PL spectroscopy to provide information about the excited states present in a sample of interest (see Figure 4.2b). Compared to PL, PLE is capable of providing much greater resolution. PLE spectra is obtained by resonant excitation with a narrow line laser, so in principle the resolution is laser line width limited. The basic procedure involves finely stepping the incident laser through a range of energies and recording a PL spectrum for each laser energy. A single metastable ground state transition is selected from the spectrum and is monitored for changes in its intensity as a function of the incident laser energy.[1] When the laser comes into resonance with an excited state energy level, the monitored metastable ground state is efficiently populated via rapid non-radiative decay originating from the optically generated excited state. This results in a dramatic increase in intensity of the metastable ground state while the laser is in resonance with an excited state. The intensity of the monitored transition may be summed over a small range about its maximum value and then plotted verses

[1] More generally, one could monitor a certain fixed spectral range as a function of the excitation energy.

the incident laser energy. The appearance of sharp intensity peaks at particular laser energies indicate the presence of excited state energy levels which have relaxed to the monitored metastable state. Consequently, PLE spectroscopy is a method for indirectly measuring the absorption of excited states and provides a map of excited state energy levels. We point out that the intensity of the PLE signal depends on whether the optical transitions are allowed, which may be affected by the symmetries of states, the relaxation rates, etc.

4.2 Description of Optical Spectroscopy Instrumentation and Setup

A diagram of the optical spectroscopy setup used for the experimental work in this dissertation is shown in Fig. 4.3. In order to obtain a relatively intense and well-resolved PL signal, the QDM samples are placed inside a microscopy chamber of a closed cycle, helium cooled cryostat capable of achieving temperatures down to 18 K with a temperature stability of better than 0.1 K. The sample is pressure clamped to a copper mounting block, optionally using indium metal and/or cryogenic grease to improve conduction, and this block is threaded into the cold finger of the cryostat. A glass cover slide may be optionally placed over the optical window of the radiation shield to further decrease radiative heating, though the optical transmission may be slightly reduced. The leads of a source meter connect through the cryostat to the Schottky diode embedded in the QDM sample in order to apply an external electric field along the QD growth axis. The source meter used for the discussed studies is able to supply a DC voltage with a range of ± 20 V with a minimum step size of 0.5 mV.

For optical excitation, we used two variable wavelength CW diode lasers operating in the approximate range from $816 - 1084$ nm and achieving a maximum power of $\sim$50 mW. Each laser has a nominal line width on the order of 10^{-6} meV with temperature dependence better than 1 μeV/K. A wavemeter provides feedback for fine tuning the laser energy and a power meter monitors the laser intensity. Neutral density filters are used for additional control of the laser power, while polarization optics, including linear polarizers, variable retarders and 1/4 waveplates, provide control over the polarization state of the laser light. Long and short pass filters are used to suppress elastically scattered laser light during PL and PLE experiments. In particular, we typically employ short pass filters for the incident laser excitation and long pass filters for the PL and PLE signals. The optical pathway includes dielectric mirrors and anti-reflection coated lenses, both optimized to minimize losses in the near infra-red emission range of our QDM samples. Position control is achieved with the use of linear translation stages and an external CCD camera aids in sample and

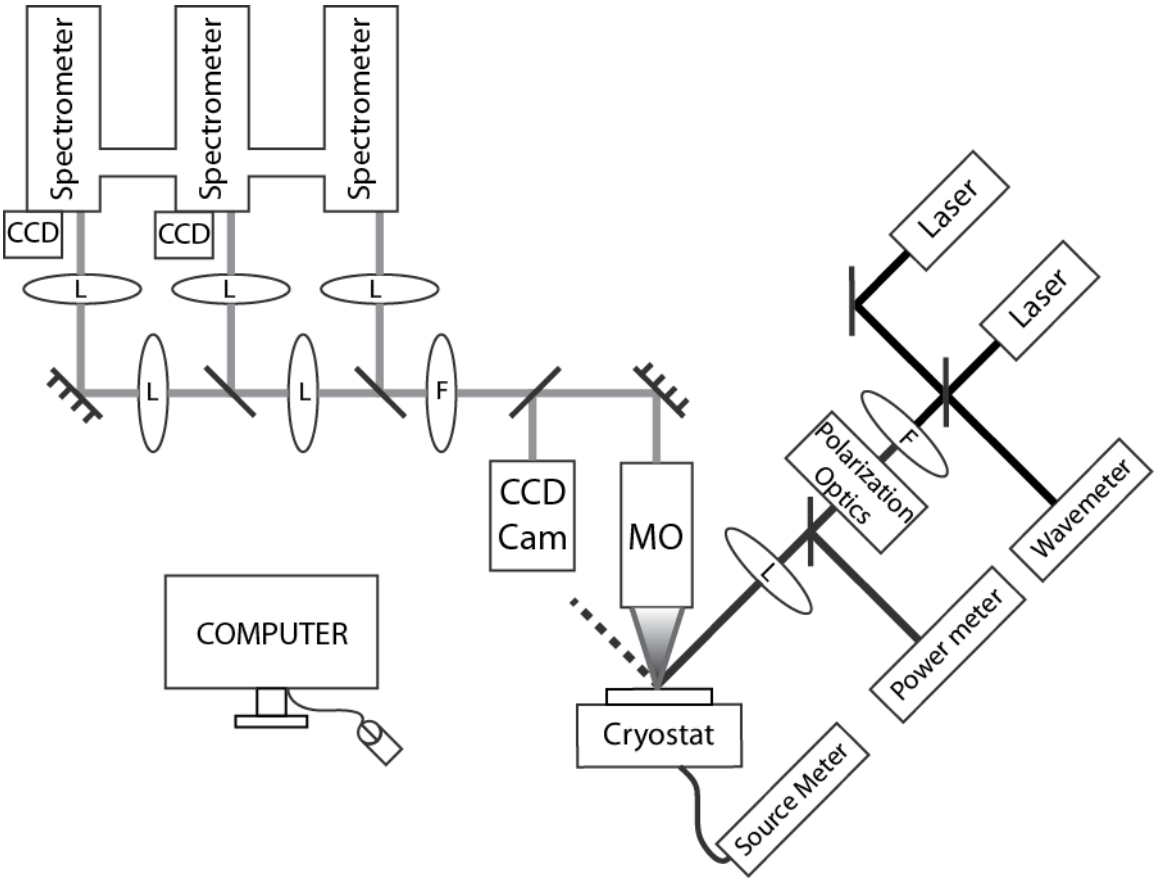

Figure 4.3: Experimental setup for optical spectroscopy. The computer controls the experimental instruments and acquires the data. Optical elements in the beam path are labeled 'L' for lens, 'F' for filter and 'MO' for the microscope objective. Free standing neutral density filters may also be placed in the beam path.

laser alignment.

The incident laser beam is directed to the sample by one of two methods: (i) it may enter the cryostat window at normal incidence by first passing through a 50× magnification microscope objective (MO) or (ii) it may bypass the MO and enter the cryostat window at an angle, as shown in Fig. 4.3. The first method enables a tighter beam waist at the sample and therefore greater excitation power density, but also delivers much more scattered laser light towards the detector. The second method achieves a lesser power density, but the PL is much easier to collect because the majority of the scattered laser light is directed away from the detector (see dashed line in Fig. 4.3). In both cases, the emitted PL is collected and focused by the MO and, after additional filtering and focusing, passes to the triple spectrometer system,

where it is dispersed and collected with a liquid nitrogen cooled 1340 × 100 pixel CCD camera. Each spectrometer is 750 mm in length and sports a three-grating turret, with diffraction gratings ranging from 750 mm^{-1} to 1,800 mm^{-1}. A maximum energy resolution of about 25 μeV is achieved by using the triple additive mode, which disperses the PL three times. When operated in triple subtractive mode, the system acts as a high quality bandpass filter to suppress scattered laser light. The highest intensities are achieved when the system is operated in single spectrometer mode. Also, the collection time may be adjusted to increase the signal intensity.

Finally, the CCD signal is sent to a computer, where it is recorded for further processing. The raw data consists of an array of intensities per CCD pixel, which is calibrated to yield a profile of PL intensity versus energy. The software allows the option to aggregate the signals from multiple pixels into customizable bins that may yield a more intense, but coarser, signal. Operational values for the various instruments modifying the laser light, PL or sample environment are also recorded. A majority of the instruments are programmable, which provides additional flexibility in experimental design and computer automation. Afterwards, the raw data from the saved text files may be analyzed and manipulated with external software to produce various graphs and figures to represent the data.

4.3 Description of Experimental Methods

In the following, we describe in detail the common experimental methods used for acquiring the data results appearing in this dissertation.

PL Bias Maps

A key data representation for studying QDMs is a so called PL bias map, which is the experimental realization of the electric field dispersed transition energy map described in theory Section 3.3 and modeled in Figures 3.8 and 3.9. A bias map is generated by finely stepping the applied electric field and, at each field strength, collecting a PL spectrum of the QDM under investigation via non-resonant PL spectroscopy. The electric field F is controlled with the source meter by supplying a bias voltage ΔV according to the equation:

$$F = -\frac{\Delta V}{s}, \tag{4.1}$$

where s is the distance between the two terminals of the Schottky diode ($s \cong 372.5$ nm in our samples). On account of the negative sign in equation (4.1), the direction of forward bias is opposite that of the electric field. Consequently, we label the PL bias maps with the bias voltage axis becoming increasingly negative in the direction

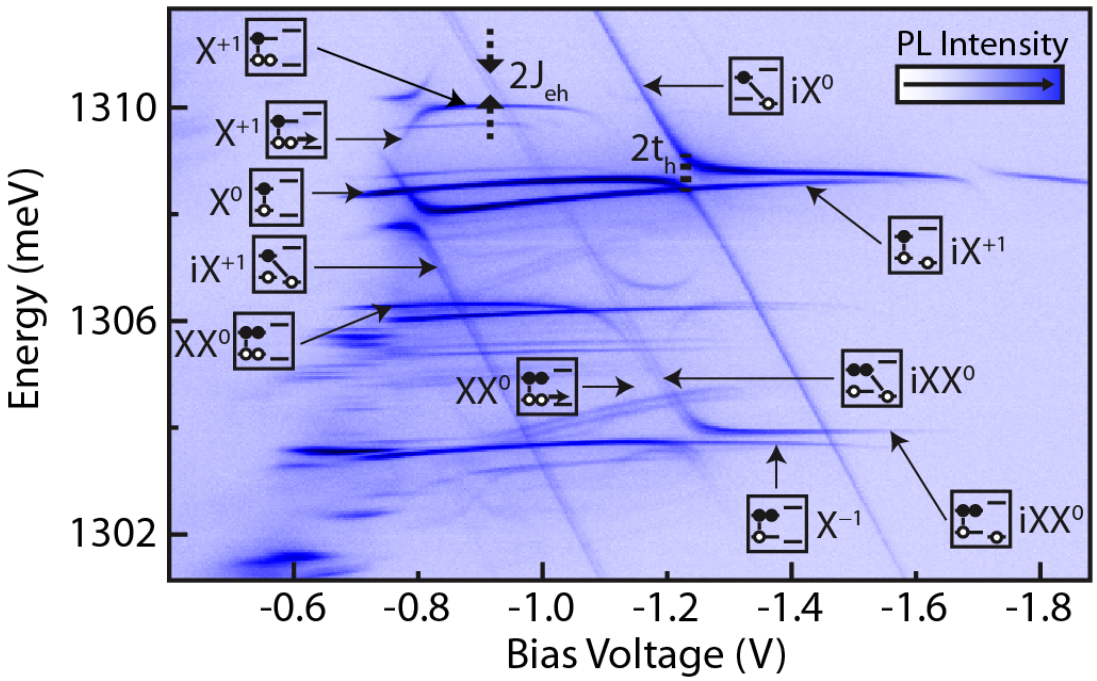

Figure 4.4: Example bias map, showing the PL intensity as a function of bias voltage and energy. The emission lines are labeled according to the initial excitonic state prior to the radiative transition. The inset spatial charge diagrams show the carrier distribution of the initial state and link the recombining charge carriers with lines. Prominent spectral feature of the QDM are described in the main text.

going from left to right. In Appendix B, we provide a detailed description of the procedure for generating a PL bias map with laboratory equipment available in the Quantum Matter Group.

An example bias map is shown in Figure 4.4. The single PL spectra at each bias value are collapsed to one dimension along the vertical energy axis, with the PL intensity indicated by the color scale. Darker shades correspond to greater PL intensity. The individual PL spectra, in this case taken at 5 mV intervals, are merged in continuous order from left to right to form the bias map. In Fig. 4.4, we observe both direct and indirect transitions with flat and negative slopes, as discussed in the theory Section 3.3. The slight curvature of the direct transition lines as a function of the bias voltage (i.e., the Stark shift) results from the polarizability of the charge states under the influence of the applied electric field, a topic we discuss at length in Chapter 6 [25, 36]. The tunneling barrier thickness of the sample may be calculated by measuring the slope of the indirect transition lines and using equation (3.27) from Section 3.3.

The bias map presents a fuller picture of the QDM energy states than can be obtained from single PL spectra, making it a useful tool for characterizing the excitonic state transitions of a QDM. Here, we briefly outline the characterization process, using as an example the QDM in Fig. 4.4. The most intense transition line typically originates from the direct neutral exciton state X^0, which in Fig. 4.4 appears as a prominent line with nearly flat slope at about 1308 meV. Following this line a little past -1.2 V, we observe the anti-crossing of the direct X^0 and indirect iX^0 exciton states. The hole tunneling energy of this AC may be determined by measuring the energy difference between the lower and upper molecular exciton states at the resonant bias value (see the dashed vertical line labeled $2t_h$ in Fig. 4.4).

We locate the X-pattern of the neutral biexciton in relation to the X^0/iX^0 AC. The right-most AC's of the biexciton X-pattern occur at the same bias voltage as the exciton AC. This is because the exciton states are the final states in the biexciton recombination. As seen in Fig. 4.4, the biexciton direct transition lines are located several meV below the X^0 transition as a result of the biexciton binding energy. We may determine the bright-dark e-h exchange energy J_{eh} by measuring the energy splitting of the negatively sloped iXX^0 doublet (see the dashed arrows labeled $2J_{eh}$ in Fig. 4.4). From the direct biexciton iXX^0 transition, we identify the negative trion transition X^{-1}. These two transitions have nearly the same energy since the states have identical charge configurations in the bottom QD. Similarly, we identify the positive trion transition iX^{+1} by its proximity to the X^0 transition, which has nearly the same energy. The iX^{+1} transition connects to the positive trion X-pattern at left, starting in Fig. 4.4 at about -0.8 V.

Transitions that require carrier tunneling to the opposite QD in the final state are indicated with a horizontal arrow in the state diagram that points from the tunneling charge carrier to the opposite QD. Examples of such tunneling-assisted transitions in Fig. 4.4 are the upward sloping transition lines in the trion and biexciton X-patterns. The probability of a transition occurring while a carrier tunnels to the final state is low, unless the two tunnel coupled energy levels are nearly degenerate. Thus, the upward sloping transition lines quickly lose intensity outside of the X-pattern region, where the tunneling energy levels become increasingly off-resonance.

The PL intensity also diminishes at lower and upper values of the bias voltage. At the limit of high bias (e.g., greater than -0.8 volts in Fig. 4.4), the electric field induced band bending causes negative charges to flood the QDMs and inhibits the formation of neutral excitonic states. In fact, we observe a series of negatively charged excitonic states towards the bottom left corner of the bias map, with states of increasingly negative charge extending sequentially to greater bias and lower energy values. At the low voltage limit, the PL intensity diminishes for a different reason (though this limit has not yet been reached in Fig. 4.4). Here, the electric field induced band bending makes it increasingly likely that negative charges will exit the QDM via incoherent tunneling (i.e., one-way tunneling) prior to radiative recombination of the

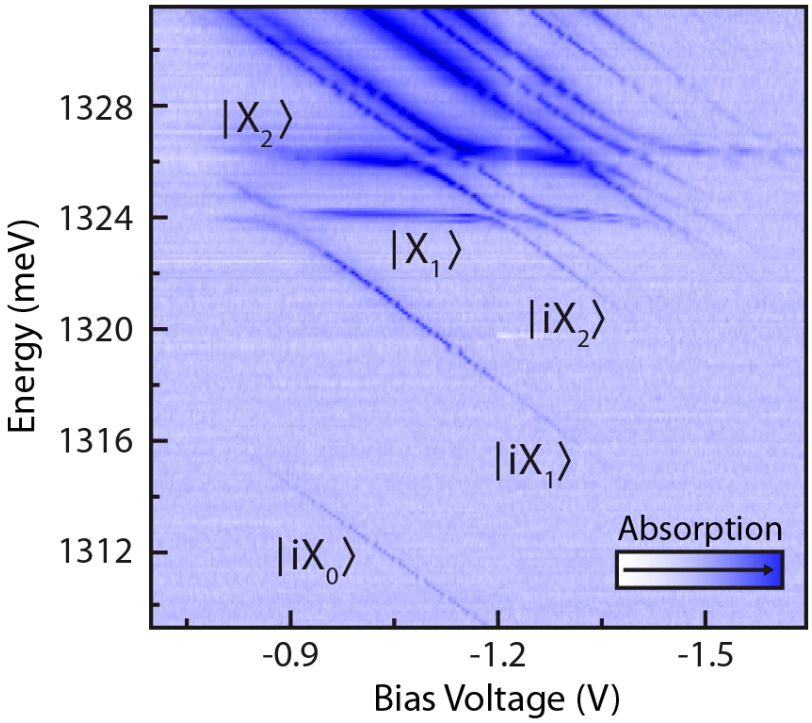

Figure 4.5: An example PLE bias map, generated from monitoring the neutral direct exciton transition for the QDM in Fig. 4.4. The PLE map displays the absorption into excited state energy levels that have decayed into the exciton ground state. The first several direct and indirect exciton levels have been labeled.

carriers.

PLE Bias Maps

A second visual data format used extensively in representing results in this dissertation is the PLE bias map. As discussed in section 4.1, the PLE bias map spectra is assembled from PL bias map spectra taken at different laser excitation energies by summing the PL intensity of a monitored metastable ground state transition. The intensity is summed over a narrow spectral range centered about the intensity maximum at each bias step. Like the PL bias map it is constructed from, the PLE bias map spectra is a two dimensional color scale plot of intensity as a function of applied bias and energy. In this case, however, it is the laser excitation energy that is plotted on the vertical axis. Unlike the PL bias map, the intensity of a PLE bias map corresponds to the absorption intensity of the excited state spectra and its relaxation into

the monitored transition.[2]

Figure 4.5 displays an example PLE spectrum that was generated by monitoring the direct exciton transition line for the QDM in Fig. 4.4. We can observe several direct and indirect excited state energy levels, with various hole tunneling anti-crossings taking place. Due to the much smaller quantum confinement energy of holes, the observable excited states are ones in which the hole state is excited. We may denote the states in terms of the type of exciton, with $|X_n\rangle$ for a single QD-like exciton with electron and hole in the same dot (here the bottom QD), or $|iX_n\rangle$ for an interdot exciton with the hole occupying the other QD (i.e., the top QD). The index n is used to indicate the number of the hole level in the respective dot, where '0' refers to the ground state level and '$n > 0$' to the nth excited state level. The lowest energy indirect state level in Fig. 4.5 corresponds to the indirect exciton ground state $|iX_0\rangle$, which anti-crosses with the direct exciton level $|X_0\rangle$ at an energy of about 1309 meV and bias value of about -1.25 V (see Fig. 4.4).

The PLE map in Fig. 4.5 displays a relatively low energy region, extending less than 25 meV above the monitored transition. In it, we observe an excited state spectrum consisting of discrete states only. In general, it is possible to extend the PLE map to regions of higher energy where continuum states appear, such as those corresponding to polaron or wetting layer states, for example.

Resonant Excitation and Phonon Satellite Acquisition

Finally, we describe a method for measuring the -1 phonon satellite emission line from a QDM using resonant PL spectroscopy.[3] This technique may be used to determine the emission energy of the LO phonons, providing information about the material into which the phonons are emitted.

To begin, we determine the zero phonon line energy of a transition for which we desire to measure the -1 optical phonon line. This is achieved by using ordinary non-resonant PL spectroscopy, as exemplified with the sample QDM shown in Fig. 4.6a. Next, the exciting laser is resonantly tuned to match the zero phonon line transition energy (e.g., the direct neutral exciton in Fig. 4.6a), meanwhile the center wavelength of the spectrometer is set to measure the energy of the -1 phonon satellite emission line. In our QDM samples, we measure a strong -1 phonon satellite at $\sim$36 meV

[2]If we choose to monitor the ground state neutral exciton, which recombines to the crystal ground state of the QDM, the resulting PLE spectra effectively yields an energy level diagram of excited states.

[3]The -1 phonon satellite emission line results from the relaxation of an excitonic state that occurs via the simultaneous emission of one photon and one phonon. The photon energy of the -1 phonon satellite is reduced from the zero phonon line emission energy (i.e., radiative relaxation without phonon emission) by an amount equal to the energy of the emitted phonon. Likewise, -2 (two phonon), -3 (three phonon), ... satellite emission lines may occur, each with a photon energy that is reduced by an amount equal to the total energy of the simultaneously emitted phonons.

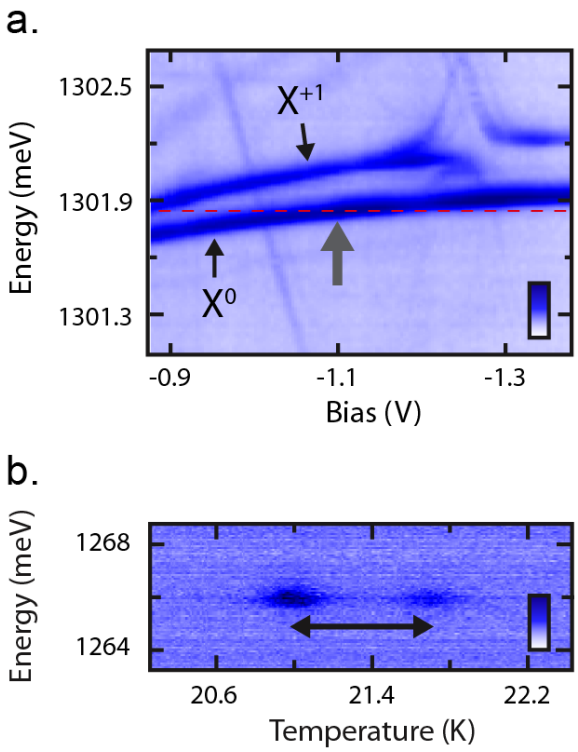

Figure 4.6: Method for measuring the −1 optical phonon satellite transition in a QDM. (a) The zero phonon line, here the direct neutral exciton transition, is characterized. (b) PL signal of the −1 LO phonon line collected while resonantly scanning the zero phonon line. The temperature was varied at a fixed bias value of −1.1 V (see grey arrow in (a)) and a fixed laser energy indicated by the red dashed line in (a). Further details are discussed in the main text.

below the zero phonon line, which corresponds to the LO phonon energy at the center of the Brillouin zone for GaAs. Since the LO phonon energy is quite large, it is easy to suppress the elastically scattered laser light with a long pass filter.

In order to resonantly excite the zero phonon line and collect the −1 phonon satellite signal, the laser must be made to finely scan through the excitonic state energy resonance. Fine scanning of the laser may be accomplished in a variety of ways. With a tunable laser that does not suffer too many mode hops, one can directly sweep the laser through the fixed transition energy. Alternatively, the transition energy may be scanned through the fixed laser by tuning a suitable parameter. In our samples, we can control the transition energy by using temperature controls to tune the band gap of the semiconductor or by applying an external bias voltage to Stark shift the energy of excitonic states.

Fig. 4.6b displays a −1 phonon satellite emission line signal that was collected by

stepping the temperature of the sample at a fixed bias value. For this QDM, the LO phonon energy is measured to be about 35.8 meV, yielding evidence that the phonon is emitted into the GaAs material rather than inside the InAs region of the QDM. The -1 phonon satellite, being a higher order process, is typically only observed when the laser is in exact energy resonance with the zero phonon line. This is a notable feature, as it provides a relatively simple mechanism for measuring the zero phonon line with laser line width limited resolution. In fact, observation of the -1 LO phonon satellite data in Fig. 4.6b reveals two separate intensity peaks occurring at slightly different temperatures. These correspond to the e-h exchange splitting of the bright direct exciton states. Converting the measured temperature difference into energy reveals an exchange splitting of about 23 μeV for this QDM. This small energy value is slightly below the resolution limit of our setup for ordinary PL spectroscopy, but is easily resolved in Fig. 4.6b.

Chapter 5

Perturbation Model of a QDM for Biexciton Transitions

In this chapter, we make use of the effective mass perturbation theory of I. V. Ponomarev introduced in Section 3.3 [49]. We begin by presenting a complete calculation of the biexciton states in a QDM according to the model. The computation is rather lengthy, so the complete result is given in Appendix B. We then consider the transitions from biexciton to exciton states and provide selection rules for the allowed transitions in the electric dipole approximation. These quantitative expressions for the biexciton states and their transitions are of general interest given the current proposals for using the biexciton-to-crystal ground state emission cascade in QDMs as a potential source of entangled photons [33, 34, 35].

We then use our model solutions to theoretically analyze a class of *dipolar* biexcitonic transitions, which occur for the biexciton states consisting of one exciton in each QD. These biexciton states differ from the neutral exciton state only in the presence of an additional exciton in the higher energy QD. Consequently, the transition energies of the indirect biexciton states are similar to that of the ground state exciton, but slightly shifted due to the weak dipole-like Coulomb interaction with the exciton in the other QD. Such transitions reveal the sensitivity of QDMs for detecting tiny charge separations and present another interaction mechanism that could potentially be used for shifting the ground state exciton transition energy or switching off its tunneling anti-crossing.

5.1 Biexciton States

Here, we calculate the biexciton states in a QDM according to the perturbation model. The biexciton states are formed from all possible configurations of two electrons and two holes occupying the spatially distinct QDs of a QDM. To satisfy the symmetriza-

tion requirement for fermions, we define the following spatial superposition states of two identical particles in separate QDs:

$$|(BT)^{\alpha}_{\pm}\rangle \equiv \frac{1}{\sqrt{2}}\big(|B^{\alpha 1}\rangle|T^{\alpha 2}\rangle \pm |T^{\alpha 1}\rangle|B^{\alpha 2}\rangle\big), \tag{5.1}$$

where $\alpha = e, h$ and the '$\pm$' sign is chosen such that the complete state (spatial and spin degrees of freedom) is anti-symmetric under the exchange of any pair of identical particles. The Pauli exclusion principle requires that two identical particles in a single QD pair up in a spin singlet configuration, so we may write the localized particle basis for two identical particles of type $\alpha = e, h$ in a QDM as follows:

$$\begin{aligned}\big\{&|B^{\alpha 1}\rangle|B^{\alpha 2}\rangle|\mathcal{S}^{\alpha}\rangle, |(BT)^{\alpha}_{+}\rangle|\mathcal{S}^{\alpha}\rangle, |(BT)^{\alpha}_{-}\rangle|\mathcal{T}^{\alpha}_{0}\rangle,\\ &|(BT)^{\alpha}_{-}\rangle|\mathcal{T}^{\alpha}_{-}\rangle, |(BT)^{\alpha}_{-}\rangle|\mathcal{T}^{\alpha}_{+}\rangle, |T^{\alpha 1}\rangle|T^{\alpha 2}\rangle|\mathcal{S}^{\alpha}\rangle\big\},\end{aligned} \tag{5.2}$$

where the kets $|\mathcal{S}^{\alpha}\rangle, |\mathcal{T}^{\alpha}_{0}\rangle, |\mathcal{T}^{\alpha}_{-0}\rangle, |\mathcal{T}^{\alpha}_{+}\rangle$ are the spin 1/2 singlet and triplet states for electrons and holes as defined in Section 3.3.[1]

All possible combinations of two electrons and two holes yield a biexciton basis of $6 \times 6 = 36$ states. This may appear unwieldy, but if we order the basis correctly, orthogonality of the spin states separates the matrix representation into ten uncoupled blocks: one 10×10 block, one 6×6 block, four 4×4 blocks and four 1×1 blocks. Still, the quantity of computations required to calculate the biexciton Hamiltonian matrix representation is large. Here, we outline the various terms in the Hamiltonian and then provide representative plots of the molecular eigenenergies. The complete calculation of the biexciton matrix representation is provided in Appendix B.

The biexciton Hamiltonian is obtained from equation (3.16) in Section 3.3 with $\alpha, \beta = e1, e2, h1, h2$ for the two electrons and two holes:

$$\hat{H}_{XX^0} = \hat{H}_{single\ particles} + \hat{H}_{Coulomb} + \hat{H}^{eh}_{exch}. \tag{5.3}$$

The single particle part of the Hamiltonian yields the localized particle energies along the main diagonal, as well as spin-conserving off-diagonal tunneling terms. Compared to the exciton, the biexciton tunneling terms acquire an additional factor of $\sqrt{2}$ since both identical particles may participate in tunneling. The complete biexciton single particle Hamiltonian is:

$$\hat{H}_{single\ particles} = \hat{h}^{e1}(\mathbf{r}_{e1}) + \hat{h}^{e2}(\mathbf{r}_{e2}) + \hat{h}^{h1}(\mathbf{r}_{h1}) + \hat{h}^{h2}(\mathbf{r}_{h2}). \tag{5.4}$$

The Coulomb part of the Hamiltonian produces corrections to the biexciton energies and tunneling rates, as well as tiny off-diagonal terms that describe simultaneous

[1] Recall that the hole spins form a pseudo-spin 1/2 system.

tunneling of two particles. The complete Coulomb operator of the biexciton Hamiltonian is:

$$\hat{H}_{Coulomb} = \frac{e^2}{4\pi\epsilon}\left(\frac{1}{|\mathbf{r}_{e1}-\mathbf{r}_{e2}|}+\frac{1}{|\mathbf{r}_{h1}-\mathbf{r}_{h2}|} - \frac{1}{|\mathbf{r}_{e1}-\mathbf{r}_{h1}|}-\frac{1}{|\mathbf{r}_{e1}-\mathbf{r}_{h2}|}-\frac{1}{|\mathbf{r}_{e2}-\mathbf{r}_{h1}|}-\frac{1}{|\mathbf{r}_{e2}-\mathbf{r}_{h2}|}\right), \tag{5.5}$$

where e is the elementary charge and ϵ is the average static dielectric constant of the QDM material.

The e-h spin exchange part of the Hamiltonian contains four terms, which are weighted by the delta function part of the operator according to the spatial location of the two spin carriers. The complete biexciton spin exchange operator, according to equation (3.19), is:

$$\hat{H}^{eh}_{exch} = A\big[\delta(\mathbf{r}_{e1}-\mathbf{r}_{h1})\hat{\sigma}^z_{e1}\hat{\sigma}^z_{h1}+\delta(\mathbf{r}_{e1}-\mathbf{r}_{h2})\hat{\sigma}^z_{e1}\hat{\sigma}^z_{h2} + \delta(\mathbf{r}_{e2}-\mathbf{r}_{h1})\hat{\sigma}^z_{e2}\hat{\sigma}^z_{h1}+\delta(\mathbf{r}_{e2}-\mathbf{r}_{h2})\hat{\sigma}^z_{e2}\hat{\sigma}^z_{h2}\big]. \tag{5.6}$$

To determine the eigenenergies of the biexciton states, we first need to calculate the matrix representation of the Hamiltonian $\hat{H}_{XX^0}$ in the localized particle basis. The complete calculation of the $\hat{H}_{XX^0}$ matrix representation is listed in Appendix B. From this result, we may determine the molecular eigenenergies of the biexciton states by diagonalizing $\hat{H}_{XX^0}$.

In Figure 5.1, we plot numerical solutions for all thirty-six of the biexciton molecular state eigenenergies. The QDM considered for this calculation consists of a 4 nm tall bottom dot and a 2.5 nm tall top dot, separated by a 4 nm tunneling barrier. The matrix element parameter values are the same as those used for the exciton eigenenergy plots in Fig. 3.8 of Section 3.3 and described in that section. There appear to be fewer states because many of the levels are either degenerate or nearly degenerate and cannot be resolved on this energy scale. Electron tunneling is observed to the left and hole tunneling to the right, though the hole tunneling anti-crossings are too small to be resolved at this scale (for an enlarged view of the hole-tunneling AC in the red boxed region in Fig. 5.1, see Fig. 5.2a).

The biexciton states reveal a variety of slopes in response to the applied electric field. The steepest slopes occur when the net charge in the top QD is $\pm 2e$, where the spatial separation of electrons and holes in separate QDs produces a maximum dipole moment. States with slopes half as steep as the maximum occur for spatial configurations in which the net charge in the top QD is $\pm e$. These biexciton states

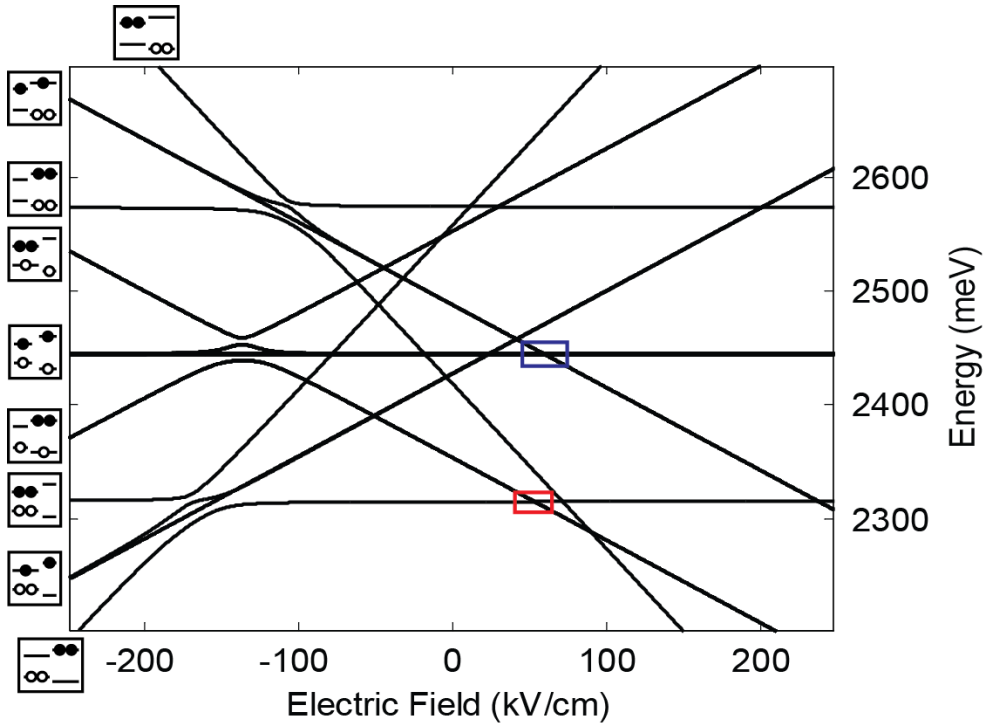

Figure 5.1: Numerical plots of the biexciton molecular eigenenergies of a QDM. Inset state diagrams label the localized particle spatial configurations of the states. The regions boxed in red and blue are enlarged to show greater detail in Fig. 5.2a and Fig. 5.4a, respectively. Further description of the biexciton energy levels is found in the main text.

have the same electric field dependence (i.e., same magnitude of slope) as the indirect exciton states. Additionally, we observe three sets of biexciton states, equidistantly spaced in energy, that show no dependence on the electric field. These correspond to biexciton states having two excitons in the bottom QD, one exciton in each QD and two excitons in the top QD, respectively, ranked from lowest to highest in energy. The spatial charge configurations of the localized particle states are labeled in Fig. 5.1 with inset state diagrams. We point out that the biexciton state with one exciton in each of the dots (i.e., the middle energy state with zero field dependence) allows for e-h exchange interactions that are absent from the other zero-slope states as a result of the Pauli exclusion principle. Even at the large energy scale of Fig. 5.1, the fine structure of this middle energy level is evident from the greater relative thickness of its line.

Selection Rules for Biexciton Transitions

The biexciton states optically transition to the exciton states when an electron recombines with a hole and a photon of commensurate energy is emitted. The transition energies are calculated as the energetic difference between the initial biexciton state and the final exciton state. The allowed transitions must satisfy optical selection rules that depend on the spin configuration of the excitonic states. In the electric dipole approximation, this can be understood in terms of conservation of angular momentum. A photon is a spin 1 particle, with possible angular momentum projections of $m = -1, 0, 1$. In order for angular momentum to be conserved when a photon is emitted, the initial and final excitonic states must satisfy the following selection rules: $\Delta l = \pm 1$ and $\Delta m = \pm 1$ or 0, where l, m indicate the quantum numbers for the total angular momentum and its projection along the z-axis for the complete excitonic state, including the spin angular momentum of the electrons and the spin and orbital angular momentum of the holes [68]. Since holes are derived from p-type orbitals in the valence band and electrons from s-type orbitals in the conduction band, the recombination of an electron-hole pair always satisfies the selection rule $\Delta l = -1$ for the total angular momentum. Thus, to determine whether a transition is allowed, it suffices to check the selection rule for the z-component of angular momentum.

Table 5.1: Allowed Biexciton Transitions

XX^0 Initial State		X^0 Final State		
Spin	m	Spin	m	Δm
$\lvert\uparrow\downarrow \pm \downarrow\uparrow\rangle \lvert\Uparrow\Downarrow \pm \Downarrow\Uparrow\rangle$	0	$\lvert\downarrow\Uparrow\rangle$ or $\lvert\uparrow\Downarrow\rangle$	$+1$ or -1	± 1
$\lvert\uparrow\downarrow \pm \downarrow\uparrow\rangle \lvert\Uparrow\Uparrow\rangle$	$+3$	$\lvert\uparrow\Uparrow\rangle$	$+2$	-1
$\lvert\uparrow\downarrow \pm \downarrow\uparrow\rangle \lvert\Downarrow\Downarrow\rangle$	-3	$\lvert\downarrow\Downarrow\rangle$	-2	$+1$
$\lvert\uparrow\uparrow\rangle \lvert\Uparrow\Downarrow \pm \Downarrow\Uparrow\rangle$	$+1$	$\lvert\uparrow\Uparrow\rangle$	$+2$	$+1$
$\lvert\downarrow\downarrow\rangle \lvert\Uparrow\Downarrow \pm \Downarrow\Uparrow\rangle$	-1	$\lvert\downarrow\Downarrow\rangle$	-2	-1
$\lvert\uparrow\uparrow\rangle \lvert\Downarrow\Downarrow\rangle$	-2	$\lvert\uparrow\Downarrow\rangle$	-1	$+1$
$\lvert\downarrow\downarrow\rangle \lvert\Uparrow\Uparrow\rangle$	$+2$	$\lvert\downarrow\Uparrow\rangle$	$+1$	-1

In Table 5.1, we display the spin configurations of the initial biexciton and final exciton states for which optical transitions are allowed. For simplicity, we specify the singlet and triplet spin states of electrons ($\uparrow, \downarrow$) and holes ($\Uparrow, \Downarrow$) with a simplified Dirac notation, stripped of additional bra-ket symbols and normalization factors. The first row of Table 5.1, for example, indicates that optical transitions are allowed for biexciton states in which the electrons and holes are in any combination of singlet or $m = 0$ triplet states (i.e., $|\mathcal{S}\rangle$ or $|\mathcal{T}_0\rangle$) and that these transitions end in bright

exciton states (i.e., $m = \pm 1$). From the table, we observe that all of the biexciton states are *bright* (i.e., they undergo optical transitions), except for the $m = \pm 4$ states (i.e., $|\uparrow\uparrow\rangle|\Uparrow\Uparrow\rangle$ and $|\downarrow\downarrow\rangle|\Downarrow\Downarrow\rangle$). The final exciton states, however, may be either bright ($m = \pm 1$ or dark ($m = \pm 2$), as indicated in the second column of Table 5.1. Consequently, applications which require an uninterrupted optical cascade from the biexciton state to the crystal ground state (e.g., entangled photon generation) must make use of the biexciton states that recombine to bright exciton states.

As an example of the model's applicability, we use it to fit the lowest energy biexciton X-pattern and neutral exciton transitions from the experimental data shown in Figure 4.4 of Section 4.3. We reproduce that experimental data set in Figure 5.2, along with a fit to the data using the perturbation model. Fig. 5.2a displays the energy levels of the initial biexciton (above) and final exciton (below) states that produce the X-pattern transition lines. The biexciton energy levels represent an enlargement of the region in Fig. 5.1 that is outlined in red. We have labeled the spatial charge configurations of the localized particle energy levels using inset state diagrams. Notice that one of the biexciton levels with negative slope passes straight through the biexciton hole tunneling resonance; it is a spin triplet state that is prevented from tunneling by the Pauli exclusion principle. We also point out the e-h exchange splitting of bright and dark direct exciton states, which shows up in the transition energies as a downward sloping doublet transition line in the biexciton X-pattern.

Several representative transitions from biexciton to exciton energy levels are indicated in Fig. 5.2a with red arrows. The allowed transition energies have been calculated from the model and are plotted in Fig. 5.2b. We observe that the fit is in quantitatively good agreement with the transition energies of the experimental data in Fig. 5.2c. We have not taken the PL intensities into account, however, which is noticeable when comparing the upward sloping transition line of the biexciton X-pattern between the model and the experimental data. Since this transition requires hole tunneling in the final exciton state, it is only likely to occur near a hole tunneling resonance. Accordingly, in the experimental data of Fig. 5.2c, this transition line fades out beyond the X-pattern region. In contrast, the modeled data in Fig. 5.2b is uniformly intense. We also point out that the experimental data includes additional transition lines from charge states that are not included in the biexciton model.

To model the data, we have measured the experimental energies labeled in Fig. 5.2c. The bright-dark splitting is given by $2J^{eh}$ and the hole tunneling energy by $|2t_h|$. For the Coulomb elements, we used the calculated transition energies from the model to form a set of linear equations. This set of equations is consistent and over-determined, so that infinitely many solutions always exist. The experimental measurements of ΔE_{XX0} and ΔE_{iXX0} (see Fig. 5.2c) can be related directly to combinations of the Coulomb matrix elements, and therefore provide sufficient inputs to solve the system of equations.

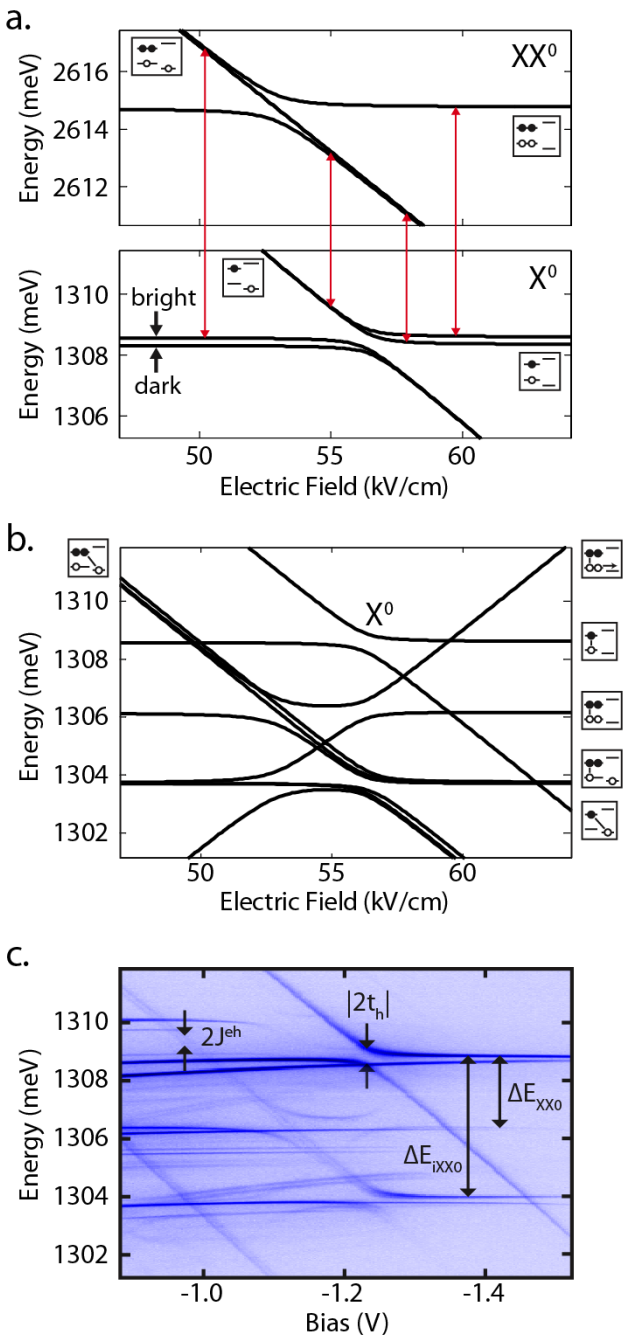

Figure 5.2: Model and experimental data of the biexciton and exciton ground state transition energies. (a) The biexciton (above) and exciton (below) molecular eigenenergies calculated from the model, with red arrows indicating representative transitions between initial and final states. (b) The corresponding transition energies computed from the model. (c) Experimental bias map data, showing the energies that were measured to fit the data to the model (see Fig. 4.4 in Section 4.3 for additional identification of the transitions).

5.2 Dipolar Biexciton Transitions

In this section, we examine the set of transitions that originate from the biexciton states with spatial configuration $|(BT)^e_\pm\rangle|(BT)^h_\pm\rangle$. That is, the biexciton states with a single exciton in each dot of the QDM. Since the two excitons in this state interact in a dipole-dipole like manner, we refer to this state and its transitions by the term *dipolar*. The dipolar transitions are interesting because of their similarity to the ubiquitous neutral exciton transition. They represent a weak, but detectable, coupling interaction between the two dots of a QDM. By adding an extra exciton to the higher energy dot, an exciton in the other dot experiences a slight shift in energy. Moreover, the usual particle tunneling observed in the exciton ground state may be inhibited if the carriers in the dipolar state form a spin triplet configuration.

To begin, we observe that the spatial biexciton state consisting of one exciton in each QD differs from the neutral exciton state only in the presence of an additional electron-hole pair in the higher energy dot. As such, we anticipate that the following biexciton and exciton transitions should be similar in energy:

$$\text{Biexciton:} \qquad |(BT)^e_\pm\rangle|(BT)^h_\pm\rangle \quad \longrightarrow \quad |T^e\rangle|T^h\rangle, \tag{5.7a}$$

$$\text{Exciton:} \qquad |B^e\rangle|B^h\rangle \quad \longrightarrow \quad |CGS\rangle. \tag{5.7b}$$

The energies of these transitions will generally not be identical, however, due to the presence of the top dot exciton in the $|(BT)^e_\pm\rangle|(BT)^h_\pm\rangle$ state, which produces additional Coulomb interactions that are absent in the $|B^e\rangle|B^h\rangle$ state. Since the top dot exciton is neutral overall, it produces a dipole-like electric field that generates a dipolar shift in the biexciton transition energy when the bottom dot exciton recombines.

The dipolar shifts in the transition energy of equation 5.7a are expected to be small. As an order of magnitude approximation, we may model the dipolar shift in a QDM as the interaction energy between two classical electric dipoles, as depicted in Figure 5.3. The classical dipole-dipole interaction energy for this configuration is given by the formula:

$$\Delta U = \frac{-2e^2}{4\pi\epsilon}\frac{a^2}{r^3}, \tag{5.8}$$

where e is the elementary charge, ϵ is the dielectric constant of the material, a is the effective dipole length and r is the effective dipole-dipole separation.[2] To approximate the dimensions of a QDM with a 6 nm tunneling barrier and two dots of height 2.5 nm, we set $a = 0.25$ nm and $r = 8.5$ nm. Using the average dielectric constant of InAs and GaAs ($\epsilon = 13.5\epsilon_0$), we calculate an interaction energy of $|\Delta U| \cong 20$ μeV.

[2]We use the symbol a to represent the dipole separation because the traditional symbol d is already reserved for the QDM tunneling barrier width.

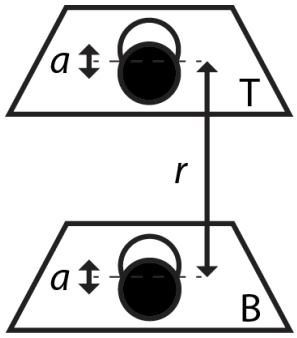

Figure 5.3: Model of the dipolar biexciton state $|(BT)^e_\pm\rangle|(BT)^h_\pm\rangle$ in a QDM as two classical electric dipoles of magnitude $|\mathbf{p}| = ea$, separated by a distance r.

To get a sense of this interaction strength, we may compare it to the monopole energy shifts of the trion transitions for a QDM with nominally the same dimensions. The transition from the positive trion state $|B^e\rangle|(BT)^h_\pm\rangle$, with an extra hole in the top dot, is typically shifted on the order of 200 μeV from the exciton transition of equation (5.7b), while the transition from the negative trion state with all charges in the bottom dot, i.e., $|B^{e1}\rangle|B^{e2}\rangle|B^h\rangle$, is shifted $5-7$ meV below the exciton transition [27]. Thus, based on this simple analysis, we expect the dipolar interaction to be comparatively weak.

To calculate the dipolar energy shift using the perturbation model, we compute the energy difference between the transitions in equations (5.7a) and (5.7b). Each of these spatial equations actually represents a multiplet of transitions between states with different spin configurations that satisfy the selection rules in Table 5.1.[3] For the biexciton states, all of the spin states are bright except for the two with total angular momentum projections of $m = \pm 4$. As for the exciton transitions in equation (5.7b), they originate from the bright exciton states as described in Section 3.3.

In order to more clearly identify the various biexciton levels, we first calculate the dipolar shifts using the approximate localized particle states. Simple analytical expressions for these states are given in Section 3.3 for excitons and Appendix B for biexcitons. Figure 5.4a shows a plot of these localized particle energy levels for the initial biexciton and final exciton states of the dipolar transitions as a function the applied electric field. The electric field range was selected to coincide with the hole tunneling anti-crossing of the ground state neutral exciton. In addition to the biexciton states with spatial configuration $|(BT)^e_\pm\rangle|(BT)^h_\pm\rangle$, we also include the downward sloping states with spatial configuration $|(BT)^e_\pm\rangle|T^{h1}\rangle|T^{h2}\rangle$, which in the molecular eigenstate solutions form superpositions with the dipolar states near the

[3]For this reason, we have not specified the exchange symmetry of the biexciton spatial kets in equation 5.7a. They depend on the particular spin configuration of the state.

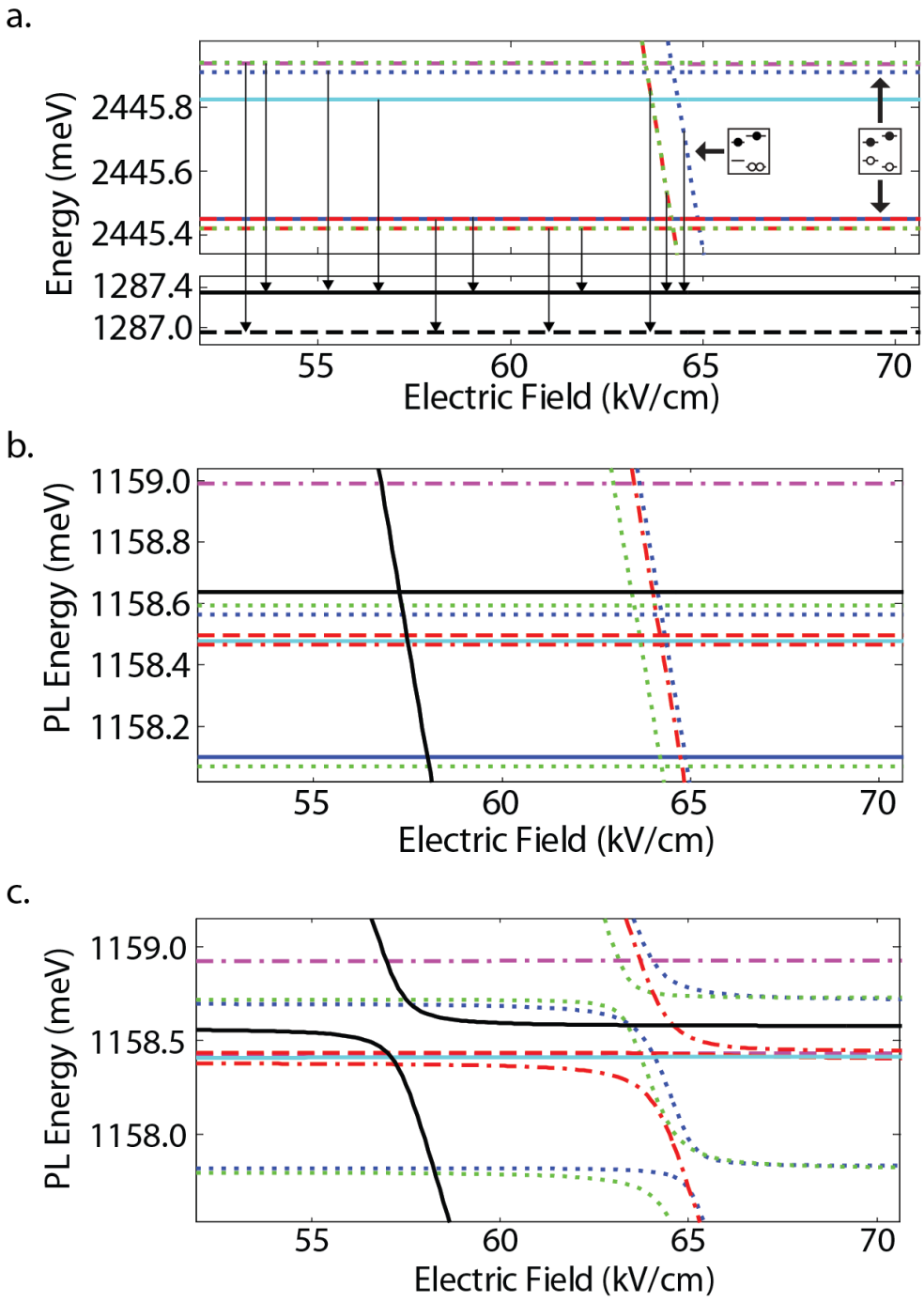

Figure 5.4: The dipolar biexciton transitions calculated from the perturbation model for a QDM with a 4 nm bottom dot, 2.5 nm top dot and 4 nm tunneling barrier. (a) Localized particle energy levels verses electric field of the initial biexciton states (above) and the final exciton states (below). Arrows indicate the allowed biexciton transitions to the bright (solid black line) and dark (dashed black line) exciton states. (b) Localized particle transition energies computed from (a). (c) The molecular transition energies. See main text for the significance of the different line styles.

hole tunneling resonance.

The dipolar biexciton states are shown in the top panel of Fig. 5.4a. In order to make sense of the numerous transitions, we have color-coded the biexciton energy levels according to the various sub-blocks of the biexciton Hamiltonian matrix to which they belong. The color coding is as follows: the levels from the 10×10 sub-block (i.e., states 1-10) are blue, the levels from the 6×6 sub-block (i.e., states 11-16) are green, the levels from the first and second 4×4 sub-blocks (i.e., states 17-20 and 21-24) are purple, the levels from the third and fourth 4×4 sub-blocks (i.e., states 25-28 and 29-32) are red, and the levels 35 and 36 from the last two 1×1 sub-blocks are light blue.[4] The exciton energy levels in the lower panel of Fig. 5.4a are colored black, with the bright exciton states indicated by solid lines and the dark exciton states by dashed lines. Likewise, the biexciton states that transition to bright excitons are shown with solid lines and those that transition to dark excitons are shown with dashed lines. Moreover, we identify the biexciton states in which one or both of the identical carriers are in a spin singlet state by dotted lines. The dashed-dotted lines indicate biexciton states that have a spin singlet configuration and that transition to dark exciton states.

It is important to distinguish the biexciton states with spin singlet configurations since these carriers are allowed to occupy the same QD. Carriers in spin triplet states, to the contrary, are prohibited from occupying a single QD by the Pauli exclusion principle. Consequently, the dotted (or dashed-dotted) biexciton states having a spin singlet configuration are less stable and shorter lived. They may relax to a lower energy state via carrier tunneling from the higher to lower energy QD. Biexciton states with both carriers in the spin triplet configuration are expected to be more stable because they require a spin flip in order for identical carriers to relax into the lower energy ground state.

The energetically distinct dipolar transitions between the biexciton and exciton states are indicated with black arrows in Fig. 5.4a. The dipolar biexciton states (i.e., those with zero-slope) are split into two bands by the e-h spin exchange interaction, which in this example amounts to $J^{eh}_{BBBB} \cong J^{eh}_{TTTT} \approx 400\ \mu$eV. Smaller splittings seen in Fig. 5.4a are due to Coulomb interactions. In Fig. 5.4b, we plot the corresponding transition energies verses the applied electric field. The same color and line coding scheme maps the transition energies to their initial and final states in Fig. 5.4a. The separation of the biexciton transitions among the bright and dark exciton states serves to disperse the energies of the direct transition lines to a band of about ± 0.5 meV about the direct neutral exciton transition (i.e., the solid black line in Fig. 5.4b). In addition, we also observe some negatively sloped transition lines that originate from

[4] In the absence of magnetic fields, there is a one-to-one energy degeneracy between the biexciton states of the 1st and 2nd 4×4 sub-blocks (i.e., states 17-20 and 21-24), the 3rd and 4th 4×4 sub-blocks (i.e., states 25-28 and 29-32), and the 1×1 sub-block states 35 and 36. For this reason, we have used the same colors for these sets of states.

the biexciton states with spatial configuration $|(BT)^e_\pm\rangle|T^{h1}\rangle|T^{h2}\rangle$. We point out that the solid blue, light blue and dashed red transition lines all originate from biexciton states in which both pairs of identical carriers are in spin triplet states. Consequently, they are not involved in particle tunneling.

The dipolar transition energies of the molecular eigenstates are plotted in Fig. 5.4c as a function of the applied electric field. They have been computed by numerical diagonalization of the biexciton and exciton Hamiltonian matrices. Compared with the localized particle states in Fig. 5.4b, we now observe hole tunneling anti-crossings in both the neutral exciton and the dipolar biexciton transitions, which occur at electric field values of about 57.5 kV/cm and 65 kV/cm, respectively. There are also two smaller anti-crossings of the dotted blue (at lower energy) and dotted green (at higher energy) transition lines that arise from e-h exchange coupling.

We are able to identify the spin configurations of the molecular transitions by comparing them with the localized particle transitions in Fig. 5.4b. In particular, we observe a nearly degenerate set of transitions less than 200 μeV below the direct neutral exciton transition that do not participate in tunneling anti-crossings. We identify these as states in which both pairs of identical carriers are in triplet spin configurations. We also point out that the solid blue level in Fig. 5.4b ($\sim$1158.2 meV), corresponding to the localized particle state $|(BT)^e_-\rangle|(BT)^h_-\rangle|\mathcal{T}^e_0\rangle|\mathcal{T}^h_0\rangle$ of the 10×10 sub-matrix, is seen to participate in a tunneling anti-crossing in Fig. 5.4c. This AC occurs because the triplet state $|(BT)^e_-\rangle|(BT)^h_-\rangle|\mathcal{T}^e_0\rangle|\mathcal{T}^h_0\rangle$ and the spin singlet state $|(BT)^e_+\rangle|(BT)^h_+\rangle|\mathcal{S}^e\rangle|\mathcal{S}^h\rangle$ hybridize via e-h exchange coupling in the molecular eigenstate solutions.

An enlarged view of the dipolar transitions near the neutral exciton anti-crossing is shown in Figure 5.5. We can easily resolve the three separate transitions from electron and hole spin triplet states. They are located slightly above 1158.4 meV in energy and do not participate in particle tunneling. Two of these arise from transitions to dark exciton states (red and purple) and one to the bright exciton state (light blue). In fact, each of these transitions is singly degenerate, so there are actually six different transitions that originate from electron and hole spin triplet states. We can identify them according to the localized particle biexciton states in Appendix B as follows: in purple are the degenerate states $|20\rangle = |(BT)^e_-\rangle|(BT)^h_-\rangle|\mathcal{T}^e_0\rangle|\mathcal{T}^h_-\rangle$ and $|24\rangle = |(BT)^e_-\rangle|(BT)^h_-\rangle|\mathcal{T}^e_0\rangle|\mathcal{T}^h_+\rangle$, in red are the degenerate states $|28\rangle = |(BT)^e_-\rangle|(BT)^h_-\rangle|\mathcal{T}^e_-\rangle|\mathcal{T}^h_0\rangle$ and $|32\rangle = |(BT)^e_-\rangle|(BT)^h_-\rangle|\mathcal{T}^e_+\rangle|\mathcal{T}^h_0\rangle$, and in light blue are the degenerate states $|35\rangle = |(BT)^e_-\rangle|(BT)^h_-\rangle|\mathcal{T}^e_+\rangle|\mathcal{T}^h_-\rangle$ and $|36\rangle = |(BT)^e_-\rangle|(BT)^h_-\rangle|\mathcal{T}^e_-\rangle|\mathcal{T}^h_+\rangle$.

We investigate the dependence of the dipolar shifts as a function of QDM dimensions in Figure 5.6, where we focus exclusively on the triplet states discussed in the previous paragraph. To compute the dipolar shifts, we have used the localized particle energy levels, which provide good accuracy for the triplet states since they do not participate in tunneling. The dipolar shifts are then calculated by subtracting the bright exciton transition energy from the dipolar state transition energies. Each

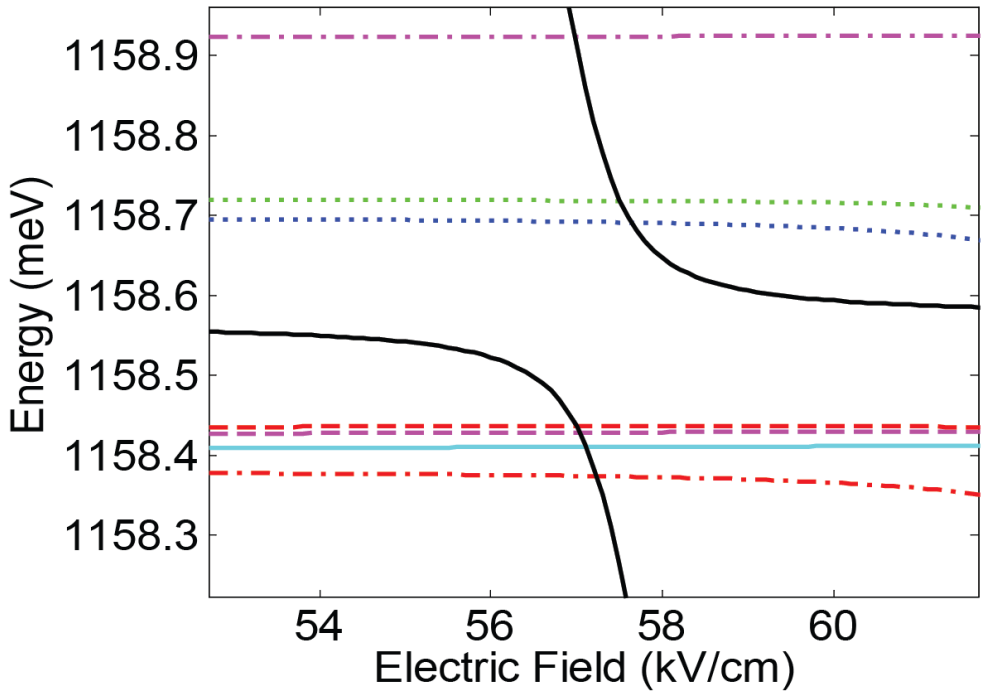

Figure 5.5: Enlarged view of Fig. 5.4c, showing the dipolar biexciton molecular transition energies as a function of the applied electric field. The solid black lines show the anti-crossing of the ground state exciton transition. The dashed red, dashed purple and solid light blue direct transition lines, positioned slightly above 1158.4 meV, represent the dipolar transitions from biexciton states in which both the electrons and holes occupy a spin triplet configuration and, therefore, do not participate in particle tunneling.

plot shows just two states, $|20\rangle$ and $|35\rangle$, since in the localized particle approximation the states $|20\rangle$, $|24\rangle$, $|28\rangle$ and $|32\rangle$ are all degenerate. Figure 5.6 reveals that the dipolar shifts for all of these states have a nearly identical dependence on the QDM dimensions.

In Fig. 5.6a, we plot the dipolar shifts as a function of the tunneling barrier width for a QDM with fixed bottom and top dot heights of 3.0 nm and 2.5 nm, respectively. The dipolar shifts are negative, indicating an attractive interaction between the two excitons in opposite dots. As is typical of a dipole-dipole like interaction, the magnitude of the dipolar shift is strongly dependent on the barrier width separating the two QDMs. At the smallest width of 2 nm, the dipolar shift has a magnitude of about 2 meV. However, it quickly approaches zero for barrier widths greater than 4 nm.[5] In relation to equation (5.8) of the classical dipole-dipole interaction, Fig.

[5]At a barrier width of 8 nm, the dipolar shift is below the 25 μeV resolution limit of our triple

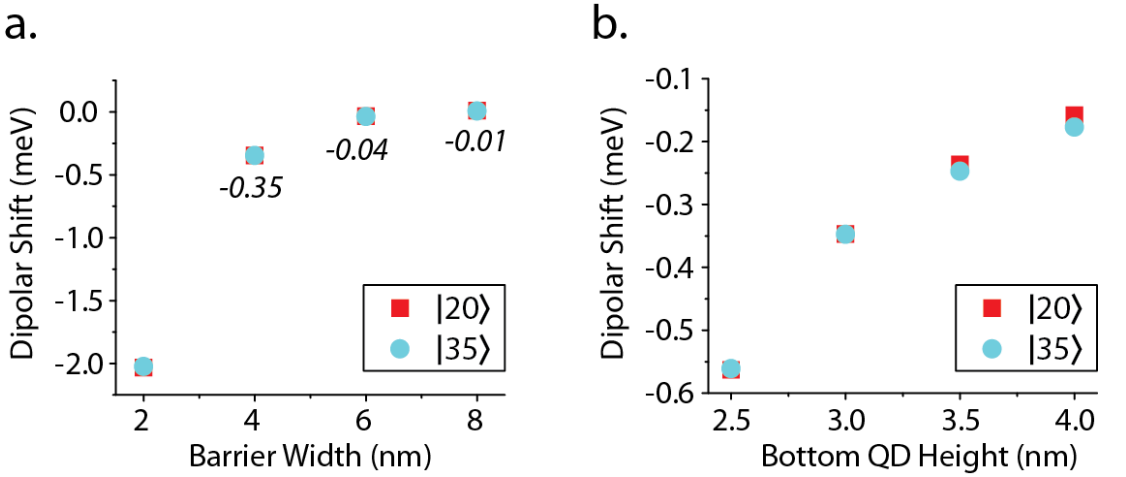

Figure 5.6: Dependence of the dipolar shifts of the electron and hole spin triplet transitions as a function of QDM size parameters. (a) Dipolar shift verses the tunneling barrier width. (b) Dipolar shift verses the bottom dot height. The dependence is nearly identical for both states shown.

5.6a effectively describes the dependence of the interaction energy on the separation r between the two electric dipoles. In this case, r is given by the effective distance $\bar{d} = d + (h_B + h_T)/2$ between the two excitons in the separate dots.

In Fig. 5.6b, we plot the dipolar shifts as a function of bottom dot height for a QDM with a fixed top dot height of 2.5 nm and a fixed barrier width of 4 nm. Similar to the result in Fig. 5.6a, we again observe a negative dipolar shift that approaches zero with increasing bottom QD height. Here, however, the magnitude of the dipolar shift does not change as rapidly as in the case where the barrier width was changed. We again seek to understand this behavior by considering the parameters of the classical dipole-dipole interaction in equation (5.8). Increasing the bottom dot height h_B clearly increases the dipole-dipole separation according to the equation $\bar{d} = d + (h_B + h_T)/2$. On the other hand, we might anticipate that the effective dipole length a could increase in a QD of greater height, which would result in a larger interaction energy. Judging by the trend in Fig. 5.6b, which shows a reduced interaction energy at increasing QD heights, it is the former effect that dominates. Thus, we can conclude that the excitonic dipole moment is relatively insensitive to the QD dimensions, at least in the perturbation model approximation. As a result, we may understand the dipolar energy shift trends in both Figures 5.6a and 5.6b as originating from the r dependence of the classical dipole-dipole interaction.

spectrometer. However, we can overcome this by searching for the dipolar transition in the region where the neutral exciton undergoes a hole tunneling anti-crossing.

Experimental Considerations for the Dipolar Biexciton Transitions

We have described the expected characteristics of the dipolar shifted transitions. However, experimental observation of these transitions will depend crucially on the intensity of the emission lines. As pointed out, charge carriers initially excited into the higher energy dot of a QDM typically under go rapid, non-radiative relaxation to the lower energy dot. Thus, one should focus on the dipolar states in which both electrons and holes form spin triplet configurations, since the Pauli exclusion principle inhibits these states from relaxing to a single QD. Nevertheless, tunneling out of the higher energy dot to an excited state of the lower energy dot remains a problem that is unsolved by the Pauli principle. Here, electron tunneling is likely to be the most problematic because the small electron effective mass increases the tunneling probability. In this case, our model suggests that it would be beneficial to work with QDMs with similarly sized top and bottom dots having small lateral diameters and a large tunneling barrier. The size symmetry of the QDs reduces the overlap of the electron ground state in the higher energy dot with excited states of the other dot, while the increased barrier width further inhibits electron tunneling.

A second challenge is the difficulty in identifying the ground state energy level of the higher energy QD, which is not typically observed in PL measurements because of (again) the ultrafast non-radiative relaxation out of this state. A possible method for observing this emission might be to employ a two laser excitation experiment. One laser could be resonantly tuned to the exciton transition in the lower energy dot, maintaining a population in that QD to reduce the likelihood of additional charges relaxing to it. Meanwhile, a second laser could be continuously tuned to search for the exciton transition in the higher energy dot.

Overcoming these technical challenges and gaining optical control over the dipolar biexciton states could allow several interesting possibilities for manipulating excitonic states in QDMs. For example, it could allow further investigations into the sensitivity of using QDMs for remote charge detection. It could also provide a mechanism for controllably shifting the ground state electron-hole recombination energy simply by generating a second exciton in the higher energy QD. Moreover, if the spin configuration of the dipolar states could be controlled, this could provide a mechanism for selectively inhibiting particle tunneling in the exciton state.

Chapter 6

The Quantum Confined Stark Effect in QDMs

In this chapter, we examine the electric field dependence of direct and indirect exciton transition energies in QDMs as a function of the tunneling barrier between separate QDs. The phenomena of electric field dependent energy shifts in quantum confined structures is known as the quantum confined Stark effect (QCSE). Previously in Section 3.3, we modeled the QCSE of excitonic state energy levels in a QDM as being linearly proportional to the net charge in the upper dot of the QDM. With this behavior, we underscored a key advantage of QDMs compared to QDs - the ability to tune the indirect exciton energy over a wide range of values simply by controlling an externally applied electric field.

In reality, the above description is a rather course approximation of the actual QCSE observed in real QDMs. We find experimentally that the QCSE is not entirely linear for indirect excitons, nor is it zero for direct excitons. A general mathematical description of the QCSE, applicable to both direct and indirect exciton states, expresses the field-dependent energy shifts as the sum of linear and quadratic responses to the applied electric field. These individual terms are closely related to the classical concepts of static electric dipole moment and electric polarizability. Consequently, we use these terms to characterize the charge distribution of an exciton state and its response to an externally applied electric field.

Our data results reveal that the QCSE of the indirect excitons is predominantly linear due to the large static dipole moment that occurs when the charge carriers are located in separate QDs, consistent with our approximate treatment in Section 3.3. For the direct excitons, the QCSE is much reduced in magnitude and displays a strongly quadratic dependence on the electric field. Interestingly, we find that the QCSE of single QD-like direct excitons in QDMs differs in certain respects from the behavior observed for excitons in single QDs. In particular, the dipole moment of direct excitons in QDMs is found to have opposite polarity in comparison to excitons

in single QDs. Moreover, we find that the magnitudes of the static dipole moment and the polarizability of direct state excitons in QDMs diverge increasingly from the single QD values at decreasing tunneling barrier widths. By modeling the QDM as a set of coupled potential wells, we are able to explain this behavior in terms of molecular wavefunction formation in QDMs. As a result, we show that molecular wavefunctions produce measurable effects for direct and indirect exciton states far away from any tunneling resonances.

6.1 Theoretical Description of the QCSE

The Stark effect is well known from atomic and molecular physics, where it describes the general shift in energy levels in response to an applied electric field. In quantum confined systems, the QCSE often results in energy shifts of much greater magnitude because the strong confinement potentials offer protection against field-ionization at large electric field strengths [53]. The energy dependence of an exciton in the presence of an applied electric field, whether in a direct or indirect spatial configuration, may be described by the following quadratic equation:

$$\varepsilon(F) = \varepsilon_0 - pF - \beta F^2, \tag{6.1}$$

where F is the externally applied electric field directed along the QDM growth axis. The energy of the exciton at zero field is equal to ε_0 and the coefficients p and β describe the linear and quadratic dependence of the exciton energy, respectively, as a function of the applied electric field. Equation (6.1) is equivalent to the exciton transition energy, since all exciton transitions end in the common crystal ground state.

We may interpret equation (6.1) in close analogy with classical electromagnetic theory. A classical electric dipole in an external electric field gives rise to an electrostatic energy in the amount of $\Delta\varepsilon = -pF$, where p represents the dipole component in the direction of F. As a result, we may interpret the coefficient p in (6.1) as the permanent electric dipole moment of the exciton along the QDM growth axis. We write this permanent dipole moment as $p = ea$, where e is the elementary charge and a is the dipole separation. In the case of an exciton in a QDM, a describes the zero field separation between the centers of mass of the electron and hole wavefunctions along the vertical growth axis of the QDM. By definition, a is directed from negative to positive charge. In our QDM samples, the positive field direction is defined to run from the bottom to the top QD. Consequently, a positive value of p in equation (6.1) implies that the center of mass of the hole wavefunction lies above that of the electron at zero electric field.

The coefficient β of the quadratic term in equation (6.1) is related to the polarizability of the exciton state. Classically, a charge distribution may become polarized

in the presence of an external electric field. This polarization results in an induced dipole moment that is linearly proportional to the field for small field values, and generates an electrostatic energy shift that is proportional to the square of the electric field [69]. As a result, we may interpret β as the shift in the center of mass positions of the electron and hole wavefunctions along the QDM growth axis in response to the applied electric field. Since polarization-induced energy shifts always decrease the electrostatic energy of the system, β as defined in equation (6.1) is necessarily a non-negative number.

The dipole moment and polarizability together determine the electric field value at which the exciton energy is maximum. To see this dependence more clearly, we may re-write equation (6.1) by completing the square to yield:

$$\varepsilon(F) = \left(\varepsilon_0 + \frac{p^2}{4\beta}\right) - \beta\left(F + \frac{p}{2\beta}\right)^2. \tag{6.2}$$

In this form, we observe that the maximum exciton energy of $\varepsilon_0 + p^2/4\beta$ occurs at the field value $F = -p/2\beta$. With β always positive, equation (6.2) implies that a positive dipole moment p translates the maximum energy to the left of the origin, while a negative p translates the maximum towards the right. In both cases, the maximum exciton energy is translated further from the origin as the magnitude of p/β increases.

The maximum exciton energy of $\varepsilon_0 + p^2/4\beta$ occurs at the electric field value for which the net dipole moment of the exciton vanishes. At this point, the electron and hole wavefunctions have the same center of mass positions along the QDM growth axis. The net dipole moment $\mu_{net}(F)$ of the exciton, defined as the sum of the static and induced dipole moments at a given field value, is related to the derivative of the exciton energy in (6.1) according to the equation:

$$\mu_{net}(F) \equiv p + 2\beta F = -\frac{d\varepsilon(F)}{dF}. \tag{6.3}$$

From this equation, we observe that the permanent electric dipole moment p may be computed as the negative of the energy slope at zero electric field. In addition, by taking the second derivative of equation (6.1), we may compute the polarizability β of the exciton state from the curvature of the exciton energy.

6.2 Experimental Dependence of the QCSE on Tunneling Barrier Width

In this section, we analyze experimental data of the QCSE measured for QDMs with tunneling barrier widths ranging from 2 to 6 nm. The experimental results were obtained by our collaborators at Ohio University using QDM samples fabricated for

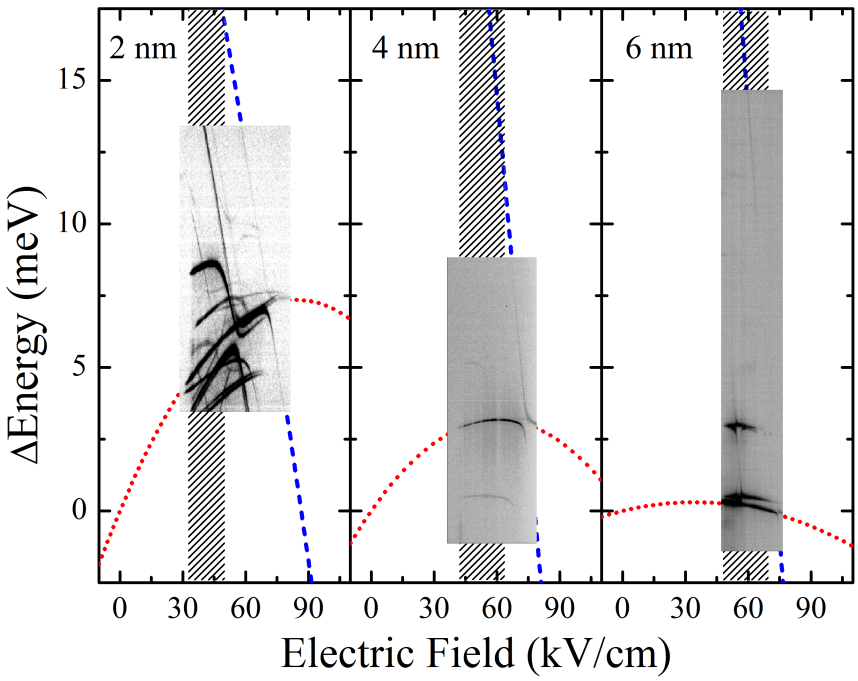

Figure 6.1: Three example data sets showing electric field dispersed PL energies of QDMs with 2, 4, and 6 nm tunneling barrier widths. The exciton transition lines have been identified and fit to the quadratic equation in (6.1). Expanded plots of the fits are shown for the direct (red dotted lines) and indirect (blue dashed lines) exciton states. The energy shifts have been referenced to the extrapolated value of the direct exciton energies at zero electric field. The shaded background areas highlight the regions where the direct exciton fits were done.

hole tunneling at the Naval Research Laboratory and described in Chapter 2. The samples were cooled to 10 K inside a cryostat and excited non-resonantly with a Ti-sapphire laser. PL spectra from the QDMs was then collected for a range of electric field values and plotted in the form of PL bias maps [36].

We present in Figure 6.1 representative PL bias map data collected from QDMs with barrier widths of 2, 4 and 6 nm. The direct and indirect exciton transition energies for each QDM have been extracted to determine best fits to equation (6.1). The resulting fits have been plotted in Fig. 6.1 and are in good agreement with the experimental data. As anticipated, the indirect transition lines show a predominantly linear dependence on the applied electric field, with steeper slopes occurring for QDMs with greater tunneling barrier widths. The QCSE of the direct excitons is by comparison greatly reduced in magnitude and displays a more prominent curvature, which indicates a significant quadratic contribution to the field-dependent energy shifts. As the

barrier width is increased from 2 to 6 nm, we observe that the experimental slopes of the direct exciton transition energies change from positive to negative, indicating a reversal of the electron and hole center of mass positions along the QDM growth axis. Equivalently, this corresponds to a reversal of $\mu_{net}(F)$ in the range of experimental electric field values.

To illustrate the experimental trends of the QCSE as a function of the QDM barrier width, we plot in Figure 6.2 the average quadratic fits of the direct and indirect exciton transition energies for barrier widths of 2, 4 and 6 nm. Each fit is derived from the average QCSE of at least four QDMs within the shaded region. To avoid any non-quadratic line shift effects due to hole anti-crossings, we have only fit data points where the energy separation between the direct and indirect exciton lines is at least a factor of five greater than the hole AC splitting energy. For clarity and to help visualize the data trends, all energies have been vertically shifted to coincide at zero electric field and the plots have been expanded beyond the shaded experimental range.

We first analyze the direct exciton transitions. The data in Fig. 6.2 reveals that the maximum exciton energy shifts towards the right, to greater electric field values, as the barrier width is decreased. According to equation (6.2), this trend is a consequence of the permanent electric dipole moment p becoming increasingly negative at smaller barrier widths, as indicated by the slope of the direct exciton transition line at zero electric field. Physically, this result implies that the center of mass of the electron wavefunction is located above that of the hole along the QDM growth axis (i.e., $a < 0$). As the barrier width is decreased, the center of mass of the electron wavefunction moves further above that of the hole and the effective separation between the charge carriers increases. In addition, the direct exciton polarizability is observed to increase with decreasing tunneling barrier width, as indicated by the curvature of the transition lines.

To gain additional insight into the origin of the observed barrier width dependence of the QCSE for direct excitons, we compare our results with the QCSE observed for excitons in single QDs. Fry, et. al., measured a negative energy slope for excitons in single QDs at electric field values in the range of our experimental data. The negative slope of the QCSE for single QD excitons implies a positive value of p, with the hole wavefunction center of mass lying above that of the electron in the direction of the growth axis. This result was initially unexpected, but could be explained if the single QDs had a graded $In_{1-x}Ga_xAs$ composition with higher In concentration toward the top of the QD, which occurs with QDs that are truncated using the indium-flush technique [70]. Interestingly, though our QDM samples are comprised of individual QDs truncated in a similar manner, the polarity of the permanent electric dipole moment p is opposite for the single QD-like direct excitons in comparison to excitons in single QDs.

We have plotted the result of Fry, et. al., alongside our QDM data in Fig. 6.2. The

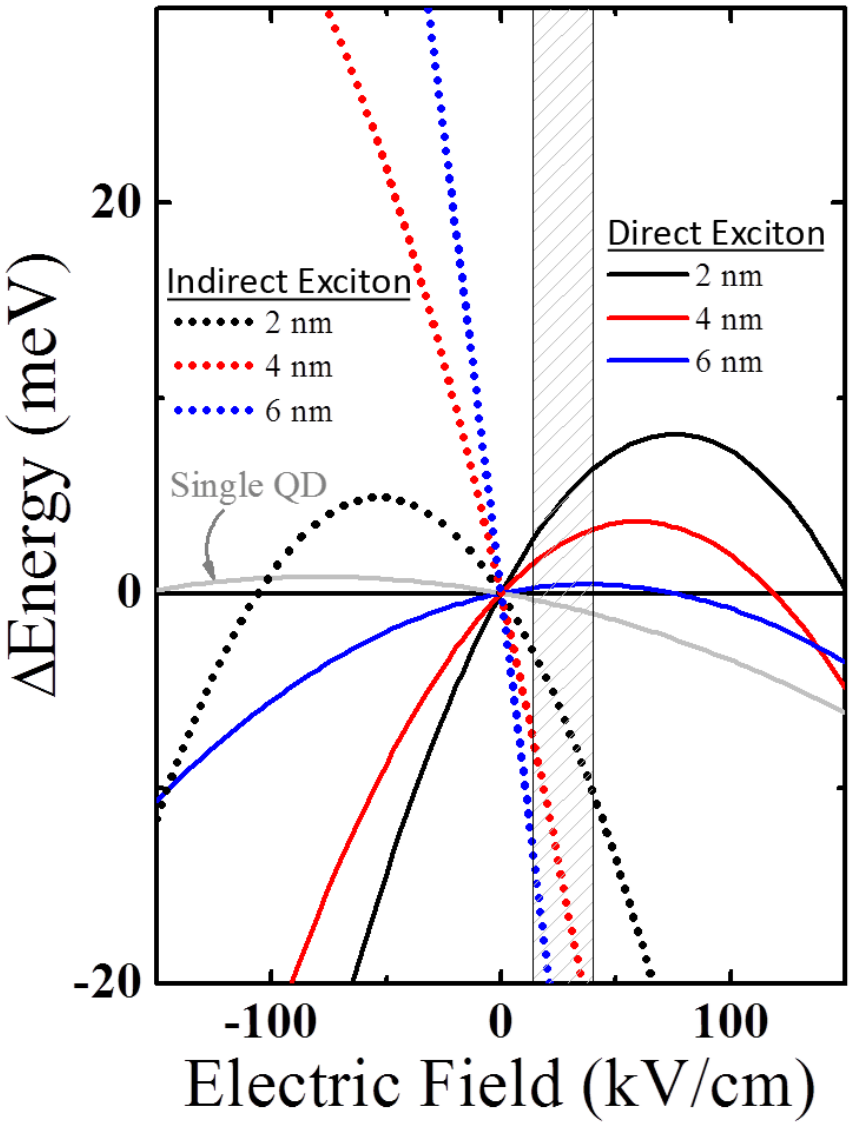

Figure 6.2: Plot of the average quadratic fits of the QCSE for direct (solid lines) and indirect (dotted lines) excitons from QDMs with barrier widths of 2, 4 and 6 nm. The average QCSE of single QD excitons is shown for comparison. To help visualize the trends, all exciton energies have been vertically shifted to coincide a zero electric field and the plots have been expanded beyond the experimental shaded region. Details of the dependence of the QCSE on barrier width are given in the main text.

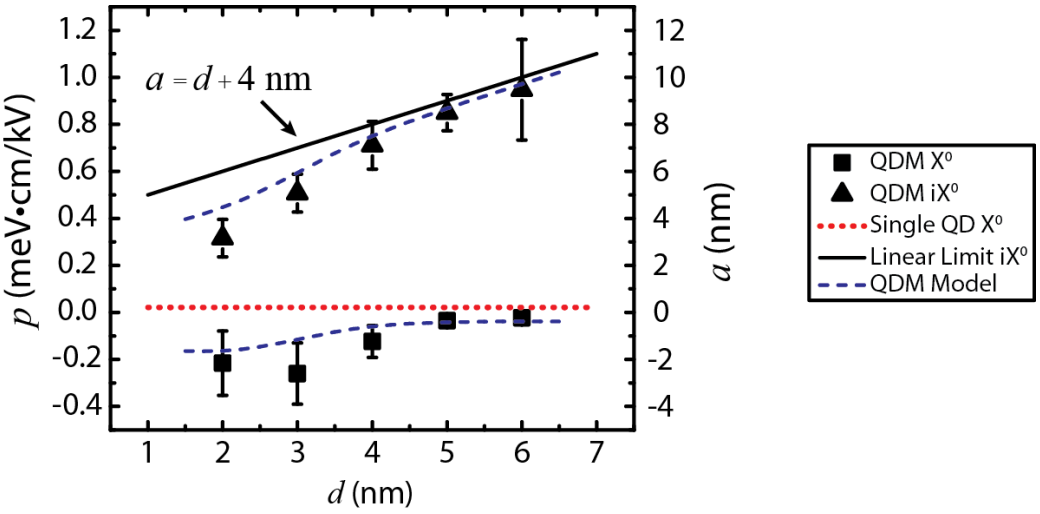

Figure 6.3: Plots of the average permanent dipole moment p and the effective dipole separation a for direct and indirect excitons as a function of barrier width d. The values correspond to the curves in Fig. 6.2. The permanent dipole moment of the direct excitons is compared with the value measured for excitons in a single QD from Ref. [70]. The solid black line represents the linear dependence of a versus barrier width for the indirect excitons according to the model of Section 3.3. The dashed blue curves are derived from a tight-binding model of a simple asymmetric coupled square well potential. Error bars represent the standard deviations of the statistical samples for p.

data results reveal that the QCSE of the direct excitons approach the single QD limit as the barrier width is increased, as we would expect. Of course, as mentioned above the sign of the permanent dipole moment p of the direct excitons and the excitons in single QDs is reversed. In addition, we observe that the magnitudes of both p and the polarizability β of the direct excitons diverge from the single QD values as the QDM barrier width is decreased. This behavior is further illustrated in Figures 6.3 and 6.4, where we plot the parameter values of p and β, respectively, that were used to generate the average plots in Fig. 6.2. Given the structural similarity of the individual QDs comprising our QDMs and the single QDs investigated by Fry, et. al., it seems likely that the diverging trends in the QCSE of the direct excitons may be related to the tunneling barrier and additional QD present in QDMs. In fact, we will show that these effects may be understood in terms of the formation of delocalized molecular wavefunctions across the two dots comprising the QDM.

To summarize our results of the QCSE for direct excitons, we find that the measured net dipole moments $\mu_{net}(F)$ lead to center of mass separations for the electron and hole of up to ~ 0.71 nm, which is maximum for QDMs with the smallest tunnel-

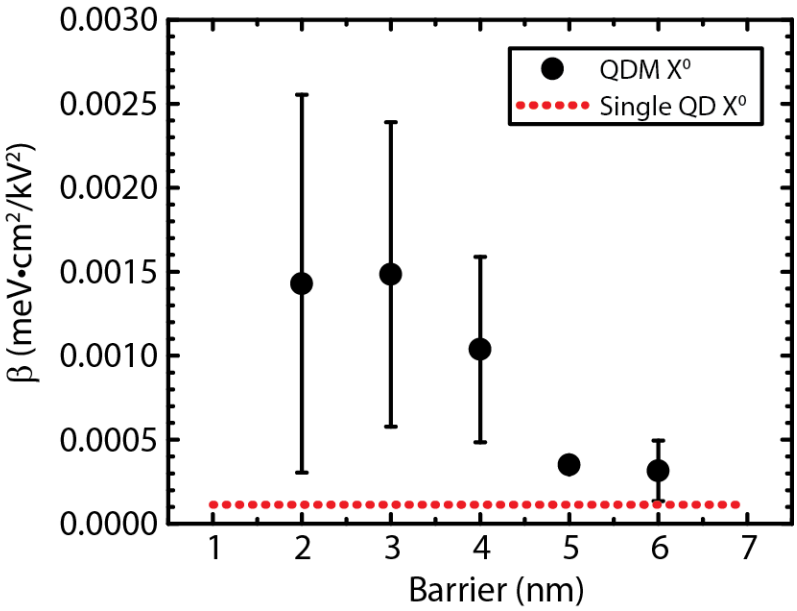

Figure 6.4: Plots of the average polarizability β of direct excitons in a QDM as a function of barrier width. The values correspond to the curves in Fig. 6.2. The polarizability of the direct excitons is compared with the value measured for excitons in a single QD from Ref. [70]. Error bars represent the standard deviations of the statistical samples for β.

ing barrier widths. Moreover, we observe a maximum tunable PL energy of ~ 2 meV for direct excitons in the range of electric field values for which emission is visible. This corresponds to an energy tuning range that is three orders of magnitude larger than the homogeneous line width of the direct exciton.

We now analyze the QCSE for the indirect excitons. As noted before, the plots in Fig. 6.2 reveal a predominantly linear QCSE for the indirect excitons. This result was anticipated since the indirect excitons have a large permanent dipole moment p, whose separation is on the order of the tunneling barrier width plus half the heights of the constituent dots that form the QDM, i.e. $a \cong d + 1/2\,(h_B + h_T)$. We plot in Figure 6.3 the average value of p as a function of the barrier width, taken from the indirect exciton energy curve fits in Fig. 6.2. Due to the large linearity of the indirect exciton energies, unconstrained fits of the data to equation (6.1) are inconclusive. Consequently, we have fixed the polarizability of the indirect excitons to have the same values as those of the direct excitons in Fig. 6.4. The resulting fits yield values of p that are in good agreement with the purely linear field-dependence assumed in the simple model. The linear model is indicated by the solid black line in Fig. 6.3, which plots the separation $p/e = a$ of the permanent dipole moment as a function of the

barrier width d. For the QDMs studied, both dots have nominal heights of 4 nm, so the effective dipole separation as a function of d is given by $a(d) = d+4\,\text{nm}$. Nevertheless, for small barrier widths the observed value of p begins to diverge below the linear limit. We show that this departure may again be understood as a consequence of the formation of electron and hole molecular wavefunctions in QDMs.

To summarize our results of the QCSE for indirect excitons, we observe a maximum tunable energy of ~ 20 meV in the range of electric field values for which emission is visible. The maximum tunability is observed for QDMs with the largest tunneling barrier widths, in this case 6 nm. The $\sim$20 meV tuning range for indirect excitons represents an order of magnitude increase over the range observed for direct excitons.

6.3 The Impact of Molecular Wavefunction Formation on the QCSE in QDMs

The observed trends in the QCSE of the direct and indirect excitons may be qualitatively understood in terms of the formation of electron and hole molecular wavefunctions in QDMs. In particular, we seek to explain the following observations: (i) the opposite polarity of the permanent electric dipole moment p of the single QD-like direct excitons compared to excitons in single QDs, (ii) the increased magnitudes of both p and the polarizability β for the direct excitons at decreased barrier widths, which diverge from the single QD limits, and (iii) the deviation of p for the indirect excitons from the linear model at small barrier widths. By modeling the QDM as a set of coupled potential wells, we obtain solutions in the form of symmetric and anti-symmetric molecular wavefunctions for both the electrons and holes. The spatial distribution of the solutions depends sensitively on the QDM barrier width and the carrier effective masses. In particular, the electron wavefunction is able to penetrate the QDM tunneling barrier to a far greater extent than the hole wavefunction due to their difference in effective masses. This different behavior for the electron and hole molecular wavefunctions, which becomes heightened at small barrier widths, provides an explanation for the observed trends in the QCSE of direct and indirect excitons in QDMs.

We model the QDM as a set of two 1D asymmetric potential wells coupled by a tunneling barrier of variable width. The QD asymmetry, in this case with greater quantum confinement for the upper dot, assures that the electron and hole energy levels in separate dots will be off-resonance at zero electric field. To compute the carrier wavefunctions in the QDM, we use a linear combination of the localized particle wavefunctions in the bottom and top QDs, i.e., a tight-binding approach. Our collaborators from Ohio University have calculated numerical solutions to this model

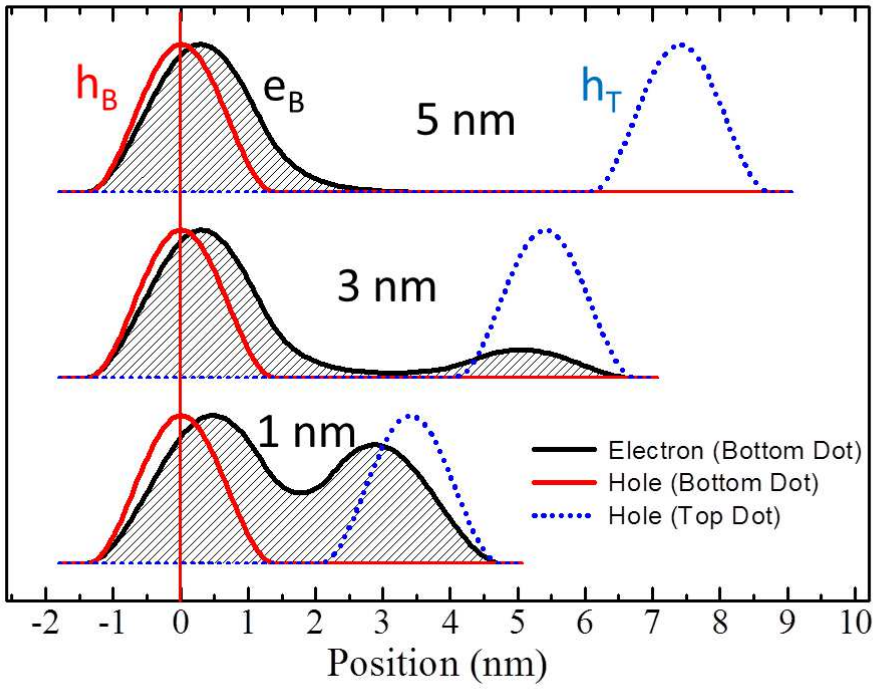

Figure 6.5: Zero-field probability distributions of the lowest energy hole states in the bottom (red) and top (blue) dots and the lowest energy electron states in the bottom dot (black with grey shading) for QDMs with tunneling barrier widths of 1, 3 and 5 nm. The probabilities are from solutions to a 1-dimensional discretized Schrödinger's equation for a QDM modeled as two 1D asymmetric potential wells coupled by a tunneling barrier of variable width. The electron's order of magnitude smaller effective mass leads to greater delocalization of the electron probability distribution at small barrier widths compared to the hole. The positions are plotted relative to the hole in the bottom dot to highlight the effective mass dependent shifts.

using the discretized Schrödinger's equation, which are plotted in Figure 6.5. The parameters of the model were chosen to be consistent with the sample structure. In particular, the electron effective mass was an order of magnitude less than the hole effective mass and the barrier potential was chosen such that the ratio of the tunneling energy to confinement energy was the same order as the experiment [36].

The plots in Fig. 6.5 show the zero-field probability distributions of the lowest energy hole states in the bottom (red) and top (blue) dots and the lowest energy

electron states in the bottom dot (black with grey shading) for QDMs with tunneling barrier widths of 1, 3 and 5 nm. The solutions exhibit molecular wavefunction character, consistent with our description in Section 3.3. Notably, we observe that the weighting of the molecular wavefunctions across the bottom and top dots, as a function of the barrier width, differs for electrons and holes. At the greatest barrier width of 5 nm, both the electron and hole states are highly localized within single QDs and hardly penetrate the tunneling barrier. As the tunneling barrier width is reduced, the hole states remain well localized. The electron probability distribution, on the other hand, increasingly penetrates the tunneling barrier and leaks into the upper dot. At the smallest tunneling barrier width of 1 nm, we observe the electron state to be almost evenly distributed across both dots of the QDM.

The different behavior of the electron and hole states in Fig. 6.5 results from the sensitive dependence of the particle tunneling probability on both the barrier width and the carrier effective mass. It is known that the tunneling probability decays in roughly exponential proportion to both of these quantities [68]. Since a greater tunneling probability leads to increased delocalization of the molecular wavefunctions across the QDM, these wavefunctions become increasingly delocalized at reduced tunneling barrier widths. The increased delocalization is markedly greater for electrons, however, since their effective mass is an order of magnitude smaller than that of the holes. Consequently, we observe a movement of the electron center of mass towards the top of the QDM in Fig. 6.5 as the tunneling barrier width is decreased. The hole wavefunctions, on the other hand, show no appreciable variation.

The different response of the electron and hole molecular wavefunctions versus tunneling barrier width provide an explanation for the observed trends in the QCSE of excitons in QDMs. We can conclude that the permanent dipole moment of the direct excitons is negative because of the propensity for the electron molecular wavefunction to leak into the top dot. As the tunneling barrier width is reduced, the electron molecular wavefunction tunnels further into the top dot and p becomes increasingly negative, in agreement with the experimental data in Fig. 6.3. For single QDs with no top dot to tunnel into, the electron wavefunction is concentrated towards the bottom of the QD and the polarity of p is reversed.

In the same way, we can understand the deviation of the permanent electric dipole moment of the indirect excitons from the linear model seen in Fig. 6.3. As the barrier width is decreased, the electron molecular wavefunction leaks increasingly into the top dot. This reduces the experimental value of p in comparison to the linear model, which considers the charge carriers to remain rigidly fixed within their respective dots.

Finally, we explain the dependence of the direct exciton polarizability β as a function of tunneling barrier width. As seen in Fig. 6.4, β is observed to increase as the tunneling barrier width is decreased. This results from the increased tunneling probability of the electron, which increases its mobility within the QDM. Thus, at

small tunneling barrier widths, the electron is able to respond to an applied electric field with greater mobility, thereby enhancing the overall polarizability of the exciton state.

To validate the qualitative understanding provided by the model, p has been computed for both the direct and indirect excitons as a function of the tunneling barrier width. The value of p is determined from the effective dipole separation a at zero field, which is computed from the model as the difference between the centers of mass of the electron and hole molecular wavefunctions. The values of p obtained in this manner are plotted as blue dashed lines in Fig. 6.3. The model values are seen to be in good agreement with the experimental data. Thus, we conclude that molecular wavefunctions in QDMs have a measurable impact on the quantum confined Stark effect, even as the two constituent QDs are off-resonance for particle tunneling.

Chapter 7

Phonon-induced Transparency and Fano Interference in QDMs

In the study of solid state nanostructures, electronic excitations coexist alongside the dynamical vibrations of the underlying crystal lattice. These phonons and electronic excitations interact and influence one another. In the past, phonons have often been considered a nuisance because they can destroy the quantum coherence of electronic and spin states in quantum confined systems [79, 61, 80]. As such, researchers have often sought to minimize the influence of phonons.

Recently, however, there is a growing interest in utilizing phonons as a technological resource in semiconductor nanostructures. In the field of optomechanics, for example, phonons provide utility as a mechanism for mediating the coupling of electronic states in quantum dots to photonic cavity modes [89, 90]. This emerging field of phononics represents a new paradigm in which phonons are being viewed not as a limitation, but as an additional resource that may be developed to provide coherent control in semiconductor nanostructures [71, 72, 73].

In this chapter, we report a mechanism by which these phonons are made non-dissipative and coherent via electric field control and the optically driven formation of a novel hybrid state, the *molecular polaron*, in a QDM [37]. An induced optical transparency, the result of a Fano-type resonant quantum interference, reveals the molecular polaron and its coherent nature. Experimentally, we observe absorption spectra characteristic of Fano effects with all different values of q_{Fano}, the parameter which controls line shape symmetry. In our system, the smallest values of q_{Fano} yield huge phonon-induced optical transparencies that dip below the background absorption level by more than 75%.

We demonstrate that the phonon-induced transparency in our QDMs is easily tuned by electronic and optical means. In particular, we observe a non-linearity in the Fano effect that allows us to continuously tune q_{Fano} as a function of the laser excitation power. We further show that, in addition to controlling optical transparency,

the non-linear Fano effect is an efficient amplifier of weak coupling channels, thereby enhancing their visibility.

In order to provide a theoretical basis for the phonon-induced Fano effect in QDMs, we first derive an equation for the Fano absorption profile of our system based on a simple model. The predictions of the model are found to be in good qualitative agreement with our experimental data and provide theoretical validation of our observations.

7.1 Theoretical Model of the Phonon-induced Fano Effect in QDMs

To begin, we provide a theoretical model of the phonon-induced Fano effect in QDMs. The model was developed by our collaborator A. O. Govorov from Ohio University and makes use of a quantum field theoretic approach to calculate the rate of energy absorption in our system [37]. The resulting formula describes the absorption line shape in QDMs as a function of the q-Fano factor.

We first recall from Section 3.5 the necessary conditions for a Fano resonance. We require a discrete excited state and a separate continuum of excited states which overlap in energy. These excited states must also be coupled to a common ground state via some external excitation. Finally, there must be an intrinsic coupling between the discrete and continuum excited states, causing them to form a hybridized final excited state.

A diagram of the corresponding states in our QDM system is illustrated in Figure 7.1. The common ground state is the crystal ground state, i.e., a QDM with no electronic excitations, which we label as $|0\rangle = |CGS\rangle$. An indirect exciton state plays the role of the discrete excited state in the Fano scheme, which we label as $|2\rangle = |iX_n\rangle$. We consider indirect exciton states in which the electron is confined to the ground state of the lower energy bottom dot and the hole is in the n^{th} excited level of the top dot ($n = 0$ is the hole ground state). The polaron states, consisting of the neutral exciton ground state $|X_0\rangle$ and a single optical phonon of mode m, correspond to the continuum of excited states in the Fano scheme. We label the polaron states as $|1, m\rangle = |X_0, m\rangle$.[1] These exciton-phonon states are continuous because of the k-space dispersion of the optical phonons, strain, intermixing of InAs and GaAs, and interface effects [5, 93]. Finally, the indirect exciton state is coupled to the polaron continuum via phonon-assisted hole tunneling, generating a hybridized final excited state, which we introduce as the molecular polaron state $|MP\rangle = |iX_n\rangle \pm |X_0, m\rangle$. Thus, we have in our QDM system the necessary conditions for a phonon-induced Fano effect.

[1] In this section, we use m as the index of phonon modes and Ω_m as the phonon frequency in order to avoid confusion with the q-Fano factor and the laser frequency ω.

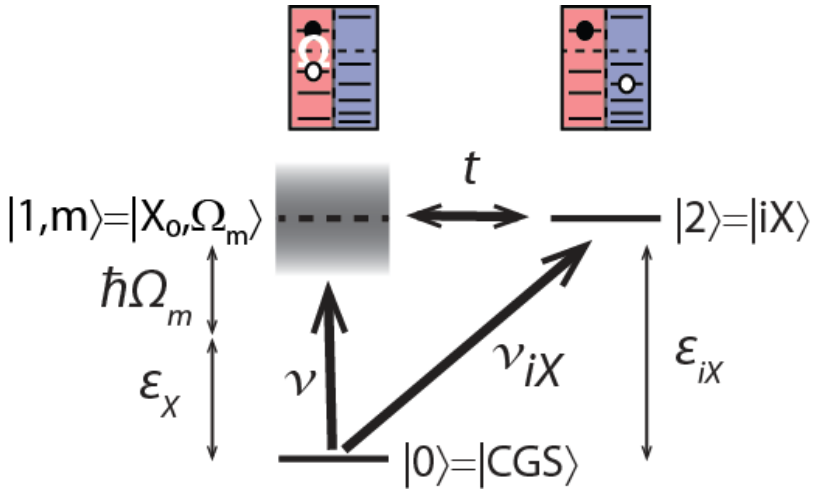

Figure 7.1: Quantum states and couplings involved in the resonant optical and phonon transitions of the Fano resonance. The photon energy $\hbar\omega \approx \varepsilon_{iX}$ hits the resonance $|iX_n\rangle$ and the indirect exciton $|iX_n\rangle$ becomes coupled with the polaron state $|X_0, m\rangle$ via phonon-assisted tunneling t. Here, we introduce notations more convenient for theory: The state $|1\rangle = |X_0\rangle$ is a direct exciton in the bottom dot, $|1, m\rangle = |X_0, m\rangle$ is the same state with an additional optical phonon mode, and the state $|2\rangle = |iX_n\rangle$ is a spatially indirect exciton. $|0\rangle = |CGS\rangle$ is the crystal ground state. The quantities ν and ν_{iX} represent the optical transition amplitudes from the common ground state to the polaron and indirect exciton states, respectively.

In addition to having the requisite states and couplings for a Fano resonance, it is important that we are able to tune the energy states of our system to resonance. Such resonances are achieved by taking advantage of the large Stark shift of the indirect exciton states in a QDM, which provides excellent versatility for manipulating the Fano effect in our system. As illustrated in the diagram of Figure 7.2a, the energy levels of different indirect exciton states may be tuned to resonance with the polaron continuum simply by varying the applied bias voltage.

The complete scheme for the phonon-induced Fano effect in QDMs is represented in Fig. 7.2b. An applied electric field tunes the band structure, bringing a discrete indirect exciton level into resonance with a mode of the polaron continuum. A laser resonantly tuned to the energy $\hbar\omega \approx \varepsilon_{iX} = \varepsilon_X + \hbar\Omega_m$ drives transitions to the polaron and indirect exciton states with transition amplitudes ν and ν_{iX}, respectively. Upon excitation, the discrete and continuum excited states become coupled via phonon-assisted hole tunneling. Here, 'phonon-assisted' means that a phonon is simultaneously created as the hole tunnels from the top to the bottom dot in the QDM, while a phonon is annihilated for hole tunneling in the opposite direction. The

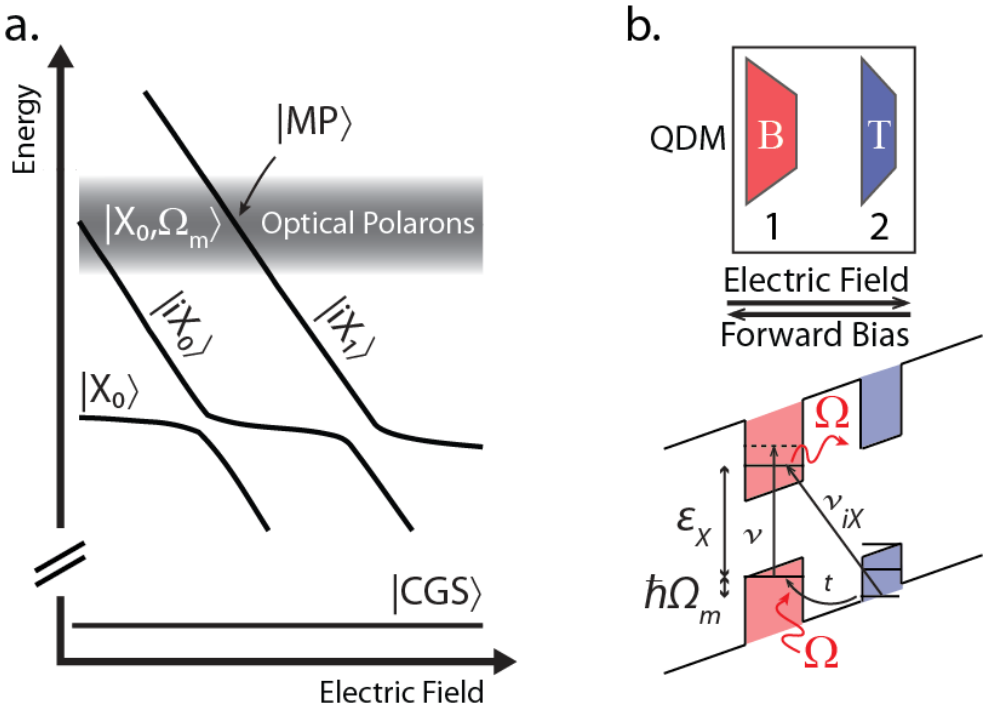

Figure 7.2: Conditions for a phonon-induced Fano effect in QDMs. (a) Representative diagram of the electric field dispersed energy levels of a QDM, showing how the indirect excitons may be electrically tuned to the energy of the polaron continuum. (b) Band diagram depiction of the phonon-induced Fano effect in QDMs. Note the essential role of the phonon-assisted hole tunneling, which couples the polaron and indirect exciton states.

final excited state is the hybridized molecular polaron state $|MP\rangle = |iX_n\rangle \pm |X_0, m\rangle$, a superposition of the polaron and indirect exciton states.

We now proceed to calculate the absorption profile of our system. In the following, we take the CGS energy as our reference point, setting it to zero. We also select a single indirect exciton state $|iX_n\rangle$, which we refer to simply as $|iX\rangle$. We begin by writing Fermi's golden rule for the rate of energy absorption in our system $I(\omega)$:

$$I(\omega) = \hbar\omega \cdot W, \tag{7.1a}$$

$$W = \frac{2\pi}{\hbar} \sum_f \left| \langle f | \hat{V}_{opt} | 0 \rangle \right|^2 \cdot \delta(\varepsilon_f - \hbar\omega), \tag{7.1b}$$

where ω is the photon frequency and $\langle f|\hat{V}_{opt}|0\rangle$ are the optical transition amplitudes from the crystal ground state to all the final states $|f\rangle$ of our system having energy

ε_f, i. e., the molecular polaron states. Equation (7.1) is analogous to the transition amplitude in equation (3.124) from Section 3.5 on the Fano effect. However, here we use Fermi's golden rule to allow for a density of states description of the polaron continuum [51].

The optical transition operator $\hat{V}_{opt}$ promotes electrons from the ground state to excited electronic states in both QDs. It may be written in terms of the electron creation and annihilation operators as follows:

$$\hat{V}_{opt} = V_{\text{indirect}} \left(\hat{c}^{\,\dagger}_{\text{CB,QD1}}\, \hat{c}_{\,\text{VB,QD2}} + \hat{c}_{\,\text{CB,QD1}}\, \hat{c}^{\,\dagger}_{\text{VB,QD2}} \right) + V_{\text{direct}} \left(\hat{c}^{\,\dagger}_{\text{CB,QD1}}\, \hat{c}_{\,\text{VB,QD1}} + \hat{c}_{\,\text{CB,QD1}}\, \hat{c}^{\,\dagger}_{\text{VB,QD1}} \right), \quad (7.2)$$

where

$$V_{\text{indirect}} = A_0 \langle \psi^e_{\text{QD1}} | \psi^h_{\text{QD2}} \rangle, \quad (7.3a)$$

$$V_{\text{direct}} = A_0 \langle \psi^e_{\text{QD1}} | \psi^h_{\text{QD1}} \rangle. \quad (7.3b)$$

For clarity, we have labeled the bottom dot as QD1 and the top dot as QD2 (see Fig. 7.2b). The creation and annihilation operators apply to electrons in the conduction band (CB) and the valence band (VB). However, it is equivalent to consider the creation and annihilation operators for electrons in the valence band as the reverse operators for holes (e.g., $\hat{c}_{\,\text{VB}}$ removes an electron from the valence band, thereby creating a hole). The two terms on the right hand side of equation (7.3a) are responsible for optical transitions to the indirect and direct exciton states, respectively. The coupling constants V_{indirect} and V_{direct} for these transitions depend on the overlap integrals of the localized electron and hole envelope wavefunctions $\psi^e_{\text{i}}, \psi^h_{\text{j}}$, as well as the inter-band transition element $A_0 = \mu_{\text{CV}} E_0/2$, where μ_{CV} is the inter-band atomic dipole and E_0 is the electric field amplitude of the laser.

To facilitate the solution of (7.1), we express the function W in terms of the optical Green's function $G(\omega)$:[2]

$$W = \frac{2}{\hbar} \operatorname{Im} \left[G(\omega) \right], \quad (7.4)$$

[2]This follows from the identity $\dfrac{1}{x + i\gamma} = P\left(\dfrac{1}{x}\right) - i\pi\delta(x)$. The resulting Green's function bears close resemblance to the Lippmann-Schwinger equation of quantum mechanical scattering theory [94].

where

$$\begin{aligned} G(\omega) &= \sum_f \frac{\left|\langle f|\hat{V}_{opt}|0\rangle\right|^2}{\varepsilon_f - \hbar\omega - i\gamma_f} \\ &= \sum_f \frac{\langle 0|\hat{V}_{opt}^\dagger|f\rangle\langle f|\hat{V}_{opt}|0\rangle}{\varepsilon_f - \hbar\omega - i\gamma_f} \\ &= -\langle 0|\hat{V}_{opt}^\dagger \frac{1}{\hbar\omega + i\gamma - \hat{H}} \hat{V}_{opt}|0\rangle. \end{aligned} \tag{7.5}$$

In the above equation, $\hat{H}$ is the system Hamiltonian in the absence of laser excitation and includes terms for both electrons and phonons. In order to compute $G(\omega)$, we need to determine the eigenstates of our system. To do so, we write $\hat{H} = \hat{H}_0 + \hat{V}_{e-ph}$, where $\hat{H}_0$ is the purely electronic part of the Hamiltonian and $\hat{V}_{e-ph}$ describes the electron-phonon interaction. We may then treat the electron-phonon interaction as a perturbation to the electronic Hamiltonian.

The electron-phonon interaction operator contains the following two important terms:

$$\hat{V}_{e-ph} = \hat{V}_{e-ph,\text{QD1-QD1}} + \hat{V}_{e-ph,\text{QD1-QD2}}, \tag{7.6}$$

where

$$\begin{aligned} \hat{V}_{e-ph,\text{QD1-QD1}} = &\sum_m \langle \psi^h_{\text{QD1}}|\Phi_m(\mathbf{r})|\psi^h_{\text{QD1}}\rangle\, \hat{c}^{\,\dagger}_{\text{VB,QD1}}\, \hat{c}_{\,\text{VB,QD1}} \left(\hat{b}_m + \hat{b}^\dagger_{-m}\right) + \\ &\sum_m \langle \psi^e_{\text{QD1}}|\Phi_m(\mathbf{r})|\psi^e_{\text{QD1}}\rangle\, \hat{c}^{\,\dagger}_{\text{CB,QD1}}\, \hat{c}_{\,\text{CB,QD1}} \left(\hat{b}_m + \hat{b}^\dagger_{-m}\right), \end{aligned} \tag{7.7a}$$

$$\begin{aligned} \hat{V}_{e-ph,\text{QD1-QD2}} = &\sum_m \langle \psi^h_{\text{QD2}}|\Phi_m(\mathbf{r})|\psi^h_{\text{QD1}}\rangle\, \hat{c}^{\,\dagger}_{\text{VB,QD2}}\, \hat{c}_{\,\text{VB,QD1}}\, \hat{b}^\dagger_{-m} + \\ &\sum_m \langle \psi^e_{\text{QD1}}|\Phi_m(\mathbf{r})|\psi^e_{\text{QD2}}\rangle\, \hat{c}^{\,\dagger}_{\text{CB,QD1}}\, \hat{c}_{\,\text{CB,QD2}}\, \hat{b}_m. \end{aligned} \tag{7.7b}$$

In the above equations, $\hat{b}^\dagger_m$ and $\hat{b}_m$ are the phonon creation and annihilation operators and $\Phi_m(\mathbf{r})$ are the Fröhlich potentials of the modes. In our case, the phonon modes come from localized phonon vibrations in a QDM and we will not specify the

modes since the details of such vibrations are not known.[3] The intra-dot operator $\hat{V}_{e-ph,\text{QD1-QD1}}$ describes the weak electron-phonon interaction in QD1 that generates the polaron states. For the inter-dot operator $\hat{V}_{e-ph,\text{QD1-QD2}}$, we only keep the resonant terms which describe phonon-assisted hole tunneling between the two QDs. The total (undriven) Hamiltonian of our system is then written as:

$$\hat{H} = \hat{H}_0 + \hat{V}_{e-ph,\text{QD1-QD1}} + \hat{V}_{e-ph,\text{QD1-QD2}}. \tag{7.8}$$

To simplify our calculation of the Green's function $G(\omega)$, we first diagonalize the partial Hamiltonian $\hat{H}_0^{'} = \hat{H}_0 + \hat{V}_{e-ph,\text{QD1-QD1}}$ by treating the intra-dot polaronic operator as a weak perturbation to the electronic Hamiltonian $\hat{H}_0$. Following the perturbation method described in Section 3.6, the new eigenstates of the system become:

$$|0_{pol}\rangle = |0\rangle|0_{\text{phonons}}\rangle + \sum_m a_m|0\rangle|1_m\rangle, \tag{7.9a}$$

$$|1_{pol}\rangle = |1\rangle|0_{\text{phonons}}\rangle + \sum_m b_m|1\rangle|1_m\rangle, \tag{7.9b}$$

where $|0_{\text{phonons}}\rangle$ indicates the vacuum of optical phonons and $|1_m\rangle$ is the state of a single optical phonon of mode m. Our system is now described by a common ground state $|0_{pol}\rangle$ and a direct exciton state $|1_{pol}\rangle$ that have acquired polaronic wavefunctions written for the weak electron-phonon coupling regime.

The continuum of polaron states are comprised of a ground state direct exciton and one optical phonon of mode m, which we write as $|1,m\rangle \equiv |1\rangle|1_m\rangle$. They have an energy equal to $\varepsilon_m = \varepsilon_X + \hbar\Omega_m$, the energy of an indirect exciton and one optical phonon. Using the polaronic states, we can express the amplitude ν_m for optical transitions from the ground state to the polaron continuum of states as:

$$\nu_m = \langle 1,m|\hat{V}_{opt}|0_{pol}\rangle = A_0 \langle \psi^e_{\text{QD1}}|\psi^h_{\text{QD1}}\rangle \int d^3\mathbf{r} \frac{\Phi_m(\mathbf{r})}{\hbar\omega_m} \left[\left(\psi^e_{\text{QD1}}\right)^2 - \left(\psi^h_{\text{QD1}}\right)^2\right]. \tag{7.10}$$

In addition, we obtain the following expression for the phonon-assisted tunneling amplitude for transitions between the indirect exciton state $|2\rangle$ and the polaron continuum of states:

$$t_m = \langle 1,m|\hat{V}_{e-ph,\text{QD1-QD2}}|2\rangle = \langle \psi^h_{\text{QD2}}|\Phi_m|\psi^h_{\text{QD1}}\rangle. \tag{7.11}$$

The phonon-assisted processes are illustrated in Figure 3.4.

[3]The matrix elements $\langle \psi^\alpha_{\text{i}}|\Phi_m(\mathbf{r})|\psi^\alpha_{\text{j}}\rangle$ in equations (7.7a) and (7.7b) represent specific forms of the generic electron-phonon coupling constant $\hbar\omega_{\mathbf{q}}\gamma$ introduced in equation (3.168) of Section 3.6.

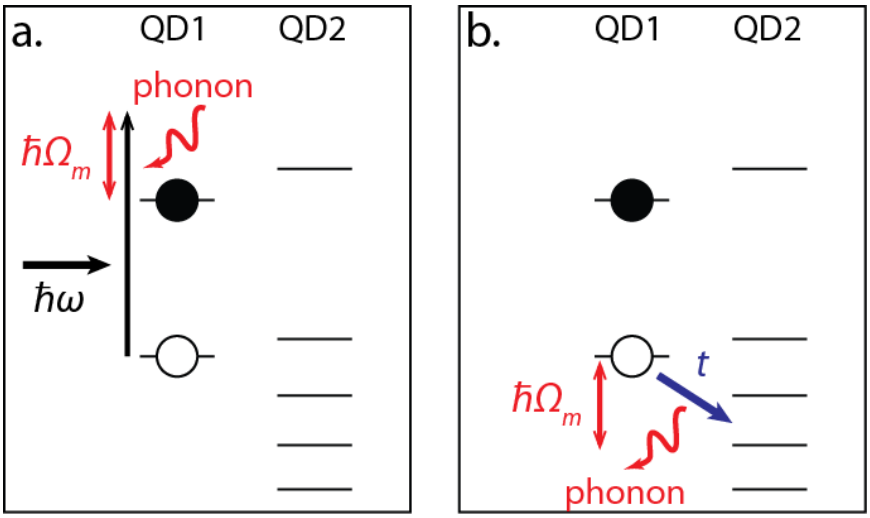

Figure 7.3: Illustration of the phonon-assisted processes. (a) Phonon-assisted optical transition from the ground state to a polaron state in QD1. A phonon is created in the process. (b) Phonon-assisted hole tunneling transition from a polaron state to an indirect exciton state. A phonon is annihilated as the hole tunnels from QD1 to QD2.

In the framework of the new states (7.9), the total Hamiltonian of our system may be written as:

$$\hat{H} = \hat{H}_0' + \hat{V}_{e-ph,\text{QD1-QD2}}. \tag{7.12}$$

Inserting the above result into equation (7.5), we may re-write $G(\omega)$ as:

$$G(\omega) = -\langle 0|\hat{V}_{opt}^{\dagger} \frac{1}{\hbar\omega + i\gamma - \hat{H}_0' - \hat{V}_{e-ph,\text{QD1-QD2}}} \hat{V}_{opt}|0\rangle. \tag{7.13}$$

In this form, we may solve for $G(\omega)$ by treating $\hat{V}_{e-ph,\text{QD1-QD2}}$ as a perturbation operator and using the diagrammatic method of quantum field theory. First, we re-write the operator in (7.13) using the following perturbation expansion:

$$\frac{1}{\hbar\omega + i\gamma - \hat{H}_0' - \hat{V}_{int}} = \frac{1}{\hbar\omega + i\gamma - \hat{H}_0'} + \frac{1}{\hbar\omega + i\gamma - \hat{H}_0'}\hat{V}_{int}\frac{1}{\hbar\omega + i\gamma - \hat{H}_0'} + \frac{1}{\hbar\omega + i\gamma - \hat{H}_0'}\hat{V}_{int}\frac{1}{\hbar\omega + i\gamma - \hat{H}_0'}\hat{V}_{int}\frac{1}{\hbar\omega + i\gamma - \hat{H}_0'} + \cdots \tag{7.14}$$

where $\hat{V}_{int}$ is taken to be $\hat{V}_{e-ph,\text{QD1-QD2}}$ [94]. The diagrammatic solution is achieved by inserting (7.14) back into equation (7.13), employing the polaronic states from equation (7.9) to write $G(\omega)$ as a sum of several infinite geometric series and then summing up the series.[4] Completing this process, one comes to the following equation for $G(\omega)$:

$$G(\omega) = -\left[\frac{\left(\nu_{iX} + \sum_{\nu t}\right)^2}{\hbar\omega - \varepsilon_{iX} + i\gamma_{iX} - \sum_{tt}} + \sum_{\nu\nu}\right], \tag{7.15}$$

where

$$\sum_{tt} = \sum_m \left(\frac{t_m t_m}{\hbar\omega - \varepsilon_m + i\gamma_{X_0,\Omega}}\right), \tag{7.16a}$$

$$\sum_{\nu t} = \sum_m \left(\frac{\nu_m t_m}{\hbar\omega - \varepsilon_m + i\gamma_{X_0,\Omega}}\right), \tag{7.16b}$$

$$\sum_{\nu\nu} = \sum_m \left(\frac{\nu_m \nu_m}{\hbar\omega - \varepsilon_m + i\gamma_{X_0,\Omega}}\right), \tag{7.16c}$$

$$\nu_{iX} \equiv V_{\text{indirect}} = A_0 \langle \psi^e_{\text{QD1}} | \psi^h_{\text{QD2}} \rangle. \tag{7.16d}$$

In the above equations, γ_{iX} and $\gamma_{X_0,\Omega}$ are relaxation rates that determine the energy broadening of the indirect exciton and the polaron continuum of states, respectively.

We now assume that the polaron band has a constant density of states ρ_0 in an energy interval of width D centered on a central polaron frequency of $\varepsilon_{ph,0} = \varepsilon_{X_0} + \hbar\Omega_0$. This model corresponds well to the experimental spectra, which shows optical polaron bands in the form of stripes. Then, the sums in equation (7.16) may be replaced with integrals:

$$\sum_m (\dots) \quad \longrightarrow \quad \int_{-D/2}^{D/2} (\dots) d\delta\varepsilon_{ph}, \tag{7.17}$$

[4] We do not provide the details of this process here, but note that it is similar to the approach used by A. O. Govorov in Ref. [95] for the case of a Stark ladder interacting with optical phonons in a semiconductor superlattice.

where the energy of the polaron continuum states is given by:

$$\begin{aligned}\varepsilon_{X_0,\Omega}(\delta\varepsilon_{ph}) &= \varepsilon_{ph,0} + \delta\varepsilon_{ph} \\ &= \varepsilon_{X_0} + \hbar\Omega_0 + \delta\varepsilon_{ph}.\end{aligned} \tag{7.18}$$

Assuming that the transition amplitudes are constant, we then obtain the Green's function and the optical absorption rate given below:

$$I(\omega, V_g) = \hbar\omega \cdot \frac{2}{\hbar}\,\mathrm{Im}\left[G(\omega)\right], \tag{7.19a}$$

$$G(\omega, V_g) = -\pi\rho_0\nu^2 \cdot \left[q_{Fano}^2 \, \frac{\Delta_{ph}\left(1 + \dfrac{1}{q_{Fano}^2}F_{ph}(\omega)\right)^2}{\hbar\omega - \varepsilon_{iX}(V_g) + i\gamma_{iX} - \Delta_{ph}F_{ph}(\omega)} + F_{ph}(\omega) \right], \tag{7.19b}$$

$$F_{ph}(\omega) = \frac{1}{\pi}\int_{-D/2}^{D/2} d\delta\varepsilon_{ph}\, \frac{1}{\hbar\omega - \varepsilon_{X_0} - \hbar\Omega_0 - \delta\varepsilon_{ph} + i\gamma_{X_0,\Omega}}, \tag{7.19c}$$

$$q_{Fano} = \frac{\nu_{iX}t}{\nu\Delta_{ph}} = \frac{1}{\pi\rho_0}\frac{\nu_{iX}}{\nu t}, \tag{7.19d}$$

$$\Delta_{ph} = \pi\rho_0 t^2. \tag{7.19e}$$

In the above equation, Δ_{ph} is the broadening of the indirect exciton transition due to its interaction with the polaron continuum states.[5] The Fano factor q_{Fano} in our system is proportional to the ratio of the indirect transition amplitude ν_{iX} to the product of the polaron transition amplitude ν and the phonon-assisted tunneling amplitude t, consistent with the general result from Section 3.5.

We point out that the absorption rate $I(\omega, V_g)$ is a function of both the laser frequency ω, which determines the relative position of the photon energy in the polaron band, and the bias (gate) voltage V_g, which tunes the indirect exciton energy. The expression for $\varepsilon_{iX}(V_g)$ depends on the particular indirect exciton state $|iX_n\rangle$ that is selected. Assuming a linear Stark shift, a general expression for the indirect exciton energy as a function of the bias voltage is:

$$\varepsilon_{iX}(V_g) = \varepsilon_{iX}^{(0)} + mV_g, \tag{7.20}$$

[5] Δ_{ph} is the specific representation in our system of the generic broadening term $|V_\varepsilon|^2$ of equation (3.117) in Section 3.5. See also in that section the discussion of $|V_\varepsilon|^2$ as it relates to the broadening and lifetime of the discrete excited state.

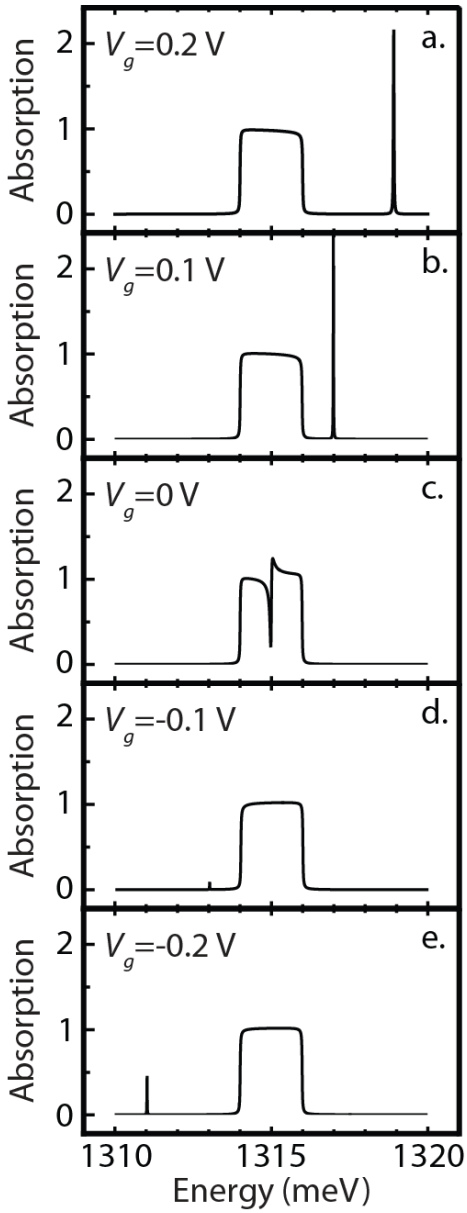

Figure 7.4: The phonon-induced Fano effect. Graphs (a-e) plot the absorption function $I(\omega, V_g)$ for various bias voltages in the case where $q_{Fano} = 0.5$. We have chosen a small value of the Fano factor to show the possibility of an optical transparency window (see graph (c), $V_g = 0$). The gate voltage has been referenced to graph (c), where the indirect exciton line crosses the center of the polaron band. The absorption into the polaron continuum has been normalized to one. The peak in (b), which is cut-off in the figure, has a height of 2.85.

where $\varepsilon_{iX}^{(0)}$ is the indirect exciton energy at zero bias voltage and m is the linear Stark shift of the indirect exciton.[6]

Equation (7.19) is reduced to the original Fano formula in the limit $D \to \infty$. The sign of q_{Fano} depends on the product of signs of the two quantum amplitudes ν and ν_{iX}. Moreover, q_{Fano} controls the nature of the quantum interference. For $|q_{Fano}| >> 1$, the Fano effect is weak and the line is symmetric. When $|q_{Fano}| \sim 1$, the line becomes strongly asymmetric. Finally, for $|q_{Fano}| \sim 0$, the spectrum shows an anti-resonance, that is, a narrow transparency window.[7] As noted, the spectrum will also depend on the relative position of the photon energy in the phonon band and the value of the applied bias V_g.

We illustrate in Figure 7.4 the optical absorption function $I(\omega, V_g)$ for the case of a small Fano factor (i.e., $|q_{Fano}| << 1$). The indirect exciton transition energy is Stark shifted through the polaron band in graphs (a-e), which plots $I(V_g)$ for five different values of the laser frequency ω. In graph (c), we observe a narrow optical transparency window, or anti-resonance, when the indirect exciton energy coincides with the center of the polaron energy band. This transparency results from destructive interference in the optical absorption pathway. Conditions for a phonon-induced optical transparency include a Fano factor of small magnitude and a discrete indirect exciton transition with a narrow line width (i.e., small γ_{iX}).

7.2 Experimental Results

Methods

The QDM samples used for our optical investigations of the Fano effect were fabricated at NRL and are described in Section 2. The density of QDMs in the region where the studied sample was taken from was between 10^8 and 10^9 cm^{-2}. The sample was engineered to preferentially exhibit hole tunneling by setting the nominal height of both dots in the QDM to 2.5 nm and separating them with a 4 nm wide tunneling barrier (see Section 2). During the optical experiments, the QDM samples were cooled to 18 K, a temperature at which the equilibrium population of optical phonons is zero ($K_BT = 1.55$ meV). For this study, detailed PLE measurements were performed on three different QDMs, all showing phonon-induced optical transparency. The data presented here are from one example QDM. In addition, the effect was also verified in a sample of QDMs with a 6 nm barrier.

We illustrate the experimental PLE scheme used to obtain our data in Figure 7.5. The experimental setup has been described in Chapter 4. We illuminate the

[6]The linear Stark shift is an excellent approximation for the QCSE of the indirect exciton state, as described in Chapter 6.

[7]See also Section 3.5.

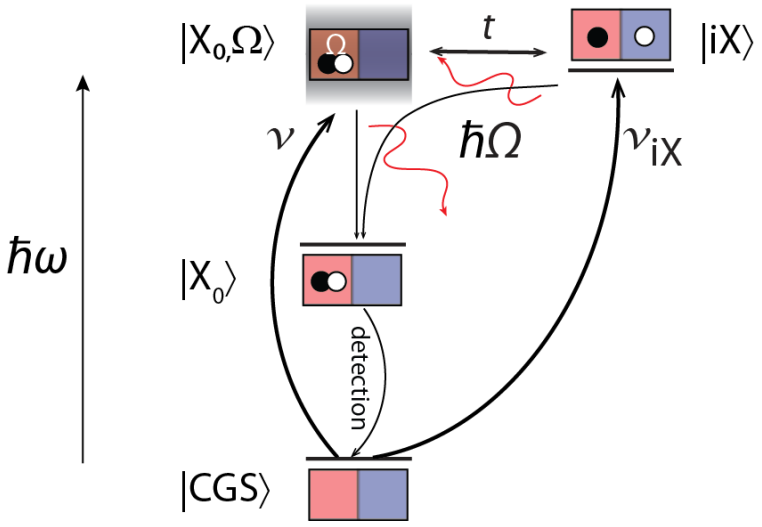

Figure 7.5: Diagram of the experimental scheme for observing the phonon-induced Fano effect in our QDM samples. A resonantly tuned laser with energy $\hbar\omega$ drives transitions from the crystal ground state to the indirect exciton and optical polaron states, which become coupled via phonon-assisted hole tunneling. The excited states relax to the ground state exciton $|X_0\rangle$ by emitting an optical phonon of energy $\hbar\Omega$. The intensity of optical emission from the ground state exciton to the crystal ground state is monitored, providing an indirect measurement of the absorption into the excited states.

cooled sample with a tunable diode laser, thereby inducing optical transitions within the QDM. By adjusting the laser energy and the bias voltage, we are able to tune different transitions within the QDM to resonance. When the QDM is electrically tuned so that an indirect exciton overlaps the energy of an optical polaron band, the conditions for observing a Fano effect are met. The excited exciton states relax predominantly via non-radiative transitions to the metastable ground state of the direct exciton. In particular, the polaron states relax by emitting an optical phonon. We indirectly measure the optical absorption into the excited states by detecting the emission intensity from the ground state neutral exciton.

The PLE bias map data that we present is aggregated from an average of about eight individual PL lines scans per meV, which reflects the typical mode hop energy of our lasers. To generate each PL scan, we have stepped the bias voltage in increments ranging from 0.001 to 0.005 mV and with exposure times ranging from 1 to 5 seconds. The PL spectra of the $|X_0\rangle \pm |iX_n\rangle$ anti-crossings at large negative bias values seen in Figure 7.6 were integrated for up to 120 seconds in order to acquire a sufficient signal strength. In this regime of large reverse bias, the PL emission rapidly decreases as the charge carriers become increasingly likely to tunnel out of the QDM prior to

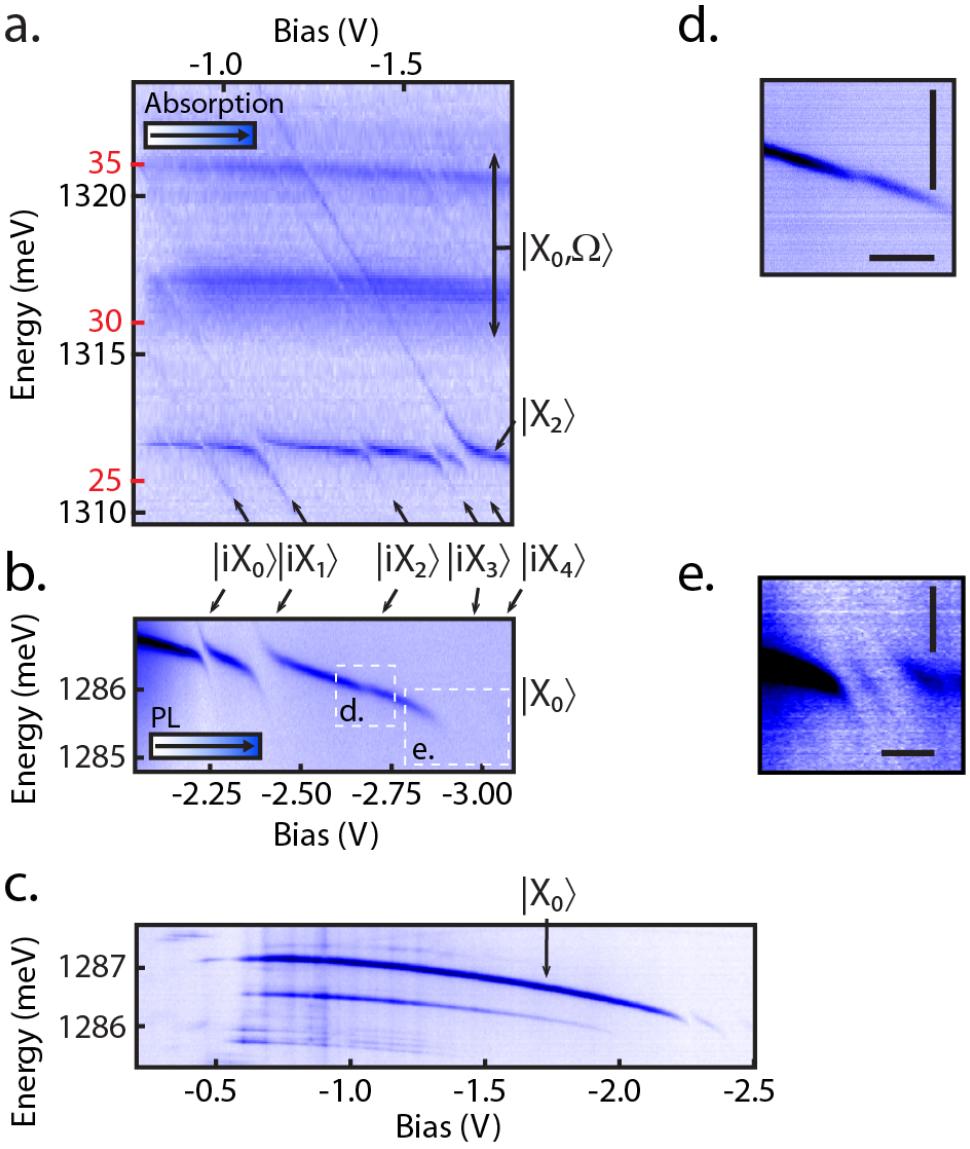

Figure 7.6: Overview of the electric field dispersed spectra of our example QDM in the region of transitions into the optical polaron states $|X_0, \Omega\rangle$. (a) PLE map showing two polaron bands as well as a sequence of indirect excitons states $|iX_0\rangle$ to $|iX_4\rangle$ and the direct exciton state $|X_2\rangle$. The energy of the optical polaron states (red labels) is referenced to the ground state neutral exciton. (b) Level-Anticrossing sequence of the indirect exciton states with the direct neutral exciton ground state $|X_0\rangle$. The resonances $|iX_2\rangle \pm |X_0\rangle$ and the resonances $|iX_3\rangle \pm |X_0\rangle$ and $|iX_4\rangle \pm |X_0\rangle$ are shown in higher contrast in panels (d) and (e). There, the vertical and horizontal scale bars measure 1 meV and 0.1 V, respectively. (c) PL map of the ground state neutral exciton. Note that the PLE map in panel (a) indicates absorption intensity, while the PL maps in panels (b-e) measure emission intensity.

radiative recombination.

Phonon-induced Transparency and Fano Interference in QDMs

We provide in Figure 7.6 an overview spectra of the investigated QDM. Panel (a) shows a PLE spectrum in the region of the transitions into the optical polaron states. Panels (b-e) show PL data from the ground state neutral exciton $|X_0\rangle$ that we monitored to collect the PLE data. In Fig. 7.6a, we observe two polaron bands with continuous energy levels at 29 meV to 31 meV and 34 meV to 35 meV above the $|X_0\rangle$ transitions. From their energies, we attribute them to GaAs-like and InAs-like LO and TO optical phonons.

We also observe in Fig. 7.6a the sequence of indirect exciton states $|iX_0\rangle$ to $|iX_4\rangle$ and the excited direct exciton state $|X_2\rangle$. The indirect states have been identified by their Level-Anticrossing sequence with the neutral exciton state, shown in panels (b),(d) and (e) [41]. The energies of the indirect exciton states are Stark shifted by about 20.5 meV/V. At an energy of about 1312 meV, the indirect excitons encounter the $|X_2\rangle$ state and form molecular eigenstates, as indicated by the hole tunneling anti-crossings. As the indirect states traverse the polaron bands, we see in certain regions a reduction in the absorption intensity. This indicates that the individual intensities of the overlapping discrete and continuum transitions do not simply add.

At higher laser power, the decreased absorption of the indirect exciton lines through the polaron bands becomes more pronounced. This is evident in Figure 7.7a, which shows a PLE map of the absorption into the indirect exciton states $|iX_3\rangle$ and $|iX_4\rangle$ collected at about 10× the excitation power of Fig. 7.6a. To compare the data with theory, we have plotted in Fig. 7.7b the theoretically expected features of a Fano resonance with $q_{Fano} = 0.5$, which we computed from our model. The experimental spectra appear qualitatively very similar to the theoretical model.

As we survey the absorption spectra from our sample QDM, we find examples of Fano resonances that correspond to different values of q_{Fano}. In Figure 7.8, we demonstrate examples of Fano interference exhibiting negative and positive values of the Fano factor. The figure plots line cuts of the absorption spectra extracted from PLE maps of the $|iX_3\rangle$ and $|iX_4\rangle$ states as they are Stark shifted through the polaron bands. Each line cut shows the absorption profile at fixed laser energy as a function of the applied bias voltage. The spectra reveal derivative and anti-resonance-like line shapes that are characteristic of the Fano effect. In Figs. 7.8c-h, we observe a progression of line shapes from the $|iX_3\rangle \pm |X_0, m\rangle$ transitions (Fig. 7.8a) that are typical of a Fano effect with $q_{Fano} < 0$. On the other hand, we observe in Figs. 7.8i-n a series of absorption line shapes from the $|iX_4\rangle \pm |X_0, m\rangle$ transitions (Fig. 7.8b) that show a reversed symmetry. This is characteristic of a Fano factor with $q_{Fano} > 0$.

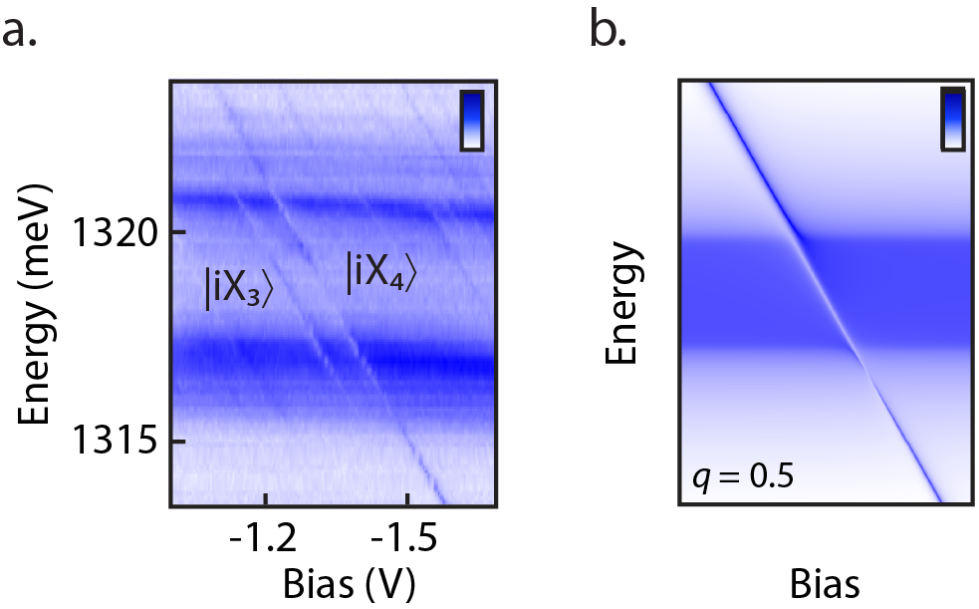

Figure 7.7: (a) A PLE map showing Fano interference as the $|iX_3\rangle$ and $|iX_4\rangle$ states pass through the polaron bands. (b) Theoretical plot of a Fano resonance with $q_{Fano} = 0.5$ computed from equation (7.19).

We point out that the maximum optical transparency observed in the two data sets shown in Fig. 7.8 occurs in panels (e) and (k) for the two respective transitions, where the absorption decreases to about 60% of the maximum signal.

We find other examples of Fano resonances that exhibit even deeper transparency dips, which are consistent with very small magnitudes of the Fano factor, i.e., $|q_{Fano}| \approx 0$. One such resonance is shown in Fig. 7.9.[8] To quantify the level of transparency, we have plotted in Fig. 7.9b a line cut from Fig. 7.9a taken at an excitation energy of 1,315.98 meV. Compared to the background absorption, we observe a huge dip of about 75% in the region where the molecular polaron state forms. This large decrease in the absorption is clear evidence of an optical interference effect and demonstrates the coherence of the laser driven molecular polaron state. Thus, we demonstrate the capability to generate very large transparency windows via phonon-induced Fano interference in our QDM samples. Moreover, the degree of optical transparency is easily tuned by controlling the applied bias voltage or the laser energy.

[8]This particular indirect transition is for an excited state with $n > 4$. We have not identified the exact number because the PL signal from the $|X_0\rangle$ transition vanishes at large negative bias values, making it impractical to perform Level-Anticrossing spectroscopy.

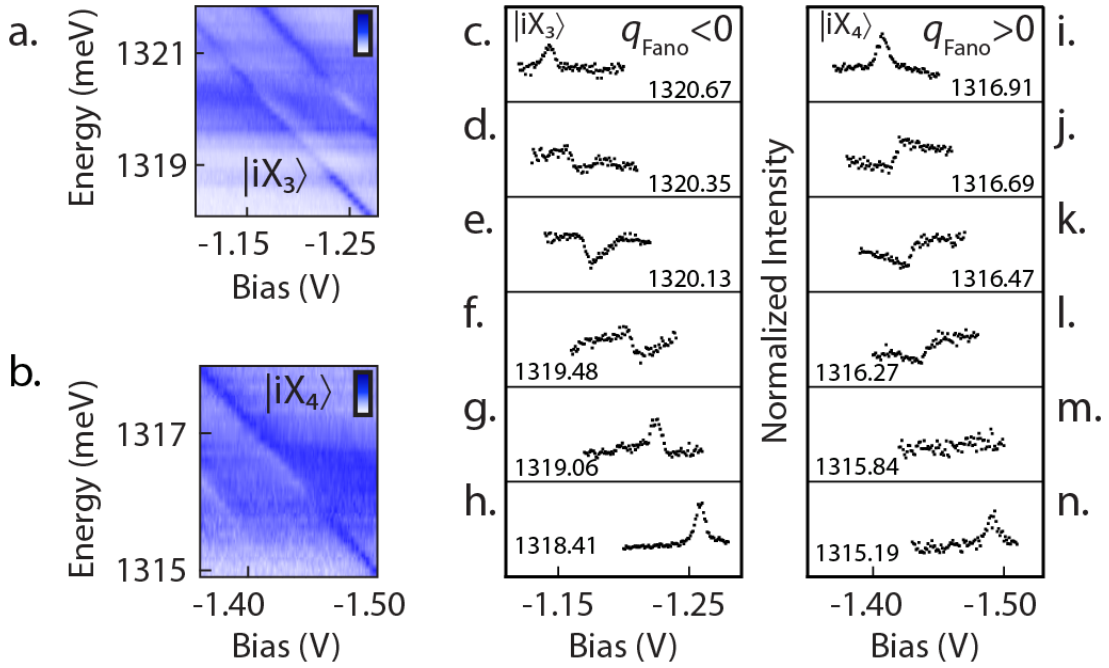

Figure 7.8: Experimental examples of Fano resonances with different signs of q_{Fano}. Panel (a) shows a PLE absorption map of the $|iX_3\rangle$ state as it interacts with the upper polaron band. The line cuts in panels (c-h), extracted from the data in (a), reveal a sequence of derivative and anti-resonance-like absorption line shapes typical of a Fano effect with $q_{Fano} < 0$. The line cuts (i-n), extracted from the data in panel (b) of the $|iX_4\rangle$ state as it interacts with the lower polaron band, display a progression of line shapes with opposite symmetry that are characteristic of a Fano effect with $q_{Fano} > 0$. The spectra in (c-h) and (i-n) were normalized to the difference between minimum and maximum signal. The numbers in the bottom of each panel indicate the laser excitation energy at which the respective spectrum was obtained.

Non-linearity of the Phonon-induced Fano Effect in QDMs

For a given Fano resonance, we regularly observe an increase in the phonon-induced transparency as a function of increasing laser excitation power. To demonstrate this non-linear behavior, we plot in Figure 7.10 the evolving absorption line shape versus power for the $|iX_4\rangle \pm |X_0, \Omega\rangle$ transition at the upper edge of the top polaron band (see Fig. 7.7). The laser energy remains fixed at 1,322.32 meV, while the laser power density is varied by a factor of about 280× going from panel (e) up to panel (a) (the power density in nW/μm^{-2} is listed in the top left corner of each plot). The spectra reveal absorption line shapes with symmetries that vary as a function of the laser power. At low power, we observe a Lorentzian-like line shape that is characteristic

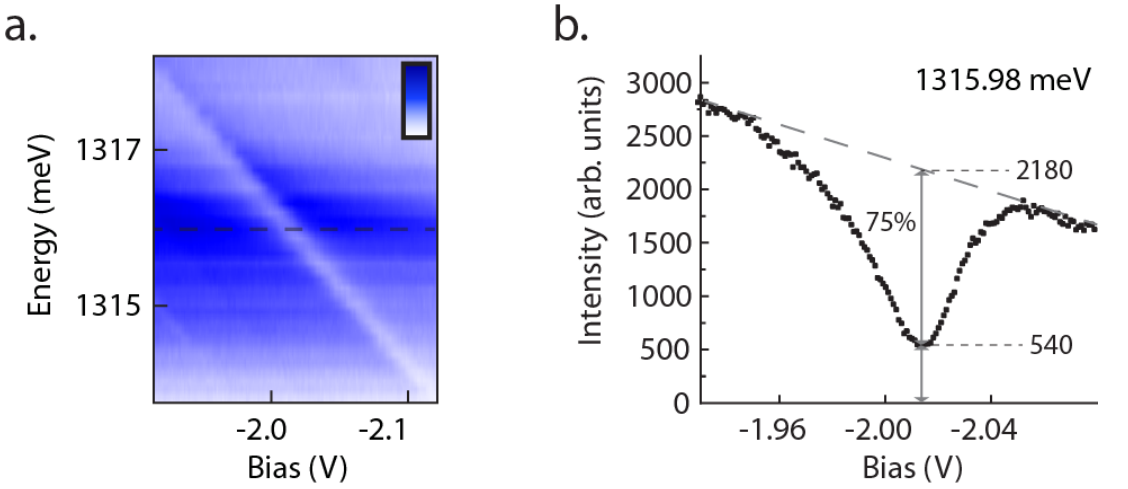

Figure 7.9: (a) PLE map of a Fano resonance in the lower polaron band with a very small magnitude of the Fano factor. (b) Line cut taken from (a) at an excitation energy of 1,315.98 meV (see horizontal dashed line), which reveals a deep anti-resonance. The phonon-induced transparency decreases the absorption to about 75% below the background intensity (indicated by the downward sloping dashed line).

of $q_{Fano} > 1$. In this low power regime, the interaction between the discrete indirect exciton state and the continuum of polaron states is minimal. As the power increases, the line shape becomes increasingly anti-symmetric and derivative-like, consistent with a decreasing value of q_{Fano}. At the highest power, we observe the greatest optical transparency, which corresponds to the least value of q_{Fano}. This is a general trend that we consistently observe in our measurements – the greatest transparencies occur at the highest laser powers. Consequently, laser power represents a convenient control parameter for tuning the strength of the Fano interference and, with it, the phonon-induced transparency.

To quantify the power dependence of the Fano effect, we have used our theoretical model to fit the data in Figs. 7.10a-e. The model is seen to be in good qualitative agreement with the experimental data. From the fits, we have extracted values for q_{Fano} and the broadening of the discrete transition line Δ_{tot}. The experimental data is inhomogeneously broadened by electric field fluctuations that are not accounted for in equation (7.19), so the extracted Fano factors need to be considered apparent Fano factors.[9] Nevertheless, since the Fano factor is a measure of the absorption line shape asymmetry, we consider the apparent q_{Fano} values to be reasonably accurate. In fact, we find that when fitting the data to the model, the values of q_{Fano} remain

[9]The large static dipole moment of the indirect exciton state increases the sensitivity to local electric field fluctuations, as discussed in Section 6.

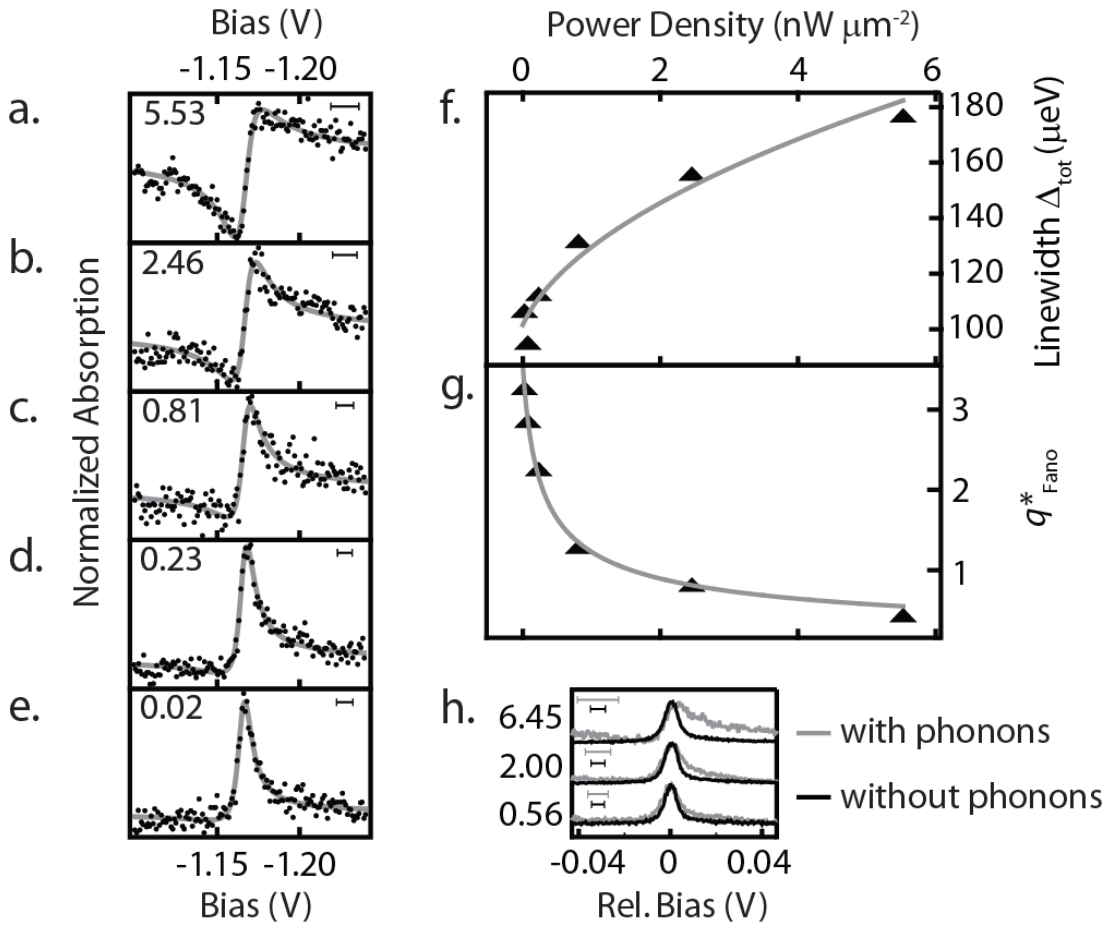

Figure 7.10: Non-linearity of the phonon-induced Fano effect. (a-e) Excitation power dependence of the Fano line shape at power densities in nW/μm^{-2}, as indicated in the top left corner of each panel. Values for (f) the line width of the indirect transition, $\Delta_{tot} = \Delta_{ed} + \Delta_{ph,eff}$, and (g) the Fano factor, q_{Fano}, obtained from fits to equations (7.21) and (7.22), yielding $q_{Fano,0} = 3.57$, $a = 7.47$ μm^2/nW, $\Delta_{ed} = 87.8$ μeV and $\Delta_{ph} = 14.40$ μeV. (h) Comparison of the $|iX_4\rangle$ transition line profiles at excitation energies 1314 meV ($\rho_0 \approx 0$, without phonons) and 1317 meV ($\rho_0 > 0$, with phonons) for excitation power densities 0.56 nW/μm^{-2}, 2.00 nW/μm^{-2} and 6.45 nW/μm^{-2}. The spectra were normalized ($I_{max} - I_{min} = 1$) and vertically offset for clarity. Scale bars in (a) and (d) indicate the full-width at half maximum, $2\Delta_{tot}$.

nearly constant even as other parameters in equation (7.19) are varied.

The non-linearity of the Fano effect may be understood in terms of the different response between the discrete and continuum optical pathways at increased laser powers [57]. At high power, the optical transitions into the discrete indirect exciton states become saturated and the transition amplitude ν_{iX} approaches a constant value. On the other hand, the transition amplitude ν into the continuum of polaron states continues to increase over the range of laser powers employed. As a result, ν grows to match, and then overtake, the discrete amplitude ν_{iX} as the laser power is increased. It then follows from equation (7.19d), i.e., $q_{Fano} = \nu_{iX}/(\pi\rho_0\nu t)$, that we observe a decreasing Fano factor and greater phonon-induced transparency as a function of increasing laser power. In addition to the optical transition amplitudes, the Fano factor also depends on the phonon density of states ρ_0 and the phonon-assisted tunneling rate t. Thus, for different Fano resonances, variations in any of these parameters can affect the power level at which the non-linear regime is observed.

We may obtain approximate analytical expressions for the power dependence of the Fano interference by considering the saturation of the indirect exciton transition to obey the equation for a driven two-state system with damping (see also Section 3.4). As we show in Appendix D, this approximation results in the following power dependence formulas for q_{Fano} and Δ_{tot}:

$$\begin{aligned}\Delta_{tot}(P) =& \Delta_{ed} + \Delta_{ph,eff}(P) \\ =& \Delta_{ed} + \Delta_{ph}\sqrt{1+aP},\end{aligned} \tag{7.21}$$

and

$$q_{Fano}(P) = \frac{q_{Fano,0}}{\sqrt{1+aP}}. \tag{7.22}$$

To support our explanation of the non-linear Fano effect, we have fit the extracted values of Δ_{tot} and q_{Fano} as a function of laser power to equations (7.21) and (7.22). The fits, plotted in Figs. 7.10f and 7.10g, are in good agreement with the simple equations based on the two-level broadening approximation. To better understand the source of the power broadening, we investigated the role of optical phonons in the line width broadening of the $|iX_4\rangle$ transition. The data, plotted in Fig. 7.10h, shows a noticeable power broadening of the transition line width at an excitation energy of 1,317 meV in the region of the lower polaron band. By comparison, no significant power broadening is observed at an excitation energy below the polaron bands. Thus, we may attribute the power dependence of Δ_{tot} to an effective increase in the phonon-assisted tunnel broadening $\Delta_{ph,eff}(P)$, as illustrated in equation 7.21 (see also Appendix D). At higher laser powers, the interaction of the indirect exciton transition with the polaron continuum is enhanced and we observe a more prominent interference effect.

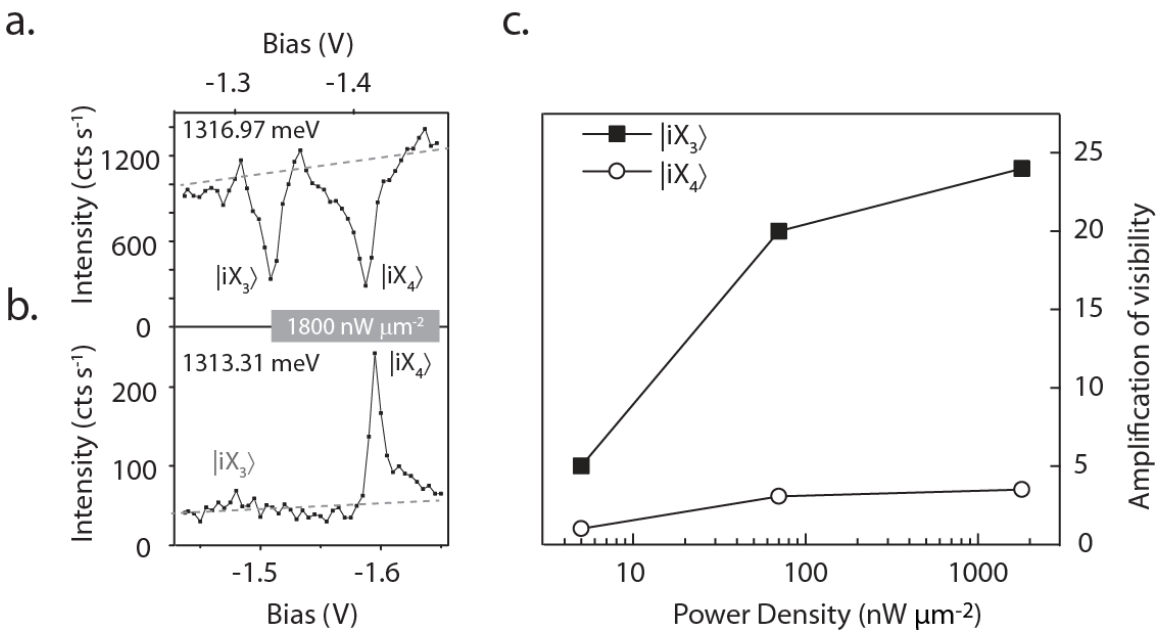

Figure 7.11: PLE intensity profiles of the indirect transitions into the states $|iX_3\rangle$ and $|iX_4\rangle$ at excitation energies in (1,316.97 meV, (a)) and off (1,313.31 meV, (b)) resonance with the polaron band. (c) Signal ratios of the transitions into the two states at excitation energies on and off resonance with the polaron band as a function of excitation power. For the signal of the transition into $|iX_3\rangle$, a lower limit of the amplification was calculated using the full width of the noise. The dashed lines indicate the base line to which we referenced the signal (dip or peak).

To fit the experimental data to the model in Figs. 7.10a-e, the relative position of the photon energy in the phonon band was determined from the PLE spectra and an offset was included in equation (7.19) to rescale the data so that the Fano minimum equals zero and the polaron background one. The value of the indirect exciton broadening was estimated to be 0.050 μeV, which is consistent with experimentally measured values of the lifetime [96]. We point out, however, that the chosen value of the indirect exciton broadening affects the magnitude, but not trend, of the extracted values of $\Delta_{ph,eff}$. Thus, we consider the plot of $\Delta_{tot} = \Delta_{ed} + \Delta_{ph,eff}$ in 7.10f to express the *relative* power dependence of $\Delta_{ph,eff}$.

Amplification of Weak Coupling Channels

A consequence of the non-linear Fano effect is that we are able to amplify the coherent coupling between the indirect exciton state and the polaron continuum simply by tuning parameters to adjust the value of q_{Fano}. This provides a mechanism for

amplifying weak coupling channels and thereby increasing their visibility. We demonstrate the amplification effect in Fig. 7.11, which plots the absorption signal into the $|iX_3\rangle$ and $|iX_4\rangle$ states for two separate conditions: (i) as they interact with the polaron continuum and form the molecular polaron state (Fig. 7.11a) and (ii) when they are below the polaron states and exhibit Lorentzian-like profiles (Fig. 7.11b). The signal (dip or peak) in panels (a) and (b) is measured with respect to the background absorption, which is indicated by grey dashed lines. For both transitions, we observe that the anti-resonance signal in the polaron band is magnified compared to the Lorentzian-like signal at lower energy. To quantify the amplification, we plot the ratio of the Fano-resonance signal to the Lorentzian-like signal in Fig. 7.11c. As the power is increased, the magnification becomes enlarged. In particular, note how the transition into $|iX_3\rangle$ is, if at all, barely visible outside the polaron band, yet reduces the signal of the polaron band by about 75%. This observation proves that the interference signal is caused not just by additive or subtractive superposition of the two paths' amplitudes, but also by amplification. Thus, the phonon-induced Fano effect may be used as an efficient and tunable coherent coupler for quantum states in QDMs and other spatially separated low-dimensional structures.

We further demonstrate the molecular polaron's power as a tunable coherent coupler in Figure 7.12. In panels (a-c), we compare the two hole tunneling resonances of the single QD-like exciton ground state $|iX_1\rangle \pm |X_0\rangle$ and $|iX_2\rangle \pm |X_0\rangle$, with the corresponding two molecular polaron resonances, $|iX_1\rangle \pm |X_0, \Omega\rangle$ and $|iX_2\rangle \pm |X_0, \Omega\rangle$. The tunneling rates of the two resonances with the bare single QD-like exciton are vastly different, having energies of (355 ± 20) μeV and (60 ± 25) μeV, respectively (Fig. 7.12a). In contrast, the molecular polaron resonances are of nearly identical transparency (Fig. 7.12b,c). From the large visibility achieved here, it follows that even much weaker coupling channels can be boosted this way. Additionally, unlike discrete excited electronic states, the optical polaron states have a well-defined energy difference to the ground state. As such, the phonon-induced transparency can be a predictable and reliable tool for revealing small coupling channels and making them usable.

Localization of Coherent Phonons

In this chapter, we have revealed a highly tunable phonon-induced transparency in QDMs and demonstrated how the effect works to amplify coupling channels. The fact that the transparency is realized via a Fano interference is proof that our system behaves in a coherent manner [97, 98]. Here, we highlight the essential role of single optical phonons in the Fano scheme, which proves that we have accomplished making typically incoherent and dissipative phonons behave in a coherent and non-dissipative manner. Moreover, the formation of the molecular polaron reveals a specific mecha-

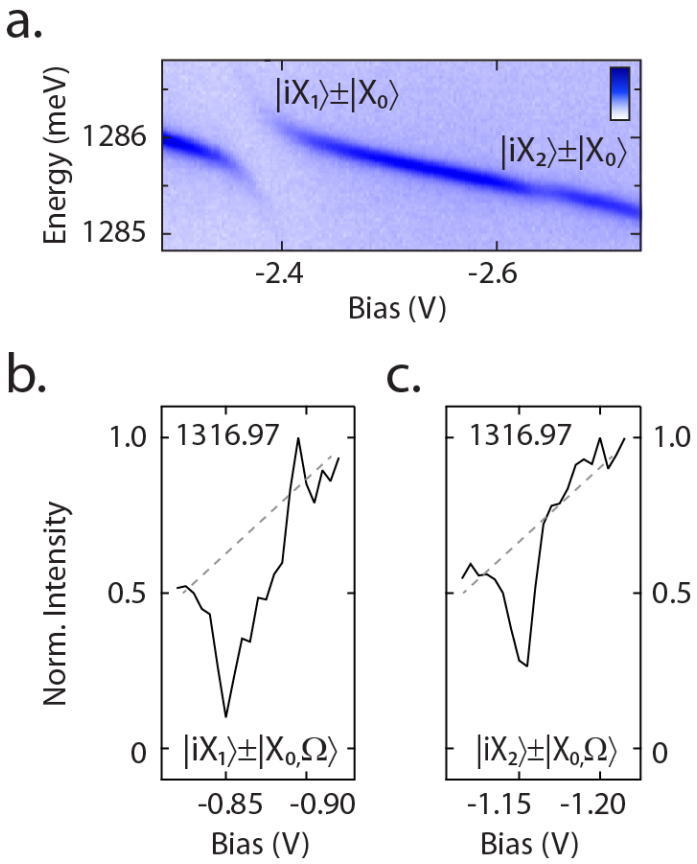

Figure 7.12: (a) Electric field-dispersed PL spectrum of the $|X_0\rangle$ state showing the anti-crossings caused by hole level resonances with the indirect excitons $|iX_1\rangle$ and $|iX_2\rangle$ with tunneling rates, $t_1 = 0.36$ meV and $t_2 = 0.06$ meV. The color scale indicates PL intensity, with darker meaning higher intensity. (b,c) The phonon-induced transparency signal caused by the phonon-assisted hole tunneling between the same single QD-like polaron state $|X_0, \Omega\rangle$ and the indirect exciton states as in (a). The dashed lines indicate the base line to which we referenced the dip.

nism by which single optical phonons can be made to interact in a coherent manner with photons and charges in coupled QDs.

One can attribute each individual dot of a QDM a marginal phonon confinement with an excellent bulk-phonon approximation for the nature of the phonons. The formation of a molecular polaron drastically changes the nature of the phonon. In the single QD-like polaron state $|X_0, \Omega\rangle$, the bulk-like nature of the phonon dominates the state – volatile, dissipative and of very short coherence. Coherent coupling to an interdot exciton state $|iX_n\rangle$ traps the phonon in the QDM system and makes it long lived. The optical transparency is the manifestation of this process of an optically driven and electrically tunable localization of phonons. That is, not only does the mechanical excitation of the system influence the electronic QDM states, but the electronic QDM states also strongly influence the mechanical excitation. With the formation of a molecular polaron in a pair of QDs, we demonstrate how single bulk-like phonons can be localized and therefore made technologically usable with the ease of an electric field control.

Chapter 8

Conclusion

In this dissertation, we have demonstrated the versatility of QDMs as an interface for coherently coupling distinct types of quantum states at the individual particle level. In addition to single spins, charges, and photons, the tunability of QDMs via the Stark shift and tunnel coupling allows us to introduce coherent interactions with single optical phonons. This is achieved with the formation of a molecular polaron state and is manifested in the phonon-induced Fano effect.

The nature of the phonon-induced Fano interference is strongly affected by the value of q_{Fano}, which is easily tuned via electronic and optical means in our QDMs. In particular, we have demonstrated that increased laser power leads to a reduced magnitude of q_{Fano} and an increased absorption line width. According to our simple model of power broadening in a two level system, the power dependence also increases the dephasing rate of the molecular polaron, affecting the coherence time.

A logical next step for future research would be to measure the time dynamics of the molecular polaron and to investigate the accuracy of our simple two-level model interpretation. The optical experiments described in this dissertation, which employed continuous wave lasers for excitation, are unable to provide quantitative measurements of the characteristic times constants. A key challenge, as noted in Chapter 7, is that the homogeneous line width broadening in our measurements is obscured by inhomogeneous ensemble broadening due to electric field fluctuations. We have assumed that these fluctuations occur on a time scale that is long compared to the dynamical time evolution of the molecular polaron. However, the quantitative relation between the time scale of the electric field fluctuations and the lifetime of the indirect exciton state is unknown. To quantitatively investigate these questions, future experiments could be devised using the techniques of ultra-fast laser spectroscopy. This would provide quantitative information about the characteristic time constants of the molecular polaron state, including their dependence on the value of q_{Fano}. Moreover, it could potentially pave the way for devising laser pulse techniques to actively manipulate the molecular polaron state.

In conclusion, the field of phononics is currently in the nascent stages of development. There remains much more to learn about the molecular polaron and coherent phonon interactions in low-dimensional quantum systems in general. In that respect, the investigations presented in this dissertation represent a promising starting point for future studies of coherent phonon interactions in QDMs and similar systems. As the principle of phonon-induced Fano interference is quite general, it could potentially be developed to provide coherent control over a wide variety of quantum systems.

Appendix A

Single Particle Wavefunctions of a QD

In this appendix, we solve the effective mass envelope wavefunctions for a single particle inside a quantum dot (QD) with parabolic confinement in the lateral directions and a band offset finite potential in the vertical direction. We assume a one band model for both electrons and heavy holes since the light holes are split off due to heterostructure strain. The potential is:

$$U(x,y,z) = \tfrac{1}{2}m_{eff}\omega^2(x^2+y^2) + U_z,$$
$$U_z(z) = \begin{cases} 0, & -d/2 < z < d/2, \\ U_0, & \text{otherwise}, \end{cases} \tag{A.1}$$

where d is the dot height, m_{eff} is the effective mass dependent on material and carrier type, $\omega = \sqrt{km}$ is the angular frequency of the parabolic potential with spring constant k and U_0 is the semiconductor band offset for electrons or holes. The time-independent Schrödinger equation is:

$$\left(-\frac{\hbar^2}{2m}\nabla^2 + U(\mathbf{r})\right)\psi(\mathbf{r}) = \varepsilon\psi(\mathbf{r}). \tag{A.2}$$

Inserting the potential of (A.1) into the Schrödinger equation (A.2) and writing the Laplacian operator in Cartesian coordinates yields:

$$-\frac{\hbar^2}{2m_{eff}}\left[\frac{\partial^2\psi}{\partial x^2} + \frac{\partial^2\psi}{\partial y^2} + \frac{\partial^2\psi}{\partial z^2}\right] + \left[\frac{1}{2}m_{eff}\omega^2(x^2+y^2) + U_z\right]\psi = \varepsilon\psi. \tag{A.3}$$

We assume separable solutions of the form $\psi(x,y,z) = X(x)Y(y)Z(z)$. After substituting in the separable solution and doing some algebra, we can write (A.3) as:

$$\begin{gathered}\left[\frac{1}{X}+\frac{\partial^2 X}{\partial x^2}+\left(-\frac{2m_{eff}}{\hbar^2}\right)\frac{1}{2}m_{eff}\omega^2 x^2\right]+\left[\frac{1}{Y}+\frac{\partial^2 Y}{\partial y^2}+\left(-\frac{2m_{eff}}{\hbar^2}\right)\frac{1}{2}m_{eff}\omega^2 y^2\right]+ \\ \left[\frac{1}{Z}+\frac{\partial^2 Z}{\partial z^2}+\left(-\frac{2m_{eff}}{\hbar^2}\right)(\varepsilon - U_z)\right]=0.\end{gathered} \tag{A.4}$$

We separate the $Z(z)$ solution by setting it equal to the separation constant $4m_{eff}\alpha/\hbar^2$, which after some algebra yields:

$$\frac{\partial^2 Z}{\partial z^2} = -\left[\frac{2m_{eff}}{\hbar^2}\left[\varepsilon - (U_z + 2\alpha)\right]\right]Z. \tag{A.5}$$

We return to solve this equation in a moment.

Quantum Harmonic Oscillator Analytical Solution

The remaining terms for $X(x)$ and $Y(y)$ in (A.4) can be separated to yield a pair of 1D quantum harmonic oscillator equations with the energies $E_{HO,x} = E_{HO,y} = \alpha$:

$$-\frac{\hbar^2}{2m_{eff}}\frac{\partial^2 X}{\partial x^2}+\frac{1}{2}m_{eff}\omega^2 x^2 X = \alpha X, \tag{A.6a}$$

$$-\frac{\hbar^2}{2m_{eff}}\frac{\partial^2 Y}{\partial y^2}+\frac{1}{2}m_{eff}\omega^2 y^2 Y = \alpha Y. \tag{A.6b}$$

The well known solutions to (A.6) are:

$$\begin{gathered}X_i(x) = A_i(a_x^\dagger)X_0(x), \\ X_0(x) = \left(\tfrac{m_{eff}\omega}{\pi\hbar}\right)^{1/4} e^{-m_{eff}\omega x^2/2\hbar}, \\ \alpha_i^x = \hbar\omega\left(i+\tfrac{1}{2}\right),\end{gathered} \tag{A.7a}$$

$$\begin{gathered}Y_j(y) = A_j(a_y^\dagger)Y_0(y), \\ Y_0(y) = \left(\tfrac{m_{eff}\omega}{\pi\hbar}\right)^{1/4} e^{-m_{eff}\omega y^2/2\hbar}, \\ \alpha_j^y = \hbar\omega\left(j+\tfrac{1}{2}\right),\end{gathered} \tag{A.7b}$$

where $X_0(x), Y_0(x)$ are the normalized ground state solutions, $a_x^\dagger, a_y^\dagger$ are the harmonic oscillator raising operators, A_i, A_j are normalization constants and α_i^x, α_j^y are the

energies of the i^{th} and j^{th} excited levels with $i, j \in \mathbb{N}$ the quantum numbers denoting the excitation levels in the x, y directions, respectively [68].

Finite Potential Well Analytical Solution

We now return to solve equation (A.5), which must be solved as a piecewise function due to the discontinuous potential U_z. We divide the domain into three regions: (i) $z < -d/2$, (ii) $-d/2 < z < d/2$ and (iii) $z > d/2$ and note the boundary conditions that both $Z(z)$ and its first derivative must be continuous at the boundaries $z = \pm d/2$. We observe that equation (A.5) has the form of a 1D finite square well potential, but with the potential well depth a function of the excitation levels of the simple harmonic oscillator states in the x, y directions through the dependence on α_i^x, α_j^y. Thus, equation (A.5) can be interpreted as a 1D finite potential well problem with a different constant potential equal to $U_0 + \alpha_i^x + \alpha_j^y$ for each pair of quantum numbers i, j. On the other hand, we point out that ε is the total energy of the quantum state and we expect it will be a sum of energies associated with each of the Cartesian coordinates:

$$\varepsilon = \alpha_i^x + \alpha_j^y + \varepsilon^z. \tag{A.8}$$

Here, ε^z is the energy due to the z-axis confinement. In this sense, we can simply substitute equation (A.8) into equation (A.5) and we will recover the standard finite potential well problem. We take this latter approach and re-write equation (A.5) as:

$$\frac{\partial^2 Z}{\partial z^2} = -\left[\frac{2m_{eff}}{\hbar^2}\left(\varepsilon^z - U_0\right)\right] Z. \tag{A.9}$$

For convenience we define the constants:

$$\kappa = \frac{\sqrt{-2m_{eff}(\varepsilon^z - U_0)}}{\hbar}, \tag{A.10a}$$

$$l = \frac{\sqrt{2m_{eff}\varepsilon^z}}{\hbar}, \tag{A.10b}$$

$$\kappa^2 + l^2 = \frac{2m_{eff}U_0}{\hbar^2}. \tag{A.10c}$$

Equation (A.9) permits both scattering and bound states, but we will focus on the bound states alone since we are interested in localized particle states in a QD. The states are bound whenever $0 < \varepsilon^z < U_0$, which implies that both κ and l are positive real numbers for bound state solutions.

We now solve equation (A.9) in each of the three regions. In the regions (i) and (iii), equation (A.9) is:

$$\frac{\partial^2 Z}{\partial z^2} = \kappa^2 Z. \tag{A.11}$$

The physically admissible solutions to (A.11) (i.e., that don't blow up as $z \to \pm\infty$) are:

$$Z(z) = Ae^{\kappa z}, \qquad z < -d/2, \tag{A.12}$$

$$Z(z) = Be^{\kappa z}, \quad z > d/2, \tag{A.13}$$

where A, B are constants. In region (ii), equation (A.9) is:

$$\frac{\partial^2 Z}{\partial z^2} = -l^2 Z. \tag{A.14}$$

The general solution to (A.14) is:

$$Z(z) = C\cos(lz) + D\sin(lz), \quad -d/2 < z < d/2, \tag{A.15}$$

where C, D are constants.

Next, we impose the boundary conditions on equations (A.12), (A.13) and (A.15). We can simplify this process by noting that the potential in (A.1) has inversion symmetry along the z-axis, so we can assume that the solutions have either even or odd parity. The advantage of this is that we only need to impose the boundary conditions at a single boundary since $Z(-z) = \pm Z(z)$. From inspection of equation (A.15), we seek even and odd solutions of the form:

$$Z_{even}(z) = \begin{cases} Be^{-\kappa z}, & z > d/2, \\ C\cos(lz), & 0 < z < d/2, \\ Z_{even}(-z), & z < 0, \end{cases} \tag{A.16}$$

$$Z_{odd}(z) = \begin{cases} Be^{-\kappa z}, & z > d/2, \\ D\sin(lz), & 0 < z < d/2, \\ -Z_{odd}(-z), & z < 0, \end{cases} \tag{A.17}$$

We must apply boundary conditions to equations (A.16) and (A.17) to solve for κ, l. We then determine the allowed energies ε^z through the energy dependence of κ, l. The constants B, C, D are to be determined by normalizing the complete 3D wavefunction. Using equation (A.10c) to facilitate the solution of equations (A.16)

and (A.17) yields a pair of transcendental equations in l for the even and odd solutions:

Even:

$$\tan\left(\frac{ld}{2}\right) = \sqrt{\frac{2m_{eff}U_0}{\hbar^2 l^2} - 1}, \tag{A.18}$$

Odd:

$$\cot\left(\frac{ld}{2}\right) = -\sqrt{\frac{2m_{eff}U_0}{\hbar^2 l^2} - 1}. \tag{A.19}$$

There may be multiple values of l that solve these equations, which correspond to different energy levels for the finite potential well. We denote this z-axis quantum number by $n = 0, 1, 2, \ldots$ and write l_n, κ_n. For notational convenience, we label the solutions to equations (A.18) and (A.19) with even and odd values of n, respectively. We note that for each l_n, we determine κ_n from equation (A.10c). We next solve for ε_n^z from equation (A.10b):

$$\varepsilon_n^z = \frac{\hbar^2 {l_n}^2}{2m_{eff}}. \tag{A.20}$$

Inspection of equation (A.20) reveals that l_n behaves as a wavenumber in the z-direction, as we may have anticipated from equation (A.15). Likewise, κ_n is related to the extent that the wavefunction penetrates the barrier material. The total energy of the quantum state from equation (A.8) may then be written as:

$$\varepsilon_{i,j,n} = \varepsilon_i^x + \varepsilon_j^y + \varepsilon_n^z = \alpha_i^x + \alpha_j^y + \frac{\hbar^2 {l_n}^2}{2m_{eff}}. \tag{A.21}$$

Numerical Solutions for the Single Particle Spatial Wavefunctions in InAs/GaAs QDs

The solutions to equations (A.18) and (A.19) require numerical values for the constants d, m_{eff} and U_0. We must be careful in our selection of carrier effective masses and confinement potentials since nanoscale semiconductor heterostructure parameters differ from their bulk counterparts due to interface strains. In Table A.1, we list the strained values of these parameters as computed by the method of Barker, et. al. [47]. The parameters $U_{c,s}$ and $U_{v,s}$ refer to the strained values of the conduction band and valence band edges and are referenced to the GaAs valence band edge. The parameter $\varepsilon_{g,s}$ is the strained band gap energy, calculated as the energetic difference between the conduction and valence band edges for a given semiconductor. The

vertical confinement potentials are calculated for electrons as the difference between conduction band edges of the two semiconductors and for holes as the difference in valence band edges. For InAs/GaAs QDs, Table A.1 yields vertical electron and hole confinement potentials of 461 meV and 192 meV (a ratio of ~ 2.4). For the effective masses, we use the strained value for electrons and heavy holes in InAs, the QD material. It is convenient to use $m_e = 57 \times 10^{-28}$ (meV $\cdot$ s^2 / nm^2) for the electron mass in vacuum so that energies and lengths can be measured in meV and nm. Using these parameters, we may solve for the vertical quantum confinement energies of electrons and holes from equation (A.9). Results for the ground state quantum confinement energies $\psi_{000}(\mathbf{r})$ of electrons and holes inside QDs of varying height are listed in Tables A.3 and A.4.

Table A.1: Strained InAs/GaAs Parameter Values at 0 K (energies in meV)

Parameter	**InAs**	**GaAs**
$m_{eff,e}/m_e$	0.042	0.059
$m_{eff,hh}/m_e$	0.34	0.37
$U_{c,s}$	1,058	1,519
$U_{v,s}$	192	0
$\varepsilon_{g,s}$	866	1,519

To compute the frequencies ω_e, ω_{hh} for the lateral part of the wavefunctions due to the harmonic oscillator potentials, we note from experimental data that the first excited hole state lies typically $\sim 15 - 20$ meV above the ground state energy. Using the effective mass for InAs, we approximate a hole frequency of $\omega_{hh} \approx 15$ meV$/\hbar = 2.3 \times 10^{23}$ Hz and a spring constant of $k_{hh} \approx 1.0$ meV/nm^2. For an electron, the spring constant should be multiplied by the electron to hole confinement potential ratio, so we set $k_e \cong 2.4 k_{hh} \approx 2.4$ meV/nm ^{2} . This yields an electron frequency $\omega_e \approx 1.0 \times 10^{14}$ Hz, which gives an approximate lateral energy spacing for electron states of ~ 66 meV. We summarize this information and the numerical value of the lateral wavefunction constants in Table A.2.

We now have all the information needed to normalize the complete 3D spatial wavefunctions $\psi_{ijn}(\mathbf{r})$ for electrons and holes in InAs/GaAs QDs subject to parabolic lateral and band offset vertical confinement. In the following, we restrict ourselves to the ground state wavefunctions, which are our main interest. By combining equations

Table A.2: Parameter Values for the Quantum Harmonic Oscillator Wavefunctions

Parameter	**hole**	**electron**
k	1.0 meV/nm^2	2.4 meV/nm^2
m_{eff}/m_e	0.34	0.042
ω	2.3×10^{13} Hz	1.0×10^{14} Hz
$\Delta\varepsilon^{x,y} = \hbar\omega$	15 meV	66 meV
$m_{eff}\omega/2\hbar$	0.033571	0.018214

(A.7), (A.8) and (A.18), we may write the general form of $\psi_{000}(\mathbf{r})$ and ε_{000} as:

$$\psi_{000}(\mathbf{r}) = \begin{cases} Be^{-\kappa_0 z}\, e^{-\beta(x^2+y^2)}, & z > d/2, \\ C\cos(l_0 z)\, e^{-\beta(x^2+y^2)}, & 0 < z < d/2, \\ Be^{-\kappa_0 z}\, e^{-\beta(x^2+y^2)}, & z < 0, \end{cases} \tag{A.22a}$$

$$\varepsilon_{000} = \hbar\omega + \varepsilon_0^z, \tag{A.22b}$$

where we recall from equation (A.20) that $\varepsilon_0^z = \hbar^2 {l_0}^2/2m_{eff}$ and for simplicity we have defined $\beta \equiv m_{eff}\omega/2\hbar$. In Tables A.3 and A.4, we compile values for the constants in equation (A.22) for QDs with various vertical heights.

In Figure A.1, we plot the electron and heavy hole probability densities calculated from equation (A.22a) for a 4 nm tall QD. Notice that the hole density is more compact and penetrates much less into the barrier region than the electron density. This is due to the electron having a much lighter effective mass. We can approximate the localized particle energy of a ground state neutral exciton in a QD, excluding the Coulomb and e-h exchange interactions, by combining the electron and hole quantum confinement energies from Tables A.3 and A.4 with the strained InAs band gap energy of 866 meV from Table A.1. For a QD of height 2.5 nm, for example, we calculate an exciton energy of $364 + 81 + 866$ meV = 1,311 meV.

Finally, we comment on the InAs wetting layer that sits at the bottom of self-assembled InAs/GaAs QDs, but which is not included in our simple model here. To gain some insight into the wetting layer, we estimate the quantum confinement energy for electrons and holes in a two monolayer (ML) thick wetting layer of InAs (~ 0.6 nm) surrounded by GaAs using the finite potential well model of equation (A.9). This yields band edge energies (i.e., $\mathbf{k} = 0$ in plane) of 446 meV for electrons and

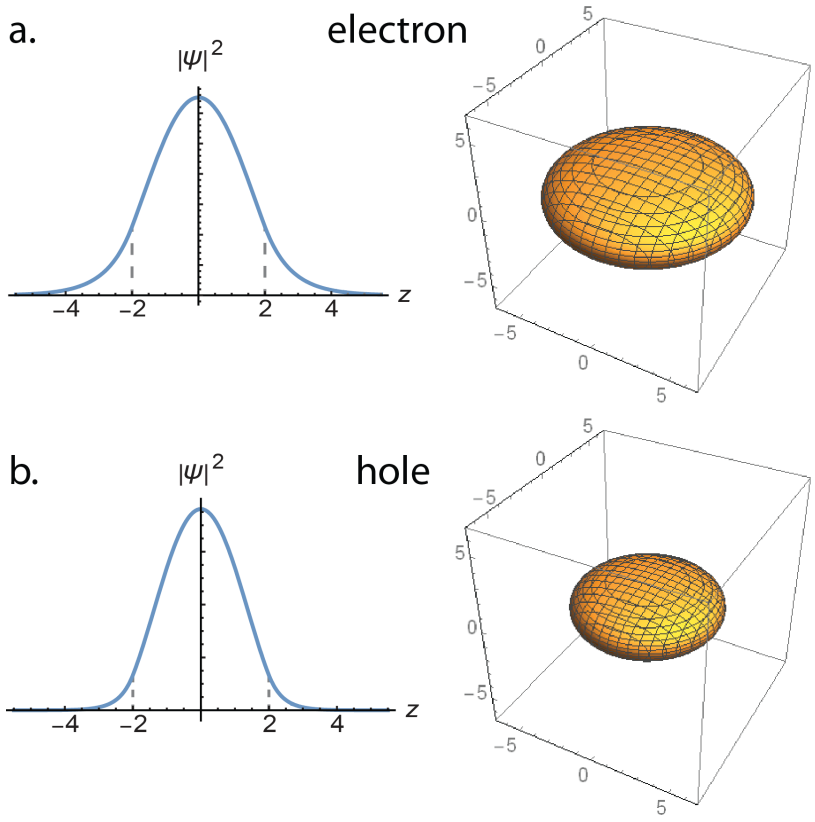

Figure A.1: Plots of the ground state probability density functions of the (a) electron and (b) heavy hole for a QD of 4 nm height (all spatial dimensions are in nanometers). The 2D plots at the right are taken along the z-axis through the center of the QDs (i.e., x = y = 0), while the 3D plots at the left are surfaces of constant probability density (the z-axis is vertical). The dashed lines at $z = \pm 2$ nm represent the upper and lower boundaries of the QD. Notice that the heavy hole probability density is more localized within the QD, while for the electron it is more spread out. Likewise, the electron is more likely to be found outside of the QD than the hole.

Table A.3: Electron Wavefunction ψ_{000} Parameter Values

QD height (nm)	B (nm^{-3})	C (nm^{-3})	β (nm^{-2})	κ_0 (nm^{-1})	l_0 (nm^{-1})	ε_0^z (meV)	$\hbar\omega$ (meV)	ε_{000} (meV)
2.4	0.08252	0.05973	0.01821	0.49	0.58	306	66	372
2.5	0.08428	0.05961	0.01821	0.5	0.57	298	66	364
2.6	0.08564	0.05981	0.01821	0.51	0.57	291	66	357
2.75	0.08901	0.05982	0.01821	0.53	0.56	279	66	345
3	0.09505	0.05951	0.01821	0.56	0.54	261	66	327
3.5	0.10668	0.05824	0.01821	0.6	0.5	227	66	293
4	0.12112	0.0571	0.01821	0.64	0.47	199	66	265

Table A.4: Hole Wavefunction ψ_{000} Parameter Values

QD height (nm)	B (nm^{-3})	C (nm^{-3})	β (nm^{-2})	κ_0 (nm^{-1})	l_0 (nm^{-1})	ε_0^z (meV)	$\hbar\omega$ (meV)	ε_{000} (meV)
2.4	0.21704	0.1006	0.03357	1.09	0.79	69	15	84
2.5	0.22801	0.09963	0.03357	1.11	0.77	66	15	81
2.6	0.23719	0.09855	0.03357	1.12	0.75	63	15	78
2.75	0.25107	0.09749	0.03357	1.14	0.73	59	15	74
3	0.27674	0.09515	0.03357	1.16	0.69	53	15	68
3.5	0.34585	0.09071	0.03357	1.2	0.62	43	15	58
4	0.42647	0.08725	0.03357	1.23	0.57	36	15	51

169 meV for holes. This is significantly more energetic than the values for electrons (364 meV) and holes (81 meV) that we have calculated for the 2.5 nm QDs in Tables A.3 and A.4. Consequently, we can assume that confined wetting layer states are effectively decoupled from the QD carrier ground states. Of course, the wetting layer does influence the carrier energies in the QDs due to the simple fact that the dots are seated atop the wetting layer. This increases the vertical width of the InAs region and thereby reduces the quantum confinement energy.

Appendix B

Laboratory Procedure for Generating a PL Bias Map

In this appendix, we provide a description of the general experimental procedure for generating a PL bias map in the Quantum Matter Group at UC Merced. This procedure also applies to the PLE bias maps, since they are formed by aggregating PL bias map data.

Once a QDM sample has been cooled down in the cryostat and is ready for optical study, the first step is to locate a suitable aperture for investigation. If the sample is patterned, then it is easy to identify the apertures from a pattern map, such as the one seen in Fig. 2.3 of Chapter 2. If the sample is unpatterned, then it is necessary to use other methods since the apertures are often invisible and many other surface imperfections may be mistaken for apertures.[1] In this case, the best method is to excite the wetting layer, which displays photoluminescence in the near IR for InAs/GaAs QDMs while the Schottky diode is operated in forward bias.[2] For the samples investigated in this work, a laser operating anywhere in the visible spectrum and up to ∼800 nm works well for this purpose. By setting the source meter to oscillate between forward and reverse bias meanwhile the wetting layer is excited, the apertures will visibly blink and can be observed and marked using the external CCD camera (see Fig. 4.3).

The next step is to locate an image of the same aperture in the spectrometer CCD camera. To do so, the CCD camera must be set to 'Use Full Chip' mode and the grating must be set to zero wavelength so that light from the sample may form an image. The spectrometer entry slits should be opened to their maximum extent. The

[1] In order to easily re-locate an unmarked aperture for additional study later on, it is highly recommended that you document the aperture location by taking numerous pictures and providing detailed notes.

[2] This technique works because the QDM becomes flooded with charges at forward bias, allowing charge carriers to fill the wetting layer and recombine optically.

aperture should be focused as best as possible in the CCD camera view by adjusting the depth of the sample with respect to the microscope objective.

With the aperture located in focus of the spectrometer camera, change the laser wavelength and increase it to a high power (several mW) in order to achieve non-resonant PL excitation of the QDMs. The incident laser spot may be viewed in the external CCD camera and it should be focused to a minimum beam waist and centered on the aperture under investigation. The camera mode must be changed to 'Use Region Of Interest' so that the integrated PL spectrum may be viewed.[3] Care should be taken not to saturate the spectrometer CCD camera during these steps by working with neutral density filters. Moreover, it is typically necessary that a short pass filter be placed between the exciting laser and the sample and a long pass filter placed between the sample and the spectrometer in order to reduce the intake of scattered laser light, which can otherwise easily drown out the PL signal.

At this point, a PL signal should be observable in the spectrometer camera. With the source meter turned off, the signal will likely be broad and without any discernible discrete peaks because most samples are flooded with negative charges at zero applied voltage. To make the discrete QDM transitions appear, the source meter should be adjusted to reverse bias. Once discrete peaks are observed, the peak intensities should be maximized by further adjusting the depth of the sample with respect to the microscope objective and making additional minor adjustments to the spectrometer entry lenses.

Finally, the aperture should be bounded by a region of interest on the CCD chip, which should be made small in order to minimize the entry of unwanted stray light, but not too small so as to attenuate the desired PL signal. The region of interest (ROI) may be set in the vertical direction using the spectrometer controller and in the horizontal direction by manually adjusting the spectrometer entry slit. There is a trade-off involving the ROI size. A higher resolution may be achieved with a smaller ROI since this minimizes the intake of scattered laser light. However, if the ROI is too small, the sample could drift out of view of the ROI as a result of local vibrations and temperature shifts. For long duration scans especially, it is often wise to allow some wiggle room with the ROI. Once the PL intensity has been optimized, all lights should be turned off inside the spectroscopy room and an automated program may be initiated to run the experiment and acquire the data.

[3]When changing between 'Use Full Chip' and 'Use Region Of Interest' modes, the ADC settings should also be adjusted.

Appendix C

Biexciton Hamiltonian Matrix

In this appendix, we present the complete biexciton Hamiltonian matrix in the localized particle basis representation. We order the localized particle basis so that orthogonality of the spin states separates the matrix representation into ten uncoupled blocks: one 10×10 block, one 6×6 block, four 4×4 blocks and four 1×1 blocks. The ordered basis is given below, where the singlet and triplet states $\{|\mathcal{S}^{\alpha}\rangle, |\mathcal{T}_0^{\alpha}\rangle, |\mathcal{T}_-^{\alpha}\rangle, |\mathcal{T}_+^{\alpha}\rangle\}$ are defined in equations (3.14) and (3.15) of Section 3.3 and the electron and hole spatial superposition states, needed to satisfy the symmetrization requirements for fermions, are defined in equation (5.1) of Section 5.1 as $|(BT)_{\pm}^{\alpha}\rangle \equiv 2^{-1/2}(|B^{\alpha 1}\rangle|T^{\alpha 2}\rangle \pm |T^{\alpha 1}\rangle|B^{\alpha 2}\rangle)$. The right-most column is an alternate description of the basis states that is used to label the H_{XX} matrix representation given later in this Appendix. It lists the carrier type (i.e., e or h), the spatial distribution of carriers in the bottom and top dots and the spin configuration (for example, $e(2,0), s; h(1,1), t0$ indicates the biexciton state having two spin singlet electrons in the bottom QD and two holes in the $m = 0$ spin triplet state, with one hole in the

top and the other in the bottom QD).

$$
\begin{array}{ll}
\underline{\text{Block 1}} & \\
|1\rangle = |B^{e1}\rangle|B^{e2}\rangle|B^{h1}\rangle|B^{h2}\rangle|\mathcal{S}^e\rangle|\mathcal{S}^h\rangle, & e(2,0),s;h(2,0),s \\
|2\rangle = |(BT)^e_+\rangle|B^{h1}\rangle|B^{h2}\rangle|\mathcal{S}^e\rangle|\mathcal{S}^h\rangle, & e(1,1),s;h(2,0),s \\
|3\rangle = |B^{e1}\rangle|B^{e2}\rangle|(BT)^h_+\rangle|\mathcal{S}^e\rangle|\mathcal{S}^h\rangle, & e(2,0),s;h(1,1),s \\
|4\rangle = |B^{e1}\rangle|B^{e2}\rangle|T^{h1}\rangle|T^{h2}\rangle|\mathcal{S}^e\rangle|\mathcal{S}^h\rangle, & e(2,0),s;h(0,2),s \\
|5\rangle = |(BT)^e_+\rangle|(BT)^h_+\rangle|\mathcal{S}^e\rangle|\mathcal{S}^h\rangle, & e(1,1),s;h(1,1),s \\
|6\rangle = |T^{e1}\rangle|T^{e2}\rangle|B^{h1}\rangle|B^{h2}\rangle|\mathcal{S}^e\rangle|\mathcal{S}^h\rangle, & e(0,2),s;h(2,0),s \\
|7\rangle = |T^{e1}\rangle|T^{e2}\rangle|(BT)^h_+\rangle|\mathcal{S}^e\rangle|\mathcal{S}^h\rangle, & e(0,2),s;h(1,1),s \\
|8\rangle = |(BT)^e_+\rangle|T^{h1}\rangle|T^{h2}\rangle|\mathcal{S}^e\rangle|\mathcal{S}^h\rangle, & e(1,1),s;h(0,2),s \\
|9\rangle = |T^{e1}\rangle|T^{e2}\rangle|T^{h1}\rangle|T^{h2}\rangle|\mathcal{S}^e\rangle|\mathcal{S}^h\rangle, & e(0,2),s;h(0,2),s \\
|10\rangle = |(BT)^e_-\rangle|(BT)^h_-\rangle|\mathcal{T}^e_0\rangle|\mathcal{T}^h_0\rangle, & e(1,1),t0;h(1,1),t0
\end{array}
\tag{C.1}
$$

$$
\begin{array}{ll}
\underline{\text{Block 2}} & \\
|11\rangle = |B^{e1}\rangle|B^{e2}\rangle|(BT)^h_-\rangle|\mathcal{S}^e\rangle|\mathcal{T}^h_0\rangle, & e(2,0),s;h(1,1),t0 \\
|12\rangle = |(BT)^e_+\rangle|(BT)^h_-\rangle|\mathcal{S}^e\rangle|\mathcal{T}^h_0\rangle, & e(1,1),s;h(1,1),t0 \\
|13\rangle = |T^{e1}\rangle|T^{e2}\rangle|(BT)^h_-\rangle|\mathcal{S}^e\rangle|\mathcal{T}^h_0\rangle, & e(0,2),s;h(1,1),t0 \\
|14\rangle = |(BT)^e_-\rangle|B^{h1}\rangle|B^{h2}\rangle|\mathcal{T}^e_0\rangle|\mathcal{S}^h\rangle, & e(1,1),t0;h(2,0),s \\
|15\rangle = |(BT)^e_-\rangle|(BT)^h_+\rangle|\mathcal{T}^e_0\rangle|\mathcal{S}^h\rangle, & e(1,1),t0;h(1,1),s \\
|16\rangle = |(BT)^e_-\rangle|T^{h1}\rangle|T^{h2}\rangle|\mathcal{T}^e_0\rangle|\mathcal{S}^h\rangle, & e(1,1),t0;h(0,2),s
\end{array}
\tag{C.2}
$$

$$
\begin{array}{ll}
\underline{\text{Block 3}} & \\
|17\rangle = |B^{e1}\rangle|B^{e2}\rangle|(BT)^h_-\rangle|\mathcal{S}^e\rangle|\mathcal{T}^h_-\rangle, & e(2,0),s;h(1,1),t- \\
|18\rangle = |(BT)^e_+\rangle|(BT)^h_-\rangle|\mathcal{S}^e\rangle|\mathcal{T}^h_-\rangle, & e(1,1),s;h(1,1),t- \\
|19\rangle = |T^{e1}\rangle|T^{e2}\rangle|(BT)^h_-\rangle|\mathcal{S}^e\rangle|\mathcal{T}^h_-\rangle, & e(0,2),s;h(1,1),t- \\
|20\rangle = |(BT)^e_-\rangle|(BT)^h_-\rangle|\mathcal{T}^e_0\rangle|\mathcal{T}^h_-\rangle, & e(1,1),t0;h(1,1),t-
\end{array}
\tag{C.3}
$$

$$
\begin{array}{ll}
\underline{\text{Block 4}} & \\
|21\rangle = |B^{e1}\rangle|B^{e2}\rangle|(BT)^h_-\rangle|\mathcal{S}^e\rangle|\mathcal{T}^h_+\rangle, & e(2,0),s;h(1,1),t+ \\
|22\rangle = |(BT)^e_+\rangle|(BT)^h_-\rangle|\mathcal{S}^e\rangle|\mathcal{T}^h_+\rangle, & e(1,1),s;h(1,1),t+ \\
|23\rangle = |T^{e1}\rangle|T^{e2}\rangle|(BT)^h_-\rangle|\mathcal{S}^e\rangle|\mathcal{T}^h_+\rangle, & e(0,2),s;h(1,1),t+ \\
|24\rangle = |(BT)^e_-\rangle|(BT)^h_-\rangle|\mathcal{T}^e_0\rangle|\mathcal{T}^h_+\rangle, & e(1,1),t0;h(1,1),t+
\end{array}
\tag{C.4}
$$

$$
\begin{array}{ll}
\underline{\text{Block 5}} & \begin{array}{ll}
|25\rangle = |(BT)^e_-\rangle|B^{h1}\rangle|B^{h2}\rangle|\mathcal{T}^e_-\rangle|\mathcal{S}^h\rangle, & e(1,1),t-;h(2,0),s \\
|26\rangle = |(BT)^e_-\rangle|(BT)^h_+\rangle|\mathcal{T}^e_-\rangle|\mathcal{S}^h\rangle, & e(1,1),t-;h(1,1),s \\
|27\rangle = |(BT)^e_-\rangle|T^{h1}\rangle|T^{h2}\rangle|\mathcal{T}^e_-\rangle|\mathcal{S}^h\rangle, & e(1,1),t-;h(0,2),s \\
|28\rangle = |(BT)^e_-\rangle|(BT)^h_-\rangle|\mathcal{T}^e_-\rangle|\mathcal{T}^h_0\rangle, & e(1,1),t-;h(1,1),t0
\end{array} \\
\underline{\text{Block 6}} & \begin{array}{ll}
|29\rangle = |(BT)^e_-\rangle|B^{h1}\rangle|B^{h2}\rangle|\mathcal{T}^e_+\rangle|\mathcal{S}^h\rangle, & e(1,1),t+;h(2,0),s \\
|30\rangle = |(BT)^e_-\rangle|(BT)^h_+\rangle|\mathcal{T}^e_+\rangle|\mathcal{S}^h\rangle, & e(1,1),t+;h(1,1),s \\
|31\rangle = |(BT)^e_-\rangle|T^{h1}\rangle|T^{h2}\rangle|\mathcal{T}^e_+\rangle|\mathcal{S}^h\rangle, & e(1,1),t+;h(0,2),s \\
|32\rangle = |(BT)^e_-\rangle|(BT)^h_-\rangle|\mathcal{T}^e_+\rangle|\mathcal{T}^h_0\rangle, & e(1,1),t+;h(1,1),t0
\end{array} \\
\underline{\text{Block 7}} & |33\rangle = |(BT)^e_-\rangle|(BT)^h_-\rangle|\mathcal{T}^e_-\rangle|\mathcal{T}^h_-\rangle, \qquad e(1,1),t-;h(1,1),t- \\
\underline{\text{Block 8}} & |34\rangle = |(BT)^e_-\rangle|(BT)^h_-\rangle|\mathcal{T}^e_+\rangle|\mathcal{T}^h_+\rangle, \qquad e(1,1),t+;h(1,1),t+ \\
\underline{\text{Block 9}} & |35\rangle = |(BT)^e_-\rangle|(BT)^h_-\rangle|\mathcal{T}^e_+\rangle|\mathcal{T}^h_-\rangle, \qquad e(1,1),t+;h(1,1),t- \\
\underline{\text{Block 10}} & |36\rangle = |(BT)^e_-\rangle|(BT)^h_-\rangle|\mathcal{T}^e_-\rangle|\mathcal{T}^h_+\rangle, \qquad e(1,1),t-;h(1,1),t+
\end{array}
\tag{C.5}
$$

$$
\tag{C.6}
$$

$$
\tag{C.7}
$$

$$
\tag{C.8}
$$

$$
\tag{C.9}
$$

$$
\tag{C.10}
$$

The non-perturbed energies of the localized particle basis states (i.e., the main diagonal of the H_{XX} matrix representation) are presented in Figures C.1, C.2 and C.3. We point out that the matrix element notation in these figures differs slightly from that used previously in this text. For example, the Coulomb matrix element V^{eh}_{TBBB} is written as $VTBeBBh$ (similar format for e-h exchange matrix elements) and the localized particle energy ε^e_B is written as EeB.

	Base States	Localized Particle Energies
1	e(2,0),s; h(2,0),s	2EeB+2EhB+(VBBeBBe+VBBhBBh+4VBBeBBh)
2	e(1,1),s; h(2,0),s	EeB+EeT+2EhB+f+(VBBhBBh+VBBeTTe+VBTeBTe)+2(VBBeBBh+VTTeBBh)
3	e(2,0),s; h(1,1),s	2EeB+EhB+EhT−f+(VBBeBBe+VBBhTTh+VBThBTh)+2(VBBeBBh+VBBeTTh)
4	e(2,0),s; h(0,2),s	2EeB+2EhT−2f+(VBBeBBe+VTThTTh+4VBBeTTh)
5	e(1,1),s; h(1,1),s	EeB+EeT+EhB+EhT+(VBBeTTe+VBTeBTe+VBBhTTh+VBThBTh)+(VBBeBBh+VTTeTTh+VBBeTTh+VTTeBBh)
6	e(0,2),s; h(2,0),s	2EeT+2EhB+2f+(VTTeTTe+VBBhBBh+4VTTeBBh)
7	e(0,2),s; h(1,1),s	2EeT+EhB+EhT+f+(VTTeTTe+VBBhTTh+VBThBTh)+2(VTTeTTh+VTTeBBh)
8	e(1,1),s; h(0,2),s	EeB+EeT+2EhT−f+(VTThTTh+VBBeTTe+VBTeBTe)+2(VTTeTTh+VBBeTTh)
9	e(0,2),s; h(0,2),s	2EeT+2EhT+(VTTeTTe+VTThTTh+4VTTeTTh)
10	e(1,1),t0; h(1,1),t0	EeB+EeT+EhB+EhT+(VBBeTTe−VBTeBTe+VBBhTTh−VBThBTh)+(VBBeBBh+VTTeTTh+VBBeTTh+VTTeBBh)
11	e(2,0),s; h(1,1),t0	2EeB+EhB+EhT−f+(VBBeBBe+VBBhTTh−VBThBTh)+2(VBBeBBh+VBBeTTh)
12	e(1,1),s; h(1,1),t0	EeB+EeT+EhB+EhT+(VBBeTTe+VBTeBTe+VBBhTTh−VBThBTh)+(VBBeBBh+VTTeTTh+VBBeTTh+VTTeBBh)

Figure C.1: Biexciton localized particle energies $1 - 12$.

	Base States	Localized Particle Energies
13	e(0,2),s; h(1,1),t0	2EeT+EhB+EhT+f+(VTTeTTe+VBBhTTh−VBThBTh)+2(VTTeTTh+VTTeBBh)
14	e(1,1),t0; h(2,0),s	EeB+EeT+2EhB+f+(VBBhBBh+VBBeTTe−VBTeBTe)+2(VBBeBBh+VTTeBBh)
15	e(1,1),t0; h(1,1),s	EeB+EeT+EhB+EhT+(VBBeTTe−VBTeBTe+VBBhTTh+VBThBTh)+(VBBeBBh+VTTeTTh+VBBeTTh+VTTeBBh)
16	e(1,1),t0; h(0,2),s	EeB+EeT+2EhT−f+(VTThTTh+VBBeTTe−VBTeBTe)+2(VTTeTTh+VBBeTTh)
17	e(2,0),s; h(1,1),t-	2EeB+EhB+EhT−f+(VBBeBBe+VBBhTTh−VBThBTh)+2(VBBeBBh+VBBeTTh)
18	e(1,1),s; h(1,1),t-	EeB+EeT+EhB+EhT+(VBBeTTe+VBTeBTe+VBBhTTh−VBThBTh)+(VBBeBBh+VTTeTTh+VBBeTTh+VTTeBBh)
19	e(0,2),s; h(1,1),t-	2EeT+EhB+EhT+f+(VTTeTTe+VBBhTTh−VBThBTh)+2(VTTeTTh+VTTeBBh)
20	e(1,1),t0; h(1,1),t-	EeB+EeT+EhB+EhT+(VBBeTTe−VBTeBTe+VBBhTTh−VBThBTh)+(VBBeBBh+VTTeTTh+VBBeTTh+VTTeBBh)
21	e(2,0),s; h(1,1),t+	2EeB+EhB+EhT−f+(VBBeBBe+VBBhTTh−VBThBTh)+2(VBBeBBh+VBBeTTh)
22	e(1,1),s; h(1,1),t+	EeB+EeT+EhB+EhT+(VBBeTTe+VBTeBTe+VBBhTTh−VBThBTh)+(VBBeBBh+VTTeTTh+VBBeTTh+VTTeBBh)
23	e(0,2),s; h(1,1),t+	2EeT+EhB+EhT+f+(VTTeTTe+VBBhTTh−VBThBTh)+2(VTTeTTh+VTTeBBh)
24	e(1,1),t0; h(1,1),t+	EeB+EeT+EhB+EhT+(VBBeTTe−VBTeBTe+VBBhTTh−VBThBTh)+(VBBeBBh+VTTeTTh+VBBeTTh+VTTeBBh)

Figure C.2: Biexciton localized particle energies 13 − 24.

	Base States	Localized Particle Energies
25	e(1,1),t-; h(2,0),s	EeB+EeT+2EhB+f+(VBBhBBh+VBBeTTe−VBTeBTe)+2(VBBeBBh+VTTeBBh)
26	e(1,1),t-; h(1,1),s	EeB+EeT+EhB+EhT+(VBBeTTe−VBTeBTe+VBBhTTh+VBThBTh)+(VBBeBBh+VTTeTTh+VBBeTTh+VTTeBBh)
27	e(1,1),t-; h(0,2),s	EeB+EeT+2EhT−f+(VTThTTh+VBBeTTe−VBTeBTe)+2(VTTeTTh+VBBeTTh)
28	e(1,1),t-; h(1,1),t0	EeB+EeT+EhB+EhT+(VBBeTTe−VBTeBTe+VBBhTTh−VBThBTh)+(VBBeBBh+VTTeTTh+VBBeTTh+VTTeBBh)
29	e(1,1),t+; h(2,0),s	EeB+EeT+2EhB+f+(VBBhBBh+VBBeTTe−VBTeBTe)+2(VBBeBBh+VTTeBBh)
30	e(1,1),t+; h(1,1),s	EeB+EeT+EhB+EhT+(VBBeTTe−VBTeBTe+VBBhTTh+VBThBTh)+(VBBeBBh+VTTeTTh+VBBeTTh+VTTeBBh)
31	e(1,1),t+; h(0,2),s	EeB+EeT+2EhT−f+(VTThTTh+VBBeTTe−VBTeBTe)+2(VTTeTTh+VBBeTTh)
32	e(1,1),t+; h(1,1),t0	EeB+EeT+EhB+EhT+(VBBeTTe−VBTeBTe+VBBhTTh−VBThBTh)+(VBBeBBh+VTTeTTh+VBBeTTh+VTTeBBh)
33	e(1,1),t-; h(1,1),t-	(EeB+EeT+EhB+EhT)+(VBBeTTe−VBTeBTe+VBBhTTh−VBThBTh)+(VBBeBBh+VTTeTTh+VBBeTTh+VTTeBBh)+(JBBeBBh+JTTeTTh+JBBeTTh+JTTeBBh)
34	e(1,1),t+; h(1,1),t+	(EeB+EeT+EhB+EhT)+(VBBeTTe−VBTeBTe+VBBhTTh−VBThBTh)+(VBBeBBh+VTTeTTh+VBBeTTh+VTTeBBh)+(JBBeBBh+JTTeTTh+JBBeTTh+JTTeBBh)
35	e(1,1),t+; h(1,1),t-	(EeB+EeT+EhB+EhT)+(VBBeTTe−VBTeBTe+VBBhTTh−VBThBTh)+(VBBeBBh+VTTeTTh+VBBeTTh+VTTeBBh)−(JBBeBBh+JTTeTTh+JBBeTTh+JTTeBBh)
36	e(1,1),t-; h(1,1),t+	(EeB+EeT+EhB+EhT)+(VBBeTTe−VBTeBTe+VBBhTTh−VBThBTh)+(VBBeBBh+VTTeTTh+VBBeTTh+VTTeBBh)−(JBBeBBh+JTTeTTh+JBBeTTh+JTTeBBh)

Figure C.3: Biexciton localized particle energies $25 - 36$.

Finally, in Figures C.4, C.5, C.6, C.7, C.8, C.9,C.10, C.11 and C.12, we give the complete biexciton Hamiltonian matrix in the localized particle basis. For the localized particle energies along the main diagonal (shaded in grey), refer to the previous Figures C.1, C.2 and C.3.

		1	2	3	4
		e(2,0),s; h(2,0),s	e(1,1),s; h(2,0),s	e(2,0),s; h(1,1),s	e(2,0),s; h(0,2),s
1	e(2,0),s; h(2,0),s	E_1	−√2te+√2(VBBeBTe+ 2VBTeBBh)	−√2th+√2(VBBhBTh+ 2VBBeBTh)	VBThBTh
2	e(1,1),s; h(2,0),s	−√2te+√2(VBBeBTe+2 VBTeBBh)	E_2	2VBTeBTh	0
3	e(2,0),s; h(1,1),s	−√2th+√2(VBBhBTh+ 2VBBeBTh)	2VBTeBTh	E_3	−√2th+√2(VBThTT h+2VBBeBTh)
4	e(2,0),s; h(0,2),s	VBThBTh	0	−√2th+√2(VBThTTh+ 2VBBeBTh)	E_4
5	e(1,1),s; h(1,1),s	2VBTeBTh	−√2th+√2(VBBhBTh+ VBBeBTh+VTTeBTh)	−√2te+√2(VBBeBTe+ VBTeBBh+VBTeTTh)	2VBTeTBh
6	e(0,2),s; h(2,0),s	VBTeBTe	−√2te+√2(VBThTTh+ 2VBTeBBh)	0	0
7	e(0,2),s; h(1,1),s	0	2VBTeBTh	VBTeBTe	0
8	e(1,1),s; h(0,2),s	0	VBThBTh	2VBTeBTh	−√2te+√2(VBBeBT e+2VBTeTTh)
9	e(0,2),s; h(0,2),s	0	0	0	VBTeBTe
10	e(1,1),t0; h(1,1),t0	2JBTeBTh	−√2(JBBeBTh- JTTeBTh)	−√2(JBTeBBh- JBTeTTh)	−2JBTeBTh

Figure C.4: Biexciton Hamiltonian matrix representation, 10×10 block, part 1.

		5	6	7
		e(1,1),s; h(1,1),s	e(0,2),s; h(2,0),s	e(0,2),s; h(1,1),s
1	e(2,0),s; h(2,0),s	2VBTeBTh	VBTeBTe	0
2	e(1,1),s; h(2,0),s	−√2th+√2(VBBhBTh+ VBBeBTh+VTTeBTh)	−√2te+√2(VBThTTh+ 2VBTeBBh)	2VBTeBTh
3	e(2,0),s; h(1,1),s	−√2te+√2(VBBeBTe+ VBTeBBh+VBTeTTh)	0	VBTeBTe
4	e(2,0),s; h(0,2),s	2VBTeTBh	0	0
5	e(1,1),s; h(1,1),s	E_5	2VBTeBTh	−√2te+√2(VBTeTTe+V BTeBBh+VBTeTTh)
6	e(0,2),s; h(2,0),s	2VBTeBTh	E_6	−√2th+√2(VBBhBTh+ 2VTTeBTh)
7	e(0,2),s; h(1,1),s	−√2te+√2(VBTeTTe+V BTeBBh+VBTeTTh)	−√2th+√2(VBBhBTh+ 2VTTeBTh)	E_7
8	e(1,1),s; h(0,2),s	−√2th+√2(VBThTTh+ VBBeBTh+VTTeBTh)	0	2VBTeBTh
9	e(0,2),s; h(0,2),s	2VTBeTBh	VBThBTh	−√2th+√2(VTThBTh+ 2VTTeBTh)
10	e(1,1),t0; h(1,1),t0	−(JBBeTTh+JTTeBBh) +(JBBeBBh+JTTeTTh)	−2JBTeBTh	√2(JBTeBBh- JBTeTTh)

Figure C.5: Biexciton Hamiltonian matrix representation, 10 × 10 block, part 2.

		8	9	10
		e(1,1),s; h(0,2),s	e(0,2),s; h(0,2),s	e(1,1),t0; h(1,1),t0
1	e(2,0),s; h(2,0),s	0	0	2JBTeBTh
2	e(1,1),s; h(2,0),s	VBThBTh	0	−√2(JBBeBTh-JTTeBTh)
3	e(2,0),s; h(1,1),s	2VBTeBTh	0	−√2(JBTeBBh-JBTeTTh)
4	e(2,0),s; h(0,2),s	−√2te+√2(VBBeBTe+2VBTeTTh)	VBTeBTe	−2JBTeBTh
5	e(1,1),s; h(1,1),s	−√2th+√2(VBThTTh+VBBeBTh+VTTeBTh)	2VTBeTBh	−(JBBeTTh+JTTeBBh)+(JBBeBBh+JTTeTTh)
6	e(0,2),s; h(2,0),s	0	VBThBTh	−2JBTeBTh
7	e(0,2),s; h(1,1),s	2VBTeBTh	−√2th+√2(VTThBTh+2VTTeBTh)	√2(JBTeBBh−JBTeTTh)
8	e(1,1),s; h(0,2),s	E_8	−√2te+√2(VTTeBTe+2VBTeTTh)	√2(JBBeBTh−JTTeBTh)
9	e(0,2),s; h(0,2),s	−√2te+√2(VTTeBTe+2VBTeTTh)	E_9	2JBTeBTh
10	e(1,1),t0; h(1,1),t0	√2(JBBeBTh−JTTeBTh)	2JBTeBTh	E_{10}

Figure C.6: Biexciton Hamiltonian matrix representation, 10×10 block, part 3.

		11	12	13
		e(2,0),s; h(1,1),t0	e(1,1),s; h(1,1),t0	e(0,2),s; h(1,1),t0
11	e(2,0),s; h(1,1),t0	E_{11}	−√2te+√2(VBBeBTe+VBTeBBh+VBTeTTh)	VBTeBTe
12	e(1,1),s; h(1,1),t0	−√2te+√2(VBBeBTe+VBTeBBh+VBTeTTh)	E_{12}	−√2te+√2(VBTeTTe+VBTeBBh+VBTeTTh)
13	e(0,2),s; h(1,1),t0	VBTeBTe	−√2te+√2(VBTeTTe+VBTeBBh+VBTeTTh)	E_{13}
14	e(1,1),t0; h(2,0),s	2JBTeBTh	−√2(JBBeBTh−JTTeBTh)	−2JBTeBTh
15	e(1,1),t0; h(1,1),s	−√2(JBTeBBh−JBTeTTh)	−(JBBeTTh+JTTeBBh)+(JBBeBBh+JTTeTTh)	√2(JBTeBBh−JBTeTTh)
16	e(1,1),t0; h(0,2),s	−2JBTeBTh	√2(JBBeBTh−JTTeBTh)	2JBTeBTh

		14	15	16
		e(1,1),t0; h(2,0),s	e(1,1),t0; h(1,1),s	e(1,1),t0; h(0,2),s
11	e(2,0),s; h(1,1),t0	2JBTeBTh	−√2(JBTeBBh−JBTeTTh)	−2JBTeBTh
12	e(1,1),s; h(1,1),t0	−√2(JBBeBTh−JTTeBTh)	−(JBBeTTh+JTTeBBh)+(JBBeBBh+JTTeTTh)	√2(JBBeBTh−JTTeBTh)
13	e(0,2),s; h(1,1),t0	−2JBTeBTh	√2(JBTeBBh−JBTeTTh)	2JBTeBTh
14	e(1,1),t0; h(2,0),s	E_{14}	−√2th+√2(VBBhBTh+VBBeBTh+VTTeBTh)	VBThBTh
15	e(1,1),t0; h(1,1),s	−√2th+√2(VBBhBTh+VBBeBTh+VTTeBTh)	E_{15}	−√2th+√2(VBThTTh+VBBeBTh+VTTeBTh)
16	e(1,1),t0; h(0,2),s	VBThBTh	−√2th+√2(VBThTTh+VBBeBTh+VTTeBTh)	E_{16}

Figure C.7: Biexciton Hamiltonian matrix representation, 6×6 block.

		17	18	19	20
		e(2,0),s; h(1,1),t−	e(1,1),s; h(1,1),t−	e(0,2),s; h(1,1),t−	e(1,1),t0; h(1,1),t−
17	e(2,0),s; h(1,1),t−	E_{17}	−√2te+√2(VBBeBTe+VBTeBBh+VBTeTTh)	VBTeBTe	√2(JBTeBBh+JBTeTTh)
18	e(1,1),s; h(1,1),t−	−√2te+√2(VBBeBTe+VBTeBBh+VBTeTTh)	E_{18}	−√2te+√2(VBTeTTe+VBTeBBh+VBTeTTh)	−(JBBeBBh−JTTeTTh)−(JBBeTTh−JTTeBBh)
19	e(0,2),s; h(1,1),t−	VBTeBTe	−√2te+√2(VBTeTTe+VBTeBBh+VBTeTTh)	E_{19}	−√2(JBTeBBh+JBTeTTh)
20	e(1,1),t0; h(1,1),t−	√2(JBTeBBh+JBTeTTh)	−(JBBeBBh−JTTeTTh)−(JBBeTTh−JTTeBBh)	−√2(JBTeBBh+JBTeTTh)	E_{20}

Figure C.8: Biexciton Hamiltonian matrix representation, $1^{\mathbf{st}}$ 4×4 block.

		21	22	23	24
		e(2,0),s; h(1,1),t+	e(1,1),s; h(1,1),t+	e(0,2),s; h(1,1),t+	e(1,1),t0; h(1,1),t+
21	e(2,0),s; h(1,1),t+	E_{21}	−√2te+√2(VBBeBTe+VBTeBBh+VBTeTTh)	VBTeBTe	−√2(JBTeBBh+JBTeTTh)
22	e(1,1),s; h(1,1),t+	−√2te+√2(VBBeBTe+VBTeBBh+VBTeTTh)	E_{22}	−√2te+√2(VBTeTTe+VBTeBBh+VBTeTTh)	(JBBeBBh−JTTeTTh)+(JBBeTTh−JTTeBBh)
23	e(0,2),s; h(1,1),t+	VBTeBTe	−√2te+√2(VBTeTTe+VBTeBBh+VBTeTTh)	E_{23}	√2(JBTeBBh+JBTeTTh)
24	e(1,1),t0; h(1,1),t+	−√2(JBTeBBh+JBTeTTh)	(JBBeBBh−JTTeTTh)+(JBBeTTh−JTTeBBh)	√2(JBTeBBh+JBTeTTh)	E_{24}

Figure C.9: Biexciton Hamiltonian matrix representation, $2^{\mathbf{nd}}$ 4×4 block.

		25	26	27	28
		e(1,1),t−; h(2,0),s	e(1,1),t−; h(1,1),s	e(1,1),t−; h(0,2),s	e(1,1),t−; h(1,1),t0
25	e(1,1),t−; h(2,0),s	E_{25}	−√2th+√2(VBBhBTh+VBBeBTh+VTTeBTh)	VBThBTh	√2(JBBeBTh+JTTeBTh)
26	e(1,1),t−; h(1,1),s	−√2th+√2(VBBhBTh+VBBeBTh+VTTeBTh)	E_{26}	−√2th+√2(VBThTTh+VBBeBTh+VTTeBTh)	−(JBBeBBh−JTTeTTh)+(JBBeTTh−JTTeBBh)
27	e(1,1),t−; h(0,2),s	VBThBTh	−√2th+√2(VBThTTh+VBBeBTh+VTTeBTh)	E_{27}	−√2(JBBeBTh+JTTeBTh)
28	e(1,1),t−; h(1,1),t0	√2(JBBeBTh+JTTeBTh)	−(JBBeBBh−JTTeTTh)+(JBBeTTh−JTTeBBh)	−√2(JBBeBTh+JTTeBTh)	E_{28}

Figure C.10: Biexciton Hamiltonian matrix representation, $3^{\mathbf{rd}}$ 4×4 block.

		29	30	31	32
		e(1,1),t+; h(2,0),s	e(1,1),t+; h(1,1),s	e(1,1),t+; h(0,2),s	e(1,1),t+; h(1,1),t0
29	e(1,1),t+; h(2,0),s	E_{29}	−√2th+√2(VBBhBTh+ VBBeBTh+VTTeBTh)	VBThBTh	−√2(JBBeBTh+JTTeBTh)
30	e(1,1),t+; h(1,1),s	−√2th+√2(VBBhBTh+V BBeBTh+VTTeBTh)	E_{30}	−√2th+√2(VBThTTh+V BBeBTh+VTTeBTh)	(JBBeBBh−JTTeTTh)−(J BBeTTh−JTTeBBh)
31	e(1,1),t+; h(0,2),s	VBThBTh	−√2th+√2(VBThTTh+ VBBeBTh+VTTeBTh)	E_{31}	√2(JBBeBTh+JTTeBTh)
32	e(1,1),t+; h(1,1),t0	−√2(JBBeBTh+JTTeBTh)	(JBBeBBh−JTTeTTh)− (JBBeTTh−JTTeBBh)	√2(JBBeBTh+JTTeBTh)	E_{32}

Figure C.11: Biexciton Hamiltonian matrix representation, $4^{\mathbf{th}}$ 4×4 block.

		33			
		e(1,1),t−; h(1,1),t−	34		
33	e(1,1),t−; h(1,1),t−	E_{33}	e(1,1),t+; h(1,1),t+	35	
	34	e(1,1),t+; h(1,1),t+	E_{34}	e(1,1),t+; h(1,1),t−	36
		35	e(1,1),t+; h(1,1),t−	E_{35}	e(1,1),t−; h(1,1),t+
			36	e(1,1),t−; h(1,1),t+	E_{36}

Figure C.12: Biexciton Hamiltonian matrix representation, four 1×1 blocks.

We point out that e-h exchange matrix elements appear on the main diagonal only for states 33 through 36, which leads to an energy splitting between the bright states 33, 34 and the dark states 35, 36 in the amount of 2×(JBBeBBh + JTTeTTh + JBBeTTh + JTTeBBh). We also observe that the biexciton tunneling rates $t_{e,h}$ are a factor of $\sqrt{2}$ greater than those for the exciton states, since both identical particles can tunnel in the biexciton state. In practice, we find that many of the biexciton matrix elements are negligibly small (as described in Section 3.3) and may be set to zero.

Appendix D

Power Dependence Formulas for the Non-linear Fano Effect

Here, we derive the power dependence formulas for $\Delta_{tot}(P)$ and $q_{Fano}(P)$ that appear in equations (7.21) and (7.22), respectively, from Section 7.2. We attribute the non-linear Fano effect to the different response of the discrete and continuum optical pathways in the Fano scheme [57]. At increased laser powers, the transition amplitude ν_{iX} for optical excitation into the (discreet) indirect exciton state becomes saturated, while the optical transition amplitude ν into the polaron continuum remains in the linear regime. We approximate the saturation and power broadening of the indirect exciton state by treating it as a laser driven two-state system with damping.

From equation (3.103a) in Section 3.4, the absorption of a damped two-level system with power-broadening is:

$$\begin{aligned}
\sigma_{bb} &= \frac{1}{2}\left[\frac{\Omega_1^2\left(\gamma_{deph}/\Gamma_{sp}\right)}{\delta^2+\gamma_{deph}^2+\Omega_1^2\left(\gamma_{deph}/\Gamma_{sp}\right)}\right] \\
&= \frac{1}{2}\frac{1}{\Gamma_{sp}\gamma_{deph}}\left[\frac{\Omega_1^2}{1+\left(\frac{1}{\gamma_{deph}}\right)^2\delta^2+\left(\frac{1}{\Gamma_{sp}\gamma_{deph}}\right)\Omega_1^2}\right] \\
&= \frac{T_1T_2}{2\hbar^2}\left[\frac{E_0^2\mu^2}{1+T_2^2\delta^2+T_1T_2\Omega_1^2}\right] \\
&\propto \frac{E_0^2\mu^2}{1+T_2^2\delta^2+T_1T_2\Omega_1^2},
\end{aligned} \tag{D.1}$$

where the Rabi frequency is $\Omega_1 = -E_0\mu/\hbar$, the radiative lifetime is $T_1 = 1/\Gamma_{sp}$ and

the dephasing rate is $T_2 = 1/\gamma_{deph}$.

To derive the non-linear equations for Δ_{ph} and q_{Fano} as a function of the laser power, we apply equation (D.1) to the indirect exciton transition. We label the transition dipole of the indirect exciton by μ_{iX}. The time constant T_1 is the radiative lifetime of the indirect exciton state and T_2 is its dephasing rate. Then, we relate the phonon-assisted tunneling energy Δ_{ph} to the *pure* dephasing rate of the indirect exciton state:

$$\begin{aligned} \gamma_{deph} &= \frac{\Gamma_{sp}}{2} + \gamma_{pd} \\ &= \frac{\Gamma_{sp}}{2} + \frac{\mathbf{\Delta_{ph}}}{\hbar}, \end{aligned} \tag{D.2}$$

where the factor $1/\hbar$ arises because Δ_{ph} is an energy, while the other terms are relaxation rates.

We consider the inhomogeneous broadening of the indirect exciton state Δ_{ed} that arises from ambient electric field fluctuations to occur on a time scale much longer than the radiative lifetime T_1. Therefore, Δ_{ed} does not effect the dynamics of the indirect exciton state and does not enter into equation (D.2). Instead, Δ_{ed} leads to inhomogeneous broadening of an ensemble of measurements and should be *added separately* to the other energy broadening terms.

We first inspect the power dependence of equation (D.1) to determine the power broadening of the indirect exciton line width, which we label as $\Delta_{ph,eff}(P)$. The broadening of the absorption line in equation (D.1) is given by the half-width at half maximum:

$$\Delta(E_0) \equiv \hbar \cdot \mathrm{FWHM} = \hbar\sqrt{\gamma_{deph}^2 + \Omega_1^2\,(\gamma_{deph}/\Gamma_{sp})}. \tag{D.3}$$

Squaring the above equation yields:

$$\begin{aligned} \Delta(E_0)^2 &= \hbar^2\gamma_{deph}^2 + \hbar^2\Omega_1^2\,(\gamma_{deph}/\Gamma_{sp}) \\ &= \hbar^2\gamma_{deph}^2\left[1 + \Omega^2\left(\frac{1}{\Gamma_{sp}\gamma_{deph}}\right)\right] \\ &= \hbar^2\gamma_{deph}^2\left[1 + \left(\frac{\mu_{iX}^2}{\hbar^2\Gamma_{sp}\gamma_{deph}}\right)E_0^2\right]. \end{aligned} \tag{D.4}$$

Then, taking the square root of (D.4), we may write:

$$\begin{aligned}\Delta(E_0) &= \hbar\gamma_{deph}\sqrt{1+\left(\frac{\mu_{iX}^2}{\hbar^2\Gamma_{sp}\gamma_{deph}}\right)E_0^2} \\ &= \Delta_0\sqrt{1+\left(\frac{\mu_{iX}^2}{\hbar\Gamma_{sp}\Delta_0}\right)E_0^2},\end{aligned} \tag{D.5}$$

where

$$\Delta_0 \equiv \hbar\gamma_{deph} = \left(\frac{\hbar\Gamma_{sp}}{2}+\Delta_{ph}\right). \tag{D.6}$$

Equation (D.5) gives the power broadening of the indirect exciton line width. Attributing this to an effective phonon-assisted tunneling broadening, we set $\Delta_{ph,eff}(E_0) \equiv \Delta(E_0)$ and write:

$$\begin{aligned}\Delta_{ph,eff}(E_0) &= \Delta_0\sqrt{1+\left(\frac{\mu_{iX}^2}{\hbar\Gamma_{sp}\Delta_0}\right)E_0^2} \\ &= \left(\frac{\hbar\Gamma_{sp}}{2}+\Delta_{ph}\right)\sqrt{1+\left[\frac{\mu_{iX}^2}{\hbar\Gamma_{sp}\left(\hbar\Gamma_{sp}/2+\Delta_{ph}\right)}\right]E_0^2} \\ &= \left(\frac{\hbar\Gamma_{sp}}{2}+\Delta_{ph}\right)\sqrt{1+\left[\frac{\mu_{iX}^2}{\hbar\Gamma_{sp}\left(\hbar\Gamma_{sp}/2+\Delta_{ph}\right)}\right]E_0^2} \\ &= \left(\frac{\hbar\Gamma_{sp}}{2}+\Delta_{ph}\right)\sqrt{1+aP},\end{aligned} \tag{D.7}$$

where

$$\begin{aligned}a &= \text{constant}\cdot\frac{\mu_{iX}^2}{\hbar\Gamma_{sp}\left(\hbar\Gamma_{sp}/2+\Delta_{ph}\right)} \\ &= \text{constant}\cdot\frac{\mu_{iX}^2}{\hbar\Gamma_{sp}\hbar\gamma_{deph}} \\ &= \text{constant}\cdot\frac{\mu_{iX}^2T_1T_2}{\hbar^2}.\end{aligned} \tag{D.8}$$

We then make two changes to the above equation. First, we note that $\hbar\Gamma_{sp}/2 << \Delta_{ph}$, so we may neglect the radiative lifetime broadening. Second, we add the inhomogeneous ensemble broadening Δ_{ed} (D.7). Making these changes, we arrive at the power dependence formula for $\Delta_{tot}(P)$:

$$\begin{aligned}\Delta_{tot}(P) =& \Delta_{ed} + \Delta_{ph,eff}(P) \\ =& \Delta_{ed} + \Delta_{ph}\sqrt{1+aP}.\end{aligned} \tag{D.9}$$

Next, we determine the power dependence of $q_{Fano}(P)$. On resonance, we have $\delta = \omega - \omega_0 = 0$, so from (D.1) we may write the resonant absorption as:

$$\sigma_{bb} \propto \frac{E_0^2\mu_{iX}^2}{1+T_1T_2\Omega_1^2} = E_0^2\mu_{iX,eff}^2, \tag{D.10}$$

where

$$\mu_{iX,eff}(E_0) \equiv \frac{\mu_{iX}}{\sqrt{1+T_1T_2\Omega_1^2}}. \tag{D.11}$$

To relate this to the Fano factor, we note that the indirect exciton transition amplitude is given by:

$$\begin{aligned}\nu_{iX,eff}(E_0) =& E_0\mu_{iX,eff}(E_0) \\ =& \frac{E_0\mu_{iX}}{\sqrt{1+T_1T_2\Omega_1^2}} \\ =& \frac{\nu_{iX}}{\sqrt{1+\left(\frac{\mu_{iX}^2T_1T_2}{\hbar^2}\right)E_0^2}}.\end{aligned} \tag{D.12}$$

We point out that in the high power limit, the indirect exciton transition amplitude approaches a constant value: $\nu_{iX,eff}(E_0) \to \hbar/\sqrt{T_1T_2}$. On the other hand, we have assumed that the transition amplitude to the polaron continuum remains a linear function of the laser field E_0:

$$\nu = E_0\mu_{X_0,\Omega}, \tag{D.13}$$

where the transition dipole $\mu_{X_0,\Omega}$ is a constant.

Finally, inserting equations (D.12) and (D.13) into the equation for the q_{Fano} Factor (7.19d) from Section 7.1, we arrive at the power dependence formula for $q_{Fano}(P)$:

$$\begin{aligned} q_{Fano}(P) &= \frac{1}{\pi\rho_0 t}\frac{\nu_{iX,eff}(E_0)}{\nu} \\ &= \frac{1}{\pi\rho_0 t}\frac{E_0\mu_{iX,eff}(E_0)}{\nu} \\ &= \frac{1}{\pi\rho_0 t}\frac{E_0\mu_{iX}}{\nu}\frac{1}{\sqrt{1+T_1T_2\Omega_1^2}} \\ &= \frac{1}{\pi\rho_0 t}\frac{\nu_{iX}}{\nu}\frac{1}{\sqrt{1+\left(\frac{\mu_{iX}^2T_1T_2}{\hbar^2}\right)E_0^2}} \\ &= \frac{q_{Fano,0}}{\sqrt{1+aP}}, \end{aligned} \tag{D.14}$$

where we have set

$$q_{Fano,0} = \frac{1}{\pi\rho_0 t}\frac{\nu_{iX}}{\nu}. \tag{D.15}$$

Bibliography

[1] D. Leonard et al. "Direct formation of quantum-sized dots from uniform coherent islands of InGaAs on GaAs surfaces". In: *Applied Physics Letters* 63.23 (1993), pp. 3203–3205.

[2] J. M. Moison et al. "Self-organized growth of regular nanometer-scale InAs dots on GaAs". In: *Applied Physics Letters* 64.2 (1994), pp. 196–198.

[3] Qianghua Xie et al. "Vertically Self-Organized InAs Quantum Box Islands on GaAs(100)". In: *Phys. Rev. Lett.* 75 (1995), pp. 2542–2545.

[4] J. Y. Marzin et al. "Photoluminescence of Single InAs Quantum Dots Obtained by Self-Organized Growth on GaAs". In: *Phys. Rev. Lett.* 73 (1994), pp. 716–719.

[5] M. Grundmann et al. "Ultranarrow Luminescence Lines from Single Quantum Dots". In: *Phys. Rev. Lett.* 74 (1995), pp. 4043–4046.

[6] D. Gammon et al. "Fine Structure Splitting in the Optical Spectra of Single GaAs Quantum Dots". In: *Phys. Rev. Lett.* 76 (1996), pp. 3005–3008.

[7] M. Bayer et al. "Coupling and Entangling of Quantum States in Quantum Dot Molecules". In: *Science* 291.5503 (2001), pp. 451–453.

[8] Alexander Högele et al. "Voltage-Controlled Optics of a Quantum Dot". In: *Phys. Rev. Lett.* 93 (2004), p. 217401.

[9] T. H. Stievater et al. "Rabi Oscillations of Excitons in Single Quantum Dots". In: *Phys. Rev. Lett.* 87 (2001), p. 133603.

[10] A. Muller et al. "Resonance Fluorescence from a Coherently Driven Semiconductor Quantum Dot in a Cavity". In: *Phys. Rev. Lett.* 99 (2007), p. 187402.

[11] Gregor Jundt et al. "Observation of Dressed Excitonic States in a Single Quantum Dot". In: *Phys. Rev. Lett.* 100 (17 2008), p. 177401.

[12] A. Nick Vamivakas et al. "Spin-resolved quantum-dot resonance fluorescence". In: *Nat Phys* 5 (2009), pp. 198–202.

[13] A. J. Ramsay et al. "Phonon-Induced Rabi-Frequency Renormalization of Optically Driven Single InGaAs/GaAs Quantum Dots". In: *Phys. Rev. Lett.* 105 (2010), p. 177402.

[14] Richard J. Warburton. "Single spins in self-assembled quantum dots". In: *Nat Mater* 12 (2013), pp. 483–493.

[15] Xiaoqin Li et al. "An All-Optical Quantum Gate in a Semiconductor Quantum Dot". In: *Science* 301.5634 (2003), pp. 809–811.

[16] Mete Atatüre et al. "Quantum-Dot Spin-State Preparation with Near-Unity Fidelity". In: *Science* 312.5773 (2006), pp. 551–553.

[17] J. Berezovsky et al. "Picosecond Coherent Optical Manipulation of a Single Electron Spin in a Quantum Dot". In: *Science* 320.5874 (2008), pp. 349–352.

[18] Daniel Brunner et al. "A Coherent Single-Hole Spin in a Semiconductor". In: *Science* 325.5936 (2009), pp. 70–72.

[19] David D. Awschalom et al. "Quantum Spintronics: Engineering and Manipulating Atom-Like Spins in Semiconductors". In: *Science* 339.6124 (2013), pp. 1174–1179.

[20] P. Michler et al. "A Quantum Dot Single-Photon Turnstile Device". In: *Science* 290.5500 (2000), pp. 2282–2285.

[21] Gediminas Juska et al. "Towards quantum-dot arrays of entangled photon emitters". In: *Nat Photon* 7 (2013), pp. 527–531.

[22] H. Bernien et al. "Heralded entanglement between solid-state qubits separated by three metres". In: *Nature* 497 (2013), pp. 86–90.

[23] H. J. Krenner et al. "Direct Observation of Controlled Coupling in an Individual Quantum Dot Molecule". In: *Phys. Rev. Lett.* 94 (2005), p. 057402.

[24] G. Ortner et al. "Control of Vertically Coupled InGaAs/GaAs Quantum Dots with Electric Fields". In: *Phys. Rev. Lett.* 94 (2005), p. 157401.

[25] E. A. Stinaff et al. "Optical Signatures of Coupled Quantum Dots". In: *Science* 311.5761 (2006), pp. 636–639.

[26] M. Scheibner et al. "Photoluminescence Spectroscopy of the Molecular Biexciton in Vertically Stacked InAs-GaAs Quantum Dot Pairs". In: *Phys. Rev. Lett.* 99 (2007), p. 197402.

[27] M. Scheibner et al. "Essential concepts in the optical properties of quantum dot molecules". In: *Solid St. Commun.* 149 (2009), pp. 1427–1435.

[28] Lucio Robledo et al. "Conditional Dynamics of Interacting Quantum Dots". In: *Science* 320.5877 (2008), pp. 772–775.

[29] A. Nick Vamivakas et al. "Observation of spin-dependent quantum jumps via quantum dot resonance fluorescence". In: *Nature* 467 (2010), pp. 279–300.

[30] Danny Kim et al. "Quantum dots with single-atom precision". In: *Nat Phys* 7 (2011), pp. 223–229.

[31] K. Müller et al. "Electrical Control of Interdot Electron Tunneling in a Double InGaAs Quantum-Dot Nanostructure". In: *Phys. Rev. Lett.* 108 (19 2012), p. 197402.

[32] N. Sköld et al. "Rabi Oscillations of Excitons in Single Quantum Dots". In: *Phys. Rev. Lett.* 110 (2013), p. 016804.

[33] C. Hermannstädter et al. "Polarization fine structure and enhanced single-photon emission of self-assembled lateral InGaAs quantum dot molecules embedded in a planar microcavity". In: *Journal of Applied Physics* 105.12 (2009).

[34] M. Scheibner et al. "Entangled photon pair generation with quantum dot molecules". In: *J. Opt. Soc. Am. B* 29.2 (2012).

[35] Markus Müller et al. "On-demand generation of indistinguishable polarization-entangled photon pairs". In: *Nat. Photon.* 8.3 (2014), pp. 224–228.

[36] Swati Ramanathan et al. "Quantum-confined Stark effects in coupled InAs/GaAs quantum dots". In: *Applied Physics Letters* 102.21, 213101 (2013).

[37] Mark L. Kerfoot et al. "Optophononics with coupled quantum dots". In: *Nat Commun* 5 (2014).

[38] A.S. Bracker et al. "Engineering electron and hole tunneling with asymmetric InAs quantum dot molecules". In: *Applied Physics Letters* 89.23 (2006), p. 233110.

[39] A. Forchel C. Schneider S. Höfling. *Quantum Dots: Optics, Electron Transport and Future Applications*. Ed. by A. Tartakovskii. Cambridge University Press, 2012. Chap. Growth of III-V semiconductor quantum dots.

[40] Z. R. Wasilewski, S. Fafard, and J. P. McCaffrey. "Size and shape engineering of vertically stacked self-assembled quantum dots". In: *Journal of Crystal Growth* 201–202 (1999), pp. 1131–1135.

[41] M. Scheibner et al. "Optically mapping the electronic structure of coupled quantum dots". In: *Nat Phys* 4 (2008), pp. 291–295.

[42] Neil W. Ashcroft and N. David Mermin. *Solid State Physics*. Belmont, CA: Brooks/Cole, 1976.

[43] Charles Kittel. *Introduction to Solid State Physics*. Hoboken, NJ: Wiley, 2005.

[44] M. I. Dyakonov. *Spin Physics in Semiconductors*. Ed. by M. I. Dyakonov. Springer Series in Solid-State Sciences, Vol. 157. Springer, 2008. Chap. Basics of Semiconductor and Spin Physics.

[45] `http://www.ioffe.ru/SVA/NSM/Semicond/InAs/`. Accessed: 2014-10-16.

[46] `http://www.ioffe.ru/SVA/NSM/Semicond/GaAs/`. Accessed: 2014-10-16.

[47] J. A. Barker and E. P. O'Reilly. "Theoretical analysis of electron-hole alignment in InAs-GaAs quantum dots". In: *Phys. Rev. B* 61 (2000), pp. 13840–13851.

[48] M. Bayer et al. "Fine structure of neutral and charged excitons in self-assembled In(Ga)As/(Al)GaAs quantum dots". In: *Phys. Rev. B* 65 (2002), p. 195315.

[49] I. V. Ponomarev et al. "Theory of spin states in coupled quantum dots". In: *physica status solidi (b)* 243.15 (2006), pp. 3869–3873.

[50] M. F. Doty et al. "Antibonding Ground States in InAs Quantum-Dot Molecules". In: *Phys. Rev. Lett.* 102 (4 2009), p. 047401.

[51] C. Fabre G. Grynberg A. Aspect. *An Introduction to Quantum Optics From the Semi-Classical Approach to Quantized Light*. Cambridge, UK: Cambridge University Press, 2010.

[52] A. M. Fox A. J. Ramsay. *Quantum Dots: Optics, Electron Transport and Future Applications*. Ed. by A. Tartakovskii. Cambridge University Press, 2012. Chap. Coherent control of quantum dot excitons.

[53] C. Klingshirn. *Semiconductor Optics,* 2nd Edition. Springer, 2005.

[54] Andrey Miroshnichenko, Sergej Flach, and Yuri Kivshar. "Fano resonances in nanoscale structures". In: *Rev. Mod. Phys.* 82 (2010), pp. 2257–2298.

[55] Yong S Joe, Arkady M Satanin, and Chang Sub Kim. "Classical analogy of Fano resonances". In: *Physica Scripta* 74.2 (2006), p. 259.

[56] Ugo Fano. "Effects of Configuration Interaction on Intensities and Phase Shifts". In: *Phys. Rev.* 124 (1961), pp. 1866–1878.

[57] M. Kroner et al. "Resonant saturation laser spectroscopy of a single self-assembled quantum dot". In: *Physica E: Low-dimensional Systems and Nanostructures* 40.6 (2008), pp. 1994–1996.

[58] Paul A. M. Dirac. *Quantum Mechanics,* 3rd Edition. Amen House, London: Oxford University Press, 1947.

[59] R. P. Feynman, R. B. Leighton, and M. Sands. *The Feynman Lectures on Physics*. Pearson Addison Wesley, 2006.

[60] L. Fedichkin and A. Fedorov. "Error rate of a charge qubit coupled to an acoustic phonon reservoir". In: *Phys. Rev. A* 69 (3 Mar. 2004), p. 032311.

[61] G. Granger et al. "Quantum interference and phonon-mediated back-action in lateral quantum-dot circuits". In: *Nat Phys* 8 (2012), pp. 522–527.

[62] Jozef T Devreese and Alexandre S Alexandrov. "Fröhlich polaron and bipolaron: recent developments". In: *Reports on Progress in Physics* 72 (2009), p. 066501.

[63] Jozef T Devreese. "Polarons". In: *Encyclopedia of Applied Physics* 14 (1996), pp. 383–409.

[64] H. Fröhlich, H. Pelzer, and S. Zienau. "XX. Properties of slow electrons in polar materials". In: *Philosophical Magazine Series 7* 41.314 (1950), pp. 221–242.

[65] Ph. Lelong and S. H. Lin. "Polaron model in self-assembled InAs/GaAs quantum dots – A perturbative approach". In: *Applied Physics Letters* 81 (2002), pp. 1002–1004.

[66] E.P. Pokatilov et al. "Polarons in an ellipsoidal potential well". In: *Physica E: Low-dimensional Systems and Nanostructures* 4.2 (1999), pp. 156–169.

[67] Edward B. Flagg et al. "Resonantly driven coherent oscillations in a solid-state quantum emitter". In: *Nat Phys* 5 (2009), pp. 203–207.

[68] D. J. Griffiths. *Introduction to Quantum Mechanics,* 2nd Edition. Upper Saddle River, NJ: Pearson Prentice Hall, 2005.

[69] D. J. Griffiths. *Introduction to Electrodynamics,* Third Edition. Upper Saddle River, NJ: Pearson Prentice Hall, 1999.

[70] P. W. Fry et al. "Inverted Electron-Hole Alignment in InAs-GaAs Self-Assembled Quantum Dots". In: *Phys. Rev. Lett.* 84 (4 Jan. 2000), pp. 733–736.

[71] Nianbei Li et al. "Colloquium: Phononics: Manipulating heat flow with electronic analogs and beyond". In: *Rev. Mod. Phys.* 84 (3 July 2012), pp. 1045–1066.

[72] Martin Maldovan. "Narrow Low-Frequency Spectrum and Heat Management by Thermocrystals". In: *Phys. Rev. Lett.* 110 (2 Jan. 2013), p. 025902.

[73] Martin Maldovan. "Sound and heat revolutions in phononics". In: *Nature* 503 (7475 2013), pp. 209–217.

[74] B. K. Ridley. "Hot electrons in low-dimensional structures". In: *Reports on Progress in Physics* 54.2 (1991).

[75] M. Scheibner et al. "Polarization dynamics in self-assembled CdSe/ZnSe quantum dots: The role of excess energy". In: *Phys. Rev. B* 67 (15 2003), p. 153302.

[76] Kushal C. Wijesundara et al. "Tunable exciton relaxation in vertically coupled semiconductor InAs quantum dots". In: *Phys. Rev. B* 84 (8 2011), p. 081404.

[77] I. Favero et al. "Acoustic phonon sidebands in the emission line of single InAs/GaAs quantum dots". In: *Phys. Rev. B* 68 (2003), p. 233301.

[78] F. Marsilgio and J. P. Carbotte. *Superconductivity: Conventional and Unconventional Superconductors. Vol. 1, Ch. 3.* Ed. by K. H. Bennemann and J. B. Ketterson. Springer, 2008.

[79] I Wilson-Rae and A Imamoglu. "Quantum dot cavity-QED in the presence of strong electron-phonon interactions". In: *Physical Review B* 65.23 (2002), p. 235311.

[80] Preden Roulleau et al. "Coherent electron-phonon coupling in tailored quantum systems". In: *Nat. Commun.* 2 (2011), p. 239.

[81] Kunie Ishioka et al. "Coherent optical phonons in diamond". In: *App. Phys. Lett.* 89.23 (2006).

[82] Muneaki Hase and Masahiro Kitajima. "Interaction of coherent phonons with defects and elementary excitations". In: *Journal of Physics: Condensed Matter* 22.7 (2010), p. 073201.

[83] Simon Wall et al. "Ultrafast changes in lattice symmetry probed by coherent phonons". In: *Nat. Commun.* 3 (2012), p. 721.

[84] Maria N. Luckyanova et al. "Coherent Phonon Heat Conduction in Superlattices". In: *Science* 338.6109 (2012), pp. 936–939.

[85] J H Kim et al. "Coherent phonons in carbon nanotubes and graphene". In: *Chemical Physics* 413 (2013), pp. 55–80.

[86] D. Leuenberger et al. "Excitation of Coherent Phonons in the One-Dimensional Bi(114) Surface". In: *Phys. Rev. Lett.* 110 (13 2013), p. 136806.

[87] J. R. Petta et al. "Coherent Manipulation of Coupled Electron Spins in Semiconductor Quantum Dots". In: *Science* 309.5744 (2005), pp. 2180–2184.

[88] Kristiaan De Greve et al. "Quantum-dot spin-photon entanglement via frequency downconversion to telecom wavelength". In: *Nature* 491.7424 (2012), pp. 421–425.

[89] S. Hughes et al. "Influence of electron-acoustic phonon scattering on off-resonant cavity feeding within a strongly coupled quantum-dot cavity system". In: *Phys. Rev. B* 83 (16 2011), p. 165313.

[90] Arka Majumdar et al. "Phonon-mediated coupling between quantum dots through an off-resonant microcavity". In: *Phys. Rev. B* 85 (19 2012), p. 195301.

[91] Markus Aspelmeyer, Pierre Meystre, and Keith Schwab. "Quantum optomechanics". In: *Physics Today* 65.7 (2012), pp. 29–35.

[92] K. Stannigel et al. "Optomechanical Quantum Information Processing with Photons and Phonons". In: *Phys. Rev. Lett.* 109 (1 2012), p. 013603.

[93] Yu. A. Pusep et al. "Raman study of interface modes subjected to strain in InAs/GaAs self-assembled quantum dots". In: *Phys. Rev. B* 58 (4 1998), R1770–R1773.

[94] J. J. Sakurai. *Modern Quantum Mechanics,* Revised Edition. Reading, Massachusetts: Addison-Wesley, 1994.

[95] A. O. Govorov. "Interband optical absorption in the Wannier-Stark ladder under the electron-LO-phonon resonance condition". In: *Solid State Communications* 92.12 (1994), pp. 977–982.

[96] A. Boyer de la Giroday et al. "Exciton-Spin Memory with a Semiconductor Quantum Dot Molecule". In: *Phys. Rev. Lett.* 106 (21 May 2011), p. 216802.

[97] A. A. Clerk, X. Waintal, and P. W. Brouwer. "Fano Resonances as a Probe of Phase Coherence in Quantum Dots". In: *Phys. Rev. Lett.* 86 (20 2001), pp. 4636–4639.

[98] Andreas Bärnthaler et al. "Probing Decoherence through Fano Resonances". In: *Phys. Rev. Lett.* 105 (5 2010), p. 056801.